UNIVERSITÉ PARIS-EST

Ecole Doctorale

Mathématiques et Sciences et Technologies de l'Information et de la Communication (MSTIC)

THÈSE

Pour obtenir le grade de

Docteur de l'Université Paris-Est

Spécialité : Electronique, Optronique et Systèmes

Présentée et soutenue publiquement par

Noha ALI ABOULELA GABER

Le 11 Septembre 2014

OPTOFLUIDIQUE
Etudes expérimentales, théoriques et de modélisation

OPTOFLUIDICS
Experimental, theoretical studies and modeling

Directeur de thèse

Professeur Tarik BOUROUINA

Professeur Elodie RICHALOT

Document confidentiel : articles en cours de dépôt

Jury

Hans ZAPPE, Professeur, Université de Freiburg, Allemagne	Rapporteur
Agnès MAITRE, Professeur, Institut des Nanosciences de Paris INSP	Rapporteur
Diaa KHALIL, Professeur, Université d'Ain-Shams, Egypte	Examinateur
Dan ANGELESCU, Professeur, Université Paris-Est, ESIEE Paris	Examinateur
Elodie RICHALOT, Professeur, Université Paris-Est, UPEMLV	Examinateur
Tarik BOUROUINA, Professeur, Université Paris-Est, ESIEE Paris	Examinateur

RESUME

Ce travail porte sur l'étude de propriétés optiques des fluides à échelle micrométrique. A cet effet, nous avons conçu, réalisé et étudié différents types de micro-résonateurs optofluidiques, sous forme de laboratoires sur puce. Notre analyse est fondée sur la modélisation analytique et numérique, ainsi que sur des mesures expérimentales menées sur des micro-cavités optiques; nous utilisons l'une d'entre elles pour des applications de réfractométrie de fluides homogènes et de fluides complexes ainsi que pour la localisation par piégeage optique de microparticules solides. Nous nous sommes d'abord concentrés sur l'étude d'une nouvelle forme de micro-cavité Fabry-Pérot basée sur des miroirs courbes entre lesquels est inséré un tube capillaire permettant la circulation d'une solution liquide. Les résultats expérimentaux ont démontré la capacité de ce dispositif à être utilisé comme réfractomètre avec un seuil de détection de $1{,}9 \times 10^{-4}$ RIU pour des liquides homogènes. De plus, pour un liquide contenant des particules solides, la capacité de contrôler la position des microparticules, par des effets de piégeage optique ou de liaison optique, a été démontrée avec succès. Dans un second temps, un résonateur optique est formé simplement à partir d'une goutte de liquide disposée sur une surface super-hydrophobe. La forme quasi-sphérique résultante est propice à des modes de galerie. Il est démontré que, jusqu'à des tailles de gouttelettes millimétriques, la technique de couplage en espace libre est toujours en mesure d'accéder à ces modes à très faible queue évanescente d'interaction, contrairement à ce qu'indiquait jusqu'ici la littérature. De tels résonateurs optofluidiques à gouttelette devraient trouver leur application notamment comme capteur d'environnement de l'air ambiant ou encore comme incubateur de micro-organismes vivants pouvant être suivis par voie optique.

Mots-clés : optofluidique, micro-résonateur optique, laboratoire sur puce, analyse des liquides, résonateur Fabry-Pérot, surfaces incurvées, résonateur à gouttelette.

ABSTRACT

This work focuses on the study of optical properties of fluids at the micrometer scale. To this end, we designed, implemented and studied different types of *optofluidic* micro-resonators in the *Lab-on-Chip* format. Our analysis is based on analytical and numerical modeling, as well as experimental measurements conducted on optical microcavities; we use one of them for refractometry applications on homogeneous fluids and on complex fluids, as well as for the localization of solid microparticles by optical trapping. We first focused on the study of a new form of Fabry-Perot micro-cavity based on curved mirrors between which a capillary tube is inserted for injecting a fluidic solution. Experimental results demonstrated the ability of this device to be used as a refractometer with a detection limit of 1.9×10^{-4} RIU for homogeneous liquids. Furthermore, for liquid containing solid particles, the ability to control the microparticles position either by optical trapping or optical binding effects has been successfully demonstrated. In a second step, an optical resonator is simply formed from a liquid droplet placed on top of a superhydrophobe surface. The resulting quasi-spherical shape supports resonant whispering gallery modes. It is shown that, up to millimeter size droplets, the proposed technique of free-space coupling of light is still able to access these modes with very low evanescent tail interaction, contrary to what was indicated in the literature so far. Such optofluidic droplet resonators are expected to find their applications for environmental air quality monitoring, as well as for incubator of living micro-organisms that can be monitored optically.

Keywords: optofluidics, optical micro-resonators, lab on a chip, liquid analysis, Fabry-Pérot cavity, curved surfaces, droplet resonator.

TABLE OF CONTENTS

LIST OF FIGURES

LIST OF TABLES

RESUME LONG EN FRANÇAIS

I.1. Introduction

Au cours des dernières années, des efforts importants ont été consacrés au développement de nouveaux dispositifs basés sur les micro- et nano-technologies et dédiés à la santé humaine, parmi lesquels ceux permettant l'analyse des systèmes biologiques -telles que des cellules vivantes- à l'aide des technologies opto-micro-fluidiques ont reçu une attention particulière. Le terme "opto-fluidique" est utilisé pour désigner un domaine tirant avantage de l'optique/photonique et de la micro-fluidique; il recouvre notamment les capteurs optiques et le piégeage optique des particules ou des cellules à détecter. La tendance dans la fabrication de nombreux appareils est à leur miniaturisation et leur intégration sur puce. Cela permet d'une part d'obtenir une analyse rapide et précise avec de petits échantillons; d'autre part ces dispositifs peuvent être alliés à d'autres modules comme les MEMS (Micro-Electro-Mechanical Systems) et l'électronique des télécommunications à haut vitesse; enfin, dans une production de masse par la technique de micro-fabrication, cette miniaturisation permet de fortement réduire le prix.

Dans ce travail, nous nous intéressons principalement à un nouveau module de détection et de piégeage optique ; il s'agit d'un Micro résonateur optique constitué de deux miroirs de Bragg cylindriques avec un micro-tube placé entre eux, formant une cavité de Fabry-Pérot stable de facteur de qualité élevé. Au début du chapitre 2, une étude analytique détaillée, appuyée par des simulations numériques, a été réalisée sur des versions simplifiées de ce dispositif pour avoir une idée de ses performances optiques. Ensuite, le chapitre 3 présente l'utilisation de l'appareil comme réfractomètre. Des travaux expérimentaux ont été réalisés pour démontrer sa possible utilisation en réfractométrie de mélanges liquides non-linéaires et étudier la possibilité de l'appliquer aux colloïdes. Puis, le chapitre 4 étudie l'utilisation de ce dispositif pour faire du piégeage optique et immobiliser les échantillons pendant leur détection. Enfin dans le chapitre 5, un autre type de résonateur optique pouvant supporter des modes avec des facteurs de qualité encore plus élevés, à savoir les modes de galerie des résonateurs sphériques, a été étudié. Nous avons pu démontrer que les grosses gouttelettes engendrant des résonances de fort facteur de qualité peuvent être excitées par une nouvelle technique d'excitation utilisant les faisceaux gaussiens en espace libre, ce qui était considéré comme inefficace dans la littérature précédente.

I.2. Micro- résonateurs Fabry-Pérot avec des surfaces incurvées

Les résonateurs Fabry-Pérot (FP) sont des composantes fondamentales dans de nombreuses applications optiques. Les cavités longues sont préférables pour leur fort facteur de qualité *Q*, mais cette longue distance provoque l'élargissement de faisceau gaussien jusqu'à ce qu'il s'échappe de la cavité ouverte ce qui dégrade ses performances. Pour être stables, ces résonateurs ont besoin de miroirs courbes pour focaliser le faisceau; cela est réalisé de façon optimale pour les faisceaux à symétrie circulaire à l'aide de miroirs sphériques. Mais ces miroirs ne peuvent pas être facilement fabriqués par les technologies de fabrication disponibles actuellement. Dans un travail antérieur [1], cette difficulté a été évitée par la combinaison de la courbure de deux surfaces: dans le plan transversal (parallèle à la tranche de silicium), la courbure est obtenue par les miroirs de Bragg silicium-Air de forme cylindrique pour fournir une stabilité dans ce plan; puis une fibre cylindrique est introduite entre les miroirs pour focaliser le faisceau dans la direction verticale. La différence de performance du confinement optique entre l'ensemble de ces structures est illustrée sur la Fig. I.1 (a) à (d). Afin d'utiliser ce dispositif pour des applications de détection, la fibre est remplacée par un micro-tube qui permet l'insertion d'un fluide et de microparticules à l'intérieur de la cavité pour l'analyser optiquement, comme illustré sur la Fig. I.1 (e).

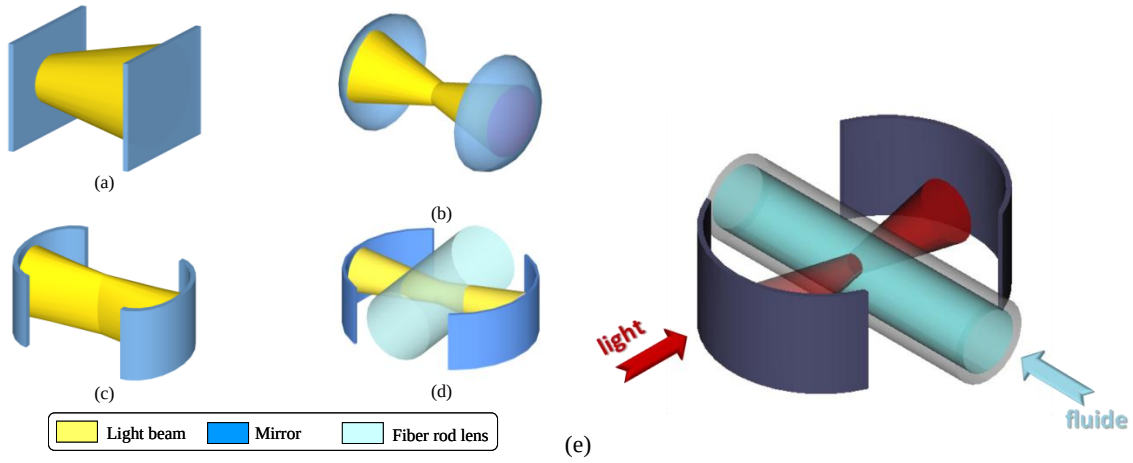

Fig. I.1 Représentation schématique des architectures de Fabry-Perot avec des formes différentes de miroir: (a) des miroirs plans, (b) des miroirs sphériques permettant un confinement 2D de la lumière, (c) les miroirs cylindriques conduisant à un confinement 1D de la lumière et (d) les miroirs cylindriques combinés avec une fibre cylindrique, en fournissant le confinement 2D de la lumière comme dans le cas (b) [1]. (e) Schéma de la cavité de Fabry-Pérot cylindrique avec le micro tube à l'intérieur.

Dans cette partie, nous présentons des simulations numériques HFSS-FEM pour vérifier les performances de confinement de ces structures. Mais en raison des limitations dans les ressources de calcul, le modèle devait être réduit d'environ 1 ordre de grandeur.

Par ailleurs, la symétrie de la structure est exploitée afin de limiter la simulation à seulement un quart de la structure. La Fig. I.2 montre ces modèles dans les cas d'une cavité FP simple avec miroirs de Bragg cylindriques, et après l'ajout de la fibre cylindrique à l'intérieur, à la longueur d'onde λ correspond à la résonance dans chaque cas. Le premier cas montre un bon confinement de la lumière dans la direction horizontal (le long de l'axe-x) uniquement en raison de la courbure dans les miroirs de Bragg; tandis que le dernier cas montre un confinement supplémentaire dans la direction verticale (le long de l'axe-z) également, ce qui permet d'avoir des niveaux d'intensité de champ plus élevés à l'intérieur de la cavité.

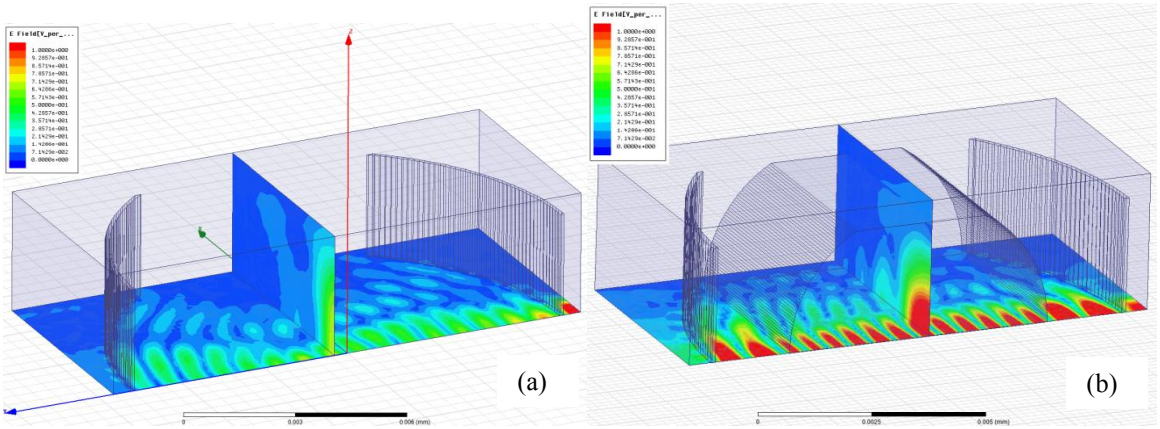

Fig. I.2 Simulations HFSS illustrant le confinement de la lumière (a) Confinement 1D à l'intérieur de la cavité FP avec des miroirs de Bragg cylindriques uniquement. Le faisceau de lumière est confiné le long de l'axe X, à λ = 1548,5 nm, grâce à des surfaces cylindriques tandis qu'elle diverge le long de l'axe Z, où la cavité se comporte comme une cavité FP classique avec des réflecteurs planaires. (b) Confinement 2D de la lumière à l'intérieur de la cavité FP formée par des miroirs de Bragg cylindriques et une fibre cylindrique. Le faisceau de lumière est confiné en 2D, à λ = 1548,5 nm, grâce à la combinaison des réflecteurs et de la fibre.

Pour notre nouvelle structure, adaptée pour effectuer des mesures de réfractométrie sur des liquides d'essai, une étude de stabilité a été effectuée afin de déterminer la gamme d'indices de réfraction pouvant être insérés à l'intérieur du micro-tube tout en préservant la stabilité de la cavité et le fort confinement. Cette gamme dépend de la géométrie de la cavité. Après avoir développé une approche analytique, nous avons montré que pour la structure réelle d'environ 280 um de longueur, cette gamme est comprise entre 1,1526 et 1,6673; tandis que pour les petits modèles simulés ici, cette gamme est comprise entre 1,15 et 2,03. La Fig. I.3 montre la répartition de champ électrique du modèle réduit à la longueur d'onde de résonance lorsque le micro-tube est rempli d'un liquide d'essai avec un indice de réfraction n_t = 1.3. Elle confirme la préservation du confinement élevé de la lumière à l'intérieur du tube.

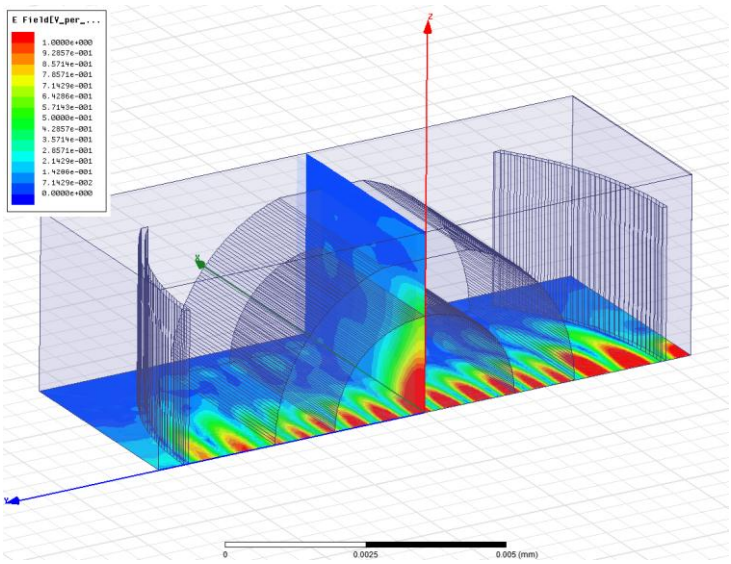

Fig. I.3 Répartition du champ électrique à la résonance pour un liquide d'essai d'un indice de réfraction n_t =1.3, à une longueur d'onde de 1576 nm correspondant au pic de résonance principal.

I.3. Réfractométrie des liquides

La mesure d'indice de réfraction dans des systèmes micro-fluidiques est d'un grand intérêt car elle est sans marqueur et permet la détection de la présence ou de la nature des liquides et des échantillons biologiques. Afin de comparer les nombreuses technologies disponibles, il convient de faire une distinction claire entre la mesure d'indice de réfraction de surface et la mesure d'indice de réfraction de volume. Les capteurs d'indice de réfraction de surface sont basés sur l'interaction entre un échantillon et une onde électromagnétique évanescente. Cela les rend sensibles à la contamination de surface. Dans le cas de capteurs d'indice de réfraction de volume, la lumière se propage à travers l'échantillon et la profondeur d'interaction est fortement augmentée. Parmi les différentes techniques de détection d'indice de réfraction de volume on trouve les cavités Fabry-Pérot, comme notre dispositif présenté dans l'encart de la Fig. I.4, qui a l'avantage sur les cavités FP précédemment présentées dans la littérature d'atteindre des facteurs de qualité élevés.

Notre dispositif consiste en une puce de silicium fabriquée en utilisant le procédé amélioré de la gravure ionique réactive profonde présenté dans [2]. La puce contient plusieurs cavités FP de longueurs différentes et de nombres de couches des miroirs de Bragg différents. Avoir plusieurs cavités disponibles sur la même puce peut faciliter la recherche de compromis entre le facteur de qualité et la gamme spectrale libre. Les cavités courtes permettent d'obtenir une large gamme pour effectuer une estimation approximative de l'indice de réfraction, alors qu'une cavité plus longue avec une sensibilité plus élevée donne une mesure plus fine. La Fig.

I.4 montre cette puce sur ses positionneurs avec les fibres d'entrée/sortie, et un encart zoomée montre les différentes cavités FP. Les miroirs sont des miroirs de Bragg cylindriques de silicium/air. Un micro-tube en silice fondue est placé entre les miroirs et relié à un tube externe de plus grand diamètre pour permettre l'injection du fluide, tout en permettant de réaliser le confinement du faisceau gaussien dans le plan vertical.

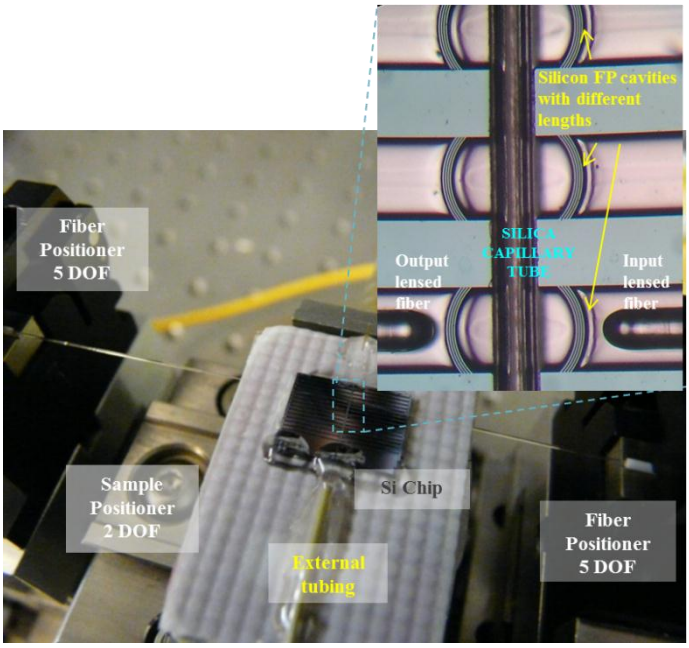

Fig. I.4 Image du dispositif de mesure illustrant la puce de silicium avec le tube capillaire relié à la colonne d'injection, et les fibres d'entrée/sortie sur leurs positionneurs. L'encart est un zoom des différentes cavités, qui indique également l'emplacement de la paire de fibres, l'une étant utilisée pour l'injection de lumière et l'autre pour l'enregistrement de la réponse spectrale de transmission.

Fig. I.5 montre le système expérimental utilisé pour tester le réfractomètre. La source lumineuse utilisée est une source laser accordable dans les bandes L et C; et le détecteur utilisé est un wattmètre. Une paire des fibres monomodes avec des extrémités dénudées et clivées est utilisée pour injecter et recueillir la lumière en entrée et sortie de la cavité. Dans certains cas, des fibres lentilles de Corning avec une taille de spot de 18 µm et une distance de travail de 300 µm sont utilisées à la place. Le rendement des fibres lentilles est supérieur, mais celles-ci ne peuvent pas être collées à la puce afin de réduire les variations d'alignement lors de la mesure, comme cela est fait avec les fibres classiques (peu chères). Une lumière laser visible à 635 nm est parfois utilisée à des fins d'alignement. La lumière visible et la lumière infrarouge sont couplées par un coupleur directionnel puis injectés dans la fibre d'entrée de la cavité. Des positionneurs à cinq axes sont utilisés pour aligner chaque fibre dans les rainures d'entrée et de sortie, tandis que l'échantillon est monté sur un positionneur à deux axes. Tous les éléments sont montés sur une table optique de réduire les effets de vibration.

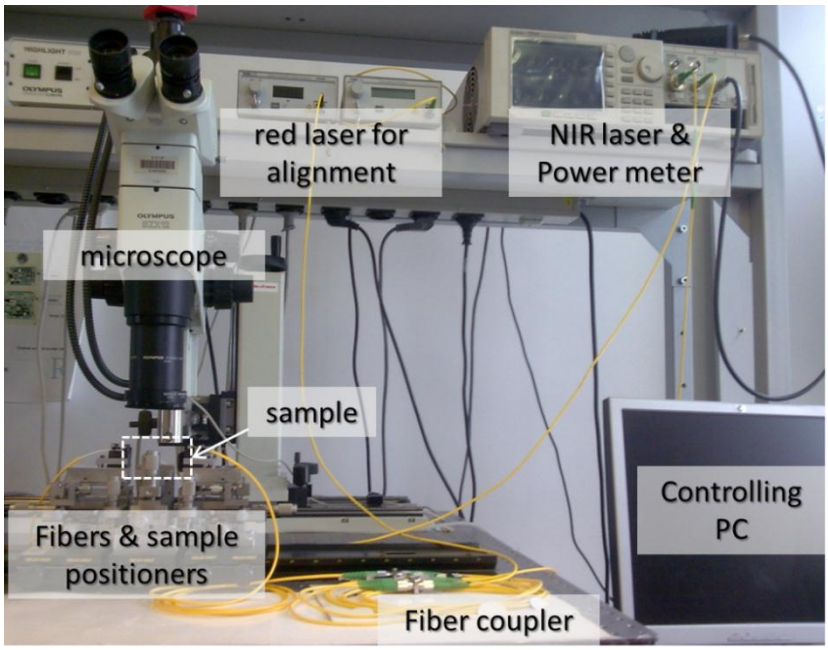

Fig. I.5 Le système de mesure en laboratoire. L'échantillon présenté sur la Fig. I.5 est inséré à l'intérieur du rectangle en pointillés blancs.

Pour caractériser la performance de notre réfractomètre, des mélanges de toluène et de l'acétone avec des ratios différents sont testés. Ces deux liquides ont été choisis car leur absorption est presque identique. Le spectre de chaque mélange a été enregistré, ces spectres sont présentés sur la Fig. I.6.

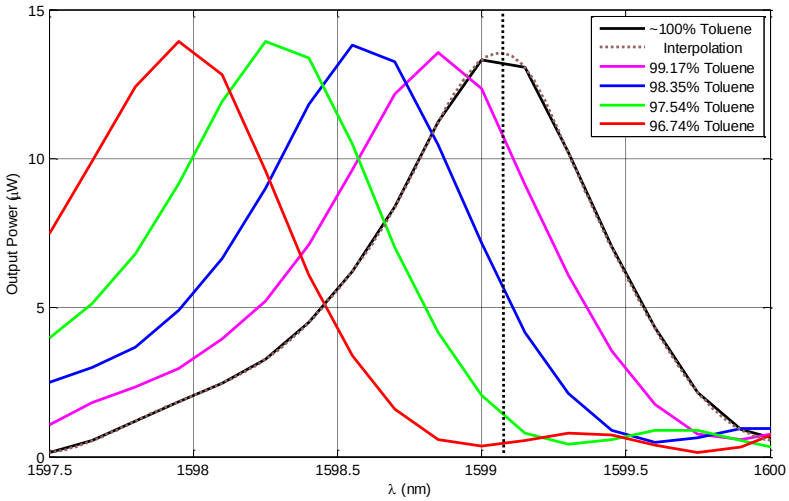

Fig. I.6 Les spectres de mélanges de toluène et d'acétone de différents ratios mesurés par le dispositif de réfractométrie proposé.

Pour déterminer le changement d'indice de réfraction en fonction du liquide, deux méthodes peuvent être utilisées:

1- Détecter la longueur d'onde des maxima:

C'est le procédé classique dans de telles mesures. La longueur d'onde du maximum du pic change lors de la modification de la longueur du trajet optique avec celle de l'indice de réfraction du liquide. Dans ce cas, on obtient une sensibilité de 353 nm/RIU et une gamme de 3,45 nm (avant d'interférer avec le pic suivant), ce qui équivaut à environ 0,01 de changement de RIU, et une limite de détection d'environ 6×10^{-4} RIU.

2- Détecter la diminution de puissance à une longueur d'onde fixe:

Pour obtenir une meilleure sensibilité, nous pouvons profiter de la rapide diminution de l'inclinaison du pic résultant du facteur de qualité élevé et de la grande visibilité pour détecter également la baisse de puissance à la place de la longueur d'onde du maximum. La longueur d'onde du maximum du graphe de toluène pur est prise comme référence (la ligne en pointillés noirs). Lorsque la longueur d'onde de résonance se décale en raison du changement d'indice de réfraction, l'amplitude du signal optique à cette longueur d'onde diminue en fonction de l'amplitude du décalage spectral de la résonance. La ligne de référence coupe donc les graphes successifs à des valeurs de puissance différentes, à partir desquelles l'amplitude des décalages spectraux et ainsi les valeurs de l'index de réfraction peuvent être évaluées (mais seulement dans la gamme sur laquelle le pic peut être approché par une droite). L'objectif de cette technique de mesure est de se débarrasser des appareils de spectroscopie sophistiqués (source à large bande ou lasers accordables). En effet, par la détermination de l'indice de réfraction à partir de la lecture de puissance à une seule longueur d'onde, un unique photodétecteur et un laser d'une seule longueur d'onde sont alors nécessaires. La sensibilité dans ce cas a été évaluée à environ 5,5 mW/RIU, et la gamme est -2,73 μW < ΔP < -12,12 μW, ce qui est équivalent à 0,0005 < Δn < 0,0022.

I.3.1 Réfractométrie de colloïdes

Après l'étude ci-dessus présentée sur des mélanges de deux fluides miscibles, la phase suivante consiste à étudier le potentiel de notre réfractomètre pour mesurer des fluides complexes, tels que les "colloïdes".

Les spectres de l'eau déionisée et de l'eau déionisée contenant des microsphères de polystyrène de diamètre 0,5 μm dans des concentrations différentes, allant de 2,5% à 0,43% ont été enregistrés à l'aide du dispositif de mesure précédent. La lumière est injectée à partir de la longueur d'onde de balayage du laser accordable et mesurée par le wattmètre en utilisant

des fibres clivées ordinaires collées à la puce, afin de minimiser les perturbations vibratoires. Les spectres mesurés sont représentés sur la Fig. I.7. En présence des microsphères, en particulier avec des concentrations élevées (les 2,5% de matières solides (par rapport au volume) en suspension aqueuse, ce qui équivaut à $3{,}64 \times 10^{11}$ particules/ml), le spectre est fortement perturbé, en comparaison avec celui du fluide exempt de particules. Ces perturbations dans le spectre prennent la forme de pointes qui pourraient être dues à la diffusion ou à d'autres types d'interactions impliquant les particules. Ces perturbations sont moins fortes pour les concentrations de particules inférieures, et elles évoluent au cours du temps. Les spectres différents sont décalés progressivement en raison de la réduction de l'indice de réfraction efficace avec celle de la teneur en solides, sachant que le polystyrène a un indice de réfraction plus élevé que l'eau DI, soit 1,6. Le facteur de qualité augmente aussi grâce à la diminution de la dispersion pour un nombre de particules inférieur. Le décalage de la résonance et l'élargissement des pics ont également été vérifiés par des simulations HFSS-FEM.

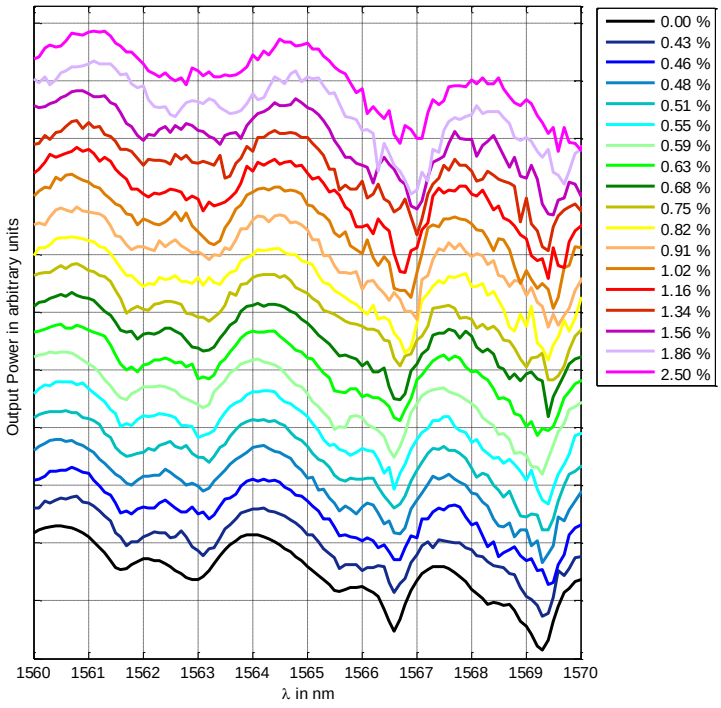

Fig. I.7 Les spectres de l'eau déionisée seule et contenant des microsphères de polystyrène de diamètre 0,5 µm avec des concentrations différentes allant de 2,5% à 0,43%. A noter que la référence de puissance a été modifiée pour chaque graphe de manière à les superposer pour une meilleure comparaison.

Si une fibre à lentille est utilisée pour injecter la lumière, l'efficacité du confinement de la lumière à l'intérieur de la cavité est plus élevée; et, par conséquent, un niveau de puissance plus élevé à l'intérieur de la cavité est attendu. Dans ce cas, un phénomène

intéressant est observé: les microsphères ont tendance à s'agréger ou à s'accumuler avec le temps pour former un nuage sous l'effet du faisceau lumineux comme le montre la Fig. I.8. La puissance de la source dans ce cas est de 4 mW.

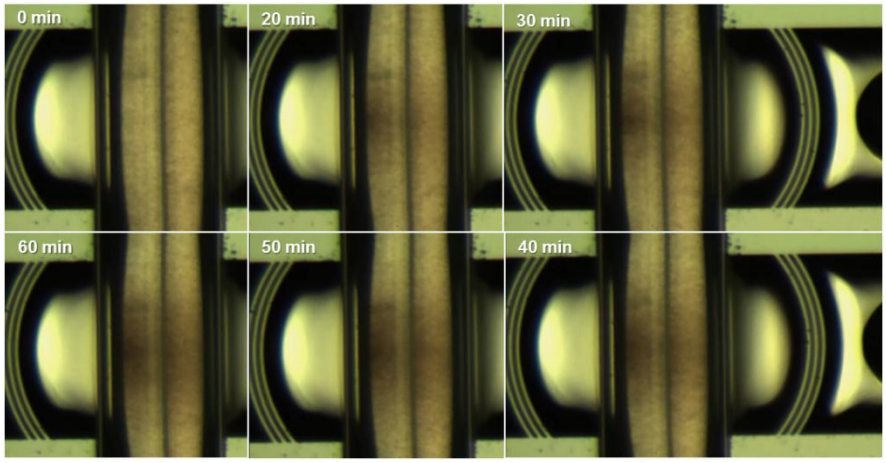

Fig. I.8 L'agrégation optique des microsphères avec le temps.

Cet effet a été attribué au phénomène de liaison optique (en lien étroit avec le phénomène de piégeage optique). Ces phénomènes sont étudiés en détails et sont démontrés expérimentalement dans la section suivante.

I.4. Piégeage optique et liaison optique

Dans la vie quotidienne, il n'est pas très commun de considérer que la lumière peut produire une action mécanique résultant d'un effet direct du champ électromagnétique. En fait, la force appliquée par la lumière a peu d'effet sur le monde macroscopique; il est trop faible pour provoquer un mouvement observable sur de gros objets. Cependant, l'avènement de la technologie laser a permis de concentrer la lumière et de produire les forces nécessaires pour déplacer des objets micro/nano sur l'échelle de l'angström et même propulser ces petits objets sur plusieurs millimètres. Depuis lors, le piégeage optique a suscité une attention considérable en raison de ses importantes applications dans le traitement et l'analyse des microparticules (en particulier les entités biologiques simples) ainsi que leur tri. A cet effet, la majorité des systèmes expérimentaux adoptent des faisceaux lumineux focalisés dans l'espace libre pour obtenir le gradient de champ électromagnétique nécessaire à l'obtention des pinces optiques; mais le plus souvent, le dispositif optique est hors puce et nécessite une puissance optique assez élevée, typiquement des centaines de milliwatts ou même quelques watts.

Pour éviter les pinces optiques universelles en espace libre que sont volumineuses, l'utilisation de structures optiques intégrées et de résonateurs optiques est largement étudiée

afin d'effectuer le piège optique sur la puce, avec de faibles puissances et une taille compacte. Ces recherches ont conduit à la mise au point de configurations différentes pour réaliser la localisation et/ou la manipulation simple des microparticules. Mais parmi toutes ces techniques, aucune ne permet le traitement en trois dimensions (3D) comme avec les pinces optiques classiques. Jusqu'à présent, la meilleure configuration miniaturisée en termes de compromis entre la simplicité et la faible puissance optique d'une part et le rendement du piégeage et la manipulation d'autre part, est probablement le piège à double faisceau en contre-propagation qui est réalisé à l'aide de deux fibres optiques monomodes. Ce type de piège a l'avantage de canaliser les objets placés entre les deux ondes opposées provenant des deux fibres sans nécessiter de composants de focalisation, parce que les forces optiques opposées générées piègent les particules. Une onde stationnaire est formée par interférence entre ces deux ondes se propageant dans des directions opposées, mais dans certains cas - si nécessaire - cette onde stationnaire peut être évitée en déplaçant légèrement les fibres afin de simplifier l'analyse du système. Bien que le piège à double faisceau soit simple, il faut diviser le trajet de la lumière pour injecter la lumière de deux côtés, ce qui rend ce dispositif fortement dépendant de l'alignement de la fibre mutuelle.

L'utilisation de notre cavité de Fabry-Pérot permet d'éviter ces problèmes en fournissant les deux ondes se propageant en sens opposés sous la forme d'une onde stationnaire résultant des réflexions multiples de la lumière (qui est injectée à partir d'un seul côté), et ceci uniquement à l'aide des miroirs des deux cavités. De cette façon, les particules peuvent être piégées et alignées suivant l'axe de la cavité, en raison de l'intensité lumineuse plus élevée aux ventres de l'onde stationnaire formée, comme on peut le voir sur la Fig. I.9, qui montre des microsphères de polystyrène de diamètre 1 μm dans l'eau déionisée alignées le long de l'axe de la cavité, quand un faisceau de longueur d'onde de 1592,4 nm -qui correspond à la résonance de la cavité - est injecté. Le facteur de qualité de cette résonance est d'environ 1090, et la finesse est d'environ 7. L'utilisation d'un résonateur stable, de facteur de qualité élevé, permet d'augmenter l'amplitude du champ à l'intérieur de la cavité proportionnellement à sa finesse, et ainsi de réaliser le piégeage avec de lumière de faibles niveaux de puissance, la puissance de la source dans le cas présenté étant seulement de 30 mW.

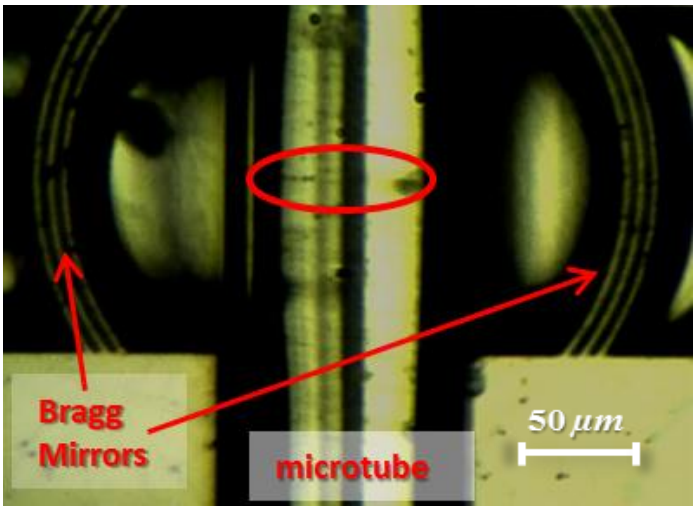

Fig. I.9 Assemblage 1D des microsphères de polystyrène de diamètre 1 μm dans l'eau déionisée formé le long de l'axe de la cavité grâce à la lumière à la longueur d'onde de la résonance fondamentale de la cavité soit 1592,4 nm.

Cependant, dans certaines conditions de taille et/ou de concentration des particules, les particules illuminées optiquement induisent leurs propres champs diffusés en interaction mutuelle, conduisant à leur auto-arrangement en grappes (comme celui présenté sur la Fig. I.10), ou ce qu'on appelle la 'matière optique'. Ce phénomène intéressant de l'interaction entre la lumière et la matière est désigné comme la 'liaison optique'. Il peut se produire pour n'importe quelles conditions d'illumination, aussi bien en résonance ou qu'hors résonance.

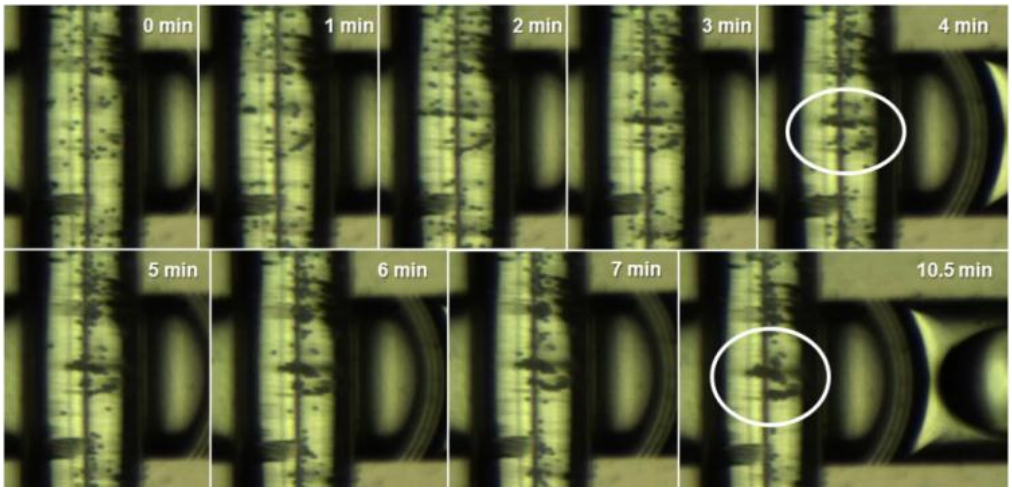

Fig. I.10 L'accumulation des microsphères de polystyrène de diamètre 3 μm à l'intérieur de la cavité sur un durée de temps d'environ 10 min.

Le comportement des particules, qu'il s'agisse uniquement de l'effet de liaison optique ou d'un effet hybride alliant liaison optique et piégeage optique, semble dépendant de la façon dont les particules perturbent le champ en raison de leur taille et/ou de leur distribution. La formation d'un assemblage 1D de particules disposées axialement se produit lorsque la taille des particules est petite et leur concentration est faible ; dans ce cas, les

particules permettent la conservation du motif d'ondes stationnaires avec ses taches de haute intensité bornées par une forte pente d' intensité optique (comme on le voit dans les résultats de simulations numériques de la section I.2), de sorte que les particules se retrouvent piégées à l'intérieur de cette région de haute intensité, principalement en raison de la force du gradient optique de ces taches.

Mais lorsque les particules sont de grand taille (comme les microsphères de 3 μm de diamètre montrées sur la Fig. I.10), ou encore lorsque les particules sont de petite taille, mais leur concentration est élevée (comme indiqué précédemment sur la Fig. I.8), la distribution du champ initial est perturbé et on observe la formation de grappes de particules de forme arbitraire liées aux forces de diffusion entre les particules.

I.5. Résonateurs sphériques

Dans cette section est étudié le couplage de la lumière avec des résonateurs optiques sous forme de gouttelettes au moyen d'un faisceau gaussien en espace libre. Cette méthode est présentée comme une alternative aux méthodes de couplage précédemment rapportées générés à travers des fibres coniques ou de prismes. Bien qu'applicable aux résonateurs optiques à l'état solide, cette méthode est étudiée ici dans le contexte de l'optofluidique pour préserver l'intégrité de la forme des gouttelettes et pour faciliter les étapes d'alignement et de couplage de la lumière. La goutte de glycérol à l'étude est supportée par une surface super-hydrophobe, qui se compose de nanostructures de silicium revêtues par une couche de Téflon et appelée 'silicium noir' -comme illustré par le schéma de la Fig. I.11-, et ceci afin de maintenir la goutte à un endroit précis, tout en conservant une forme presque sphérique.

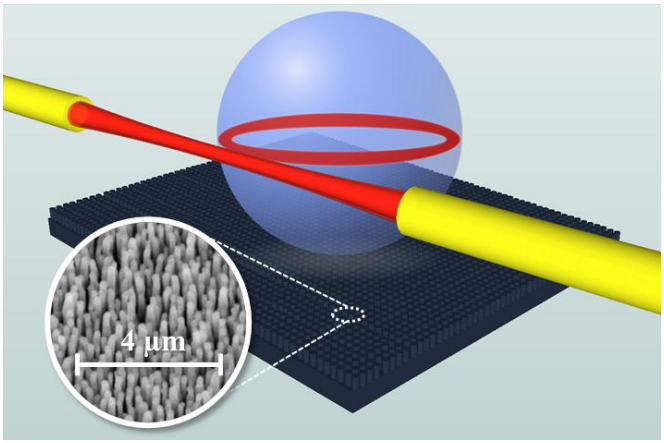

Fig. I.11 Le couplage en utilisant un faisceau gaussien en espace libre, la gouttelette est supportée sur un substrat de silicium noir, revêtu de Téflon, qui forme une surface super-hydrophobe. L'encart est une image par un microscope électronique à balayage du substrat.

L'efficacité de cette méthode est testée pour des gouttelettes de taille millimétrique et des gouttelettes de centaines de micromètre de diamètre avec la mesures de leurs réponses spectrales, ainsi que l'observation directe de modes dans le domaine visible, comme illustré sur la Fig. I.12, et la Fig. I.13, respectivement. Les facteurs de qualité aussi élevées que 6,7 × 10^3 ont été enregistrés. Le dispositif expérimental est similaire à celui des mesures précédentes, après avoir bien sûr remplacé la puce des cavités FP par le résonateur sphérique.

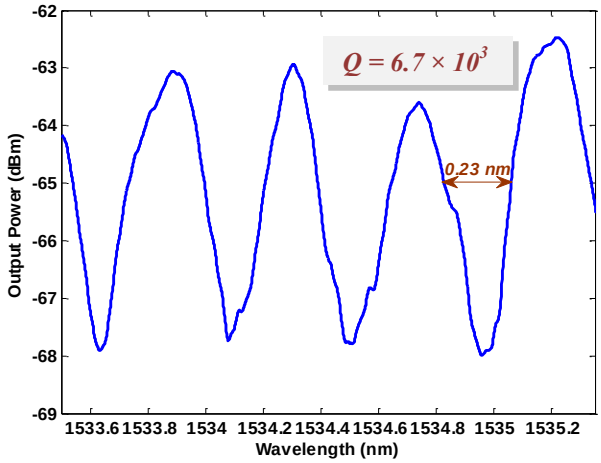

Fig. I.12 Spectre de puissance de sortie pour une gouttelette de diamètre1,16 mm excitée par un faisceau gaussien avec une taille de rayon de 9 µm. La largeur de bande à 3dB est de 0,23 nm, le facteur de qualité total est de 6,7 × 10^3.

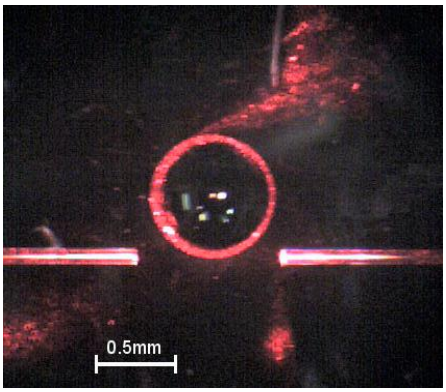

Fig. I.13 La démonstration expérimentale d'un mode de galerie excité par un faisceau gaussien à l'aide d'un ensemble de fibres à lentilles émettant un faisceau gaussien de largeur 25µm, dans une goutte de glycérol de diamètre environ 0,86 mm. Bien que les mesures aient été effectuées en utilisant la lumière infrarouge, la lumière visible dans la figure est celle d'un laser rouge secondaire utilisé pour l'alignement.

Un modèle analytique pour le facteur de qualité externe (ou couplage) associé à cette technique de couplage est développé. Un exemple de l'effet des paramètres de couplage et des dimensions du résonateur est présenté sur la Fig. I.14. Les valeurs élevées des facteurs de

qualité de couplage prouvent que le facteur de qualité global ne sera probablement pas limité par la technique de couplage dans le cas présent.

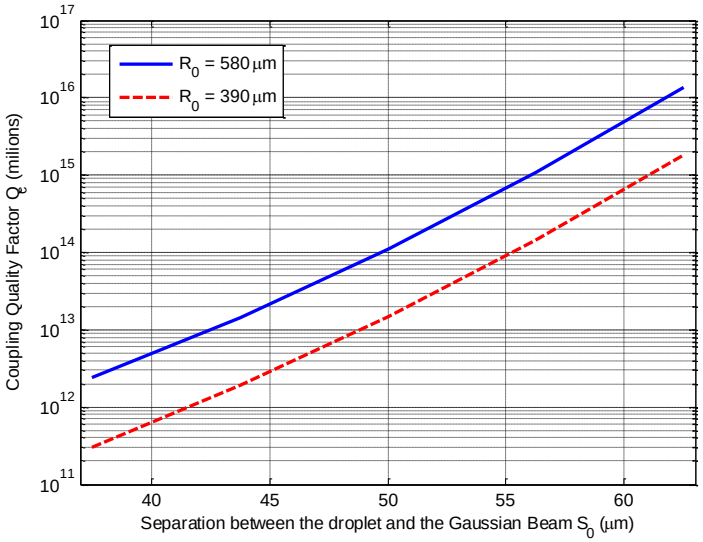

Fig. I.14 Facteur de qualité de couplage Q_c à une distance de séparation S_0 différente pour des gouttelettes de glycérol avec des rayons de 580 µm and 390 µm; en utilisant un faisceau gaussien de largeur W_0 = 25 µm.

I.6. Conclusion et perspectives

Dans cette thèse, nous avons présenté la conception, la modélisation et les mesures de différentes architectures de microcavités optiques, et utilisé l'une d'elles pour des applications de réfractométrie et de piégeage optique. Tout d'abord, nous nous sommes concentrés sur l'étude d'une nouvelle génération de cavités de FP à base de miroirs de Bragg courbes et d'un tube capillaire entre les deux miroirs pour permettre l'insertion de la solution de mesure -qui peut être un liquide homogène ou contenant des particules – pour la caractériser optiquement. Les résultats expérimentaux ont démontré la capacité de ce dispositif à être utilisé comme réfractomètre, ainsi que sa capacité à piéger des microparticules par piégeage optique et/ou liaison optique. Dans un second temps, un autre type de résonateurs pouvant supporter des modes de facteur de qualité plus élevés, à savoir les modes galerie à l'intérieur des résonateurs sphériques, a été étudié. Il a été démontré que la technique de couplage en l'espace libre permet d'exciter ces modes supportés par de grosses gouttelettes, ce couplage s'effectuant en très faible interaction avec la queue évanescente du mode d'extension réduite. Un facteur de qualité de $6,7 \times 10^3$ a été atteint, pour une gouttelette en glycérol de diamètre 1,16 mm et supportée par une surface hydrophobe. Cette valeur est censée être limitée seulement par la perte d'absorption de la glycérine dans cette gamme de longueur d'onde.

Ce travail fournit des axes de recherches nombreux. On peut citer parmi eux, pour le premier dispositif constitué de la cavité FP avec un micro-tube, la possibilité de piégeage et d'analyse simultanée des particules et des cellules pourrait être étudiée expérimentalement par le couplage d'une source laser à la résonance de la cavité avec une lumière à large spectre d'une source à large bande, tout en enregistrant le spectre par un analyseur de spectre.

Pour le deuxième résonateur formé d'une gouttelette de liquide supportée par la surface hydrophobe, des petites particules pourraient être introduites à l'intérieur de la gouttelette afin d'étudier la capacité à les piéger par l'onde résonant dans la région équatoriale, ce qui introduirait un décalage de résonance permettant la détection.

I.7. Références

[1] M. Malak, "A Contribution to Photonic MEMS: Study of Optical Resonators and Interferometers Based on All-Silicon Bragg Reflectors," PhD thesis, Université Paris-Est, 2011.

[2] F. Marty, L. Rousseau, B. Saadany, B. Mercier, O. Français, Y. Mita, T. Bourouina, "Advanced Etching of Silicon Based On Deep Reactive Ion Etching For Silicon High Aspect Ratio Microstructures and Three-Dimensional Micro and Nano Structures," Microelectron. J., vol. 36, pp. 673-677, 2005.

CHAPTER (1)

INTRODUCTION

1.1 General Background

In recent years, the research effort devoted to human health started taking significant benefit from the high potential of micro- and nano-technologies in various forms. This holds true, to a certain extent, to the field of environment as well. Research on so-called *Lab-on-a-Chip* or alternatively, *Micro Total Analysis Systems* (μTAS), started in the early 90s [1,2] and has attracted increasing interest since that time, not only for the purpose of biochemical analysis and point-of-care diagnosis, but also in order to provide new tools for the advancement of science. In particular, studies involving the analysis of living organisms combined with sorting and manipulation capabilities received special attention; DNA analysis, immunoassays, blood cell cytometry, analysis of bacterial content of drinking water and airborne particles analysis are typical applications that can be implemented on-chip. Today, Lab-on-a-chip devices are on the margin of becoming self-contained laboratories confined to the size of integrated chips. These devices have enabled the miniaturization of many of the important operations done before on a much larger scale for chemical and biochemical processes. The last two decades has seen the development of devices which allow for mixing, separation, and detection of chemical and biological species, all done with reduced costs and increased efficiency not seen in conventional beaker-scale laboratory techniques. Advantages of these techniques include: (1) decreased use of the samples and reagents volumes to nano-liters and even femto-liters of fluids, (2) the confinement of chemical processes to small volumes, which decreases the time needed for reactions and sensor detection mechanisms, and (3) the ability to build complex architecture networks on chip, allowing for multiplexed processing and high throughput.

An important key of the development of these devices is the co-integration of microfluidic environments with the transducers needed for actuation and detection purposes. These are mainly consisting of two categories: electrical and optical. While electrical transduction means have been intensively studied, '*Optofluidics*' represents a quite recent subfield of microfluidics and microphotonics. It involves the exploitation of the unique

physics presented by the coupling of micro- nanophotonics with micro- nanofluidics [3-4] taking advantage of downscaling. Numerous devices have already demonstrated the ability to actively manipulate optical energy within such systems as a means to generate complex trapping fields [5], sort flowing targets in microfluidic channels [6], and levitate particles through radiation pressure [7]. On the other hand, light also provides the ability to implement various kinds of measurements based on fluorescence, optical spectroscopy, refractometery, image processing or even simply through modulation of light intensity.

1.2 Novelty of the thesis

In this work, we investigate various novel optofluidic concepts at the micro-scale, with emphasis on curved geometrical shapes, which are found to be advantageous regarding optics as compared to Cartesian shapes, as they provide confinement of the electromagnetic field, enabling several functionalities including collimation, focusing and high quality resonance. Curved shapes are also found naturally in several fluidic materials in the form of droplets, bubbles and even in the form of complex fluids, which include foams, emulsions and colloids. Combining optics and fluidics within the same miniaturized component, in the Lab-on-Chip format, enabled characterization of fluid properties through implementation of both optical measurement and optical manipulation techniques. To this end, optical resonators have been developed and studied, some of which being suitable for both sensing and optical trapping applications. More specifically, the following two different types of optical resonator are studied in this thesis:

The first type of resonator is a new architecture of Fabry-Pérot micro-cavity based on curved surfaces. Taking advantage of curved surfaces shows higher performance in terms of the quality factor compared to the conventional planar cavities due to improved light confinement. It consists of two silicon-Air Bragg mirrors of cylindrical shape to provide confinement of light in the horizontal plane; it also contains a micro-tube that holds the sample to be analyzed, and also acting as a lens to confine light along the vertical plane. Such device provides good functionality as a refractometer for both homogeneous and complex fluids, with the additional capability of achieving optical trapping of suspended solid micro particles. Such trapped micro-particle (which are here polystyrene microspheres, but they also could be a living cell for instance or a DNA strand) can be therefore immobilized in the fluid in a specific location within the fluid. Such intra-cavity trapping is found to be a novel on-

chip optical trapping configuration, which requires only single-side injection of light and reduced optical power. This on-chip trapping technique also has the ability to perform further analysis of the trapped partricle, namely through *in situ* spectral analysis. Finally, this same device also shows a good potential to operate as on-column, non-destructive detector (refractometer) for liquid chromatography applications.

The second type of optical resonator is a liquid version of the spherical optical resonators, which is a droplet optical resonator that support ultra-high quality factor resonant modes named Whispering Gallery modes (WGMs). These nearly spherical liquid droplets are formed on the top of a super-hydrophobic surface, which is consisting of Teflon-coated nanostructured silicon, called 'black silicon'. We could demonstrate that rather large droplets, in the millimeter and hundreds of micrometers diameters range, supporting high quality factor resonance, could be excited by free space excitation technique using Gaussian beams, which was believed to be inefficient in previous literature. Such excitation technique preserves the integrity of both the resonator and the optical tools, which is not guaranteed in the conventional excitation techniques, while harnessing the full benefit from large size resonators with extra-high quality factors.

1.3 Objectives and Motivation

On the quest for miniaturized and cost-effective optofluidic device for sensing applications, the use of silicon micro-fabrication technology comes as a natural choice. It allows distributing the cost on many integrated devices fabricated at once by mass fabrication, while taking advantage of unrivaled dimensional accuracy in the micrometer range, by a proper combination of photolithography and plasma etching techniques. Also optical-based instrumentation is well known for its superior metrological performance and increasing maturity, especially following the recent advances in micro-optics and fiber-coupled miniaturized sources and detectors. Optical resonators are widely used for spectroscopy in sensing application. They can be used to obtain the transmission and/or reflection spectra of the analyte samples under test. Due to their optical field enhancement, optical microresonators found a wide place in the field of *optomechanics* and more specifically in this thesis, an extension within the optical trapping research area. This capability of intra-cavity field enhancement also enables the reduction of the required optical source power levels to achieve optical trapping over those required for off-chip optical trapping techniques.

Fabry-Pérot micro-cavity exploiting curved surfaces can achieve better performance over the conventional cavities based on planar mirrors, according to the better confinement of light. This ultimate performance is achieved in principle by spherical mirrors. But such mirrors cannot be easily fabricated by the available micro-fabrication technologies so far. This difficulty could be overcome by emulating the "3D surface" of a spherical mirror by distributing the curvature on two orthogonal "2D surfaces" both having a cylindrical shape, which are more easily accessible: the first curvature along the transverse plane (parallel to the silicon substrate) is defined by lithography and subsequent plasma etching of silicon, the resulting cylindrical curvature is also used to construct silicon-Air Bragg mirrors of cylindrical shape, whose role is to confine the beam within this plane. Then, a second cylindrical surface, made of a Fiber Rod Lens (FRL) is placed in-between the mirrors in a post-fabrication step, whose role is to focus the beam along the vertical plane. After achieving high quality factors over 8000 with such resonant cavity despite its rather long cavity physical length of more than 260µm in a previous project [8], it was very appealing to benefit from such high performance in sensing and trapping applications in a fluidic environment. To do so, we replaced the solid cylindrical FRL by a cylindrical hollow micro-tube, which provides available space to introduce liquid samples –that may also contain solid particles and even micro-bubbles- inside that tube. The promising fast roll-off of the resonant peak with high quality factor can be exploited for performing sensitive detection for any small change in the refractive index by tracing the change in the output power at a fixed wavelength tuned at the steep side of the peak. Upon success in doing that, the required optical source and detector to perform the measurement will be much cheaper than those required to capture a wide spectral response. Beside the rather low cost of a single silicon chip fabricated by mass production process, the overall price of the refractometre can be therefore reduced in a significant manner.

On the other hand, if the initial design and fabrication process of an integrated device is not affordable, other types of resonators -that can be realized by other methods and still give high performance- are in need. We thereby present a second device realized as a liquid droplet spherical resonator of millimeter size, which can be used as a very sensitive detector of both external and internal environmental changes, and even to interactions through its interface, such as nanoparticle adsorption events. The ultra-high quality factors that can be achieved using such resonator are very motivating. Also its rather easy, fast and casual fabrication by just forming a droplet make it –in cases when the optical fiber alignment setup

and skills are available– a competitive device to the complex MEMS fabricated devices that need design, mask layout, and other lengthy, expensive and time consuming fabrication steps.

1.4 Organization of the thesis

This first chapter serves as an overall introduction to the thesis, to present a brief background explaining the meaning and domain of the field: "optofluidic lab-on-a-chip". Then, the thesis is presented in other four chapters.

Chapter 2 gives a general background on Fabry-Pérot cavities, explaining the concepts of field enhancement and field confinement inside the optical cavities. Then more specific analytical theoretical models, numerical analyses and design considerations are presented for different versions of Fabry-Pérot micro-cavities exploiting curved surfaces for better light confinement: (1) Simple cavity with cylindrical silicon-air Bragg mirrors. (2) The previous cavity after inserting Fiber Rod Lens (FRL) for additional confinement in the orthogonal plane. (3) The previous cavity after replacing the FRL by a capillary tube to allow inserting a fluid inside the cavity for sensing and trapping applications. A performance evaluation between the different versions is presented, with the focus on the third cavity that is studied in more details since it is introduced for the first time in this thesis and it will be used in various applications through the next chapters.

Then Chapter 3 explores the use of the third version (the cavity with the hollow micro-tube filled with liquid) in refractometry applications. A brief introduction is stated to discuss the different refractometry devices and their application domains. Then a study on mixing optically non-linear liquids is done in order to assign their optical parameters values, which are needed to characterize our refractometer. Then, experimental study and evaluation of our device are done using optically non-linear liquids, while operating the refractometer with two different modes of operations: (1) Tracing the peak maxima shift in wavelength upon changing the analyte refractive index. (2) Tracing the power drop at a fixed wavelength on the peak slope upon shifting the peak, with the objective of putting away the expensive spectrum analyzers. Also experiments on the refractometry of colloids are performed, where some exotic spikes in the spectrum are observed and attributed to temporally varying scattering of light, with the help of numerical simulations. Besides the observation of another interesting phenomenon due to optical binding, that is studied in detail within the next chapter.

After that, Chapter 4 presents the domain of optical trapping. At the beginning, a theoretical background is introduced to explain the principle of optical trapping and to state the physics and mathematical theories behind it. Also a thorough literature review is done to present the advent of optical trapping tools and their different configurations, whether to be in free-space or guided propagation of light, whether it is implemented on a macroscopic bench or on-chip, and to evaluate and compare their performance with respect to our newly introduced on-chip intra-cavity configuration. Then, another related phenomenon, named optical binding, is introduced as a part of the literature review, since it helps explaining the experiment results that follow this section. Different experimental observations are shown, using variety of micro-particle sizes and concentrations injected inside our device. These observations are explained –with the help of numerical FEM-HFSS simulations– to be attributed to different effects of optical trapping and binding.

Finally, chapter 5 investigates another type of optical resonator that can support modes with even higher quality factor values, which are Whispering Gallery modes (WGMs) in spherical resonators. Such resonators are realized as liquid nearly spherical droplets supported by a hydrophobic surface. But before presenting this device, a literature review is done to present different versions of cavities that can support WGMs; followed by the different coupling methods used previously in literature to couple light inside large cavities that supports such WGMs, to compare them with our new free-space coupling technique using a Gaussian beam. Then a comparison between small droplets of micrometer size and the millimeter droplets is presented to assist understanding the exclusivity of our work. The resonance WGMs supported by spherical resonators are presented analytically and numerically by HFSS simulations. The experimental section states the study done on the shape of droplets on the hydrophobic surface by measuring the contact angles and the diameter ratios to ensure their ability to support proper circular paths for the resonant modes. Then comes the demonstration of the successful experiments of coupling the light into the droplets by our new method. Finally, a study on the effect of different losses on the total quality factor, along with a derivation of the analytical model to calculate the coupling quality factor in this method are presented to evaluate the limits of the proposed coupling method.

1.5 References for chapter 1

[1] A. Manz, N. Graber, H. M. Widmer, "Miniaturized total chemical analysis systems: a novel concept for chemical sensing," Sensors and Actuators B, vol. 1, pp. 244-248, 1990.

[2] D. R. Reyes, D. Iossifidis, P-A. Auroux, A. Manz, "Micro total analysis systems. 1. Introduction, theory, and technology," Anal. Chem., vol. 74, pp. 2623-2636, 2002.

[3] D. Psaltis, S. R. Quake, C. H. Yang, "Developing optofluidic technology through the fusion of microfluidics and optics," Nature, vol. 442, pp. 381-386, 2006.

[4] Y. Fainman, D. Psaltis, L. Lee, and C. Yang, *Optofluidics: Fundamentals, Devices and Applications*, McGraw-Hill, 2009.

[5] D. G. Grier, "A revolution in optical manipulation," Nature, vol. 424, pp. 810-816, 2003.

[6] K. Grujic, O. G. Hellesø, J. P. Hole, and J. S. Wilkinson, "Sorting of polystyrene microspheres using a Y-branched optical waveguide," Opt. Express, vol. 13, pp. 1-7, 2005.

[7] T. Lei and A. W. Poon, "Silicon-on-insulator multimode-interference waveguide-based arrayed optical tweezers (SMART) for two-dimensional microparticle trapping and manipulation," Opt. Express, vol. 21, pp. 1520-1530, 2013.

[8] M. Malak, "A Contribution to Photonic MEMS: Study of Optical Resonators and Interferometers Based on All-Silicon Bragg Reflectors", PhD thesis, Université Paris-Est, 2011.

CHAPTER (2)

FABRY-PEROT MICRO-RESONATORS WITH CURVED SURFACES

2.1 Introduction

Optical resonators are usually needed for one of their two main purposes or even both: (i) as a filter to select or reject certain wavelength bands, (ii) building up field intensity at specific resonance frequencies inside the resonator using moderate or low input power levels. The ability of a resonator to perform these tasks depends on its ability to confine the electromagnetic field according to specific mode shapes and also to enhance its magnitude, which is measured by its quality factor Q or its Finesse as will be detailed hereafter.

Most of the optical resonators are *open* cavities. To get the reason behind that, we need to recall the well-known fact that the light is an electromagnetic wave with very high frequencies (typically hundreds of THz), so the wavelength is in the order of micro- and nano-meters. Besides the numerous achievements related to nano-photonics, which includes quantum dots, it is not very common to realize a *closed* cavity whose dimensions are comparable to the wavelength, to enable supporting only the fundamental mode or those low order modes like what is usually done at the microwave frequencies by closed resonators. For more accessible dimensions like millimeter or centimeter ranges, the number of such resonant modes will be too high. Consider for example a 3D closed cavity with a volume V = 1 cm^3, operated at a frequency υ_0 = 300 THz (equivalent to $\lambda \sim 1$ μm), the average number of modes per unit resonator volume within a frequency interval $d\upsilon$ calculated from Weyl's law (restricted to its first term using the high frequency approximation) [1, 2]:

$$N \cong \frac{8\pi\upsilon^2 n_0^{\,3} n_r^{\,3}}{c^3} d\upsilon \qquad (2.1)$$

will give $N \sim 2.5 \times 10^9$ modes over a frequency range of 1% $d\upsilon = 3 \times 10^{10}$ Hz, all having comparable values of Q in a closed cavity, which will not be practical in realizing functional components such as filters lasers, etc...

In the previous formula, c is the speed of light in vacuum, $n_0 n_r$ represents the index of the medium within the cavity volume.

It has to be noticed that this mode density corresponds to a cavity with no privileged propagation axis (due to the cavity geometry or excitation conditions).

This obstacle of *closed* cavities is much overcome by the use of *open* resonators, which mostly consists of a pair of opposite reflectors (typically a Fabry-Perot cavity). In such configuration, for the majority of modes optical rays don't travel at right angles to the reflectors, and hence, they will escape the resonator after one or few trips; this results in very low Q values due to the high diffraction losses. However, if curved reflectors are in use, the few surviving modes will have most of their energy localized near the axis; this property is used to simplify the wave solution inside the cavity by benefiting from the paraxial approximation [3]. In general, such concept of open cavities applies not only to Fabry-Perot cavities but also to other optical resonators, when their shape and conditions of light coupling dictate the dominant resonant modes.

Fabry-Perot resonators are fundamental components in many optical applications. Long cavities and large mirror sizes are preferable for the high quality factor Q that they can produce, but this is obviously not compatible with miniaturization. Indeed, cavity based on small mirrors imposes using small spot size for the light beams, which cause excessive Gaussian beam expansion if the cavity is too long, until light escapes the open cavity increasing the diffraction loss when planar mirrors are used (a schematic is shown in Fig. 2.1 (a)), and hence degrades the performance. Stable resonators of sub-millimeter size need curved mirrors to focus the Gaussian beam; this is optimally done by spherical mirrors to focus the circularly symmetric beams (schematic in Fig. 2.1 (b)). But such mirrors can't be easily realized by the available micro-fabrication technologies so far. In a previous work [4], this difficulty was avoided by distributing the curvature on two surfaces: along the transverse plane (parallel to the silicon wafer), the curvature is achieved by the silicon-Air Bragg mirrors of cylindrical shape to provide stability in this direction (schematic of Fig. 2.1 (c)); then a Fiber Rod Lens (FRL) in introduced between the mirrors to focus the beam in the vertical direction (schematic of Fig. 2.1 (d)). This structure led to high quality factors despite the rather long cavity whose physical length is hundreds of micrometers [5]. In this chapter, we provide a numerical simulation for such structures. Also we study an evolved version of this device after replacing the FRL by a micro-tube allowing inserting a fluid inside the cavity,

which facilitates using this device for applications related to sensing, analysis, trapping in an optofluidic configuration, as will be shown in the next chapters. But first, a quick review, presented here below, contains some basic concepts about the FP resonators and design principles of the cavities with spherical mirrors (which can be partially applied to ours with cylindrical mirrors). It is introduced here to assess understanding of the later sections.

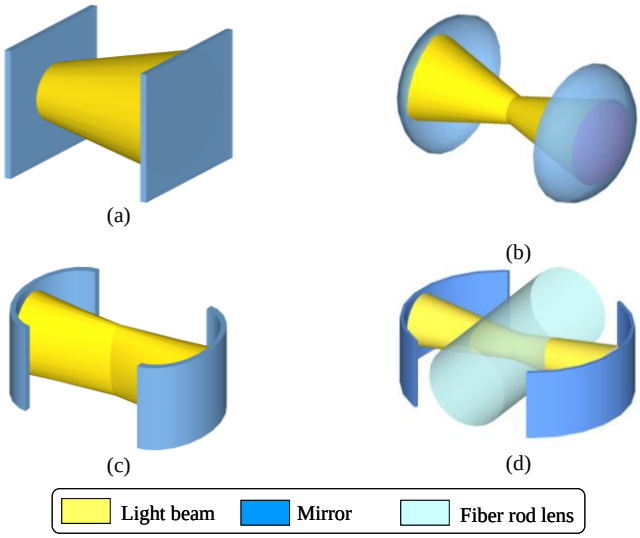

Fig. 2.1 Schematic representation of Fabry-Perot architectures with different mirror shapes: (a) Planar mirrors, (b) Spherical mirror providing 2D-confinment of light, (c) Cylindrical mirrors providing 1D-confinment of light and (d) Cylindrical mirrors combined with a fiber-rod-lens, also providing 2D-confinment of light as in case (b) [4].

2.2 General concepts for Fabry Pérot cavities

A Fabry–Pérot cavity is typically an open cavity confined between two reflecting surfaces, or two parallel highly reflecting mirrors. For on-chip schemes where light propagates in-plane of the supporting substrate, similar to conventional optical-bench configuration, these mirrors can be made of multilayer Bragg mirrors formed of Silicon/air bilayers of quarter wavelength thicknesses, fabricated using silicon micro-fabrication technology. The transmission spectrum as a function of wavelength exhibits peaks of large transmission corresponding to resonances of the cavity. This type of filters is typically used as a band pass transmission filter to transmit a narrow band of wavelengths and reject those outside that band. It is an important building block of lasers and wavelength-sensitive environmental sensors.

2.2.1 Principle of operation

For a simple explanation of the principle of operation, a simplified ray representation of the light will be adopted. When a light beam is incident on the resonator, most of the light power encountering the first mirror is reflected, but a small fraction of it transmits and travels through the cavity and hits the second mirror. At the second mirror most of the light reflects, while part of it transmits. The reflected light travels backwards, hitting the first mirror, where most of it again reflects and some transmits. The overall result depends on the mutual phase between these rays, and hence depends on the spacing and the refractive index of the medium between the mirrors, i.e. the optical path length. At some wavelengths, the multiply-reflected rays interfere constructively at the cavity output because they are in-phase. Hence, the cavity resonates and this corresponds to a high-transmission peak. These wavelengths are considered as resonance wavelengths of the cavity. At other wavelengths, the transmitted rays add out-of-phase, while the reflected ones add in-phase. At these wavelengths, the resonator overall transmission is low and the overall reflection is high. Whether the rays are in-phase or not, depends on the wavelength in vacuum, λ_0; the incidence angle of the light with respect to the cavity axis, θ; the thickness of the cavity or the separation between the two mirrors, d; and the refractive index of the material between the reflecting surfaces (i.e. inside the cavity), $n_0 n_r$; as indicated in Fig. 2.2.

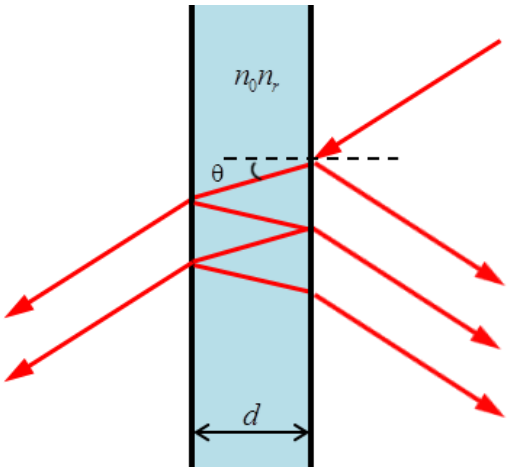

Fig. 2.2 A schematic of the basic Fabry–Pérot cavity. Light enters the cavity and undergoes multiple internal reflections.

The phase difference between each round trip is given by δ:

$$\delta = \left(\frac{2\pi}{\lambda_0}\right) 2 n_0 n_r d \cos\theta \qquad (2.2)$$

If both surfaces have reflectance $\mathbf{R}$, the total equivalent transmittance function is given by:

$$T_e = \frac{(1-\mathbf{R})^2}{1+\mathbf{R}^2-2\mathbf{R}\cos\delta} \tag{2. 3}$$

Maximum equivalent transmission ($T_e = 1$) occurs when the optical path length difference ($2n_0 n_r d\cos\theta$) between each transmitted beam is an integer multiple of the wavelength. In the absence of absorption, the total equivalent reflectance R_e is the complement of the transmittance, so that $T_e + R_e = 1$. The maximum equivalent reflectivity is then given by:

$$R_e\big|_{\max} = \frac{4\mathbf{R}}{(1+\mathbf{R})^2} \tag{2.4}$$

and this occurs when the path difference *2d($n_0 n_r$cosθ)* is equal to half an odd multiple of the wavelength.

The wavelength separation between adjacent transmission peaks is called the free spectral range (FSR), and is given in frequency domain by:

$$FSR_{\upsilon} = \frac{c}{2n_0 n_r d} \tag{2.5}$$

and is given in the wavelength domain by

$$FSR_{\lambda} = \frac{\lambda_0{}^2}{2n_0 n_r d} \tag{2.6}$$

where λ_0 is the central wavelength in vacuum of the nearest transmission peak.

The full-width half-maximum is the spectrum width at the value of $T_{\max}/2$ and is given, for low losses, by:

$$\Delta\upsilon_{FWHM} = \frac{c}{2\pi n_0 n_r d}\frac{1-\mathbf{R}}{\sqrt{\mathbf{R}}} = FSR_{\upsilon}\frac{1-\mathbf{R}}{\pi\sqrt{\mathbf{R}}} \tag{2.7}$$

The FSR is related to the full-width half-maximum, $\Delta\upsilon_{FWHM}$, of any one transmission band by a quantity known as the *finesse*:

$$\mathscr{F} = \frac{FSR_{\upsilon}}{\Delta\upsilon_{FWHM}} = \frac{\pi\sqrt{\mathbf{R}}}{1-\mathbf{R}} \tag{2.8}$$

Cavities with high finesse show sharper transmission peaks with lower minimum transmission coefficients.

Another important and frequently used quantity is the quality factor Q, which is the resonator ability to store energy. It is also defined as a measure of the sharpness or the selectivity of the resonance in the cavity. Theoretically, it is given by:

$$Q = \frac{2\pi\left(\text{energy stored in the system at resonance}\right)}{\left(\text{energy lost in a cycle of oscillation}\right)} \tag{2.9}$$

An equivalent definition used in experimental works is,

$$Q = \frac{\upsilon_0}{\Delta\upsilon_{FWHM}} = \frac{\lambda_0}{\Delta\lambda_{FWHM}} = q.\mathcal{F} \tag{2.10}$$

where q is the longitudinal mode order. These quantities are illustrated in Fig. 2.3.

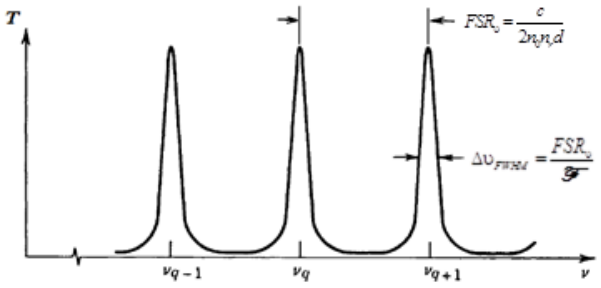

Fig. 2.3 The transmission of a Fabry-Perot cavity as a function of frequency [amended from: 2]

2.2.2 Wave analysis inside the cavity

Provided a good laser source is used with a convenient coherence length, the waves reflected successively at the front and back mirrors add coherently. This results in a constructive interference leading to field building up continuously with each round trip. Here, we will investigate this effect on the forward and backward waves formed inside the cavity, which paves for deriving an expression for this field enhancement within the cavity in the next section. Ray picture will also be adopted here.

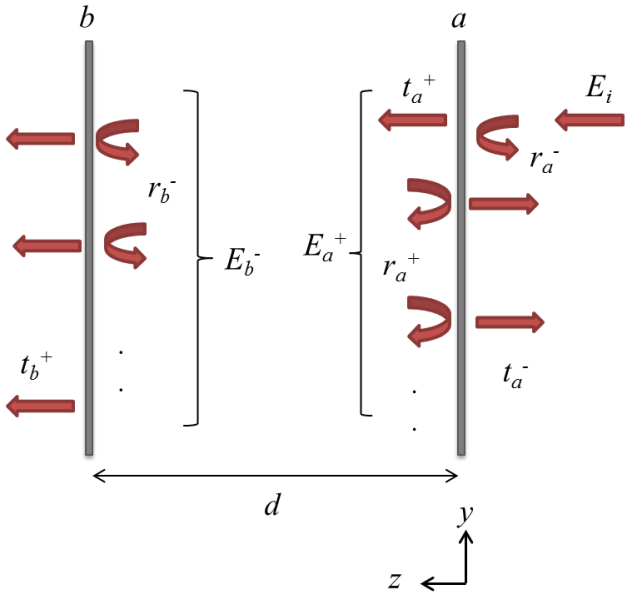

Fig. 2.4 Symbols used in calculating the summation of the rays traveling in counter directions inside the cavity.

We consider absorption in the cavity with absorption coefficient α, light propagating with propagation constant *k*, along or reverse the *z* direction, and the symbols used are as illustrated in Fig. 2.4.

The sum of the electric field of the rays inside the cavity in the forward '+' direction E_a^+ is given by:

$$\begin{aligned} E_a^+(z) &= E_i t_a^+ e^{-\alpha z} e^{-jkz} + E_i t_a^+ r_a^+ r_b^- e^{-2\alpha d} e^{-j2kd} e^{-\alpha z} e^{-jkz} \\ &\quad + E_i t_a^+ e^{-\alpha z} e^{-jkz} \left(r_a^+ r_b^- e^{-2\alpha d} e^{-j2kd} \right)^2 + \ldots \\ &= E_i t_a^+ e^{-\alpha z} e^{-jkz} \left[1 + r_a^+ r_b^- e^{-2\alpha d} e^{-j2kd} + \left(r_a^+ r_b^- e^{-2\alpha d} e^{-j2kd} \right)^2 + \ldots \right] \\ &= E_i t_a^+ e^{-\alpha z} e^{-jkz} \Big/ \left(1 - r_a^+ r_b^- e^{-2\alpha d} e^{-j2kd} \right) \end{aligned} \tag{2.11}$$

Where t_a^+ is the transmission coefficient from the right side mirror *a* to the interior of the cavity, r_a^+ is the reflection coefficient from the right side mirror *a* to turn the propagation into the forward '+' direction, r_b^- is the reflection coefficient from the right side mirror *b* to turn the propagation into the backward '-' direction, *d* is the separation between the two mirrors which is considered the cavity physical length.

Similarly, the sum of the electric field of the rays inside the cavity in the backward '-' direction E_b^- is given by:

$$\begin{aligned} E_b^-(\mathrm{z}) &= E_i t_a^+ r_b^- e^{-\alpha(2d-z)} e^{-jk(2d-z)} + E_i t_a^+ r_b^- r_a^+ r_b^- e^{-\alpha(4d-z)} e^{-jk(4d-z)} \\ &\quad + E_i t_a^+ r_b^- e^{-\alpha(2d-z)} e^{-jk(2d-z)} \left(r_a^+ r_b^- e^{-2\alpha d} e^{-j2kd} \right)^2 + \ldots \\ &= E_i t_a^+ r_b^- e^{-\alpha(2d-z)} e^{-jk(2d-z)} \left[1 + r_a^+ r_b^- e^{-2\alpha d} e^{-j2kd} + \left(r_a^+ r_b^- e^{-2\alpha d} e^{-j2kd} \right)^2 + \ldots \right] \\ &= E_i t_a^+ r_b^- e^{-\alpha(2d-z)} e^{-jk(2d-z)} \Big/ \left(1 - r_a^+ r_b^- e^{-2\alpha d} e^{-j2kd} \right) \end{aligned} \tag{2.12}$$

The wave intensities I^+ and I^- are simply related to E^+ and E^- respectively by $I = |E|^2 /2\eta$ where η is the intrinsic impedance. The intensity at the at the inner surface of the right side mirror a (i.e. $z = 0$)

$$I^+ = \frac{|E_i|^2}{2\eta} \left\{ \frac{\left(t_a^+ \right)^2}{1 - 2 r_a^+ r_b^- e^{-2\alpha d} \cos(2kd) + \left(r_a^+ r_b^- e^{-2\alpha d} \right)^2} \right\} \tag{2.13}$$

As for the intensity at the inner surface of the left side mirror b (i.e. $z = d$), we have,

$$I^- = \frac{|E_i|^2}{2\eta} \left\{ \frac{\left(t_a^+ r_b^- e^{-\alpha d} \right)^2}{1 - 2 r_a^+ r_b^- e^{-2\alpha d} \cos(2kd) + \left(r_a^+ r_b^- e^{-2\alpha d} \right)^2} \right\} \tag{2.14}$$

For a symmetric cavity, a and b are identical, so we can drop the notation a and b; also we can drop the + and – superscripts on the transmission and reflection coefficients used for the purpose of direction illustration only. And for simplicity, we will also assume a lossless cavity with $\alpha = 0$. Then the expressions for the forward and backward electric fields, respectively, become

$$\begin{aligned} E^+(\mathrm{z}) &= E_i \frac{t\, e^{-jkz}}{1 - r^2 e^{-j2kd}} = E_i \frac{t\, e^{-jkz}}{1 - r^2} \\ E^-(\mathrm{z}) &= E_i \frac{t\, e^{-jk(2d-z)}}{1 - r^2 e^{-j2kd}} . r = E_i \frac{t\, e^{jkz}}{1 - r^2} . r \end{aligned} \tag{2. 15}$$

noting that d is selected to give a phase shift of multiples of π, which makes $e^{-j2kd} = 1$. For the intensity, we have:

$$\begin{aligned} I^+ &= I_0 \frac{t^2}{1 - 2r^2 + r^4} = I_0 \frac{t^2}{\left(1 - r^2 \right)^2} \\ I^- &= I_0 \frac{t^2}{1 - 2r^2 + r^4} . r^2 = I_0 \frac{t^2}{\left(1 - r^2 \right)^2} . r^2 \end{aligned} \tag{2.16}$$

From equations (2.16) we deduce that the two waves propagating in opposite directions don't have equal intensities; the one travelling in the backward '-' direction suffers from extra reflection on the mirror *b*, and hence it will always be of less magnitude even in a lossless cavity. These counter-propagating waves interfere together, forming a standing wave inside the cavity, but unbalanced due to the unequal intensity magnitudes [6]. This result will be highlighted in explaining the behavior of the trapped particles inside the cavity, as will be discussed in chapter 4.

2.2.3 Field enhancement inside the cavity

The phenomenon related to the field building up inside the cavity achieves enhancement of the levels of the power within the cavity that could be obtained from lower amounts of power injected from outside. This phenomenon is of great use in many applications; for example to reach optical nonlinearity regimes, necessary to study the field-matter interaction in the quantum electrodynamics studies [7], or in the applications that includes optoelectronic devices to enhance their performance such as the photo detector efficiency and the contrast of optical modulators [6], or even to achieve particle trapping as will be governed in a latter chapter of this thesis. To have an idea about the amount and the location of this enhancement, we will adopt the model presented in the previous section to get expressions of the total field and intensity maxima and their positions.

The two counter-propagating waves introduced above interfere constructively; hence by adding their two fields, we have

$$\begin{aligned} E_{total} &= E^{+} + E^{-} = E_i t \frac{e^{-jkz} + r\, e^{jkz}}{1 - r^2 e^{-j2kd}} \\ &= E_i\ t\ e^{-jkz} \frac{1 + r\, e^{j2kz}}{1 - r^2 e^{-j2kd}} \end{aligned} \tag{2.17}$$

At the antinodes of this standing wave, where the distance z is equivalent to $\lambda/2$, we have a total field of the magnitude

$$E_{total}\big|_{antinodes} = \pm\, E_i\ t \frac{1+r}{1-r^2} \tag{2.18}$$

the sign '±' is used since the result depends on whether the (distance z gives an even or odd multiples of $\lambda/2$. Assuming that the mirrors are lossless, we have $t^2 = 1 - r^2$, then at the points of maximal intensity, the total intensity have the value

$$I_{total}\big|_{\max} = I_0 \frac{(1+r)^2}{1-r^2} \tag{2.19}$$

If we set the mirror reflectance or the power reflection coefficient as $\mathbf{R} = r^2$ then we have a local intensity enhancement at the maxima spots of the following value

$$\text{Intensity enhancement} = \frac{I_{total}\big|_{\max}}{I_0} = \frac{\left(1+\sqrt{\mathbf{R}}\right)^2}{1-\mathbf{R}} \tag{2.20}$$

which depends only on the reflectivity of the mirrors used (assuming lossless cavity). It can be expressed it terms of the cavity finesse $\mathscr{F}$ as

$$\text{Intensity enhancement} = \frac{\left(1+\sqrt{\mathbf{R}}\right)^2}{\pi\sqrt{\mathbf{R}}}\mathscr{F} \tag{2.21}$$

2.2.4 Field solution and resonance mode shapes

The ray picture is not sufficient to fully depict the exact electromagnetic field distribution inside the cavity, especially when considering the Gaussian shape of the input beam injected into the cavity from an optical fiber cable or a laser source. Hence, the electromagnetic treatment will be adopted in this section to find the solution of the wave inside the cavity.

There are many ways to find the resonant modes solution [3]. Here we will adopt the analytical method, which is probably the easiest and most straightforward. Starting from seeking a simple solution to Maxwell's equations that take the form of narrow beams, one get the family of the Hermite-Gaussian beams, which is the solution of the propagating beam modes in a homogeneous medium [8],

$$E_{m,n}(x,y,z) = E_0 \frac{W_0}{W(z)} H_m\left[\sqrt{2}\frac{x}{W(z)}\right] H_n\left[\sqrt{2}\frac{y}{W(z)}\right] e^{-k\frac{x^2+y^2}{W^2(z)}} e^{-jkz - jk\frac{x^2+y^2}{2R(z)} + j(m+n+1)\eta(z)} \tag{2.22}$$

where H_m is a Hermite polynomial of order *m; m* and *n* are the mode orders for the *x* and *y* lateral directions; and *W(z), R(z), η (z)* are given as:

$$W^2(z) = W_0^2\left[1+\left(\frac{\lambda z}{\pi W_0^2 n_0 n_r}\right)^2\right] = W_0^2\left[1+\left(\frac{z}{z_0}\right)^2\right] \tag{2.23}$$

$$R(z) = z\left[1+\left(\frac{\pi W_0^2 n_0 n_r}{\lambda z}\right)^2\right] = z\left[1+\left(\frac{z_0}{z}\right)^2\right] \tag{2.24}$$

$$\eta(z) = \tan^{-1}\left(\frac{\lambda z}{\pi W_0^2 n_0 n_r}\right) = \tan^{-1}\left(\frac{z}{z_0}\right) \tag{2.25}$$

where $z_0 = \frac{\pi W_0^2 n_0 n_r}{\lambda}$ is the Rayleigh range, W_0 is the beam waist radius, and the beam waist diameter $2W_0$ is also called the spot size. Fig. 2.5 illustrates the transversal intensity profile for the lowest order Hermite-Gaussian modes, the mode TEM_{00} is the fundamental mode with a pure Gaussian intensity distribution.

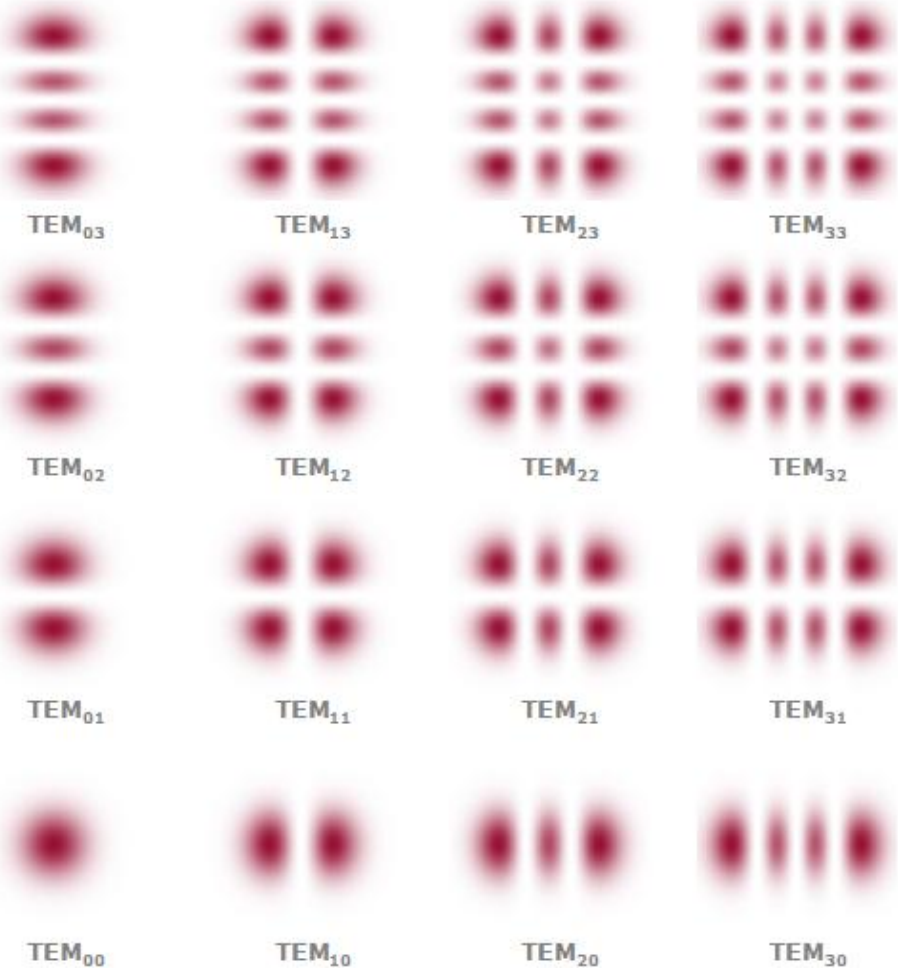

Fig. 2.5 The transversal intensity profile for the lowest order Hermite-Gaussian modes.

The phase shift on the axis ($x = y = 0$) is

$$\theta = kz - (m + n + 1)\tan^{-1}\left(\frac{z}{z_0}\right) \tag{2.26}$$

which is important in determining the resonance frequencies as will be shown. Remember that this is a general family of solutions, from which we have the simpler and famous special cases of the plane wave, spherical wave and the Gaussian beam. The last one is the fundamental mode of this family and compatible with the output of the single mode fibers and wide variety of laser sources. Hence it can be easily produced. The plane wave is unpractical to be achieved in the lab (it can be approximately realized by a large-beam waist Gaussian beam, but only over a small propagating distance around the waist; or by taking a small area formed by a small solid angle very far away from a source like the sun). The spherical waves may result from a Gaussian beam with a small beam waist (approximately a point source), noting

that the wave fronts of a Gaussian beam are more approximated by spherical shapes as we go further away after the Rayleigh distance. But such waves diverge fast and escape very soon from open cavities.

Then, to form a resonator, we can intersect the beam at two points with two mirrors having radii of curvature that match the wave fronts of the propagating beams, thus ensuring the reflection of the wave back exactly on itself since the surfaces are normal to the propagating beams. Finally, by ensuring that the optical path length between the two mirrors is multiple of $\lambda/2$ (equivalent to a phase shift of π), a self-reproducing stable field can be achieved.

2.2.5 Field confinement inside the cavity

In the previous section, to find the mode shapes that survive inside a resonator, we assumed a propagating wave that is fitted by the resonator mirrors. Here we need to work the problem reversely: given two mirrors with spherical radii of curvature R_1 and R_2 and certain separation distance d, we can -under certain conditions- adjust the position of the beam waist of a Gaussian beam and its beam waist radius, so that the reflectors coincide with the wave fronts of the propagating beam. Finally, the mirrors are expected to be large enough to contain most of the incident beam and minimize the "spilling over" of the light from the mirror edges, known as the diffraction loss, and hence sustain the mode for enough time inside the cavity ensuring high quality factor. Note that the straight planar mirrors, according to their shape could be, in principle compatible with plane waves, but the latter are, by nature, not confined in space and hence, are not compatible with producing a resonance inside a cavity.

For simplicity, symmetric resonators formed by spherical mirrors will be considered here, in which $R_1 = -R_2 = R$. The general case, in which $|R_1| \neq |R_2|$, can be found elsewhere [3]. Also, the design will be held on a simple Gaussian beam to be adopted as the fundamental mode. The mirrors should be put on a distance z_1 from both sides of the cavity center which hosts the beam waist, and their requisite radius of curvature is:

$$R(z_1) = R = z_1 + \left(\frac{{z_0}^2}{z_1} \right) \tag{2.27}$$

with z_0 the Rayleigh range. It leads to

$$z_1 = \frac{d}{2} = \frac{R}{2} \pm \frac{1}{2}\sqrt{R^2 - 4{z_0}^2} \tag{2.28}$$

For a given half spot size $W_0 = \sqrt{\lambda z_0 / \pi n_0 n_r}$, the mirrors positions can be easily determined. In an alternative situation, in which the cavity distance d, and the mirrors' curvature R, are predefined, the problem is to find the beam waist radius W_0, its location z_1, and the beam radius at the mirrors $W(z_1)$, noting also that $z_1 = d/2$, then from equation (2.28), we have

$${z_0}^2 = \frac{(2R-d)d}{4} \tag{2.29}$$

from which we can calculate the beam waist radius as

$$W_0 = \sqrt{\frac{\lambda z_0}{\pi n_0 n_r}} = \left(\frac{\lambda}{\pi n_0 n_r}\right)^{1/2} \left(\frac{d}{2}\right)^{1/4} \left(R - \frac{d}{2}\right)^{1/4} \tag{2.30}$$

and the beam at the mirrors has a radius

$$W(z_1) = \left(\frac{\lambda d}{2\pi n_0 n_r}\right)^{1/2} \left(\frac{2R^2}{d(R-d/2)}\right)^{1/4} \tag{2.31}$$

For the best confinement, the ratio of R/d needs to be determined. Plotting the previous relation (Fig. 2.6Fig. 2.5) versus this ratio, we find that the beam is best confined when $R = d$.

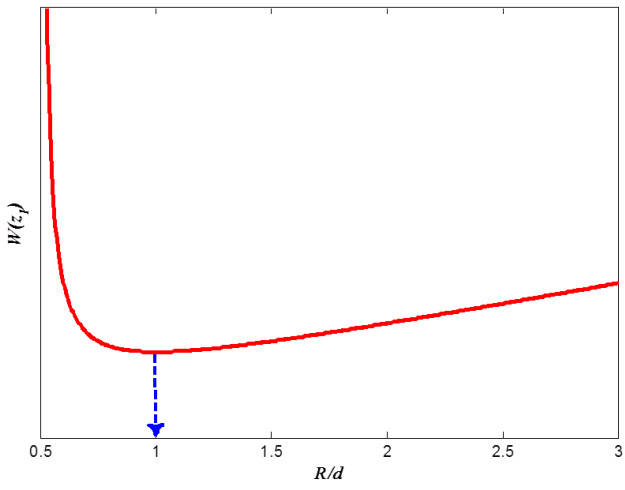

Fig. 2.6 The beam radius at the mirrors versus the ratio between the mirror curvature and the cavity length. The minimum occurs at ratio =1.

By achieving this best confinement condition (illustrated in Fig. 2.7(b)), we obtain what is called a symmetric confocal resonator, since the two foci -occurring at a distance $R/2$ from the mirrors- coincides. And the beam waist radius in this best confinement case is

$$W_0\big|_{conf} = \left(\frac{\lambda d}{2\pi n_0 n_r}\right)^{1/2} \tag{2.32}$$

with the spot at the mirrors with a best confinement or minimum radius of

$$W(z_1)\big|_{conf} = \sqrt{2}\ W_0\big|_{conf} \tag{2.33}$$

so the beam spread by only $\sqrt{2}$ from its value at the center of the mirrors.

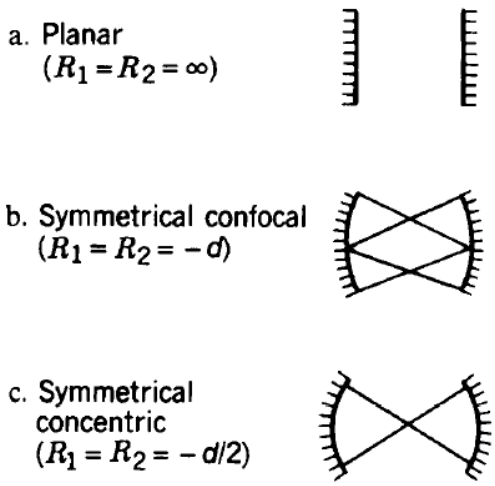

Fig. 2.7 Different resonator conditions dictating the best confinement case of the symmetrical confocal (b), and the two worst cases of unconfined beam of: (a) the planar, and (c) the symmetric concentric [3].

Now for evaluating the confinement achieved in other cases of the mirror curvature, we get the quantity

$$\frac{W(z_1)}{W(z_1)\big|_{conf}} = \left(\frac{1}{d/R(2-d/R)}\right)^{1/4} \tag{2.34}$$

This ratio is plotted in Fig. 2.8. For the two extreme cases of $d/R = 0$ (flat mirrors) and $d/R = 2$ (two concentric mirrors), the value of the spot size is unbounded. That means the diffraction loss is very high since most of the beam fall outside the mirror. Fig. 2.7 (a) and (c) illustrates these cases of the plane-parallel mirrors, and symmetric concentric one [3].

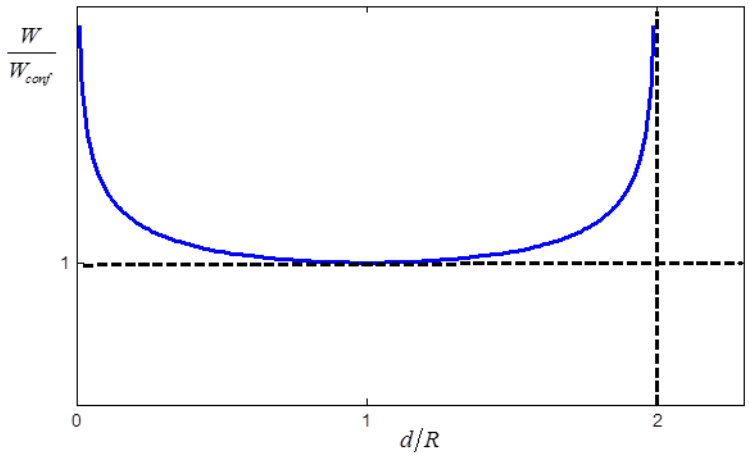

Fig. 2.8 Ratio of the beam spot size at the mirrors of a symmetrical resonator to its confocal ($d/R = 1$) value [3].

2.2.6 *Resonance frequencies*

As was stated previously, the phase shift on the axis associated with the transversal modes of orders m and n is

$$\theta_{m,n}(z) = kz - (m+n+1)\tan^{-1}\left(\frac{z}{z_0}\right) \tag{2.35}$$

The resonance condition implies to have a phase delay over each complete round trip equivalent to 2π. Suppose that the mirrors are put at distances z_1 and z_2, then we have

$$k_q d - (m+n+1)\left(\tan^{-1}\left(\frac{z_1}{z_0}\right) - \tan^{-1}\left(\frac{z_2}{z_0}\right)\right) = q\pi \tag{2.36}$$

where $z_2 - z_1 = d$ is the resonator length, and q is some integer equivalent to the number of $\lambda/2$ along the axis and is considered as the longitudinal mode order. Consider two successive modes with the same transversal distribution (m and n indices), we have

$$k_{q+1} - k_q = \frac{\pi}{d} \tag{2.37}$$

by taking $k = 2\pi\upsilon n_0 n_r / c$, we have it expressed in terms of the frequency as

$$\upsilon_{q+1} - \upsilon_q = \frac{c}{2n_0 n_r d} \tag{2.38}$$

which is the resonator free spectral range (FSR) stated previously. But note that if the transverse mode order (*m* or *n*) is different, we have a different situation. From equation (2.35), we deduce that the phase shift only depends on the sum *m* + *n*. So at fixed *q*, all the modes having the same value of *m* + *n* are degenerate, which means that they have the same resonance frequency. Now concerning the spacing between two modes with two different values of *m* + *n* and same *q,* we have [3],

$$\Delta k_q d = \Delta(m+n)\left(\tan^{-1}\left(\frac{z_1}{z_0}\right) - \tan^{-1}\left(\frac{z_2}{z_0}\right)\right) \tag{2.39}$$

and in terms of frequency

$$\Delta\upsilon = \frac{c}{2\pi n_0 n_r d}\Delta(m+n)\left(\tan^{-1}\left(\frac{z_1}{z_0}\right) - \tan^{-1}\left(\frac{z_2}{z_0}\right)\right) \tag{2.40}$$

2.3 Numerical simulations of FP cavities with cylindrical mirrors and with/without FRL

Earliest reports about FP cavities with spherical mirrors have demonstrated their excellent focusing capability. The curvature of the mirror focuses the beam in both transverse directions. But despite their high performances, the spherical resonators are difficult to miniaturize practically since the standard micro-fabrication technologies set limitations on the realization of in-plane curved surfaces only. As a step towards enhancing the performance, these in-plane curved cylindrical mirrors are adopted to achieve partial confinement in one lateral direction only. Then a Fiber Rod Lens (FRL) is used to provide additional light confinement in the out-of-plane direction. A detailed study of these configurations with experimental results has been performed in a previous work [4].

In this work, HFSS-FEM software has been used to numerically simulate the above-mentioned optical resonator. In general, the simulation conditions applied for the different cases are as following:

i. All the results are obtained using a driven model with Gaussian beam excitation that has TE polarization (corresponding to an electric field polarized along the cylinder axis at the middle of the beam waist). The beam waist, propagating along the positive Y-direction (coinciding with the cavity axis), is located at the cavity

entrance, and its spot size will be specified for each case accordingly. Radiation boundary conditions have been applied for the studied geometries to specify that the surrounding external media is free space.

ii. If cavities with real dimensions were to be simulated, enormous calculations resources would be required. To overcome this problem, scaled down miniaturized versions of the cavities have been designed and simulated. Moreover, to render the simulation more efficient, we exploited the symmetries of the design in respect to the XY and the YZ planes to simulate only one quarter the cavity volume.

iii. For further simplification and size reduction, cavities with single silicon Bragg layer per mirror have been simulated. Also the thickness of the silicon layer is taken equal to 111.4 nm equivalent to only one quarter of the wavelength (in silicon) with respect to the reference central wavelength of 1550 nm in vacuum.

iv. The transmission response is calculated as the ratio between the transmitted power through the cavity and the incident power at the cavity entrance. These powers components are obtained by integrating the Poynting vector over surfaces perpendicular to the propagation direction and located before and after the cavity. For calculating the input power, only the incident field is considered on the input surface while the calculation of the transmitted power is obtained by integrating the total field transmitted through the cavity.

As mentioned above, 1D confinement of the beam in the horizontal direction is achieved by the cylindrical Bragg mirrors, while 2D confinement is further provided by the FRL. However, an analytical model of the electromagnetic field cannot be easily produced for this specific architecture, which involves 2 cylindrical surfaces whose axes are orthogonal to each other. This lack in analytical modeling has justified the need for numerical HFSS-FEM simulations as demonstrated in Fig. 2.9 that shows the field intensities at the cavities' resonance wavelengths of 1546 nm. The simulations have been done on scaled-dawn parameters of the structure: the simple curved cavity has a physical length of 12.8 μm, mirrors' radius of curvature of 7.5 μm. The spot size of the exciting Gaussian beam is 0.9 μm. The second case of study pertains to the FRL cavity, it has geometrical parameters of 9.85 μm for the physical length of the cavity, also 7.5 μm for the radius of curvature and 6.25 μm for the fiber rod length diameter; the spot size of the exciting Gaussian beam is also 0.9 μm. Note

that these length values give equivalent optical path lengths on both cases since the FRL has a refractive index of 1.47.

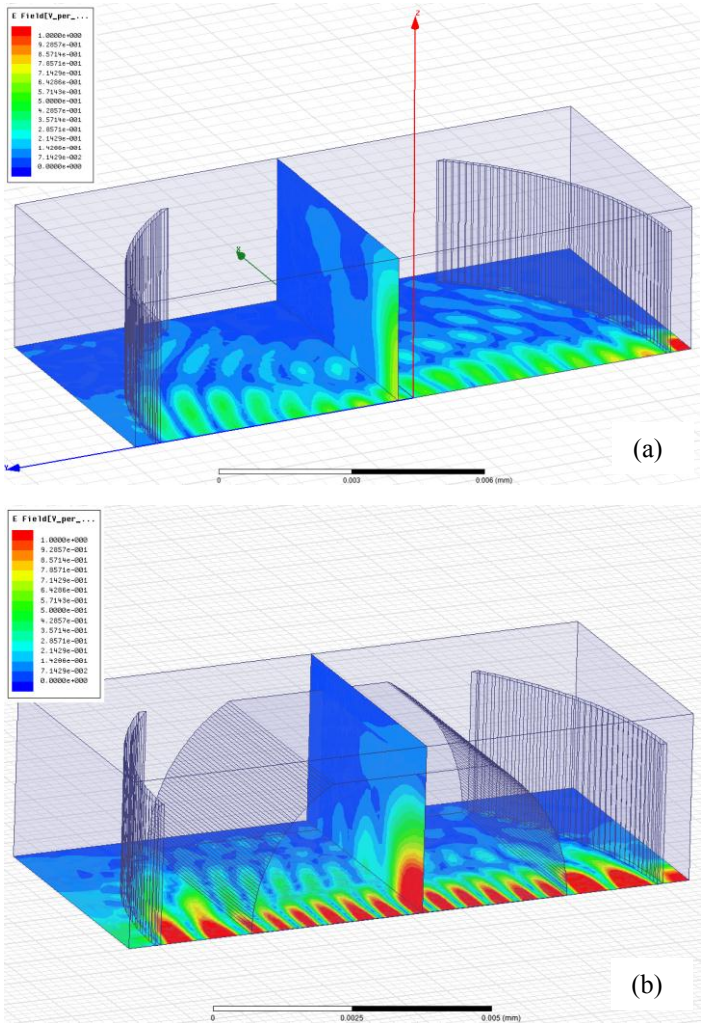

Fig. 2.9 HFSS simulations illustrate the light confinement (a) 1D confinement inside FP cavity by the cylindrical Bragg mirrors only. The light beam is confined along X-axis, at λ = 1548.5 nm, thanks to the cylindrical surfaces while it diverges along the Z-axis where the cavity behaves as a conventional FP cavity with planar reflectors. (b) 2D light confinement inside FP cavity formed by the cylindrical Bragg mirrors and a Fiber-Rod-Lens (FRL). The light beam exhibits 2D confinement, at λ = 1548.5 nm, thanks to the combination of cylindrical reflectors and the FRL.

Obviously, the cavity with cylindrical mirrors (Fig. 2.9 (a)) exhibits elliptical spots for the standing wave formed inside the cavity, as observed on the mid-plane screen inserted inside. For the FRL cavity instead (Fig. 2.9 (b)), the spot size shrinks to almost a circle of much higher intensity, which confirms our prior expectations about the 1D and the 2D confinements. The acquired spectral responses are shown in Fig. 2.10; which proofs the *Q*-factor improvement upon the addition of the FRL as in the second design. In fact, the simple curved cavity exhibits a *Q*-factor of 51 at λ = 1548.5 nm while the FRL design exhibits a *Q*-factor of 111 at λ = 1548.5 nm; that is more than 2.3 times improvement with respect to the

simple curved cavity. Also the transmission at the main resonance peaks is much higher in the case of the cavity with the FRL over the simple cavity case, as well as the contrast (which is the ratio of the maximum to the minimum of the intensity transmission factor).

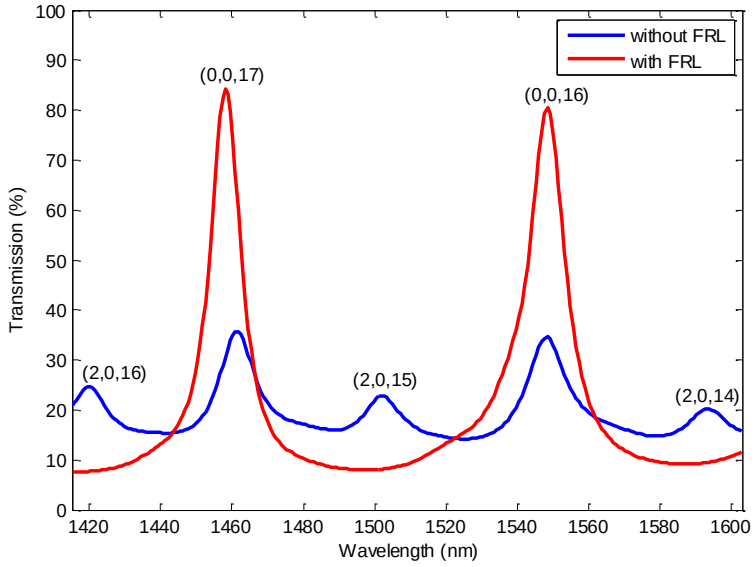

Fig. 2.10 Spectral response obtained by HFSS simulation for the simple curved cavity, the mode orders are mentioned beside each resonance peak, and for the cavity with FRL obtained by HFSS simulation.

Beside the difference in the performance at the resonant fundamental mode, the numerical spectral response obtained for the simple curved cavity reveals the excitation of higher order modes of Hermite-Gaussian transverse distribution, like the mode with order (2,0,15) excited at wavelength of 1502 nm, whose electric field distribution is shown in Fig. 2.11. The simulated quarter structure shows one and half spots in X-direction and half spot in Z-direction, which tells us that we have 3 horizontal spots (and hence order m = 2) and one vertical spot (and hence order n = 0), beside the longitudinal 15 spots along the cavity axes which gives mode order q = 15.

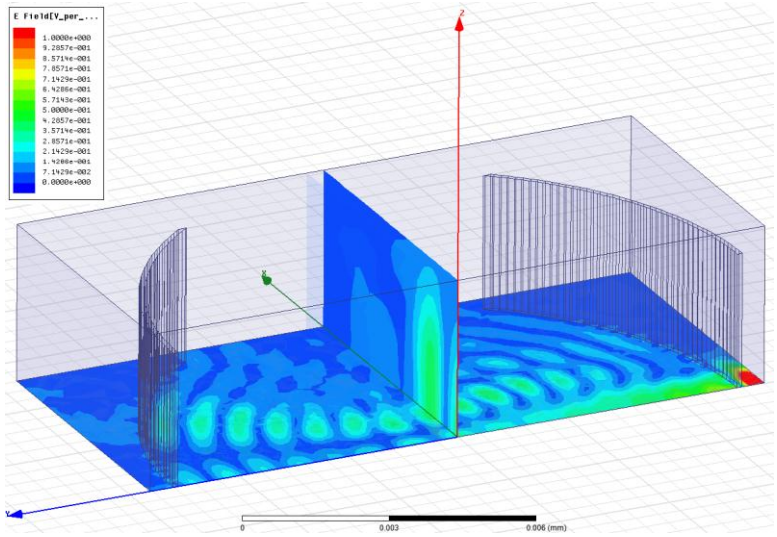

Fig. 2.11 HFSS simulation for the curved mirror cavity at the side peak at λ = 1502 nm. Multi-spot are observed at the mid-plane and they reveal the excitation of higher order modes in the FRL cavity.

These side modes are expected to exhibit resonance frequencies from the following analytical formula derived for cylindrical mirrors [4]:

$$\upsilon_{m,n,q} = \frac{c}{2n_0 n_r d}\left[q + (m+n+1)\frac{\arccos(1-d/R)}{\pi} \right] \tag{2.41}$$

where m is the transverse mode order, q is the longitudinal mode order, the mode order n was taken equal to *0; c* is the speed of light in free space and n_r is the relative refraction index of the medium inside the cavity, which is air in this case and hence it is equal to 1. The cavity length is d, while R is the mirror's radius of curvature. But actually d is not the physical length of the cavity, it is rather the effective one d_{eff} seen by the electromagnetic wave at such high frequencies; so it is expected to be slightly higher (due to the partial transmission through the mirrors).

By trials to fit the resonance wavelengths obtained by equation (2.41) and the simulation result obtained by HFSS, d_{eff} is taken equal to 12.978 μm. A comparison is established between the values obtained by both methods in Table 2.1.

Table 2.1 Theoretical and numerical resonance wavelengths for the different *(m,n,q)* cavity modes in nm of a simple cylindrical cavity with physical length of 12.8 μm., and the error between both.

Transverse mode ordre (*m,n*)	**Longitudinal mode order *q***	***q* = 15**	***q* = 16**	***q* = 17**
(0,0)	**Analytical model**		1548.57	1461.38
	Numerical simulation		1548.51	1460.98
	Error %		0.0035 %	0.0274%
(2,0)	**Analytical model**	1501.86	1419.7	
	Numerical simulation	1501.97	1420	
	Error %	0.007%	0.021%	

In this table, the values are pretty close with error less than 0.028%, which is reasonably small. The excitation of certain modes rather than others also depends on the shape of the excitation beam. We notice the excitation of the mode with $m = 0$, then $m = 2$ directly (without having $m = 1$). This is probably because the excitation is a Gaussian beam, whose lateral distribution has a maximum intensity at the center, while the transversal field of the 1st higher order Hermite-Gaussian beam has null value in the center; hence, no high correlation between both distributions. A detailed study on the modes shapes and the injected field distribution and the coupling efficiency between them can be found in [4].

2.3.1 Effect of changing mirror curvature and cavity length

By changing the mirror curvature, the mode shape whose phase front fits this new curvature also changes, and hence the excited modes are expected to be different. Not to mention the change in the resonance frequency, that is directly deduced from equation (2.41). Here, a cavity with FRL similar to the one shown above, except with mirror radius of curvature of 6 μm (instead of 7.5 μm), is simulated. The transmission spectrum is shown in Fig. 2.12.

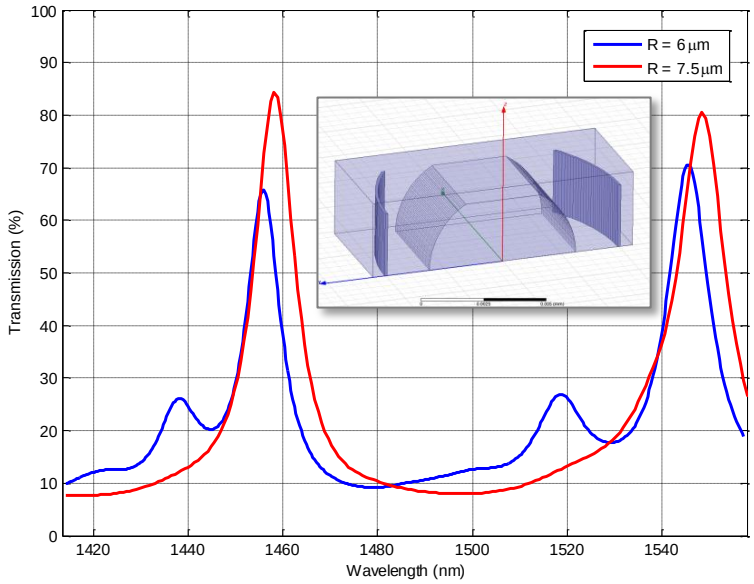

Fig. 2.12 The transmission from a cavity with cylindrical Bragg mirrors and a Fiber-Rod-Lens (FRL) with a lower radius of curvature of the mirror R = 6 µm. The excitation of higher order modes can be noticed at wavelengths of 1437.5 and 1518.7 nm. The spectrum of the larger curvature of R = 7.5 µm, mentioned above is plotted here again for comparison. The inset is an illustration of the cavity structure.

From the previous spectrum, we notice additional small peaks at wavelengths of 1437.5 and 1518.7 nm. Most probably, they are due to the excitation of higher order modes (similar to the TEM_{20} modes observed in pure cylindrical cavities) as demonstrated by the simulation result presented in Fig. 2.13 where we observe multi-spots for the mid-plane cartography. Oppositely to the case of simple cavity without FRL, this cavity does not have a robust analytical model and so, a similar rigorous treatment cannot be conducted as in the previous study.

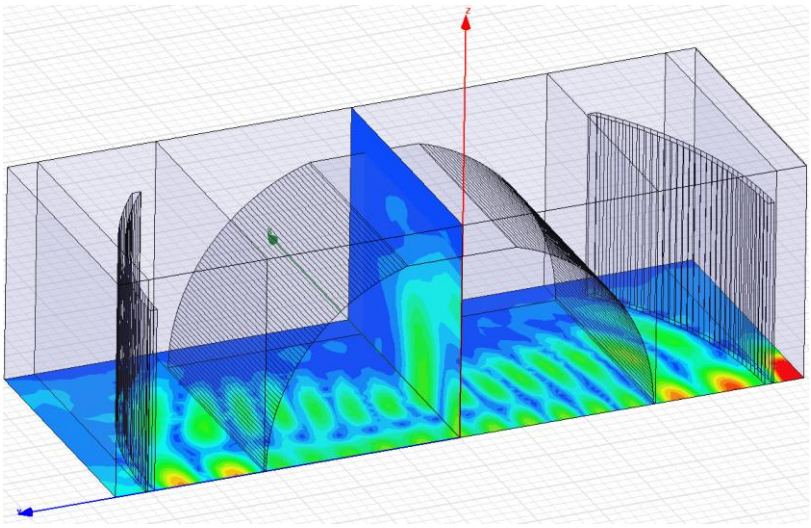

Fig. 2.13 HFSS simulation for the FRL cavity at λ = 1518.7 nm. Multi-spot are observed at the mid-plane and they reveal the excitation of higher order modes in the FRL cavity.

Note that reducing the mirror curvature makes the cavity more closed from the sides (less open cavity), which led to the excitation of more modes inside the cavity with lower quality factors. This demonstrates -to certain extent- the advantage of using open cavities to get rid of the modes with low quality factor that was discussed in the introduction of this chapter. This effect is also more pronounced with a less open cavity: a simple curved cavity has a short physical length of 3.98 µm, mirrors' radius of curvature of 3 µm. The spot size of the exciting Gaussian beam is 1.56 µm. The spectrum plotted in Fig. 2.14 reveals the excitation of more side peaks at wavelengths near those of the higher order modes calculated using equation (2.41), the mode order associated with each peak is indicated on the graph.

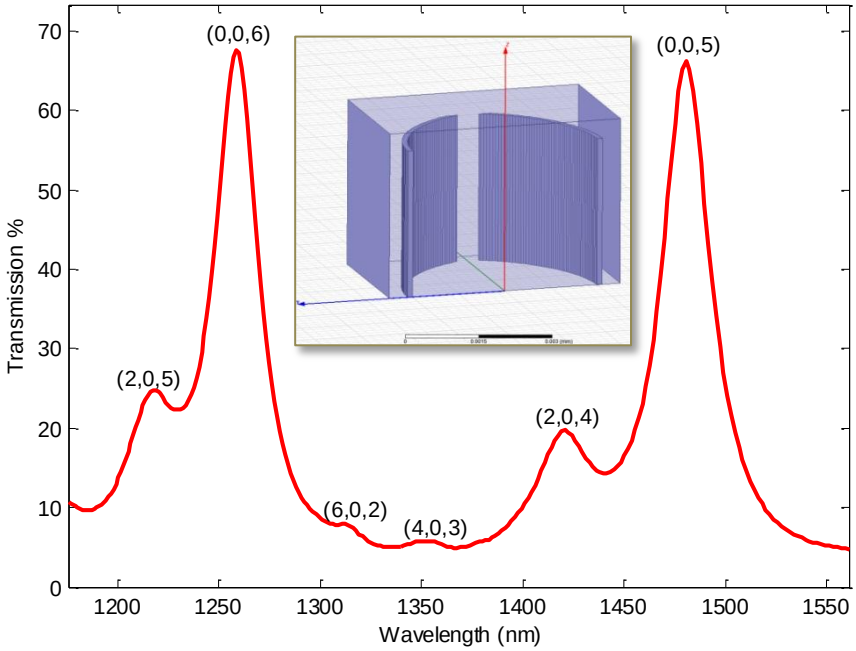

Fig. 2.14 Spectral response obtained by HFSS simulation for the simple less closed curved cavity, the mode orders are mentioned beside each resonance peak.

Like described previously, trials have been done to fit the resonance wavelengths obtained by equation (2.41) and the simulation result obtained by HFSS, d_{eff} in this case is estimated by 4.167 µm. A comparison is established between the values obtained by both methods in Table 2.2.

Table 2.2 Theoretical and numerical resonance wavelengths for the different *(m,n,q)* cavity modes in wavelength range between 1250 and 1560 nm for a simple cylindrical cavity with short physical length of 3.98 µm.

Transverse mode order (m,n)	Longitudinal mode order q	q = 3	q = 4	q = 5	q = 6
(0,0)	Analytical model			1481.4	1257.8
	Numerical simulation			1480.5	1258.3
(2,0)	Analytical model		1417.8	1211.3	
	Numerical simulation		1420.8	1218.6	
(4,0)	Analytical model	1358.4			
	Numerical simulation	1353.5			

In this table, the values are rather close with error less than 0.6%. A proposed reason behind this relatively higher error (20x to 200x more as compared with those on table 2.1 related to a simple cylindrical cavity with a longer physical length of 12.8 µm), especially for the highest order modes is that these modes are not purely (2,0,4) or (2,0,5), but they involve a non-negligible contribution coming from the neighbor fundamental mode and this effect also, leads to the shift of their resonance wavelengths. This contribution of the fundamental mode can be noticed from the field distribution shown in Fig. 2.15. The simulation is carried out at λ = 1420.8 nm, associated nominally to mode (2,0,4). Accordingly, we were expecting four lobes inside the cavity under these conditions. Instead, the result, reveals a combined effect of four lobes (side part of the cavity) and five lobes (central part of the cavity) corresponding to modes (2,0,4) and (0,0,5). As noticed from the field map, the lobes amplitudes diminish due to the difference between the periodicity of both modes.

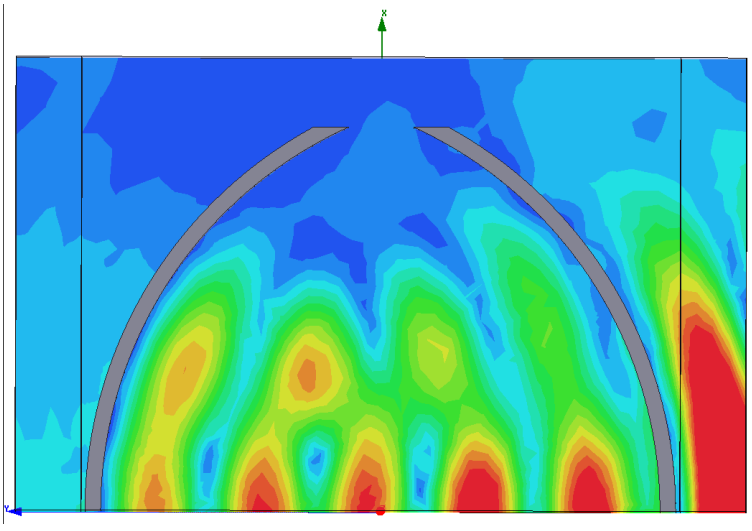

Fig. 2.15 Field map of the numerical simulation carried for the simple curved cavity at λ =1420.8 nm along the XZ plane. The combined effect of modes (2,0,4) and (0,0,5) is illustrated.

2.4 FP cavities with cylindrical mirrors and microtubes

In this section, we investigate the previously introduced device but after replacing the FRL by a micro-tube allowing inserting a fluid inside the cavity to be optically analyzed, as indicates the schematic in Fig. 2.16. In this section, the stability of this device will be checked along with its numerical model simulation.

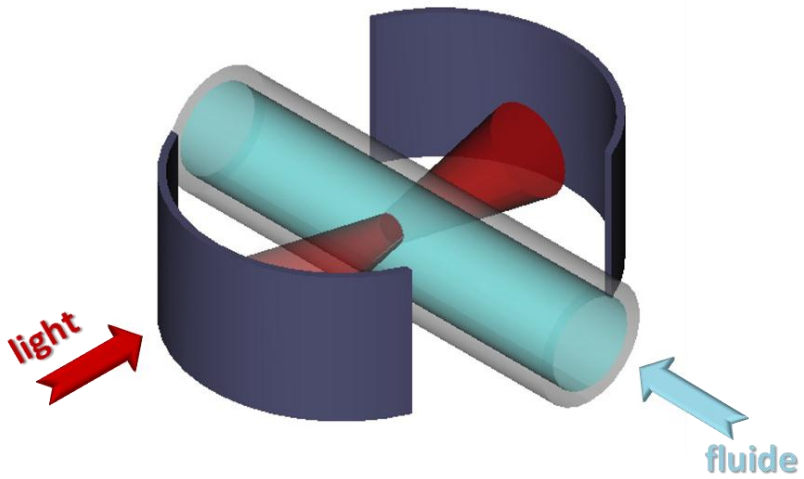

Fig. 2.16 Schematic diagram of the cylindrical Fabry–Pérot cavity with the micro tube inside.

2.4.1 Stability Study

The stability of the FP cavity shall be investigated by the ray matrix approach [2]. We assume that the light behavior is decoupled in XZ (horizontal) and YZ (vertical) planes. Hence, each cross section is treated as a 1D problem with schematics shown in Fig. 2.17 and Fig. 2.18.

For XY cross section:

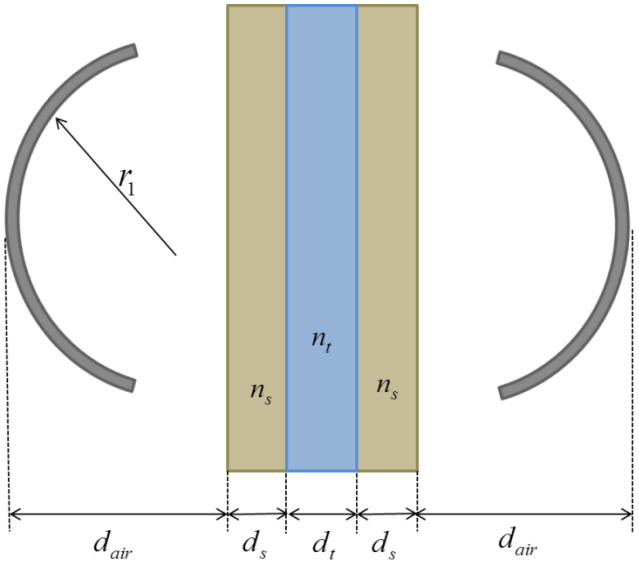

Fig. 2.17 Schematic diagram for the horizontal cross section of the cylindrical Fabry–Pérot cavity with the micro tube inside indicating the design parameters and geometry.

The equivalent matrixes for the 1D problem indicated in Fig. 2.17 are as follows,

The matrix for the reflection from a concave mirror is given by:

$$K_1 = \begin{pmatrix} 1 & 0 \\ -\frac{2}{r_1} & 1 \end{pmatrix} \tag{2.42}$$

The matrix for free space propagation region is given by:

$$K_2 = \begin{pmatrix} 1 & d_{air} \\ 0 & 1 \end{pmatrix} \tag{2.43}$$

The matrix for the refraction from air to the silica microtube:

$$K_3 = \begin{pmatrix} 1 & 0 \\ 0 & \frac{1}{n_s} \end{pmatrix} \tag{2.44}$$

The matrix for the propagation inside the silica wall of the microtube:

$$K_4 = \begin{pmatrix} 1 & d_s \\ 0 & 1 \end{pmatrix} \tag{2.45}$$

The matrix for the refraction from the silica walls of the microtube to the test liquid inside the tube:

$$K_5 = \begin{pmatrix} 1 & 0 \\ 0 & \dfrac{n_s}{n_t} \end{pmatrix} \tag{2.46}$$

The matrix for the propagation inside the test liquid inside the tube:

$$K_6 = \begin{pmatrix} 1 & d_t \\ 0 & 1 \end{pmatrix} \tag{2.47}$$

The matrix for the refraction from the test liquid inside the tube to the silica walls of the microtube:

$$K_7 = \begin{pmatrix} 1 & 0 \\ 0 & \dfrac{n_t}{n_s} \end{pmatrix} \tag{2.48}$$

The matrix for the refraction from the silica walls to air

$$K_8 = \begin{pmatrix} 1 & 0 \\ 0 & n_s \end{pmatrix} \tag{2.49}$$

The round trip equivalent matrix is:

$$K_{eq} = K_2K_8K_4K_7K_6K_5K_4K_3K_2K_1K_2K_8K_4K_7K_6K_5K_4K_3K_2K_1 = \begin{pmatrix} A & B \\ C & D \end{pmatrix} \tag{2.50}$$

The equivalent matrix is obtained by multiplying the indicated matrixes, either symbolically or numerically by Matlab. Let the equivalent matrix components be A, B, C, and D, then applying the stability condition, that is the stability parameter $(A+D)/2$ should be less than or equal to 1:

$$\left|\frac{A+D}{2}\right| \le 1 \tag{2.51}$$

we obtain the condition symbolically:

$$0 \le \frac{2}{r_1}\left(2d_{air} + \frac{2d_s}{n_s} + \frac{d_t}{n_t}\right) - \frac{4d_{air}}{r_1^2}\left(d_{air} + \frac{2d_s}{n_s} + \frac{d_t}{n_t}\right) - \frac{1}{r_1^2}\left(\left(\frac{d_t}{n_t}\right)^2 + 4\frac{d_s}{n_s}\left(\frac{d_s}{n_s} + \frac{d_t}{n_t}\right)\right) \le 1 \tag{2.52}$$

For YZ cross section:

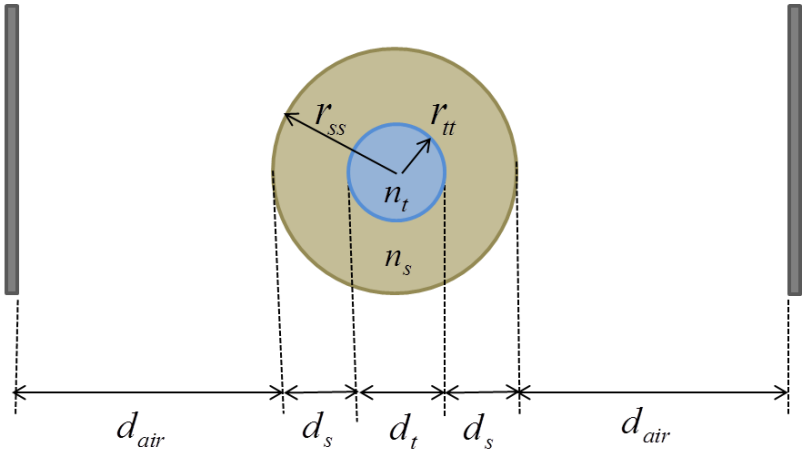

Fig. 2.18 Schematic diagram for the vertical cross section of the cylindrical Fabry–Pérot cavity with the micro tube inside indicating the design parameters and geometry.

Note that:

$$\begin{aligned} d_s &= r_{ss} - r_{tt} \\ d_t &= 2r_{tt} \end{aligned} \tag{2.53}$$

The procedures and the matrixes are the same as previous, except for the following ones,

The matrix for the reflection from the silicon mirror since it is straight in this case, hence it is given by:

$$K_1 = \begin{pmatrix} 1 & 0 \\ 0 & 1 \end{pmatrix} \tag{2.54}$$

The matrix for the refraction from air to the curved plane of the silica microtube:

$$K_3 = \begin{pmatrix} 1 & 0 \\ \dfrac{1-n_s}{n_s r_{ss}} & \dfrac{1}{n_s} \end{pmatrix} \tag{2.55}$$

The matrix for the refraction from the curved silica walls of the microtube to the test liquid inside the tube:

$$K_5 = \begin{pmatrix} 1 & 0 \\ \dfrac{n_s - n_t}{n_t r_{tt}} & \dfrac{n_s}{n_t} \end{pmatrix} \tag{2.56}$$

The matrix for the refraction from the test liquid inside the tube to the curved silica walls of the microtube:

$$K_7 = \begin{pmatrix} 1 & 0 \\ \dfrac{n_s - n_t}{n_s r_{tt}} & \dfrac{n_t}{n_s} \end{pmatrix} \tag{2.57}$$

The matrix for the refraction from the curved silica surface to air

$$K_8 = \begin{pmatrix} 1 & 0 \\ \dfrac{1-n_s}{r_{ss}} & n_s \end{pmatrix} \tag{2.58}$$

For this plane, the symbolic stability condition is:

$$\begin{aligned} 0 \le 4\frac{{d_{air}}^2}{{n_s}^2}\left(\frac{n_s - n_t}{r_{tt} n_t} + \frac{1-n_s}{r_{ss}}\right)^2 + \frac{4}{r_{tt}}\frac{(n_s - n_t)}{{n_s}^2 n_t}\left(4d_{air} + 2r_{ss} - n_s\left(3d_{air} + r_{ss}\right)\right) \\ + 4\frac{d_{air}}{r_{ss}}\left(\frac{2}{{n_s}^2} - \frac{3}{n_s} + 1\right) + 4\frac{r_{ss}}{{r_{tt}}^2}\left(\frac{n_s - n_t}{{n_s}^2 n_t}\right)^2\left(2d_{air} + r_{ss}\right) + 4\frac{1-n_s}{{n_s}^2} + 1 \le 1 \end{aligned} \tag{2.59}$$

Now applying these conditions to our real device with design parameters of:

$r_1 = 140\mu m$

$d_{air} = 76\mu m$

The used capillary tube has:

$d_t \simeq 75\mu m$

$d_s \simeq 26\mu m$

The stability may or may not be guaranteed according to the refractive index of the fluid inside the tube n_t. Calculating the stability parameter for a range of refractive indexes from 1 to 2 to cover the condition of air and the majority of fluids that can be introduced inside the tube, as indicated in Fig. 2.19, the stability is always assured in the horizontal plane. But the vertical plane restricts it to the liquids whose refractive indexes are between 1.1526 and 1.6673. These results have been calculated using the deduced expression and compared to the results from the direct multiplication of the numerical matrixes using Matlab to check the exactness of these symbolic formulas. The proposed range of indexes constrains the applications of such device to liquids only, which means gases are excluded as their refractive index is close to 1 -if a high quality factor is to be exploited-, as will be employed in the next chapters.

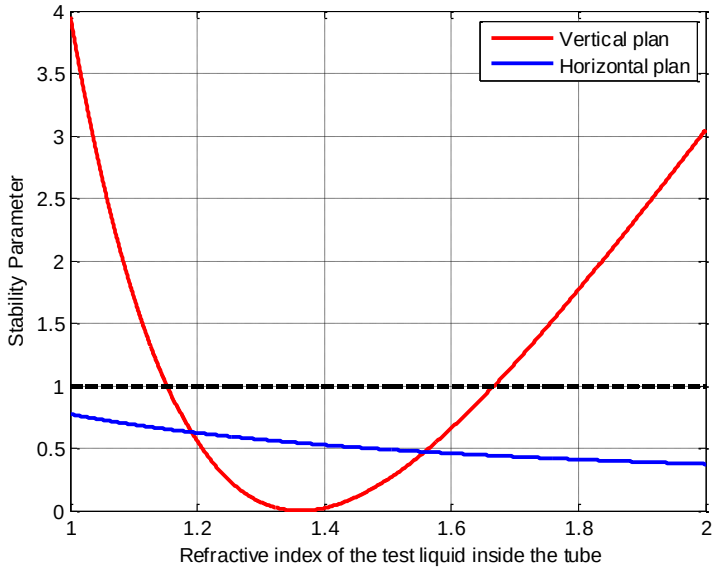

Fig. 2.19 Stability parameter for different fluids inside the tube.

2.4.2 Numerical simulations

In this section, a cavity with the same dimensions used in the previous HFSS-FEM simulations in section 2.3 will be adopted but after replacing the FRL with a silica microtube (the tube has the same external diameter as the FRL, and the internal diameter is taken as 0.75 μm). Checking the stability of such downscaled cavity with an empty tube (filled with air, i.e. n_t = 1), it will not be stable. Rather than that, the range of the filling liquid n_t that achieves stability is in this case between 1.15 and 2.03. Now we will therefore simulate a tube filed with different fluids that have different indexes near the limits of that RI values range that achieves stability, lower and higher than the silica refractive index that is 1.47 (the material of the walls of the tube). The selected values of the test fluid n_t are 1.18, 1.3, 1.6, and 1.8, all within the stability range. The transmitted output power spectra for these cases are shown in Fig. 2.20.

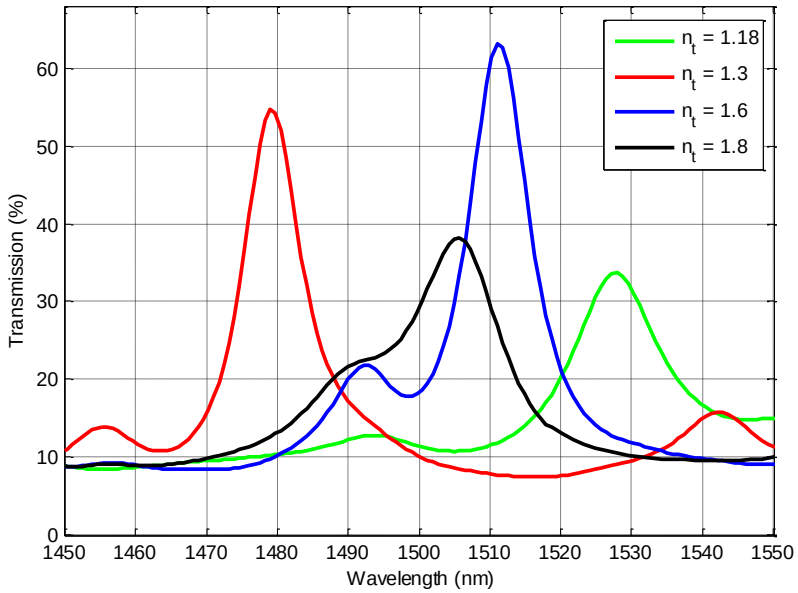

Fig. 2.20 The transmission spectra of the curved cavity with a microtube filled with a test liquid of different refractive indices n_t.

Now to investigate the field confinement, Fig. 2.21 plots the field distribution at resonance in each case. And Table 2.3 states the quality factor values the confinement distances (taken as the lateral distance from the maximum field value at the center of the spot to the value of half the maximum).

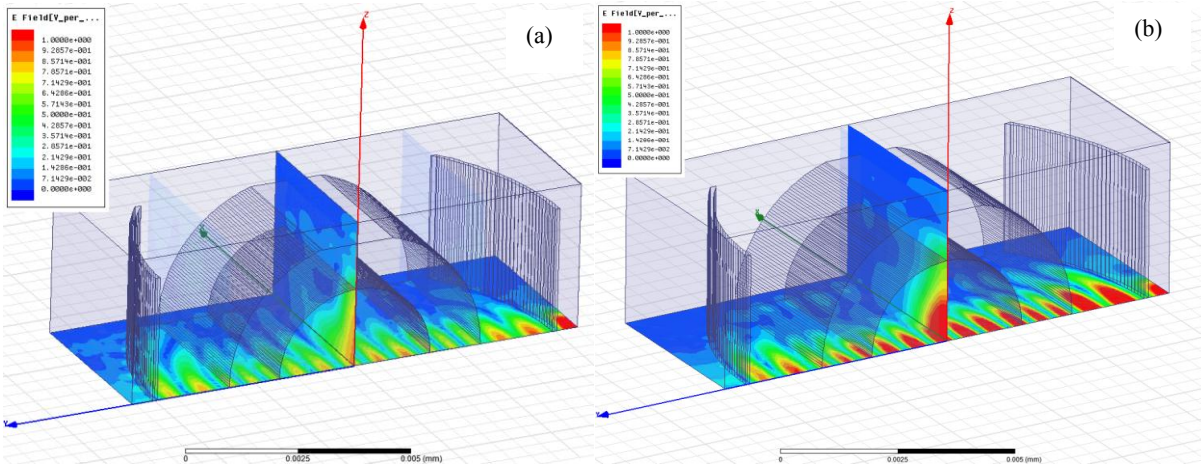

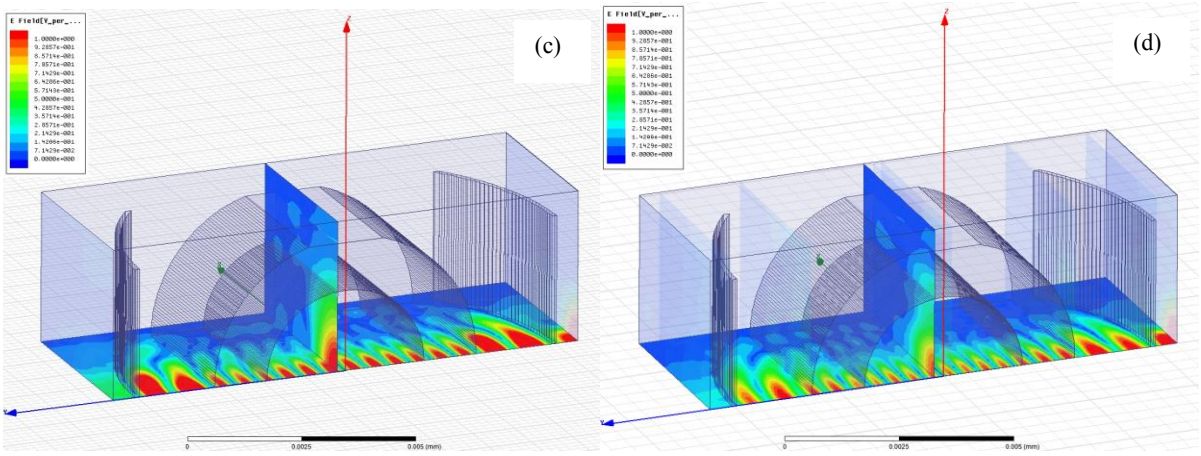

Fig. 2.21 The electric field distribution at resonance for different test liquids (a) n_t =1.18, resonance at 1528 nm. (b) n_t =1.3, resonance at 1576 nm. (c) n_t =1.6, resonance at 1511 nm. (d) n_t =1.8, resonance at 1505.7 nm.

Table 2.3 Comparison between the quality factor and the confinement distance between different test liquid filling the tube.

	$n_t = 1.18$	$n_t = 1.3$	$n_t = 1.6$	$n_t = 1.8$
Q_{peak}	70	129.5	128	55.2
Confinement distance	1.88 um	1.34	1.24	1.11

As theoretically predicted and as can be inherited from the field distributions in Fig. 2.21, when the test fluid has refractive index less than that of silica, that may cause divergence of the beam after it refract at the internal surface of the microtube, which is the silica/test liquid interface. On the other hand, the test fluid with refractive index higher than that of the silica helps in confining the beam better and increasing the quality factor. But this happens until certain extend, as the interspacing between the modes with same longitudinal mode order q but different transversal ones (given by equation (2.40)) decreases with increasing the refractive index. When the interspacing is not enough to separate different peaks, intermodal interference occurs, like what is observed in the case of n_t = 1.8 of Fig. 2.20; in which, a strong coupling between the main peak and the side peak appears in the spectral response and hence the main peak seams shorter and less sharp; which renders the field spots to be of less intensity as in Fig. 2.21 (d). The best performance regarding high transmission at the main peak, well confinement of light, and quite high quality factor, is obtained with the case n_t =

1.6, which is larger than the refractive index of the tube material, but not too large to reduce the separation between modes much, causing their coupling; it is also away from the critical values of the stability conditions.

A better quantitative comparison for the quality factors and the confinement distances between the different cases is held in Table 2.3, from which we can noticed that the confinement distance is smaller as n_t increases, which is predicted; but the separation between the main modes and the side ones decreases as can be noticed from the spectral responses, which may cause interference between them, leading to reduction in the quality factor, as most pronounced for $n_t = 1.8$.

2.5 Conclusion

In this chapter, a study on FP cavities has been done, starting from the basic operation principle of the FP resonators with the definition of the main related quantities. Then, some basic concepts about the field performance inside the cavity like the field enhancement and field confinement, which are the main reasons behind using a cavity resonator. In addition to that, an analytical study on the mode shapes and the resonance frequencies is also presented. Inclusively, the design parameters to obtain high cavity performance are introduced. This study adopts the design method of cavities with spherical mirrors available in literature, which can be partially applied to our cavities with cylindrical mirrors.

After that, a theoretical study has been done on the different types of FP cavities with curved surfaces:

1. Simple cavity with cylindrical Bragg mirrors, achieves 1D confinement.
2. The previous cavity with additional FRL to achieve confinement in 2D.
3. Cavity similar to the previous but replacing the FRL with a microtube to allow the flow of a liquid, allowing its optical analysis.

The study includes both analytical analyses and numerical simulations. A comparison between the performance of the first two cavities showed that an improvement of light confinement and quality factor upon introducing the additional FRL; but of course this comes on the expense of an additional post fabrication step of inserting the fiber into its groove. Then the third cavity with the microtube is analyzed for performance understanding and optimization, which is necessary for the next chapters employing this device in optofluidincs applications.

2.6 References for chapter 2

[1] D. A. Hill, *Electromagnetic Fields in Cavities: Deterministic and Statistical Theories*, John Wiley & Sons, 2009, chapter 1.

[2] B. E. A. Saleh and M. C. Teich, *Fundamentals of Photonics*, John Wiley & Sons, 1991, chapter 9.

[3] A. Yariv, *Quantum electronics*, 3rd edition, John Wiley & sons, 1989, chapter 7.

[4] M. Malak, "A Contribution to Photonic MEMS: Study of Optical Resonators and Interferometers Based on All-Silicon Bragg Reflectors," PhD thesis, Université Paris-Est, 2011.

[5] M. Malak, N. Pavy, F. Marty, Y. -A. Peter, A. Q. Liu and T. Bourouina, "Micromachined Fabry–Perot resonator combining submillimeter cavity length and high quality factor," Appl. Phys. Lett., vol. 98, pp. 211113-1-211113-3, 2011.

[6] M. S. Unlu, S. Strite, "Resonant cavity enhanced photonic devices," J. Appl. Phys., vol. 78, pp. 607-639, 1995.

[7] I. Pupeza, "Power Scaling of Enhancement Cavities for Nonlinear Optics," PhD thesis, max-planck-institut fur quantenoptik, 2011.

[8] A. Yariv, *Quantum electronics*, 3rd edition, John Wiley & sons, 1989, section 6.9.

CHAPTER (3)

REFRACTOMETRY OF LIQUIDS AND COLLOIDS

3.1 Introduction

Refractive index (RI) is a property of dielectric materials. Though it is applicable in principle to the whole frequency spectrum of electromagnetics, the low frequency range traditionally refers to the dielectric constant instead (in conjunction with the magnetic permeability constant). RI is widely used in the optical frequency domain, originally in solid-state optics. Refractometry relates to measurement techniques of RI of materials in various forms. It can be used to infer the nature of fluids, or as a label-free technique to distinguish different types of cells, or to determine the concentration of a solute in a solvent. This may have important biomedical, industrial and environmental applications. For example, the state of biological systems may be inferred through the refractive index of its constituent fluids, such as glucose dissolved in blood plasma that is important for the management of diabetes. Examples of optical RI sensors include surface plasmon resonance, 2-D photonic crystal structure, and various forms of resonators supporting Whispering Gallery Modes, such as ring resonators [1, 2], or spherical resonators [3]. In these sensors, an optical resonance can easily be observed; at least a fraction of the corresponding mode is interacting with the test sample located at the vicinity of those kinds of optical resonators interacting through their surface with the surrounding environment. In this case we refer to *surface* refractometry (opposed to *volume* refractometry, which will be discussed later). A change in RI of the region probed by the resonant mode causes a corresponding frequency shift of the optical resonance of the sensor. The change in resonant frequency is converted to the sensing signal. Many of the optical RI sensors offer real-time results and minimal sample preparation with no fluorescent labeling required. Hence, optical refractive index sensors are widely researched for many of applications and are of good demand among the commercial landscape of current sensing technologies [4].

In order to compare the numerous available technologies, one should make a clear distinction between surface RI and volume RI measurement. Surface RI sensors are based on the interaction between a sample and an evanescent electromagnetic wave. Important

examples of this type of sensors are surface plasmon, integrated dielectric waveguides, and resonant spherical optical microcavities. Their resolution can be as high as about 10^{-7} RIU (RI units) according to Ref. 4, but the depth of interaction with the sample is typically small (less than 1 μm). This makes them very sensitive to surface contamination and not suitable for applications requiring thick surface penetration or measurements through big biological samples bigger than the evanescent tails of the surface waves), such as living cells. Volume RI sensors for microfluidic systems are based on the beam deviation technique [5], on laser cavities [6] or, as our device presented in Fig. 3.1, on Fabry–Pérot (FP) cavities. In each case, the light propagates through the sample and the depth of interaction is greatly increased. The previously reported microfluidic Fabry–Pérot refractometers [7-13] were made of planar Bragg reflectors not curved ones; which implied the need for a short cavity length to satisfy low diffraction-loss of the optical resonators; however this shortness constraint renders the fluidic channel more readily clogged by cells, especially those whose sizes are comparable to the channel depth, such as HSA cells in a 16 μm deep channel [12]; or the channel is even not wide enough to allow a single cell pass through it for some types of large cells. Such short cavity length done previously in literature limits the quality factor (Q) to small values (for example Q = 400 for n_t =1.400 [13]), and hence the detection is vulnerable to uncertainty due to the amplitude noise that is superimposed to the resonance spectrum [13]. For example, if a slightly longer cavity length is employed -for cell characterization for instance-, while using straight mirrors, detection limit of only 1.365×10^{-3} is reached with a channel gap of 35.5 μm [8]. Using our device of curved mirrors achieves stability in the lateral plane; beside functionalizing the microtube itself to achieve vertical confinement, and hence stability in the orthogonal plane as well, as detailed in the previous chapter. This allows reaching quality factors over 1,000 with a space exceeding 70 μm, which is enough for large samples, while achieving quite acceptable RI detection limits despite such large channel width, as will be demonstrated in this chapter.

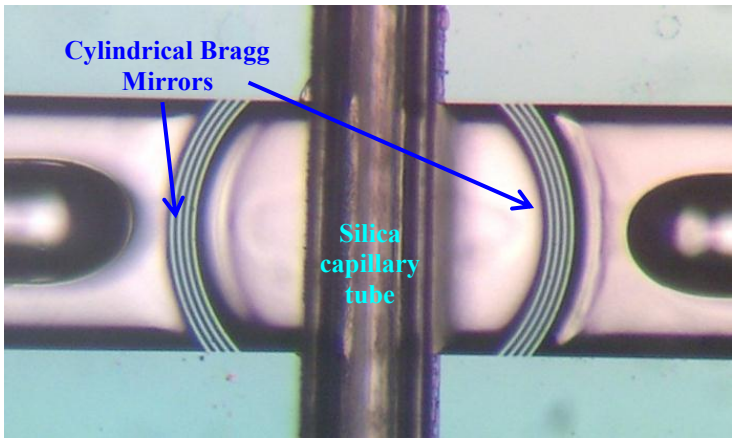

Fig. 3.1 Photograph of the refractometer consisting of Fabry–Pérot cavity made of cylindrical mirrors with the micro tube inside.

Most of the resonance-based RI sensors operate in a peak-detection operation by tracing its wavelength shift upon changing the RI from a reference value. Alternately, resonance-based RI sensors can operate in another detection scheme in which a single wavelength only is used instead of a band of wavelengths. The system is designed so that the wavelength of the laser is initially near the spectral location of the maximum intensity peak, or at the mid-point of the resonance peak slopes, almost at half-maximum intensity, on either side of the extremum (maximum or minimum). According to this operation scheme, when the resonant wavelength shifts due to RI changes, the amplitude of the optical signal at the sensor output increases or decreases according to the shape of the resonance peak and to the magnitude of the spectral shift of the resonance, as illustrated in Fig. 3.2. The objective of this measuring technique is to get rid of the sophisticated spectroscopy devices, broadband source or tunable lasers; by determining the refractive index from the power reading at a single wavelength; hence, only a photo detector and a single wavelength laser are needed.

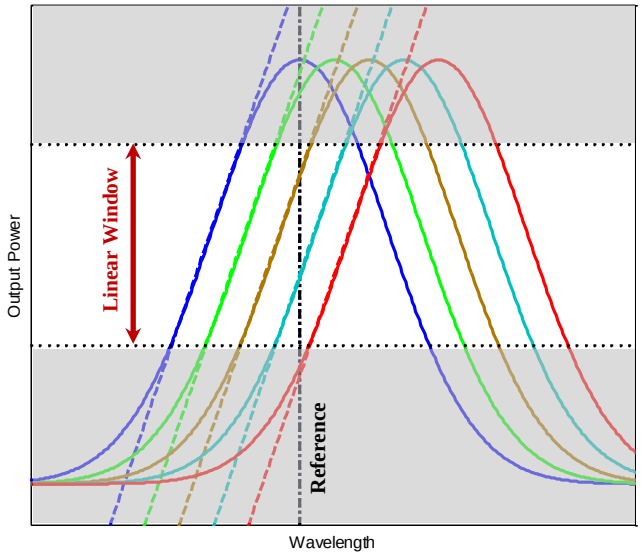

Fig. 3.2 Schematic indicates the new measuring criterion of the power level at a fixed wavelength in dBm/RIU.

Some trials have been done in literature to reach the same objective, but on ring resonators [1, 2] operated in surface refractometry. However, in the first reference, this objective couldn't be fully reached since the spectra had to be normalized probably due to intensity variations during the measurement. Up to our knowledge, our work is the first demonstration of this technique with a sensor based on FP resonator and the first time it is implemented to achieve volume refractometry. Also it might be proposed as a novel measuring technique for the Cavity-Enhanced Volume Refractometry (CEVR), whose numerous capabilities are demonstrated for the study of fluids in various forms.

Another advantage of our device is that it is compatible with on-column measurement (the column here could be part of the micro-capillary tube), which may be useful in liquid chromatography analysis, where refractometry is one of the main detection techniques at the output of liquid separation columns. A major trend in analytical chemistry is miniaturization of liquid separation systems to achieve extremely high separation power; this has led to growing interest in micro-separation systems such as capillary and micro- liquid chromatography (μLC). Unfortunately, such micro-separation systems have the drawback that detection volumes that can be tolerated without deteriorating the high separation efficiency are no more than a few nano-litres [14]. Hence we need efficient irradiation of small detection volumes; and therefore the concern is not only about achieving high optical quality factors (Q) for good spectral separation, but also small modal volumes (V) to efficiently pass through

the small sample volume. So this novel structure offers a non-destructive, on-column refractometer that needs a volume less than one nano-litre within the detection volume, and doesn't need disconnecting the tube or using extra fluidic connections to transfer the fluid into the chip; neither performing some severe modifications of the tube holding the output liquid from the column. As an example, in [15] a coating sensitive to certain fluids only like glucose is put inside the tube, whereas in [16] the tube wall thickness is reduced by stretching in a ring resonator detector. In our system, the measurements might be done on column without any modification (except removing a small part of the coating), by just mounting the column onto the silicon chip, in a groove between the two Bragg Mirrors of the Fabry–Pérot cavity. Up to our knowledge, this will be the first use of an integrated FP cavity as on column refractive index detector for LC applications.

In this chapter, our device is employed as a refractive index sensor and used for study of different liquid mixtures with different concentrations. Both schemes of peak wavelength tracing and intensity level tracing at single wavelength have been studied, and the sensor performance has been evaluated in both cases. But to accomplish this task, a study on the behavior of the tested liquids upon mixing has to be done to assign their refractive indexes that will be used for sensor characterization. Also, using our device, the refractometry of colloids is demonstrated, where the variation of the refractive index of an aqueous solution mixed with microsphere suspensions is correlated to the change in particles' concentration; the limitations of this technique is discussed as well.

3.2 Selecting suitable test liquids

As indicated in section 2.4.2, the optical stability of our resonator, which is necessary to achieve high quality factor, puts a first restriction on the fluids in use to have RI between 1.1526 and 1.6673. That is easily satisfied by most of the liquids available in the lab. But another important issue is the light absorption of the liquid in the used optical wavelength range in the near infra-red (NIR). Our refractometry device is intended to determine onlythe real part n of the complex refractive index $\tilde{n}$, which can be written as $\tilde{n} = n + j\alpha(\lambda)$. But the imaginary part α, which is responsible for the attenuation or absorption, adds a second unknown to the measurements. It is worth mentioning that the absorption spectrum $\alpha(\lambda)$ might be determined using the same device, by implementing the so-called Cavity-Enhanced Absorption Spectroscopy. For the moment, let us focus on pure refractometry, namely on the

measurement of the real part n of the refractive index. Hence, low absorption liquids have to be selected. Usually the available spectra in literature focus on the mid-infra-red range; yet, the absorption graphs corresponding to our NIR range for some liquids available in the lab could be found [17]. The first liquid one may think of is the distilled water, since it is easily available and nonhazardous; but unfortunately it exhibits high absorption within our working wavelength range between 1520 and 1630nm. Ethanol has moderate absorption and is also not very hazardous, which renders it a possible candidate but with no special advantage. Toluene and acetone are the best candidates. Interestingly, they have close absorption values in this wavelength range, also acceptably low. Besides, toluene has high RI value which may be useful for the resonator performance in achieving higher confinement and higher quality factor as was demonstrated in the previous chapter. But on the other hand, toluene should be handled with intensive care since it is highly hazardous as indicates its safety datasheet, but still it is less hazardous than most of the liquids in the family of hydrocarbons that exhibit nearly similar characteristics like chloroform or benzene.

Considering the refractive index values, very close RI values should be used to test the resolution of our refractometer. Such close values are not easily available in pure materials; alternatively, mixtures of two liquids may be used, of course after checking their reaction tendency. The data of RI values upon mixing acetone and water are available in literature as will be presented in the next section. Hence, such mixture will be used but with very small water ratios to avoid its high absorption. Also, as stated above, toluene and acetone have low absorption in this range with close values. Hence, different mixing ratios of both probably will exhibit similar attenuation; which is useful for testing our device.

3.3 Optical parameters upon mixing liquids

If no chemical reaction takes place on the mixing of two liquids, then the properties of the solution obtained might be calculated from those of its constituents by means of the so-called mixture rule; which may be additive linearly with certain physical quantity. These quantities may be the masses, volumes, or molecular quantities, and the correct method of representation depends on the property under investigation. At the first glance, one may think that the RI property is linear with volume mixing ratios, which has been experimentally tested to be true for some liquids [18]. But it is more expectted it have a linearly additive diectric

constant rather that RI on volume basis since the dielectric constant has a direct relation to the number of dipoles per volume.

Unfortunately the case is not always as simple as that, there are some liquid mixtures - particularly aqueous solutions- that exhibit nonlinear behavior with volume fractions due to the volume change after mixing. Hence, their properties cannot be predicted with certainty from the properties of the pure constituting materials; rather, they must be quantitatively evaluated from experimental data.

Ideal volume % is the volume percentage calculated from the weight percentage assuming no volume change on mixing. By definition, density (ρ) must vary linearly against ideal volume % if there is no volume change on mixing; therefore the deviation from linearity when density is plotted versus ideal volume % is a direct measure of deviation from ideality. If there is no volume change on mixing, density is also additive on volume % basis. Therefore, if it is desired to emphasize the agreement with, or deviation from ideality, it is desirable to plot density against ideal volume % composition.

In considering volume change and related effects, there is appreciable amount of free volume or "expansion volume" in liquids, since there is a molecular increment associated with each dissolved unassociated molecule which is called "the molecular solution covolume". This may be the reason behind this deviation from the linear addition. To overcome this deviation, a new physical concept called the refractivity intercept (*r*) has been introduced [19] as

$$r = RI - 0.5\rho \tag{3.1}$$

This quantity shows good linearity dependence when plotted against % compositions. The choice between ideal volume % and weight % for such plots depends upon the use for which the graphs are intended. In general, a high degree of linearity is achieved with the ideal volume % plot, for instance in the aqueous-acetone mixtures. Nonetheless, refractivity intercept is nearly linear with weight % for many binary mixtures [20].

3.3.1 RI of Acetone-Water mixture

The physical properties of refractive index and density for acetone-water mixture has been studied in literature [20]. Their behavior substantially deviates from linearity as shown in Fig. 3.3.

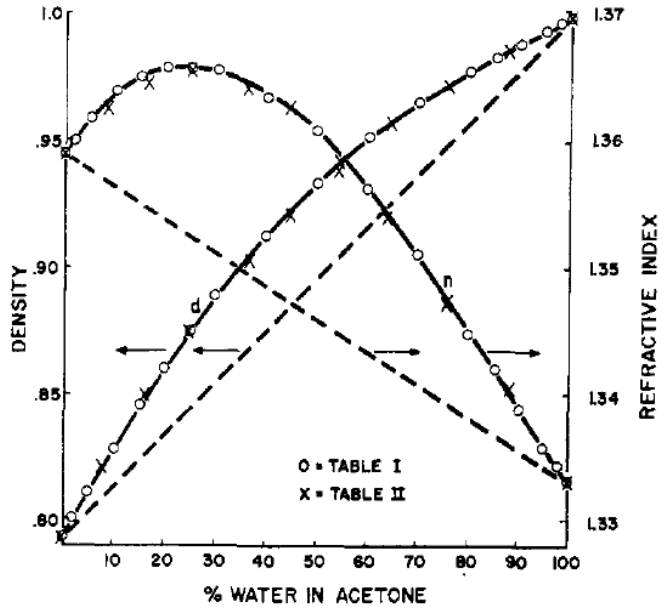

Fig. 3.3 Refractive index (at wavelength of 589.3 nm) and density versus ideal volume % for acetone and water mixtures at temperature of 20°C. The dashed lines are the behavior is case of ideal linear dependence, but the measured points show high deviation from ideality [20].

But as mentioned above, the Acetone-Water binary mixture gives good linearity if its refractivity intercept is plotted versus ideal volume %, as shows the black line in Fig. 3.4, whose data are at the wavelength of 589.3 nm of the Sodium D-line, obtained from ref. 20. Unfortunately, similar values are not available in our range of the near infra-red. The only available data are those of the pure compounds near the wavelength of 1550 nm, which are 1.34855 for acetone [21], and 1.3167 for distilled water (DI water) [17], both at temperature of 20°C. From these two points and with making a reasonable assumption that the density values are the same at both wavelengths, the linear red plot in Fig. 3.4 could be obtained. From which, the RI values of the mixture can be calculated for the 1550 nm wavelength, as plotted in Fig. 3.5.

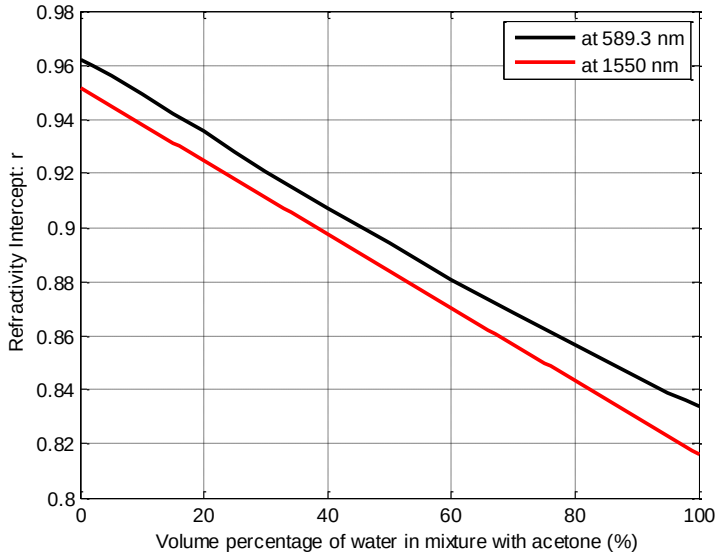

Fig. 3.4 Refractivity intercept versus the ideal volume mixing rations of water with acetone, which shows linear relation (extrapolated from the data found in ref. 20).

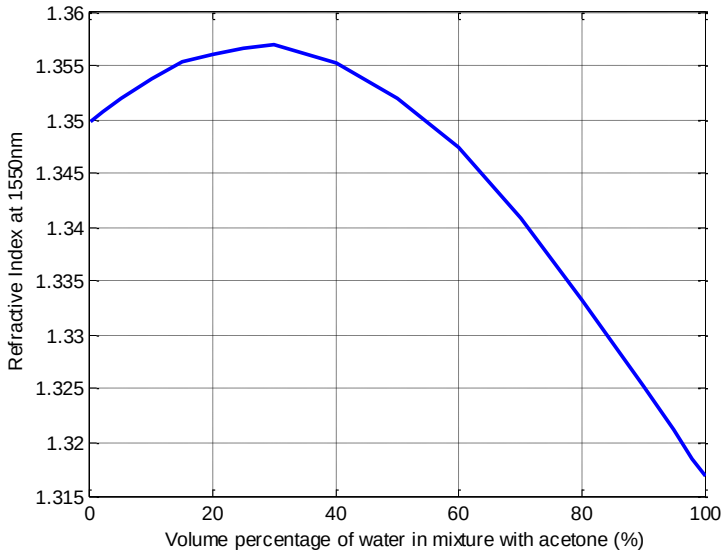

Fig. 3.5 The refractive index of the water-acetone mixture at the wavelength of 1550nm versus the water volume percentage.

3.3.2 Absorption of Toluene-Acetone mixture

To check the absorption of the toluene and acetone mixtures, spectroscopy of pure toluene and that of different mixing ratios was performed using IR-Affinity-1 Fourier transform infrared spectrophotometer from Shimadzu connected in transmission mode to an absorption cell of length 10 µm filled with the liquid samples. The measured spectra are

shown in Fig. 3.6, which demonstrate that toluene and acetone mixtures have acceptably low absorption in this range with very close values despite the different contents ratios of toluene and acetone.

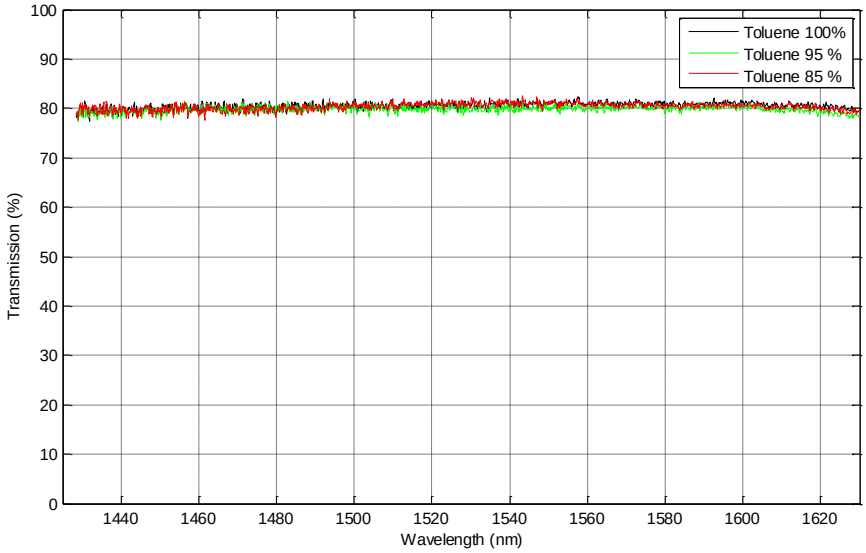

Fig. 3.6 Transmission of pure toluene and different mixing ratios with acetone, which shows almost similar absorption.

3.4 Experimental setup

Fig. 3.7 shows the experimental setup used to test the refractometer. The light source used is a Tunable Laser Source (TLS) of model 81949A from Agilent; and the used detector is a Power meter (PM) of model 81634B from Agilent also, both are in the same platform that is Agilent 8164B mainframe. It is equipped with a GPIB interface to enable controlling by a computer. Telecommunication single mode (SM) fibers from Go4Fiber are used for the connections. A pair of such fibers but with bare, cleaved ends is used to inject and collect the light into and from the cavity. Sometimes, lensed fibres from Corning with spot size of 18 μm and 300 μm working distance are used instead. The performance of the lensed fibre is superior, but they can't be glued to the chip to reduce the alignment changes during the measurements like the normal (cheap) fibres. A visible laser light at 635 nm is used sometimes for alignment purposes. The visible light and the infrared light are coupled through a nearly 50/50 directional coupler and injected into the input fibre to the cavity. Five axis positioners are used to align each fibre in the input and output grooves, while the sample is

mounted on a two axis positioner. All elements are mounted on an optical table to reduce vibration effects.

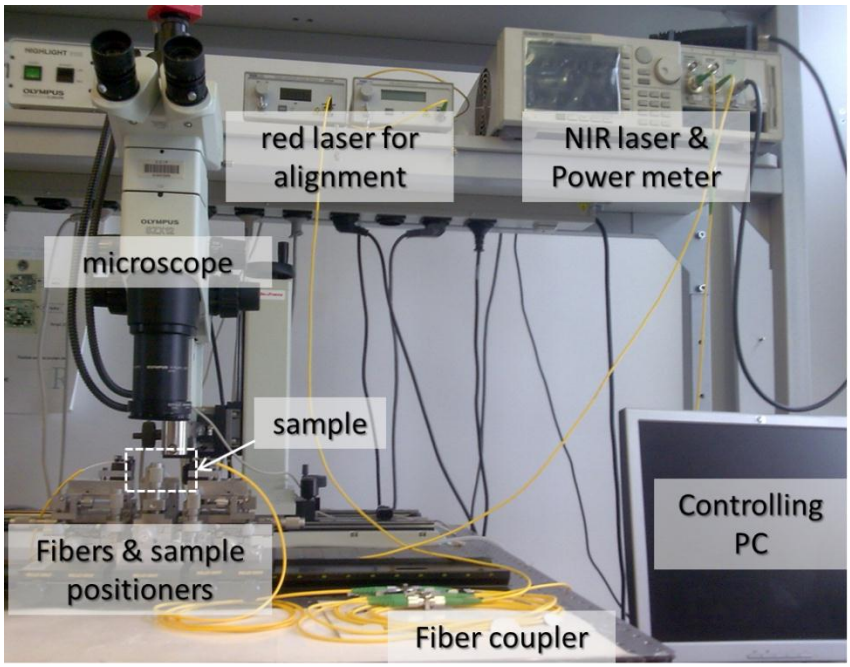

Fig. 3.7 The measurement setup in the lab. The sample presented in Fig. 3.8 is inserted in the white dashed rectangle.

The sample is a silicon chip fabricated using the improved Deep Reactive Ion Etching (DRIE) process presented in [22]. The chip contains several FP cavities of different lengths and different number of layers for the Bragg mirrors. Having such several cavities available on the chip facilitates trade-offs between the quality factor and the free spectral range (FSR). The mirrors are silicon/air multi-bilayers cylindrical Bragg mirrors, whose radius of curvature are R = 140 µm. The silicon layer has a thickness of 3.67 µm, while the air has a thickness of 3.49 µm; both thicknesses correspond to an odd multiple of quarter the central wavelength - which is 1550 nm- in silicon and in air, respectively. Then a fused silica micro-tube with outer diameter of 128.1±1.2 µm and inner diameter of 75.3±1.2 µm (from Polymicro Technologies with part number TSP075150) is placed between the mirrors and is connected with an external larger diameter tube to allow injecting the fluid, beside achieving the confinement of the Gaussian beam in the vertical plan. Fig. 3.8 shows such sample on its positioners and the input/output fibres, with a zoomed inset indicating the different FP cavities.

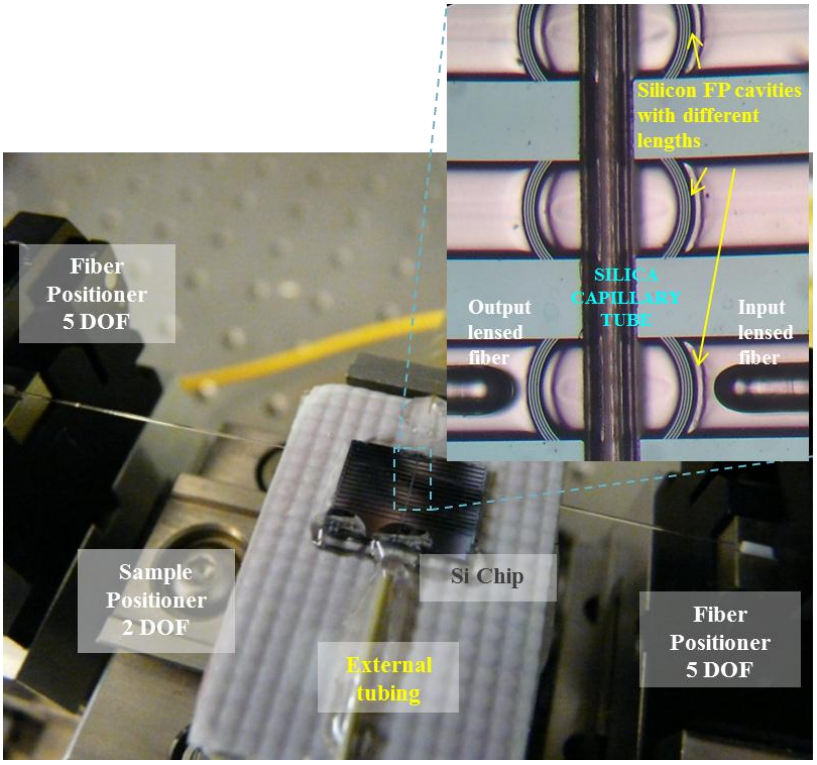

Fig. 3.8 Photo of the setup illustrating the silicon chip with the capillary tube connected to the injection tubing, and the Input/Output fibers on their positioners. The inset is a zoom of the different cavities, also indicating the placement of the fiber pair, one being used for light injection and the other for recording the spectral transmission response.

3.5 Refractometer performance evaluation

As stated previously, our device provides high quality factor despite its long cavity length, due to the confinement achieved by the curved surfaces of the cylindrical mirrors and the capillary tube. But on the other hand we have a limitation in the RI range due to the long cavity length that shortens the FSR and hence the range of the wavelength shift that the traced peak will experience while changing the refractive index until this peak will be confused with the neighbor peak. The cavity length can't be shorter than a distance that supports the tube inside and the mirror curvature. Also the sensitivity is not optimal since the light path of interest is only the tube inner diameter which contains the liquid; in our case the sensitivity is expressed by:

$$\frac{\delta\lambda}{\delta n_t} = \lambda \frac{d_{tube}}{total\ path\ length} \tag{3.2}$$

so the best case would be when the path inside the detected fluid (inside the tube) to the total cavity length should be maximum, i.e. the solution fills the whole cavity.

A compromised design to enhance the performance can be done by facilitating different cavities with different dimensions on the same chip to offer different sensitivity/range tradeoffs. Short cavities can achieve large range determining a rough estimation of the refractive index, and then a longer cavity with higher sensitivity gives more fine measurement. To get even better sensitivity, we can take advantage of the peak's fast roll-off resulting from the high quality factor and the large visibility to detect also the drop of power rather than the peak's wavelength shift only.

It is comprehensible that the sensitivity does not wholly articulate the capability of the device to detect and quantify the RI of the sample. Equally important is the ability to precisely and accurately quantify the change in the measured quantity due to the sample changes. Here, we introduce the concept of sensor resolution, which characterizes the smallest possible shift that can be accurately measured. The sensitivity and the sensor resolution combine to form the detection limit (DL) of the device [2, 4], which is the smallest change in RI that can be detected:

$$DL=\frac{\text{Resolution}}{\text{Sensitivity}} \tag{3.3}$$

In literature, different estimations for the resolution are employed. Either as the resonance line-width of the spectral peak [23], or as three times the root mean square value (rms) of the noise in the system, i.e 3σ [2, 4] .

3.5.1 Error Analysis

To analyze the error in the measurements, repeated data acquisition is achieved; the spectral response of the cavity with the tube filled with acetone is recorded every 10 min using the TLS and the PM. Fig. 3.9 shows part of the spectra, indicating low differences between the different outputs over time.

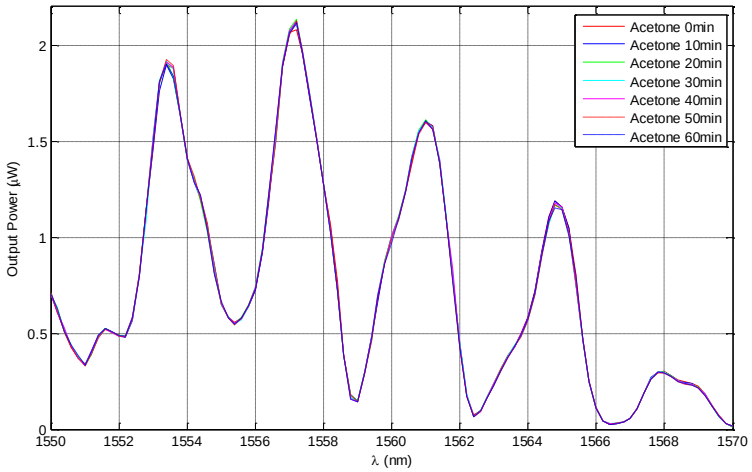

Fig. 3.9 The spectrum of the cavity with the tube filled with acetone recorded every 10 min to investigate the error in the system performance.

The peak that has the highest quality factor of about 2600 is shown in Fig. 3.10. It also shows good stability of the maxima position over different runs, as it always occurs at 1621.4 nm. An error of 0.05 nm in such position between the measurements and an interpolation fitting curve is recorded due to the poor measurements wavelength step of 0.2 nm.

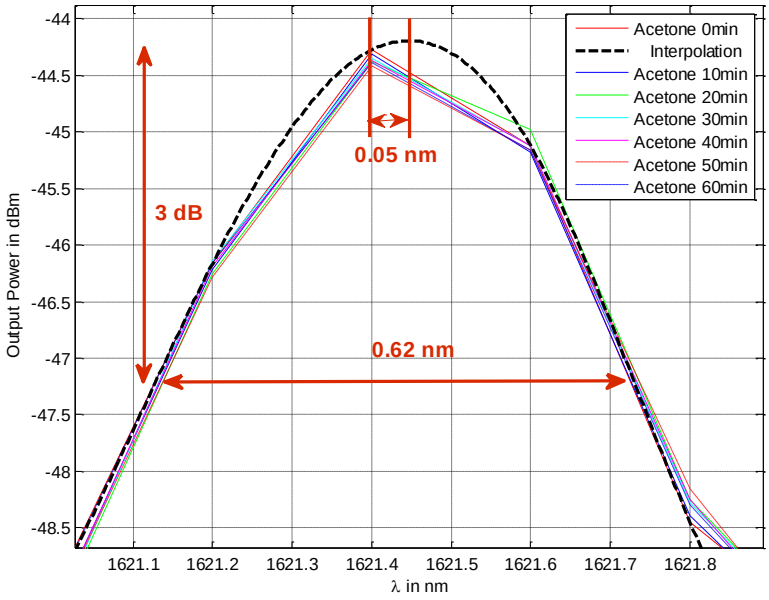

Fig. 3.10 The peak that have the highest quality factor

To quantify the error due to the power variations, the root mean square (rms) value of the error between each curve and the first one at time 0 min, taken as a reference, is calculated and plotted in Fig. 3.11. Maximum error of 0.011 μW is obtained over an hour.

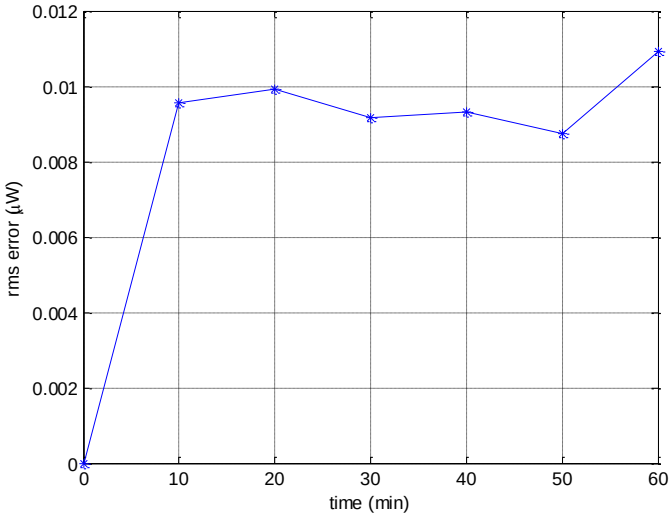

Fig. 3.11 Root mean square error between different spectra recorded every 10 minutes by TLS and PM.

3.6 Refractometry of liquids

3.6.1 Water-Acetone mixture

Performing the experimental testing, the measurements are done using a tunable laser source and a power meter. The light is injected and collected using a pair of lensed fibers. The spectra of different mixture rations between acetone and deionized water are shown in Fig. 3.12.

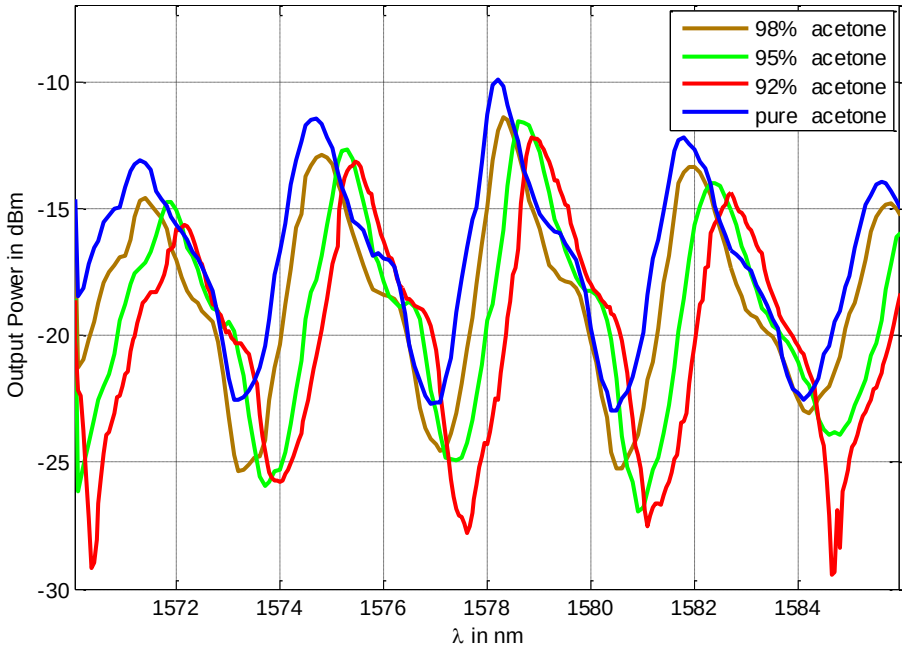

Fig. 3.12 The spectra of different mixture ratios between acetone and deionized water measured by the refractometer consisting of a cylindrical Fabry–Pérot cavity with the micro tube inside.

From the previous figure we notice that the power levels get reduced with the increasing water concentrations due to water absorption in this wavelength range. Hence we need to normalize each curve to its maximum value, also to get rid of any power fluctuations due to noise superimposed on the measured spectrum. The normalized curves are presented in Fig. 3.13.

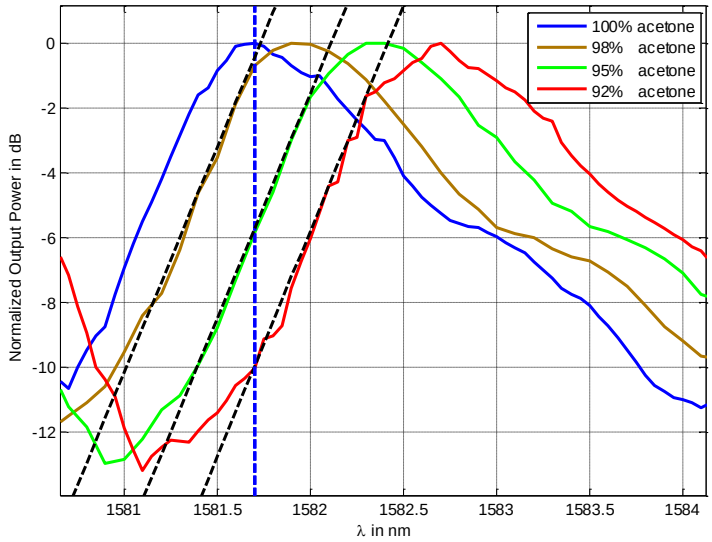

Fig. 3.13 The normalized spectra of different mixture ratios between acetone and deionized water measured by the refractometer consisting of a cylindrical Fabry–Pérot cavity with the micro tube inside. The blue dashed line represents a reference for detecting the power level shift linked to the refractive index.

Although the slope of the roll-off depends on the peak width that increases with losses, the slope of the tangents to the left side of all curves (black dashed lines) is almost constant; probably the loss is not of large effect in this case; which allows measuring the refractive index dependence on the power level but in the linear region only: The peak of the pure acetone is taken as a reference (the blue dashed line). It cuts the nearest curve of 98% acetone before the linear region; so only refractive index n larger than the reference solution by $0.0023 < \Delta n < 0.0045$ can be measured. This configuration can achieve sensitivity of 4,094 dBm/RIU and range of 9.3 dB that is equivalent to 0.0023 RIU, as calculated from the linear region in Fig. 3.14. Note that the visibility is this case is about 12 dB.

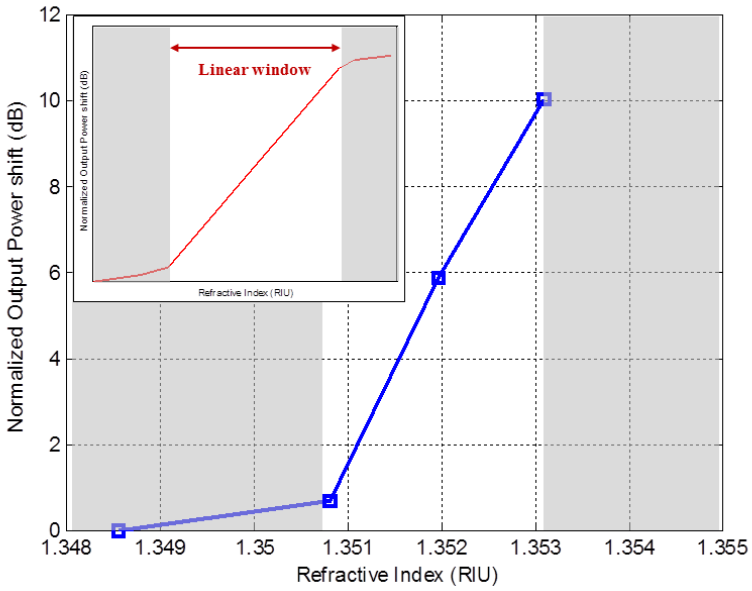

Fig. 3.14 The shift in the normalized power at the reference line with the change of the analyte refractive index.

By using also the shift of the peak maximum wavelength, larger range of 3.6 nm (equivalent to 0.0163 RIU) can be reached, but the sensitivity is 221 nm/RIU, as inherited from Fig. 3.15. As for the detection limit (DL), it has been previously indicated that there are two ways to determine the sensor resolution and hence its DL. Here, we will choose the resolution as 3σ. The error in determining the maxima wavelength is taken as the difference between the measured peak and the one estimated from an interpolation curve; which is found to be less than 0.05 nm (the error bars in Fig. 3.15 are equivalent to this value); that gives a DL of about 6.79×10^{-4} RIU.

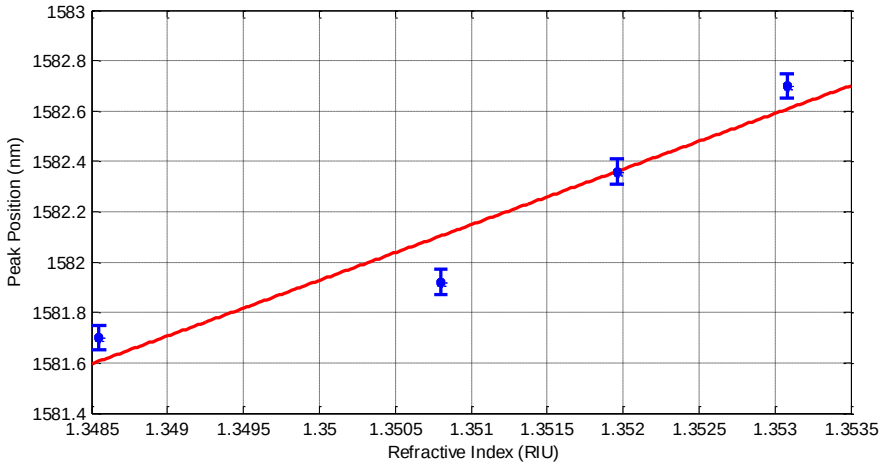

Fig. 3.15 The shift in the wavelength of the peak with the change of the analyte refractive index.

3.6.2 Toluene-Acetone mixture

We now use a mixture of toluene and acetone, for the absorption of both being almost the same, as demonstrated is section 3.3.2. The problem of the difference in transmission levels can be avoided as inherited from Fig. 3.16, where the peaks between the wavelengths of 1588 nm and 1600 nm (surrounded by the circle) have the same power transmission values, despite the different mixing ratios of toluene and acetone. The discrepancy between the maximal power values of the different curves at this peak is found to be less than 0.53 μW, which may be attributed to slit temperature changes, laser power instability, or alignment variations upon changing the liquids and running the scan.

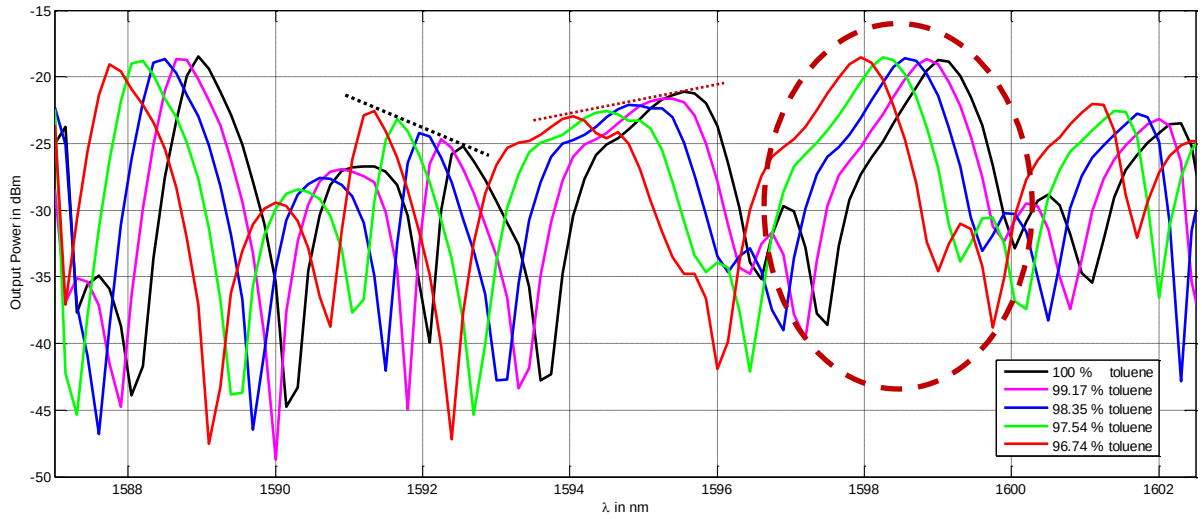

Fig. 3.16 The spectra of different mixture ratios of toluene and acetone measured by the proposed refractometry device.

Note that the peaks do not all behave in the same way, some have decreasing levels upon increasing the concentration of toluene like those around the wavelength 1592 nm (indicated by the tangent dashed black line with negative slope); other peaks have decreasing levels like those between the wavelengths of 1594 nm and 1596 nm (indicated by the tangent dotted red line with positive slope). To investigate the reason behind that, let's take a close look at the two extreme curves (100 % and 96.74 % concentration of toluene), which are magnified around the wavelength 1595 nm in Fig. 3.17. We notice that the side peak of the higher order mode in the black curve (at wavelength of 1597 nm for the 100 % toluene) is merged with the main peak for the red curve of the lower toluene concentration as the refractive index changes. This is probably the reason behind reducing the transmission level

of the later spectrum. Note that, similar behavior was numerically demonstrated with HFSS simulations is section 2.4.2 in the previous chapter as the refractive index test liquid changes.

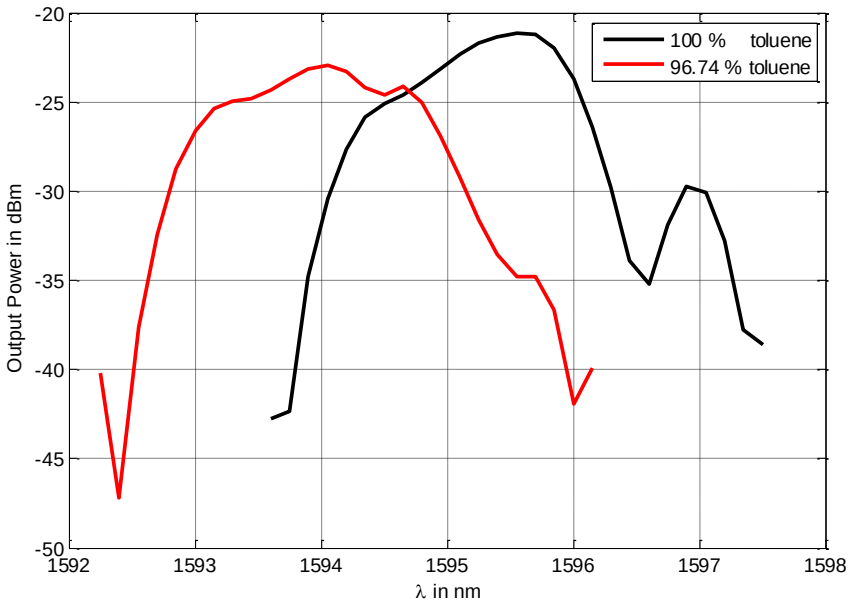

Fig. 3.17 Comparing the spectra of the two extreme cases to indicate that the decrease in the transmitted power level upon changing the RI is due to the modal interference between the main peak and that of the higher order mode.

To characterize the performance of the refractometer in this case, Fig. 3.18 shows the zoomed view of the output power in μW versus wavelength in nm, which gives better linearity, around the selected peak. A reference line from the peak of a fitting curve of the pure toluene spectrum is used to trace the power drop upon the spectrum shift with the liquid RI changing. The error in wavelength between the measured peak and an interpolation is found to be less than 0.07 nm for all the curves and it is due to the poor measurement wavelength step.

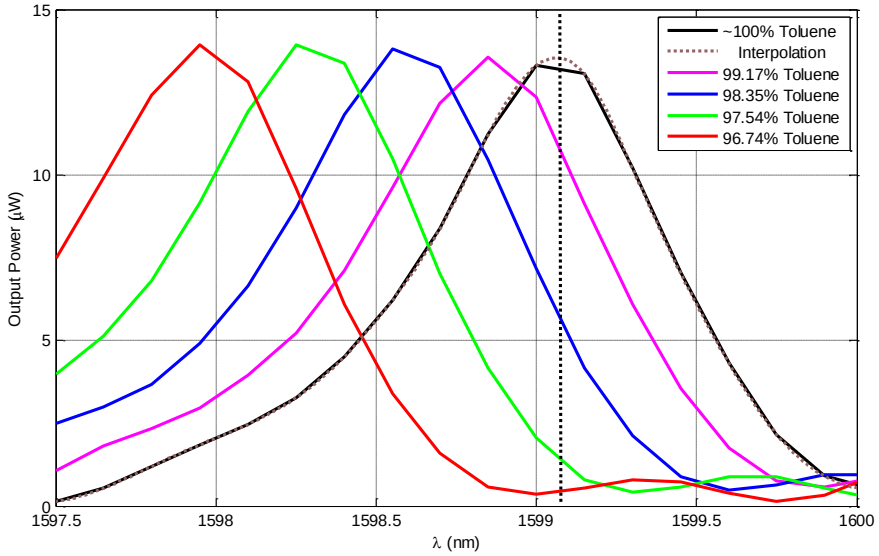

Fig. 3.18 Zooming of the output power in µW versus wavelength in nm around the selected peak for refractometry analysis.

The last two curves fall outside the nearly linear region. Unfortunately the refractive indexes for these liquid mixtures can't be found in literature. The available data is only the RI of pure toluene, which is taken to be 1.4773 at a temperature of 20°C near the wavelength of 1600 nm [12]. Tracing the peaks' wavelength shift upon changing the concentration, as shown in Fig. 3.19, reveals that the relation is quadratic rather than linear, which indicates that the RI property for this liquids mixture is not additive linearly upon volume ratio (similar to the water-acetone case), hence it can't be calculated from the values of pure acetone and pure toluene available in literature. Therefore, experimental characterization of the sensor can't be done in this case, and a similar processing like the previous to get the actual values of sensitivity and range is not possible, due to the lack of the RI reference values.

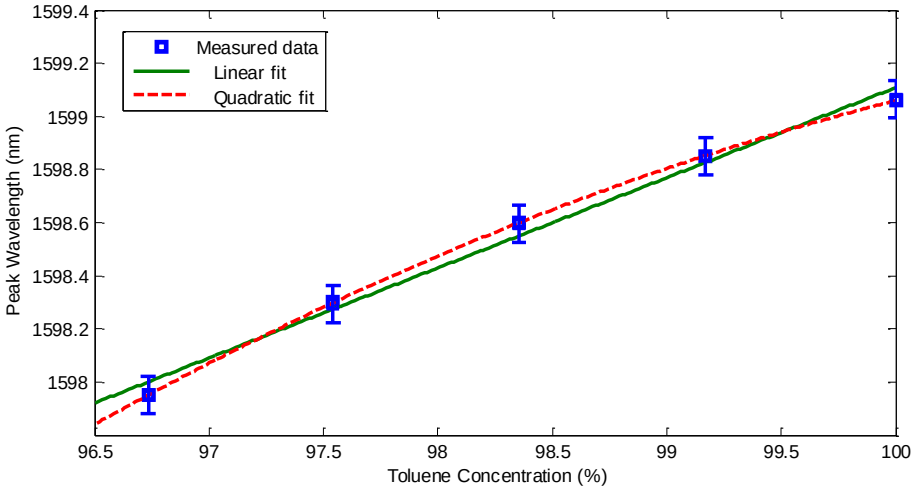

Fig. 3.19 The position of the maxima wavelength versus the toluene concentration in the toluene-acetone mixture.

Hence, to evaluate the performance in this case, approximate analytical calculation is employed as follows: For the conventional method of tracing the peaks' wavelength shift, the calculated value of $\delta\lambda/\delta n_t$ from equation (3.2), gives sensitivity of 353 nm/RIU and a range of 3.45 nm before interfering with the next peak, which is equivalent to about 0.01 RIU change. The error in the maxima wavelength between the measured peak and the one estimated from an interpolation curve is found to be less than 0.07 nm (the error bars in Fig. 3.19 are equivalent to this value); which gives a DL of about 6×10^{-4} RIU, calculated using equation (3.3). Then the calculated RI of the unknown mixture obtained by this method is employed to calibrate the sensor operating in the second mode while tracing the power drop from the reference, to get the sensitivity of $\delta P/\delta n_t$. Fig. 3.20 The estimated refractive index versus the toluene concentration in the toluene-acetone mixture. shows the obtained RI values versus Toluene concentration, a good agreement between both methods is obtained at $\delta P/\delta n_t$ of approximately 5,500 µW/RIU. And the range in this case is - 2.73 µW < ΔP < -12.12 µW, that is equivalent to 0.0005 < Δn < 0.0022. Note that the last point is far from the linear region, and hence it doesn't fit with the expected RI value.

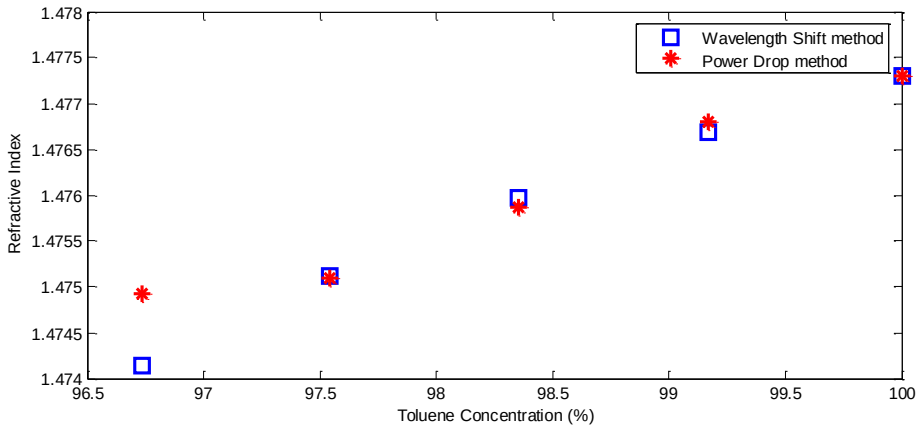

Fig. 3.20 The estimated refractive index versus the toluene concentration in the toluene-acetone mixture.

For this case, the resolution can't be estimated by the line spectral width method, because the sensed quantity is not the spectral shift; rather, only the value of three times the noise variations (3σ) could be employed. The rms value (σ) of the peak power variations is found to be 0.35 µW. In this case, the DL is estimated by 1.9×10^{-4} RIU.

3.7 Refractometry of colloids

After the above-presented study on mixtures of two miscible fluids, the next phase is to investigate the potential of our refractometer for measuring complex fluids. In general, those complex fluids include non-miscible liquids (leading to emulsions), gas-liquid mixtures (leading to foams or gels) and solid liquid mixtures (leading to sols). In order to illustrate such behavior, we have chosen to perform experiments on sols, referred as "colloids" in what follows.

3.7.1 Experimental

The spectra of DI water and that of DI water containing 0.5 μm polystyrene microspheres (reference 17152 from Polysciences) with different concentrations ranging from 2.5 % to 0.43 % has been recorded using the previous setup. Light is injected from the swept-wavelength tunable laser and measured by the power meter using ordinary cleaved fibers glued to the chip, in order to minimize the vibrational disturbances. The measured spectra are presented in Fig. 3.21. With the presence of the micro beads, especially with high concentrations (the 2.5% solids (w/v) aqueous suspension, which is equivalent to 3.64×10^{11} particles/ml), the spectrum has a lot of perturbations, as compared with the sample free from particles. These perturbations in the spectrum take the form of spikes that might be due to scattering or to other kinds of interactions involving the particles. These perturbations are less for lower particle concentrations; and the spectrum is shifted due to reduced effective refractive index with the reduction of the solid contents, noting that the polystyrene has higher refractive index than the DI water, that is 1.6.

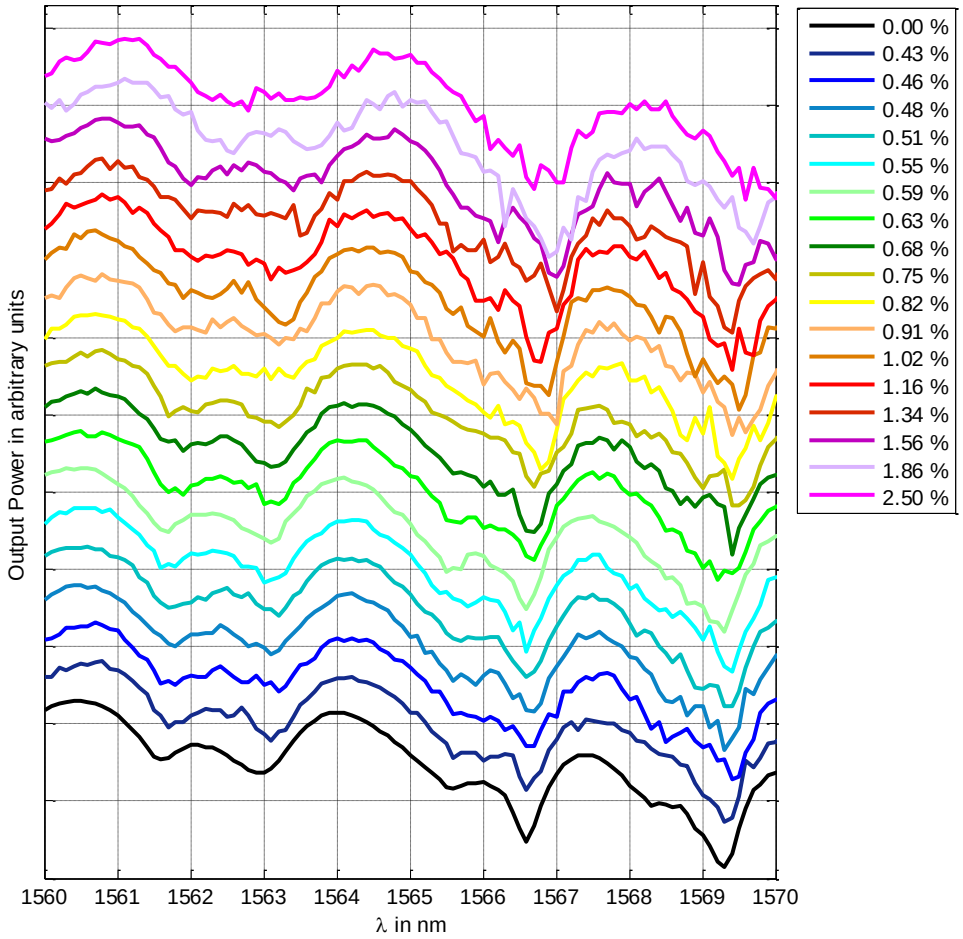

Fig. 3.21 The spectra of DI water and DI water containing 0.5µm polystyrene microspheres with different concentrations ranging from 2.5 % to 0.43 %. Note that the power reference has been changed for every curve in order to superpose them for better comparison.

As shown in the previous figure, the spectra of the DI water with the beads show perturbations in the spectral response. These perturbations are time-dependent as shown in Fig. 3.22, which shows different spectra for the solution of 2.5% concentration recorded at different times. Significant differences can be noticed.

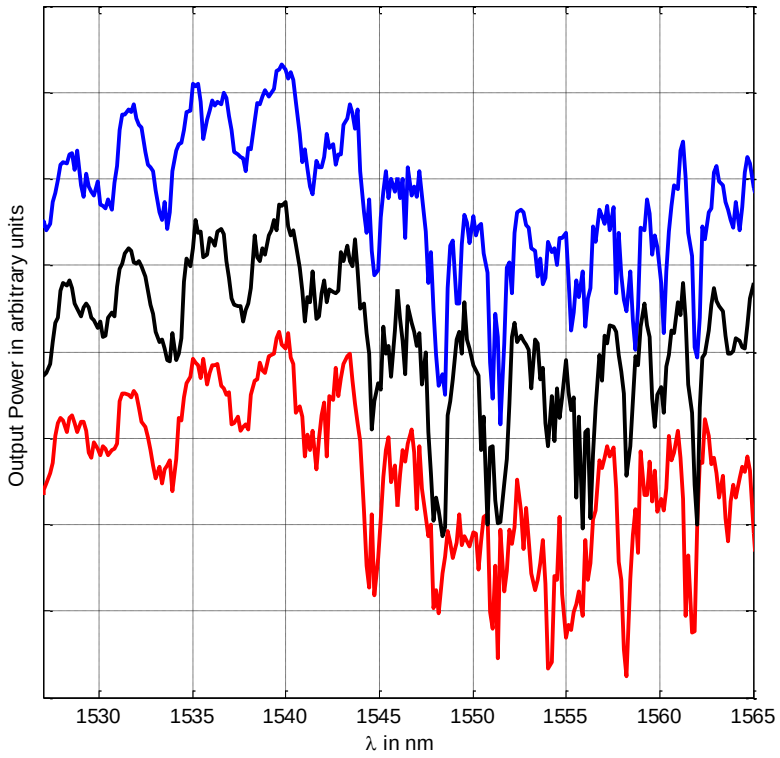

Fig. 3.22 Spectra of DI water solution with 2.5% beads concentration recorded at different times. Note that the power reference has been changed for every curve in order to superpose them for better comparison.

To get an idea about the amount of error in such measurements, an appropriate peak (with reasonable amount of perturbation that doesn't distort its shape significantly) is selected and the wavelength of the maxima and the 3dB bandwidth (BW) are determined from the measured spectra and from a smoothed version of them (done by a simple filtration using averaging of 5 successive points), as illustrated in Fig. 3.23. The mean value of the maxima wavelength of such peak is 1557.25 nm, while the mean value of the BW is 1.34 nm. This gives a mean quality factor value, which equals the peak maxima wavelength over the BW, of 1162.

The rms error in the maxima wavelength position is found to be 0.106 nm, and that in the BW is 0.186 nm. To determine the maximum error in the quality factor, the maximum estimation of the wavelength position of the peak maxima (equals to the mean value plus the rms error) is divided by the minimum estimation of the BW (the mean value negative the BW rms error), that gives the maximum estimation of the quality factor, then the mean value is subtracted from it, which gives maximum error value of 187.4.

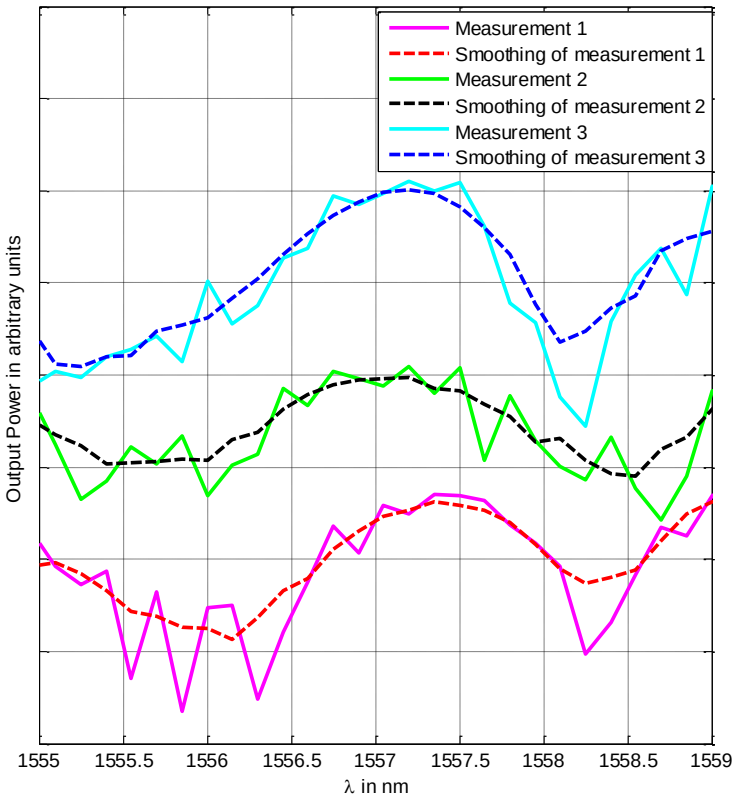

Fig. 3.23 Zoom on the selected peak from the spectra of DI water solution with 2.5% beads concentration recorded at different times, with the smoothing of the curve to allow data extraction. Note that the power reference has been changed for every curve in order to superpose them for better comparison.

Now the change in the resonance positions and in the quality factor with difference beads' concentrations will be determined. For that, the spectra in Fig. 3.21 will be used to estimate the mean values for the peak maxima wavelengths and the BW. Then the values of error stated above will be used as the worst case scenario.

First, the peak maxima wavelength values for different particles' concentrations are plotted in Fig. 3.24. The error in the maxima wavelength position of 0.106 nm stated above is used to plot the error bars. It is clear that there is a shift in the peak wavelength, as expected, due to the different effective refractive index in each case. This shift is approximately linear as determined from the red fitting curve.

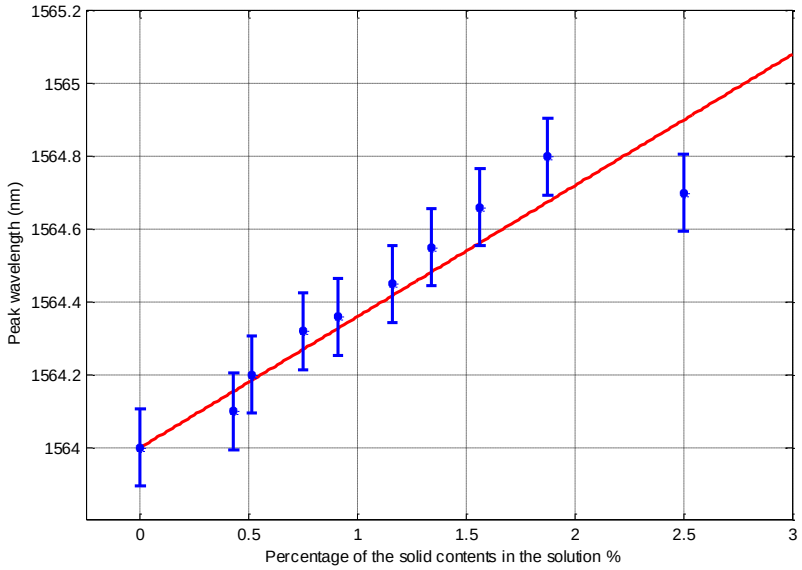

Fig. 3.24 The peak maxima wavelength position versus the beads concentration.

From the slope of the fitting curve in Fig. 3.24, the sensitivity is about 0.36 nm/concentration percentage unit. Note that the difference between the data and the fitting generally increases with increasing the solid volume percentage, which is reasonable since there are more scattering microspheres in the solution, which causes higher scattering and renders the curve more disturbed, which in turn, makes the peak maxima position more difficult to assign.

Second, to determine the quality factor for different beads concentrations, the mean values are calculated as follows: the previous mean values of the peak maxima wavelength are divided by the mean BW values determined from the spectra in Fig. 3.21. These calculated quality factor values are plotted in Fig. 3.25. The error bars are equivalent to the previously stated maximum error value in quality factor of 187.4. The fitting red line highlights the trend of these values with varying the particles' concentration.

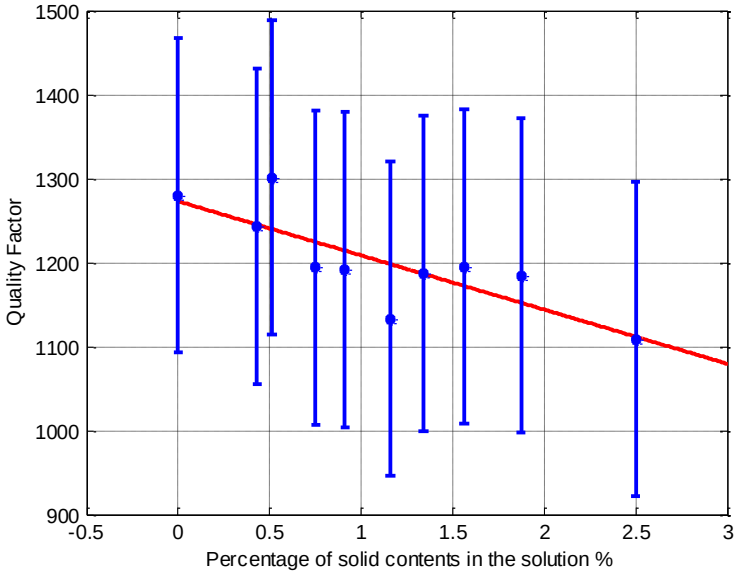

Fig. 3.25 The quality factor versus the beads concentration.

As expected, the quality factor is decreasing with the beads' concentration due to the higher scattering loss, as inherited from Fig. 3.25.

To emphasize if these fluctuations in the spectrum are temporal variations due to different scattering from the moving beads or due to secondary resonances within the spherical beads, the input laser power is set at a single wavelength and the output power is recorded with time at shown in Fig. 3.26. The recorded power shows high variations with an rms value of 0.18 μW around the mean value of 1.46 μW. This variation is much larger than the normal error in the system, which is 0.011 μW, as previously stated in section 3.5.1. This manifests the fact that these power variations are due to the motion of the beads. Also certain amount of correlation can be noticed, which is expected in this situation, since the beads exhibit close distribution patters over short time intervals [24].

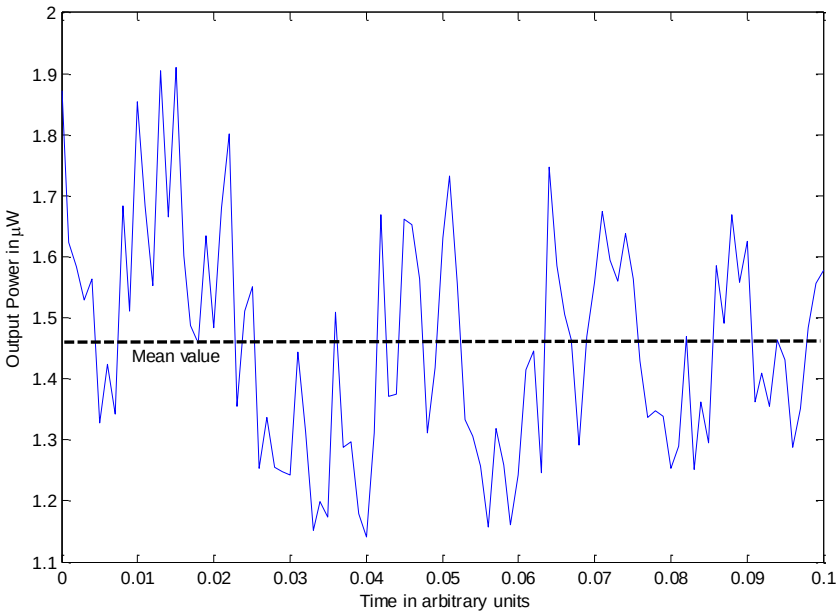

Fig. 3.26 Output power fluctuations over time even at a single wavelength input.

3.7.2 Numerical simulations

Numerical finite element method (FEM) simulations have been performed to observe the effect of such suspended particles on the spectral response. The ANSOFT High Frequency Structural Simulator (HFSS) software is used, to get an idea about the spectral response, and determine if it has the same variations observed experimentally or not. Also an idea about the field distribution inside the cavity could be obtained from such simulations so as to be able to detect localized resonances, if any, involving the suspended particles. Since the behavior of beads suspension depends on the relative wavelength/particles relation, actual sizes of microspheres should be simulated; the cavity and the capillary dimensions as well as the beam waist size should be also at least in the same order of magnitude as the actual ones. To accomplish the simulation task with the limited computational resources, we adopted what may be called 2D simulations. A cavity with a small height (a slice) is modeled, and symmetry conditions are imposed as boundary conditions on the parallel planes delimiting the cavity height to mirror the structure. The height of the slice is taken as 0.1 μm. The planar dimensions are taken as the cavity actual size presented in section 3.4 divided by 4; also to limit the number of unknowns and thus the memory requirement, the cylindrical mirrors are modeled as one single layer having the smallest possible thickness that is one quarter of

wavelength in silicon. The light source was chosen as a TE-polarized Gaussian beam located at a distance from the input side equivalent to the working distance of the lensed fiber used in the experiments. Despite the few differences between the model and the actual physical case, this simulation may give an idea about the spectra and the lateral field distribution at different resonance conditions. The spectral responses have been obtained by performing a frequency sweep and plotting the integrated power on a sheet at the output area versus the frequency (which can be scaled into wavelength in post processing). This output power is then normalized to the input power to obtain the spectral transmission for the cases where the capillary tube is filled with deionized (DI) water without any particles, and with a pattern of randomly dispersed polystyrene beads of 0.5 μm diameter, leading to the resonance wavelengths in each case. Fig. 3.27 compares the spectrum of pure DI water with that of DI water with a random distribution of 0.5 beads.

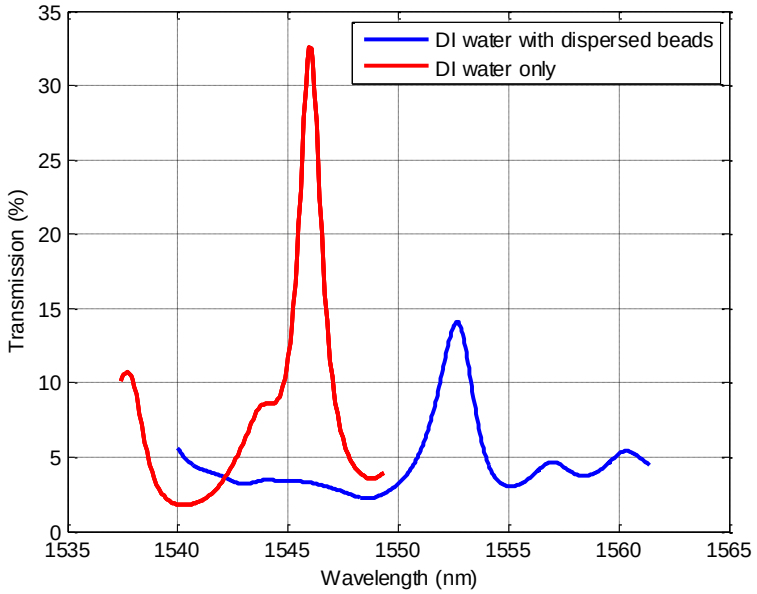

Fig. 3.27 The spectra of pure DI water and of DI water with a random distribution of 37 beads with diameter of 0.5 µm.

As can be noticed, the spectrum of the dispersed beads is smooth and doesn't exhibit the same fluctuations as in the measured spectra, which implies that this effect is temporal, probably due to Brownian motion as will be detailed in the next section. Also the peak is shifted to higher wavelengths due to the longer optical paths within the polystyrene beads that have higher refractive index; and also it suffers from less transmission magnitude and more broadening -which means less finesse and probably less quality factor as well- due to higher loss done by the scattering from the micro beads.

The wavelengths corresponding to the resonance in each case are obtained from Fig. 3.27, and then the field distribution is plotted at these wavelengths as shown in Fig. 3.28 for the pure DI water case, and in Fig. 3.29 for the DI water with dispersed beads case.

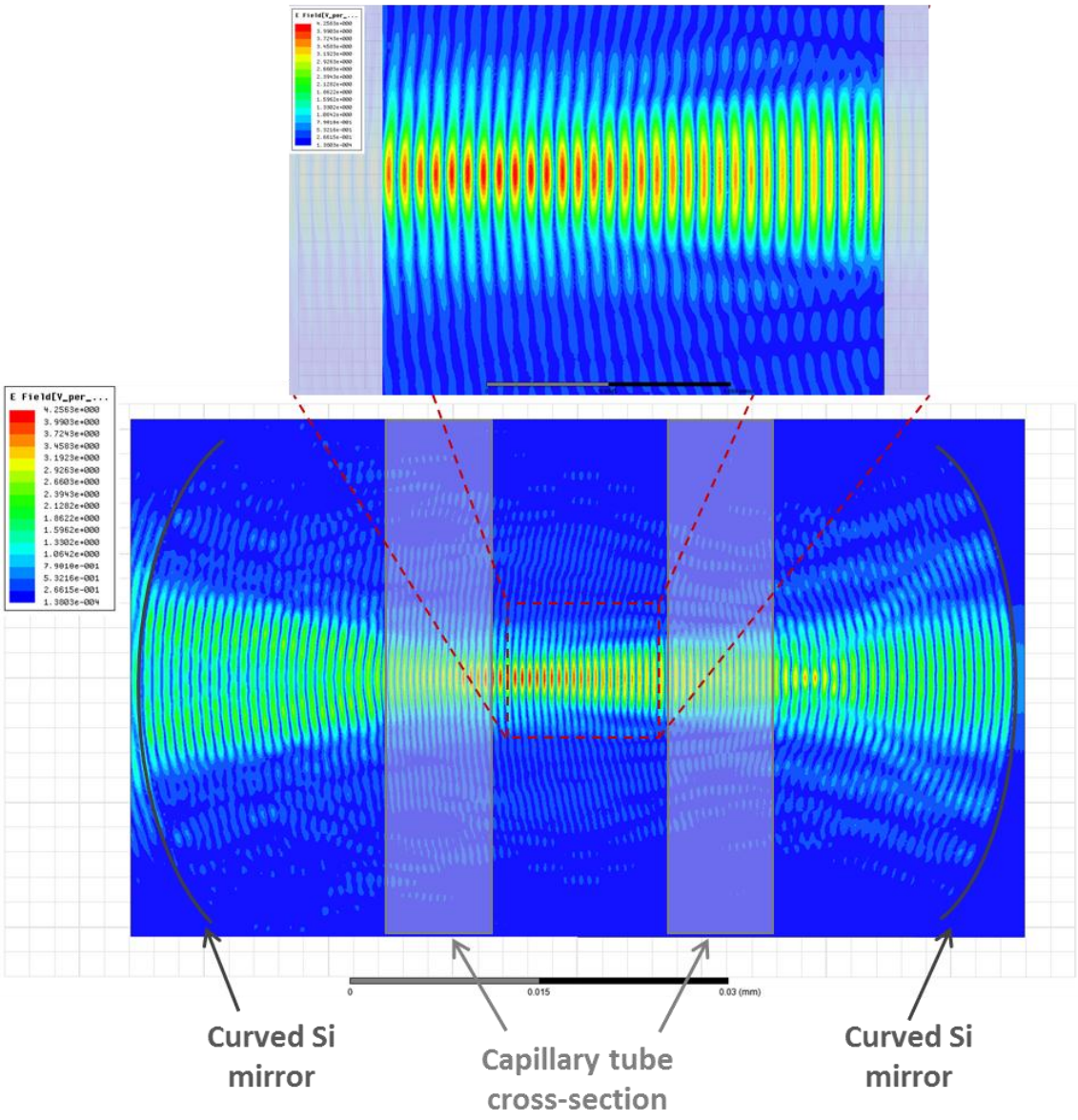

Fig. 3.28 The field distribution for the cavity with tube filled by DI water, at the maxima wavelength of 1545.96 nm.

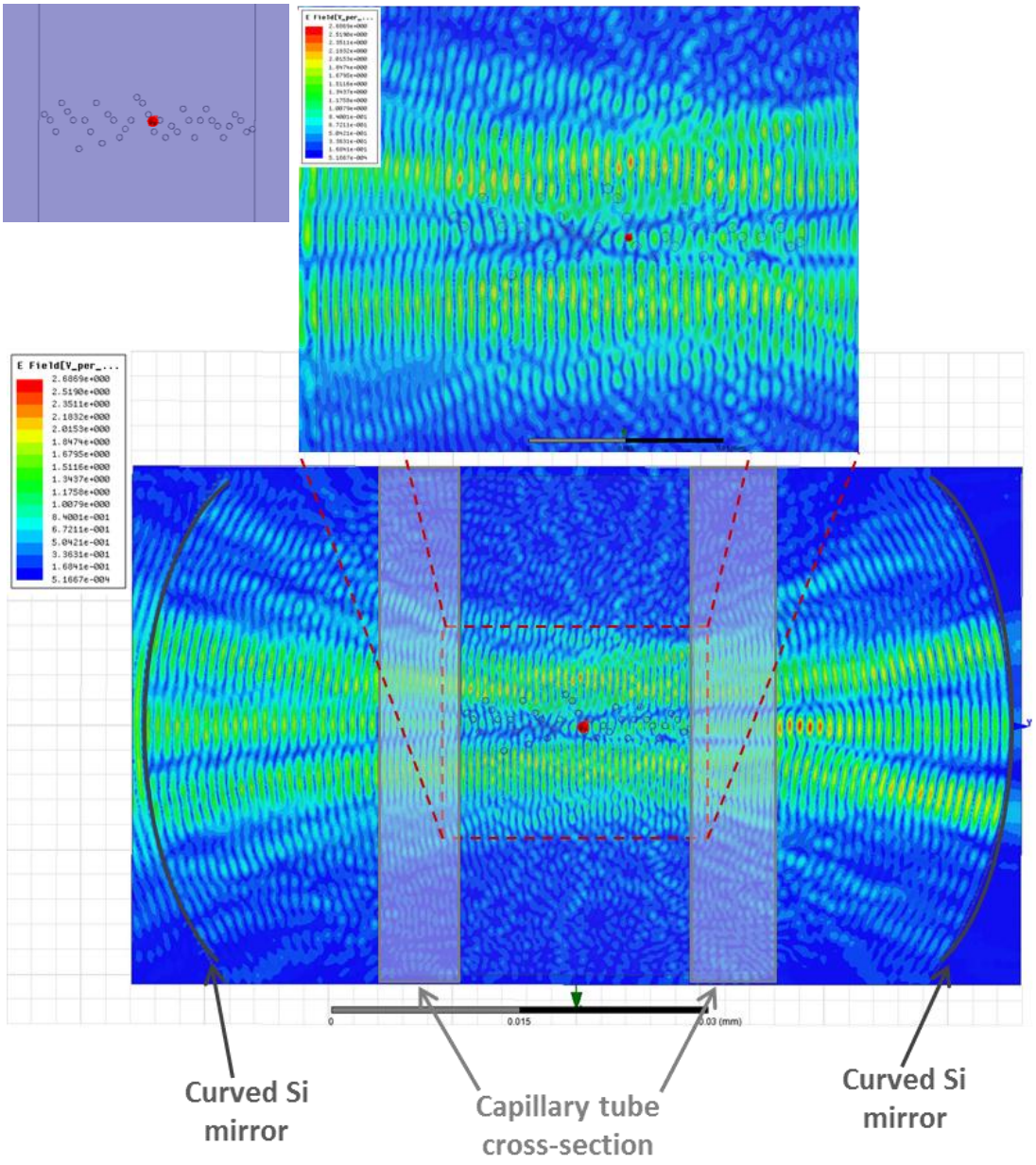

Fig. 3.29 The field distribution for the cavity with tube filled by DI water and random distribution of 0.5 µm diameter polystyrene beads, at the maxima wavelength of 1552.6 nm. The inset at the left upper corner is the distribution of the beads within the middle region.

3.7.3 Phenomenological analysis

When a coherent light is sent inside the material, the light diffuses inside the volume up to a depth depending on the optical properties of this material (diffusion and absorption). The photons experience many scattering whenever they encounter optical index inhomogeneities or microscopic objects like the micro beads with dimensions comparable to or larger than the light wavelength, as represented schematically in Fig. 3.30.

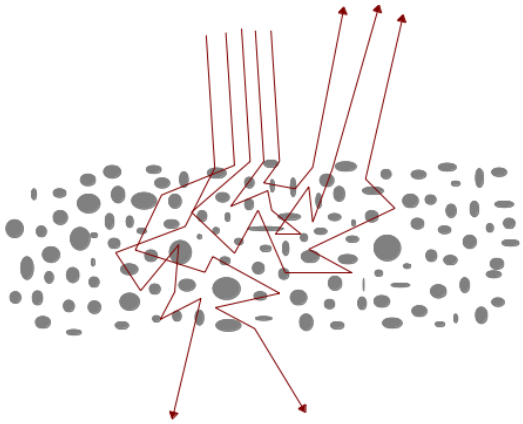

Fig. 3.30 The scattering of light when it encounters optical index inhomogeneities like micro particles [25].

Assume for instance that the microscopic objects are static. If a white screen is put in front of the assembly to collect the diffused light, a pattern of dark and bright dots with different intensities is observed like that in Fig. 3.31. At each point of the screen, the light intensity is the result of interferences between all the photons coming from the diffusive pattern. Each photon has passed a different path length. And so the resulting light intensity is the result of the sum of many waves having the same frequency but not the same phase shift (due to differences of path length). It is known that such interferences produce “fringes” called speckle. These fringes look like small grains of light. Some points receive no light at all, and hence are dark, where the light waves coming to them interfere destructively. The brightest points have the waves coming to them interfere constructively.

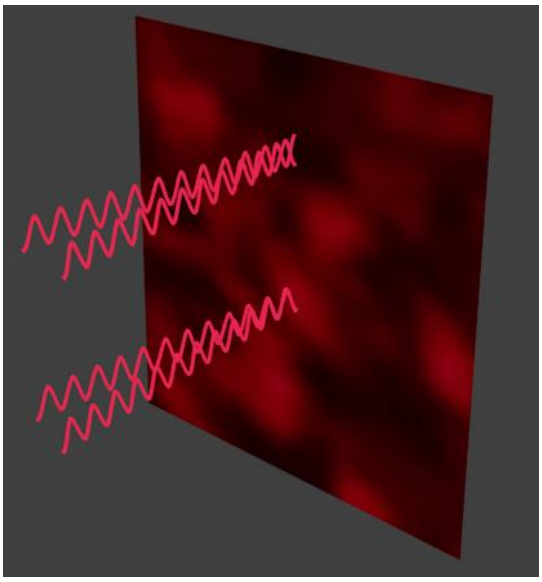

Fig. 3.31 A laser sends photons inside the medium and the scattered rays create the speckle pattern on the screen. Black zones are due to destructive interferences and bright spots are due to constructive interferences [25].

In our experiments, a detector is put instead of this screen; and it typical gives one effective light intensity value equivalent to integrating the incident light on its aperture. Now if the natural Brownian motion of the microscopic objects is taken into consideration, the rays scattered by these objects will have their paths modified due to their movements and so the interference state that comes from the phase shift of each ray coming to the sensor will change with time. The sensor will thereby detect variations of light intensity. An illustrative video for this action is found in ref. 25. Certain correlation can be found in that recovered intensity signal over time [24].

3.7.4 Aggregation of beads in the light

If a lensed fibre is used to inject the light, the efficiency of confining the light inside the cavity is higher; and hence, the power level inside the cavity is expected to be higher. In that case, an interesting phenomenon is observed: the beads tend to aggregate or accumulate over time to form a cloud due to the effect of the light beam as demonstrated in Fig. 3.32. The source power in this case is 4 mW. Faster aggregation can be achieved if higher power values are used as will be demonstrated in the next chapter.

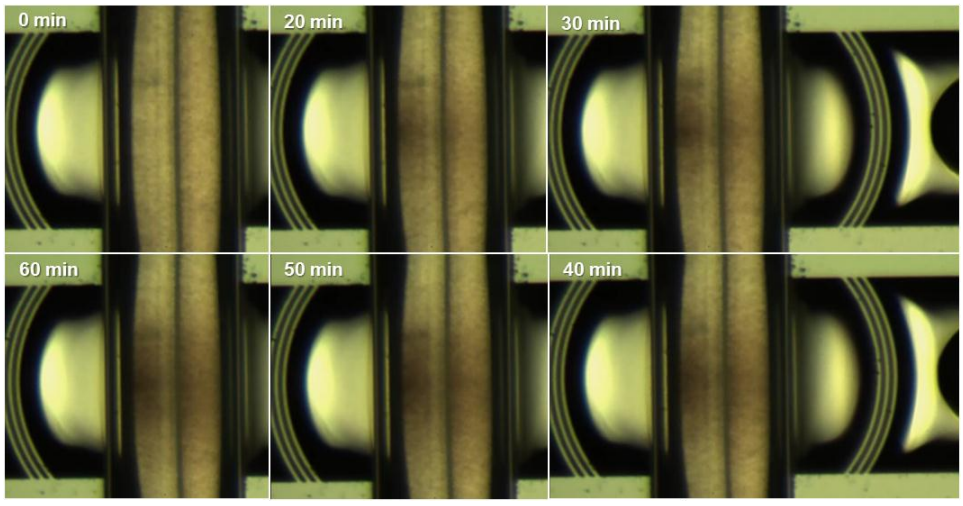

Fig. 3.32 Aggregation of the beads optically over time.

This effect has been attributed to the optical binding phenomenon (which has a close relation to the optical trapping phenomenon). These phenomena are studied in detail and demonstrated experimentally in the next chapter.

3.8 Conclusion

In this chapter, a study on using our devise as a refractometer has been performed. Two different modes of operations have been performed:

1- Tracing the peak maxima shift in wavelength upon changing the analyte RI.

2- Tracing the power drop at a fixed wavelength on the peak slope upon shifting the peak.

The first method achieves wider range but low sensitivity. The second one, which is considered rather new for this type of resonators, can attain high sensitivity –which also still could be improved further – but on the expenses of the limited range of accessible values of the refractive index. To characterize the refractometer, mixtures of two liquids have been employed; but some difficulties have been faced due to the light absorption within our wavelength range and/or the nonlinear behavior of the RI property of the resulting mixture upon mixing these liquids on volume bases. These challenges have been addressed and solved.

Then the area of the refractometry of colloids has been explored. Some interesting phenomena have been observed due to temporally varying scattering of light, and due to optical binding. Nonetheless, rough estimation of the RI could be obtained.

3.9 References for chapter 3

[1] C. -Y. Chao, W. Fung, and L. J. Guo, "Polymer microring resonators for biochemical sensing applications," IEEE J. Sel. Top. Quantum Electron., vol. 12, pp. 134-142, 2006.

[2] A. Yalcin, K. C. Popat, O. C. Aldridge, T. A. Desai, J. Hryniewicz, N. Chbouki, B. E. Little, O. King, V. Van, S. Chu, D. Gill, M. Anthes-Washburn, M. S. Unlu and B. B. Goldberg, "Optical sensing of biomolecules using microring resonators," IEEE J. Sel. Top. Quantum Electron., vol. 12, pp. 148-155, 2006.

[3] S. Arnold, D. Keng, S. I. Shopova, S. Holler, W. Zurawsky, and F. Vollmer, "Whispering gallery mode carousel – a photonic mechanism for enhanced nanoparticle detection in biosensing," Opt. Express, vol. 17, pp. 6230-6238, 2009.

[4] I. M. White, and X. Fan, "On the performance quantification of resonant refractive index sensors," Opt. Express, vol. 16, pp. 1020-1028, 2008.

[5] A. Llobera, R. Wilke, and S. Büttgenbach, "Poly(dimethylsiloxane) hollow Abbe prism with microlenses for detection based on absorption and refractive index shift," Lab Chip, vol. 4, pp. 24-27, 2004.

[6] X. Liang, A. Liu, C. Lim, T. Ayi, and P. Yap, "Determining refractive index of single living cell using an integrated microchip," Sens. Actuators A, vol. 133, pp. 349-354, 2007.

[7] P. Domachuk, I. Littler, M. Cronin-Golomb, and B. Eggleton, "Compact Resonant Integrated Microfluidic Refractometer," Appl. Phys. Lett., vol. 88, pp. 093513, 2006.

[8] W. Song, X. Zhang, A. Liu, C. Lim, P. Yap, and H. Hosseini, "Refractive index measurement of single living cells using on-chip Fabry-Pérot cavity," Appl. Phys. Lett., vol. 89, pp. 203-901, 2006.

[9] L. Chin, A. Liu, C. Lim, X. Zhang, J. Ng, J. Hao, and S. Takahashi, "Differential single living cell refractometry using grating resonant cavity with optical trap," Appl. Phys. Lett., vol. 91, pp. 243901-3, 2007.

[10] H. Shao, W. Wang, S. Lana, and K. Lear, "Optofluidic intracavity spectroscopy of canine lymphoma and lymphocytes," Photon. Technol. Lett., vol. 20, pp. 493-495, 2008.

[11] H. Shao, W. Wang, S. Lana, and K. Lear, "Optofluidic Intracavity Spectroscopy of Canine Lymphoma and Lymphocytes," Photon. Technol. Lett., vol. 20, pp. 493-495, 2008.

[12] W. Wang, D. W. Kisker, D. H. Thamm, H. Shao, and K. L. Lear, "Optofluidic Intracavity Spectroscopy of Canine Hemangiosarcoma," IEEE Trans. Biomed. Eng., vol. 58, pp. 853-860, 2011.

[13] R. St-Gelais, J. Masson, and Y.-A. Peter, "All-silicon integrated Fabry–Pérot cavity for volume refractive index measurement in microfluidic systems," Appl. Phys. Lett., vol. 94, pp. 243905, 2009.

[14] T. Beer, G. P. Hoornweg, A. Termaten, U. A. Brinkman, N. H. Velthorst, and C. Gooijer, "Forward-scattering degenerate four-wave mixing for sensitive absorption detection in microseparation systems: Coupling to micro-column liquid chromatography," J. Chromatogr. A, vol. 811, pp. 35-45, 1998.

[15] C. Thammakhet, P. Thavarungkul, and P. Kanatharana, "Development of an on-column affinity smart polymer gel glucose sensor," Anal. Chim. Acta., vol. 695, pp. 105-112, 2011.

[16] I. M. White, H. Oveys, and X. Fan, "Liquid-core optical ring-resonator sensors," Opt. Lett., vol. 31, pp. 1319-1321, 2006.

[17] S. Kedenburg, M. Vieweg, T. Gissibl, and H. Giessen, "Linear refractive index and absorption measurements of nonlinear optical liquids in the visible and near-infrared spectral region," Opt. Mater. Express, vol. 2, pp. 1588- 1611, 2012.

[18] W. M. Farlane, and R. Wright, "Binary Liquid Systems and the Mixture Rule," J. Chem. Soc., pp. 114-118, 1933.

[19] S. S. Kurtz Jr., and A. L. Ward, "The refractivity intercept and the specific refraction equation of newton. i. development of the refractivity intercept and comparison with specific refraction equations," J. Franklin Inst., vol. 222, pp. 563-592, 1936.

[20] S. S. Kurtz Jr., A. E. Wikingsson, D. L. Camin, and A. R. Thompson, "Refractive Index and Density of Acetone-Water Solutions," J. Chem. Eng. Data, vol. 10, pp. 330-334, 1965.

[21] C. -B. Kim, and C. B. Su, "Measurement of the refractive index of liquids at 1.3 and 1.5 micron using a fiber optic Fresnel ratio meter," Meas. Sci. Technol., vol. 15, pp. 1683-1686, 2004.

[22] F. Marty, L. Rousseau, B. Saadany, B. Mercier, O. Français, Y. Mita, and T. Bourouina, "Advanced Etching of Silicon Based On Deep Reactive Ion Etching For Silicon High Aspect Ratio Microstructures and Three-Dimensional Micro and Nano Structures," Microelectron. J., vol. 36, pp. 673-677, 2005.

[23] P. Skafte-Pedersen, P. S. Nunes, S. Xiao, and N. A. Mortensen, "Material Limitations on the Detection Limit in Refractometry," Sensors, vol. 9, pp. 8382-8390, 2009.

[24] G. Maret, and P. E. Wolf, "Multiple light scattering from disordered media. The effect of brownian motion of scatterers," Z. Phys. B - Condensed Matter, vol. 65, pp. 409-413, 1987.

[25] Online website: http://photonlyx.com/2013/10/09/dynamics-of-microstructure-and-diffusing-wave-spectroscopy-dws/

CHAPTER (4)

OPTICAL TRAPPING AND BINDING

4.1 Introduction

In daily life, it is not very common to consider that light can produce mechanical action as a direct effect of the electromagnetic field. Indeed, the force applied by light has little effect on the macroscopic world; it is too weak to cause observable motion on large objects. However, the advent of laser technology has allowed light to be focused and produce the forces necessary to move micro/nano objects on the angstrom scale and even to propel such small objects over several millimeters. The corresponding theory is related to the rather new field of optomechanics. Arthur Ashkin started exploiting the optical force effect in 1970 to trap and move particles with light emanating from two focused Gaussian beams [1] ; this was later known as 'Counter-propagating dual-beam traps'. Sixteen years later, Ashkin and coworkers showed that a single tightly focused laser beam can hold a dielectric particle in a stable, 3D potential well [2], which became known as the 'optical tweezers'. Since then, optical trapping has grasped huge attention due to its important applications in handling and analysis of micro particles (especially single biological entities [3]) as well as their sorting [4]. To this end, the majority of experimental setups adopt free space tightly focused light beams to achieve the gradient in the electromagnetic field needed for obtaining optical tweezers; but most often than not, the optical setup is off-chip and requires rather high optical power, typically hundreds of milliwatts or even few watts [1- 4].

To overcome the bulky, free space universal optical tweezers, the use of optical integrated structures and optical resonators is being extensively investigated to achieve on-chip, low power and compact size optical traps; these researches have led to the development of different configurations to achieve localization control and/or simple manipulation. To name some of these on-chip optical trapping modules: evanescent fields from waveguides and Whispering Gallery Mode (WGM) resonators, in the form of ring resonators [5], disks [6], or spheres [7] are used to propel particles along the light propagating path. Multimode-interference (MMI) structures [8], and photonic crystals are used to trap particles at specific

locations [9]. Among all these techniques, none has the full three-dimensional (3D) handling capabilities provided by the conventional optical tweezers.

So-far, the best miniaturized configuration regarding simplicity, and low optical power in tradeoffs with trapping and manipulation performance is probably the counter-propagating dual-beam trap that is formed by two single-mode optical fibers [10, 11]. This kind of trap has the advantage of confining the objects placed between the two opposite waves coming from the two fibers without the need of focusing components, because the generated opposed optical forces trap the particles. A standing wave is formed due to interference between these two waves traveling in opposite directions [12], but in some cases – if needed – this stationary wave can be avoided by slightly misaligning the fibers to simplify the system analysis [13]. Although the dual-beam trap is simple, it requires splitting the light path to provide double-side injection of light and it also strongly depends on the mutual fiber alignment. Using a Fabry–Pérot (FP) cavity avoids these issues by providing the two counter-propagating waves in the form of a standing wave resulting from the multiple reflections of the light –injected from a single side only– by both cavities' mirrors, as indicated in Fig. 4.1.

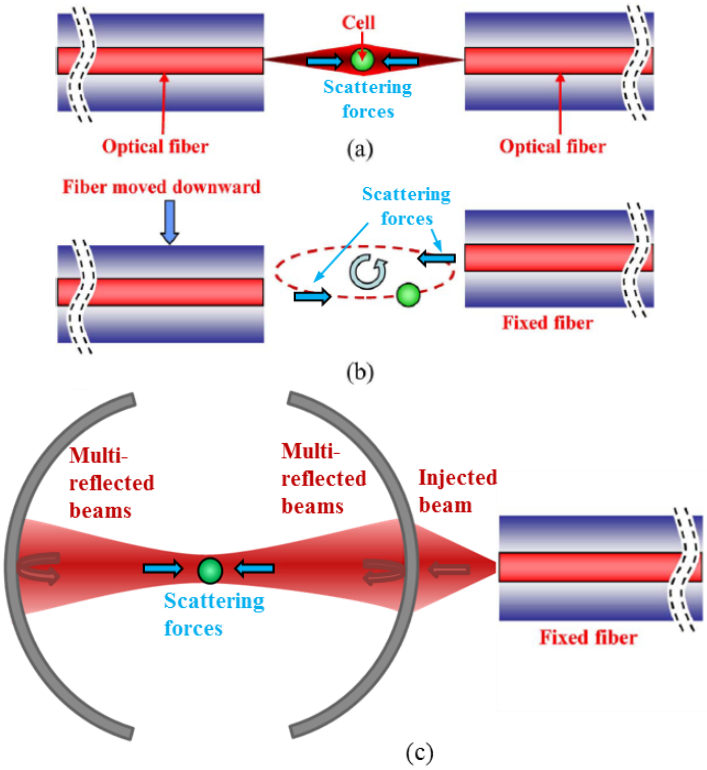

Fig. 4.1 Schematic diagram indicates the difference between the cases of (a) dual-fiber beam trap in case of the aligning the fibers. (b) dual-fiber beam trap in case of the mis-aligning the fibers [adapted from ref. 11]. (a) Fabry–Pérot cavity with single sided injection (the standing wave pattern is neglected for simplicity).

This way, particles can be trapped and aligned axially, due to the highest light intensity in the antinodes of the formed standing wave [14]. Also, the use of a stable, high quality resonator achieves field enhancement inside the cavity proportionally to its finesse (ratio of free spectral range over the full width at half-maximum bandwidth), thus allowing the operation of trapping with low levels of input light power. Furthermore, the stable resonance provides the additional advantage of field confinement inside the cavity and forms well-focused field pattern that provides high intensity gradients for efficient trapping of particles. However, under some conditions of the particles size and/or concentration, the optically illuminated particles exhibit their own mutually interacting scattered fields, leading to their self-arrangement into clusters, or what is called 'optical matter' [15]. This interesting phenomenon of light-matter interaction is referred as 'optical binding' [13, 16]. The behavior of either optical binding or hybrid effect of combined optical trapping and binding mechanisms appear as dependent on how particles disturb the field due to their size and/or distribution as will be shown through this chapter.

Up to our knowledge, our contribution presented in this chapter describes for the first time, the use of on-chip resonant FP cavity for trapping micrometer particles. This is a particularly difficult challenge since the stability with a Gaussian beam input is not easily achievable on-chip: it requires very challenging micro-fabrication of spherical micro-mirrors facing each-other. Our group could overcome this problem by adopting a combination of cylindrically-curved surfaces to obtain stable, high quality factor FP resonators with a cavity length extending up to 280 μm [17], thus providing enough space for injecting fluid samples through capillary tubes, as demonstrated in this chapter, where the tubes have also an optical confinement effect.

It is worth-mentioning that short, unstable FP microcavities based on planar mirrors were occasionally reported for being used mainly for refractometry of single particles but not for their trapping [18]. On the other hand, bulky, off-chip FP cavities (of spherical mirrors) are also used in quantum electrodynamics (QED) studies to investigate the interaction between trapped atoms and the strong cavity field, but this is out of scope of our study [19-21].

In this chapter, our optofluidic stable Fabry–Pérot cavity is used to study the behavior of particles suspended in liquid environment when exposed to a resonant light field. The phenomena of optical trapping and optical binding have been observed experimentally inside such devices and explained upon behavioral analysis with the help of numerical simulations.

4.2 Principle of optical trapping

Optical traps use light to manipulate microscopic objects in nanometer and micrometer range using optical forces from a laser beam. Optical force includes optical radiation (scattering) force and optical gradient force. Both scattering forces and gradient forces result from the transfer of momentum from the incident photons to the particle, with strong dependence of the particle size with respect to wavelength. In case light field is not homogeneous, a gradient force develops, related to the beam intensity gradient, that causes small particles to be attracted to regions where the light intensity is the highest leading eventually to optical trapping. On the other hand, whatever the field distribution, there will be always a scattering force, which is due to light reflection, refraction, and scattering by the particle. The direction of the most contributing part of the scattering force is –in most cases – related to the direction of incident light. That is why two counter-propagating waves are sometimes required to achieve trapping by compensating the corresponding opposed scattering forces, when the gradient forces are insufficient or completely absent. That is also why a microparticle can be propelled when using only a single light beam propagating in one direction only.

Both forces are produced by the change of optical momentum of light through optical reflection or scattering by an object, which contributes to the total force through an optical radiation force, locally at the incident region on the object. The net optical force is then the sum of all such forces contributions over the particle area.

From electromagnetics theory point-of-view, the optical force originates from the Lorentz force, which is the force applied on a dielectric particle that has a higher refractive index than the medium due to the applied electromagnetic field. The Lorentz force per unit volume for an arbitrary charge distribution is generally expressed as:

$$\vec{f} = \rho\vec{E} + \vec{J} \times \vec{B} \tag{4.1}$$

where ρ is the electric charge density $\vec{E}$ is the total electric field affecting the particle, $\vec{J}$ is the electric current density $\vec{B}$ is the magnetic induction. After a rigorous mathematical development which can be found in [22], the optical force per unit volume takes the following form:

$$\vec{f} = \varepsilon \left[\left(\nabla . \vec{E} \right) \vec{E} + \vec{E} . \nabla \vec{E} \right] + \frac{1}{\mu} \left[\left(\nabla . \vec{B} \right) \vec{B} + \vec{B} . \nabla \vec{B} \right] - \frac{1}{2} \nabla \left(\left| \vec{E} \right|^2 + \frac{1}{\mu} \left| \vec{B} \right|^2 \right) - \varepsilon \frac{\delta}{\delta t} \left(\vec{E} \times \vec{B} \right) \tag{4.2}$$

where $\varepsilon = \varepsilon_r \varepsilon_0$ and $\mu = \mu_r \mu_0$ are the permittivity and permeability of the background medium in which the particle is inserted.

To simplify the notation of equation (4.2), it may take the form

$$\vec{f} = \nabla . \vec{\vec{T}} - \varepsilon \mu \frac{\delta \vec{S}}{\delta t} \tag{4.3}$$

where $\vec{S}$ is the Poynting vector, $\vec{\vec{T}}$ is the Maxwell stress tensor and can be given as

$$T_{ij} \equiv \varepsilon \left(E_i E_j - \frac{1}{2} \delta_{ij} \left| \vec{E} \right|^2 \right) + \frac{1}{\mu} \left(B_i B_j - \frac{1}{2} \delta_{ij} \left| \vec{B} \right|^2 \right) \tag{4.4}$$

where δ_{ij} is Kronecker's delta, and the indices i and j denote the field components. The optical force on a large target can be obtained by integrating the optical forces per unit volume on the entire particle volume.

$$\vec{F} = \iiint \vec{f} dV = \iiint \left(\nabla . \vec{\vec{T}} - \frac{\varepsilon_r \mu_r}{c^2} \frac{\delta \vec{S}}{\delta t} \right) dV \tag{4.5}$$

Applying the divergence theorem, the total force can be written as

$$\vec{F} = \oint_S \vec{\vec{T}} . \vec{n} \, dS - \frac{\varepsilon_r \mu_r}{c^2} \frac{\delta}{\delta t} \iiint_V \vec{S} \, dV \tag{4.6}$$

with $\vec{n}$ the outward normal to the surface S. In harmonic regime, the calculus of the average on time of the optical force (denoted < >) eliminates the second term of this expression and leads to [23],

$$\left\langle \vec{F} \right\rangle = \left\langle \oint_S \vec{\vec{T}} . \vec{n} \, dS \right\rangle = \oint_S \left\langle \vec{\vec{T}} \right\rangle . \vec{n} \, dS \tag{4.7}$$

Using the complex field amplitudes $\underline{\vec{E}}$ and $\underline{\vec{H}}$, the time averaged Maxwell stress tensor is given by:

$$\vec{\vec{T}} = \frac{1}{2} \mathrm{Re} \left[\varepsilon \underline{\vec{E}} \underline{\vec{E}}^* + \mu \underline{\vec{H}} \underline{\vec{H}}^* - \frac{\vec{I}}{2} \left(\varepsilon \left| \underline{\vec{E}} \right|^2 + \mu \left| \underline{\vec{H}} \right|^2 \right) \right] \tag{4.8}$$

where * denotes the complex conjugate and $\vec{I}$ is the unit tensor.

Practically, these equations can be simplified in some cases, depending on the particle size with respect to the light wavelength. Indeed, depending on its size, the particle can be treated either as a dipole, as a diffracting object or as a Mie scatterer. Hence we have different models to calculate the optical forces in different regimes [24], presented in the following sections. One need to keep in mind that the particle trapping only occurs if the refractive index in the particle is higher than the one of the surrounding medium. If not, the bead is pushed out of the light beam.

4.2.1 Rayleigh Regime:

When the dielectric particle is very small compared to the wavelength of light (as a rule of thumb, R < λ/20 for a spherical particle, where R is the radius of the corresponding nanosphere and λ is the laser wavelength [25]), it can be approximated as a point dipole in an inhomogenous electromagnetic field (Fig. 4.2 Different contributions to the optical force in the Rayleigh Regime [27].). In this regime, the optical force on the nanosphere can be calculated analytically using the Rayleigh scattering theory [25]. The force applied to the particle is separated into two terms, related to the incident light effect and to the re-radiated field from the particle [26]. Under the Rayleigh approximation, we can write the time averaged scattering force as

$$\langle F_{scat} \rangle = \frac{k^4 \alpha^2}{6\pi c n^3 {\varepsilon_0}^2} I \tag{4.9}$$

where k is the wave number in the surrounding medium given by $k = 2\pi/\lambda$, α is the bead polarizability (proportional to the particle refractive index and volume), c is the speed of the light in vacuum, n is the refractive index of the surrounding medium, and I is the light beam intensity (or irradiance).

The Lorentz force applied on a particle due to the gradient of the electromagnetic incident field is given as:

$$\vec{F}_{grad} = (\vec{p}.\nabla)\vec{E} + \frac{1}{c}\frac{d\vec{p}}{dt} \times \vec{B} \tag{4.10}$$

where $\vec{p} = \alpha \vec{E}$ is the dipole electric moment of the particle, and $(\vec{p}.\nabla)$ is the advection operator that can be expressed as $p_x \frac{\partial}{\partial x} + p_y \frac{\partial}{\partial y} + p_z \frac{\partial}{\partial z}$. Hence, the temporal gradient force becomes

$$\vec{F}_{grad} = \frac{1}{2}\alpha \nabla \vec{E}^2 + \frac{1}{c}\frac{d\vec{p}}{dt} \times \vec{B} \tag{4.11}$$

In a steady state, the particle experiences the time average gradient force:

$$\left\langle \vec{F}_{grad} \right\rangle = \frac{1}{2}\alpha \nabla \left\langle \vec{E}^2 \right\rangle = \frac{\alpha}{cn\varepsilon_0} \nabla \vec{I} \tag{4.12}$$

The square of the magnitude of the electric field is proportional to the intensity of the beam, which is a function of position. In other words, the result indicates that the gradient force on the dielectric particle, when treated as a point dipole, is proportional to the gradient along the intensity of the beam. Therefore, the gradient force described here tends to attract the particle to the region of highest intensity. In reality, the scattering force of the light works against the gradient force in the axial direction of the trap, resulting in an equilibrium position that is displaced slightly off the intensity maximum.

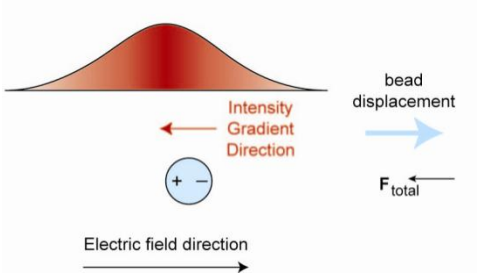

Fig. 4.2 Different contributions to the optical force in the Rayleigh Regime [27].

4.2.2 Ray Optics Regime:

When the particle size is much larger than the wavelength of the trapping light (usually R > 10λ), the optical forces on the object can be calculated by ray optics, where the beam is refracted by the object that has a higher refractive index than the medium. Fig. 4.3 (a) sketches a diagram to explain the case of using a lens to focus a laser beam to trap the particle at the focal point. In the absence of the bead, the rays *a* and *b* are focused through the objective lens to the position *f*, that is the focal point. When a microsphere is introduced to the

right of the laser focus, the rays gets refracted through the bead, causes the new focus to lie to the right of the initial focus f. The momentum change of these photons imparts an equal and opposite momentum change to the microsphere. From the force point of view, F_a and F_b vectors represent the forces imparted to the bead by the rays *a* and *b* successively; F_{total} is the sum of these two vectors that points to the left. For a realistic case of a Gaussian laser mode whose schematic is shown in Fig. 4.3 (b), in a cross section perpendicular to the direction of propagation, the intensity is higher in the middle and gradually decreases outwardly. Hence the central ray *a* is of higher intensity than the extreme ray *b*, and it exerts higher force on the bead, that gives a total force F_{total} points also to the left.

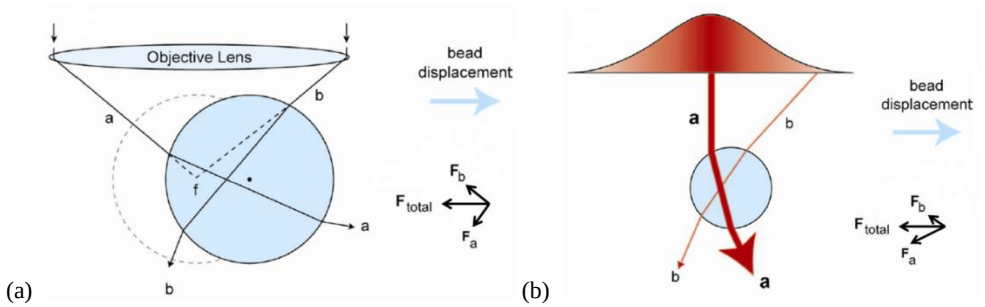

Fig. 4.3 Different models for the optical force in the Ray Optics Regime: (a) focused beam by a lens. (b) Gaussian beam [27].

4.2.3 Mie Regime:

When the particle size is comparable to the wavelength, neither ray optics nor Rayleigh scattering is accurate. However, there exists an analytic solution for describing the field scattering by an illuminated dielectric sphere. Generalized Lorentz–Mie theory is valid from very small particles right up to the ray optics region. Mie theory treats the trapping light as an electromagnetic wave (unlike the ray optics model) and also takes the exact dimension of the trapped sphere into account (unlike Rayleigh scattering). This combination means that it can explain the resonances observed due to 'whispering gallery modes' within the trapped objects. Fig. 4.4 shows the importance of selecting the correct model depending on the involved particle size. It presents the theoretical stiffness of the optical traps (which indicates the ability of the optical trap to hold the particle) calculated using Rayleigh scattering (point dipole approximation), using Lorentz–Mie theory and using ray optics model. Lorentz–Mie scattering calculations are the most sophisticated, but valid for all of the size ranges usually considered in optical trapping; and it can also detect small variations that are overlooked by

the two other methods, which are only valid for very small or very large particles. But working with Mie calculations is computationally demanding, and the solutions required for multi-spheres or non-spherical particles even more so. Therefore, the numerical simulations are sometimes preferred [26].

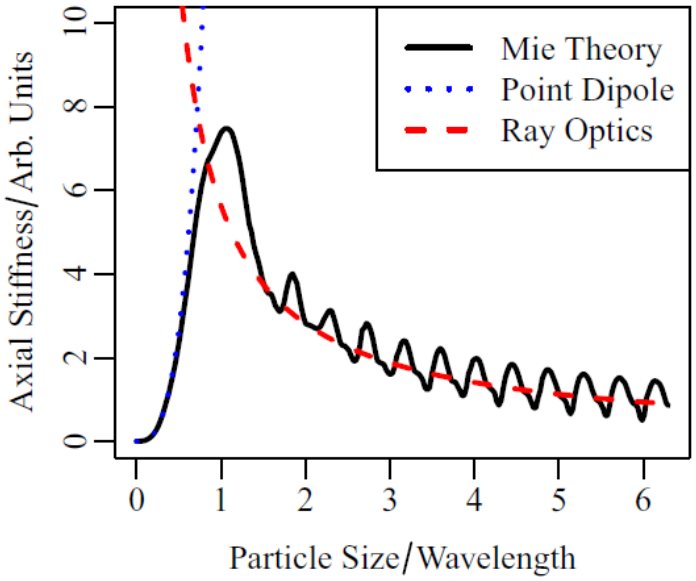

Fig. 4.4 Theoretical stiffness of optical traps calculated using Rayleigh scattering (point dipole approximation), Lorentz–Mie theory and ray optics model [26].

4.3 Optical trapping configurations

Optical manipulation has proven to be a noninvasive and noncontact method of manipulation. Since a while, it attracted a lot of attention to enhance the performance of the optical trapping configurations and reduce their disadvantages; recently, one can find a lot of different trapping configurations in literature. Generally, one can divide them into two major groups: Free-space tweezers, and On-Chip traps. This section will introduce some examples of each group and summarize the main attributes and advantages/drawbacks of each type with the aim of positioning our method and highlighting its advantages with respect to others.

4.3.1 Free-space optical tweezers

This is the wide-spread, conventional technique; based on using a strongly focused 3D propagating laser beam, and usually known as optical tweezers. The majority of the commercially available optical tweezers mostly uses one of these configurations. They

provide universal manipulation for translating objects in 3D space. But in the other hand, although optical tweezers have been proven as a technology for manipulation in the micro and nano-scale world, they still have several shortcomings: they use a lot of precious and bulky optical components and this reflects on their high price and inconvenience for limited-space locations. Moreover for temporary, non-assembled setups, they require precise alignment for many components simultaneously on multi-degrees of freedom, which requires a special vibration-immune, dust-free and temperature-regulated working environment. Besides they require high power lasers which – beside their high cost – may require some safety precautions; and for certain applications like cellular and organic particle trapping, they have to be at certain wavelengths to minimize the cellular photo damage. This damage is induced by the intense trapping light intensities necessary to generate sufficient trapping forces. Laser power intensities of approximately 10^5–10^7 W/cm^2 are typically used, which can adversely affect cellular behavior. Practically, such damage limits the exposure time for the trapped specimens and has proved to be a problem for some studies, particularly those in vivo because they lead to a laser-induced death of specimens due to local heating or other effects. In attempts to decrease the photo damage in optical trapping systems, careful choice of the trapping lasers with wavelengths has to be made: a waveband that is comparatively transparent to biological material, situated between the absorption bands of many biological chromophores (which is the part of a molecule responsible for its color that arises when a molecule absorbs certain wavelengths of visible light and transmits or reflects others) in the visible range, and the high absorption band of water and other bio-chemicals in the near-infrared region. Intensive studies have been made to pick up suitable wavelengths: for example the wavelengths 970 nm and 830 nm showed minimum damage for certain kinds of bacterial cells [28].

4.3.1.1 Single beam trap

The majority of the most powerful optical manipulation techniques are derived from the single-beam optical trap known as the optical tweezers illustrated in Fig. 4.5. It was originally introduced by Arthur Ashkin at Bell Laboratories by using a lens to focus a high power laser beam to trap or accelerate dielectric microspheres in water [1].

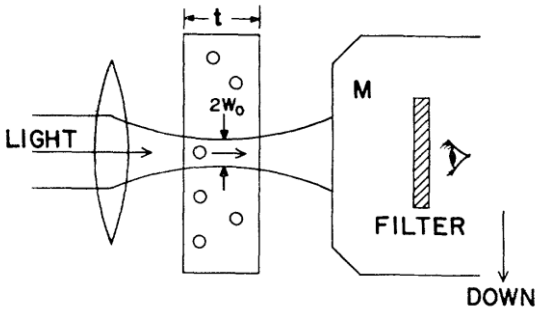

Fig. 4.5 A schematic of the first optical tweezer originally introduced by Ashkin [1].

The key components in this setup are the high numerical aperture (NA) objective lens (typical with NA between 1.2 and 1.4, which can't be achieved by a lensed fiber for instance, limiting the possibility to miniaturize this configuration), and the high power laser (usually 500 mW up to 2 W). Although this kind of traps obviously can't handle many objects simultaneously, they are still attractive for cellular biologists (when considering the previously mentioned precautions with cell handling). Cellular-level manipulation facilitates the study of single-cell behavior, such as the measurement of cellular forces or cell-to-cell interactions. Single-cell manipulation can also aid in sample preparation or purification [29].

Later, more general and more complex systems have been invented to set multi-traps at many points at once, which is very appealing in the science and engineering microscopic world. Such multifunctional optical traps can be crafted from single beams of light by spatial division and/or time division as will be indicated.

4.3.1.2 Holographic optical tweezers

In this type of tweezers, the single laser beam is spatially divided or splitted using a holographic element, either a programmable Spatial Light Modulator (SLM) like Liquid-crystal-based SLMs, or Diffractive Optical Element (DOE), let it be reflective or transmissive. Such beam splitters can be a computer-generated hologram, and hence the resulting trapping patterns are known as Holographic Optical Tweezers (HOTs) [30].

Holographic tweezers really achieve amazing performance when a computer-addressed SLM is used to project a sequence of trapping patterns in real time. An SLM can impose a prescribed amount of phase shift at each pixel in an array by varying the local optical path length. Typically, this is accomplished by controlling the local orientation of molecules in a layer of liquid crystal. Arrays of micro-electro-mechanical (MEMS) mirrors can also be used for SLM applications [30].

Fig. 4.6 schematically shows an optical tweezers system in which a diffractive beam splitter is used. It is placed at the pupil's image to convert a single laser input beam into several beam spots, each of which forming a separate optical trap. To see how this works, consider multiple rays all passing simultaneously through point A on their way to being focused into optical traps. The superposition of these rays by the action of the diffraction grating, creates an interference pattern at point A. Imprinting this pattern onto the wave fronts of the input beam, transforms it into the desired fan-out of beams all emanating from point A, and thus forms the needed pattern of the optical traps. Then, a strongly converging lens such as a microscope objective focuses these beams of laser light into optical traps. Now to control the elevation of the focused beam waist, the incidence angle is adjusted. Consider a collimated TEM_{00} beam passing straight into the input pupil of the lens; it comes to a focus in the middle of the focal plane of the objective lens, where it forms a trap. When the angle of incidence is swept to another value, the trap is translated across the field of view. If the beam is diverged, it focuses downstream of the focal plane, whereas if it is converged, it focuses upstream [30].

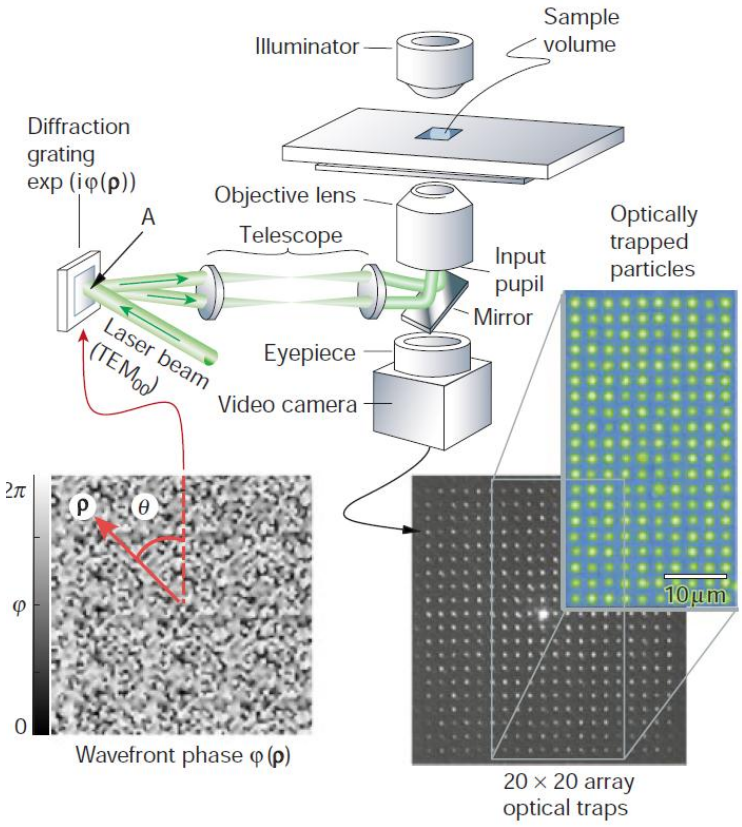

Fig. 4.6 The creation of multi optical tweezers by using computer-generated holograms. The example phase grating $\varphi(\rho)$ creates the 20×20 array of traps shown in the video micrograph, which demonstrates the trapping of 800 nm diameter polystyrene spheres dispersed in water [30].

This technique, on the other hand –beside the forehead mentioned disadvantages for all the free-space tweezers– needs extremely high laser power (in the order of hundreds of milli-watts or even watts) to account for the power division on the multi-traps and still provide enough power for efficient trapping at each one. This high power may for example boil the liquid crystal if used as a splitting element, and hence requires cooling and certain extra procedures that further complicate the system, and requires additional cost.

4.3.1.3 Time-division tweezers

If the position of the optical trap is scanned at a rate faster than the Brownian relaxation time of the trapped objects, multiple traps can be created by time sharing a single laser beam. This can be achieved by using rapid-scanning techniques based on Acousto-optic deflectors (AODs) or galvano-mirrors [31]. AOD consists of a transparent crystal inside which an optical diffraction grating is generated by the density changes associated with an acoustic traveling wave of ultrasound. They offer a faster solution than the traditional galvanometer scanning mirrors which have step response times as short as 100 μs. The response times of AOD are limited by the ratio of the speed of sound within the crystal to the laser spot diameter that is around 1.5 μs per millimeter of laser diameter for typical crystals. However, it results in almost 40% of power loss due to their poor diffraction efficiency. In addition, the diffraction efficiency often varies slightly as a function of the deflection angle, which may result in a position-dependent stiffness variation of the optical trap [31].

An inherited drawback of this technique is that the switching of the beam patterns usually reduces the spatial stability of the trapped particle due to their Brownian motion. Therefore, it is necessary to investigate the spatial-temporal stability of the trapped particles inside the time-modulated beam spots and well control it [32].

4.3.1.4 Counter-propagating dual-beam traps

The bulky form or the free space form of these traps were the first invented technique for trapping, introduced by Arthur Ashkin in 1970 to trap latex microspheres with two focused Gaussian beams [1]. Later, this technique could be miniaturized and formed by using two single-mode optical fibers [10]. The mechanism by which particles are trapped laterally is the same as that for a single-beam tweezer and is due to that lateral field distribution of Gaussian

beams. But for the axial trapping, it is mediated by the (opposed) scattering forces only. A good consequence of this is that the scattering forces from the two beams cancels in the center, making the trap symmetric (in contrast to a single-beam trap), and the working distance is also longer in this case since the high NA is not needed, and the trapped object doesn't need to be illuminated by fully focused light; as a consequence, there is a significant reduction of power density it is exposed to. This also means that these traps can hold more highly scattering objects than single-beam traps or even multi objects arranged axially between the two beams, whereas several objects can't be supported simultaneously by a single focused beam. However, the axial stiffness in such system is typically low [26].

In some other setups, only a single objective could be used in conjunction with a mirror. The incident wave interferes with the reflected wave to create a standing wave trap, and hence produces a strong axial gradient force, even higher than the single beam trap, without the need for high NA focusing optics. Then, nano-particles could be trapped inside an array of stable positions separated by λ/2 along the beam axis. The axial trap stiffness is claimed to be several orders higher than that in the single beam trap [33].

4.3.2 On-Chip trapping Configurations

After the above-described macroscopic setups, now we switch to discussing the on-chip miniaturized schemes. Up to our knowledge, no trapping configurations done on chip can offer a universal manipulation that competes with the optical tweezers. But on the other hand, they may offer compact, low-power, cheaper solution for some applications. Especially if they can be manufactured using a mass micro fabrication technology, which may reduce the price/chip in a large market. Meanwhile, different integrated structures offer a limited manipulation for the micro-objects, or their localization at certain positions only, or even just propelling particles along the light propagating path like the case of the evanescent-field optical trapping. But some miniaturized setups have a manipulation advantage over the optical tweezers of facilitating objects rotation like the counter-beam traps. Nevertheless, this field is still in the phase of research and new setups are currently being invented and elaborated on.

In this section, examples of different trapping schemes will be presented and evaluated to be compared to our setup. In literature, there are different criteria for classifying various setups like the type of field used (propagating or evanescent), the use of diffractive

optical objects (usually objective lenses) or on the contrary lens-less optical tweezers (LOTs). Here, they are organized upon their performances: the type of manipulation they facilitate.

4.3.2.1 Propelling

Evanescent fields from waveguides and Whispering Gallery Mode (WGM) resonators, in the form of ring resonators [5], disks [6], or spheres [7] are used to propel particles along the light propagating path. The evanescent field is a residue optical field that "leaks" during total internal reflection (TIR) and fades off at an exponential rate. An advantage of these configurations over the free space optical trapping geometries, lies in the fact that the optical waves propagating through such devices stay highly confined over larger distances, and consequently are capable of delivering larger optical forces over larger areas. But from some points of view, this can be hardly considered as trapping, since the evanescent field has a directional sense and will only propel microparticles along its propagating path.

Planar waveguide structures: Solid-core waveguide devices serve to confine light within solid structures through total internal reflection. They can interact with small particles via their evanescent field. This interaction generates optical scattering forces to propel the particles along the waveguide, and also generates gradient (trapping) forces for confining them on their way at the vicinity of the waveguide surface, which results in an efficient ‘optical train track’ for particle transport and handling [34]. This idea also can be used for particles sorting by using a Y-branch waveguides as shown if Fig. 4.7. The path of a particles or cells can be efficiently switched into one of the two waveguide branches by changing the field distribution in the multimode input trunk, when the position of the light injecting fiber is changed [35]. Such structures can be easily implemented on-chip, so they are of particular interest to chip based integrated microfluidic systems. But on the other hand this technique suffers from poor efficiency and requires rather high optical input power (in the order of tenth or even hundreds of milliwatts) since only a small amount of the injected field is actually used.

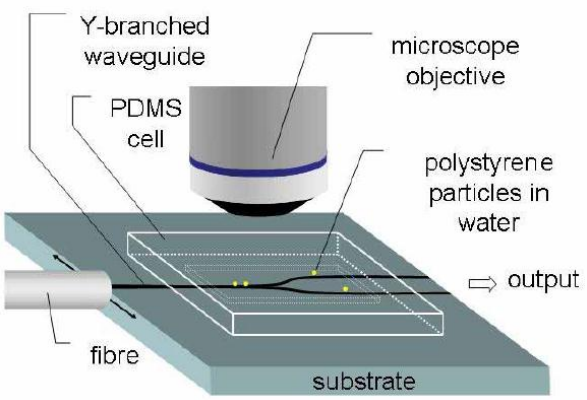

Fig. 4.7 Experimental setup used for particle sorting by a Y-branch waveguide [35].

WGM resonators: Compared to the waveguide trapping configuration, resonant cavities adopting WGM present two primary advantages: Firstly, high field confinement and enhancement inside the resonant cavity leads to strong optical forces with reduction source power. Secondly, using the cavity perturbation induced by the trapped object is a highly sensitive probe for analyzing the physical properties (size, refractive index, absorption) of those objects. For instance with a micro-ring of radius of 5 μm a 5-8 times enhancement of the optical force was measured, compared to a straight waveguide [5]. In addition, the power required for stable trapping is reduced to be in the order of fractions of a milliwatt. This varies according to the used scheme and the corresponding attainable quality factors and confinement capabilities, the modes formed within a sphere –such as that demonstrated in Fig. 4.8– are more efficient than that of a disk, and then a ring comes at the last stage. As for sensing applications, such resonators with high quality factors provide sensitive tools for sizing individual particles or detecting their refractive index due to the interaction with the resonator surface. The strong effects produced by the evanescent mode trapping are unavoidable in the case of nanoscale sized particles such as the viral HIV or Influenza A. This is because the attractive potential due to the evanescent field extends to tens of nanometers from the surface and reaches out into the surrounding solution and draws the suspended nanoparticles to the sensing region close to the surface, which provides the optical sensing based on evanescent waves with a distinct advantage not afforded by non-optical devices [7]. However, in case the nanoparticles are too far from the evanescent wave region, which is typical of extremely low concentrations of nanoparticles, those particles will have a chance to reach the evanescent wave region only through diffusion, which will significantly increase the time for such event to happen.

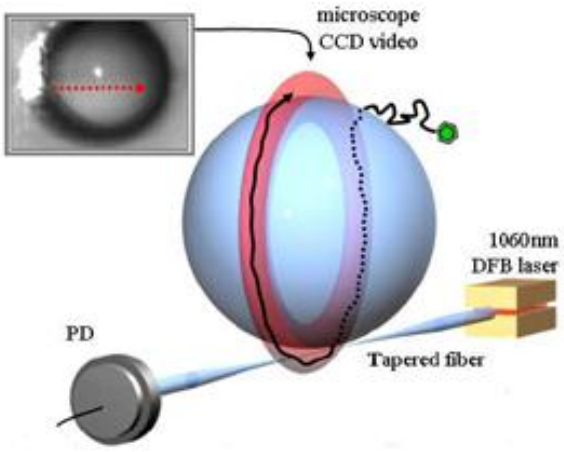

Fig. 4.8 WGM Trap: WGM excited in a microsphere (radius R = 53 μm) with $Q = 1.2 \times 10^6$ by a 1060 nm tunable laser using fiber-evanescent-coupling. The resonance wavelength is tracked from a dip in the transmitted light recorded by a photo detector (PD). An elastic scattering image shows a polystyrene particle (radius a = 375 nm) trapped and circumnavigating at 2.6 μm/s using a drive power of 32 μW [7].

4.3.2.2 Localization

An interesting scheme to locate nanoparticles at specific fixed locations with on/off states of light is done by using optical nanocavities designed within photonic crystal (PC) structures, which are periodically (in space) nanostructured dielectric materials. The optical traps are then implemented in a microfluidic chip that allows the flow of the liquid containing the particles. The trapping is achieved by very low power light (< 120 μW), pumped through a waveguide consisting of a missing line of holes in the PC that provides light throughout the structure to the optical cavity where the sharp field variation creates the trapping forces. Such structure is illustrated in Fig. 4.9. Such low power can be enough since the resonant enhancement of optical fields effectively reduces the source power required for stable trapping. This configuration allows trapping particles smaller than 100 nm in diameter, which is difficult either using free space optics or evanescent trapping configurations with the limitation imposed by laser spot size and power, because of the strong field spatial variation required on this scale. But on the other hand, it suffers from the back action effect, which results from *mutual* interaction between the position of the trapped particle and the cavity field that may shift the cavity resonance wavelength, due to the perturbation of the cavity produced by the trapped particle. And hence, more precise analysis is required to determine the correct trapping regimes [9].

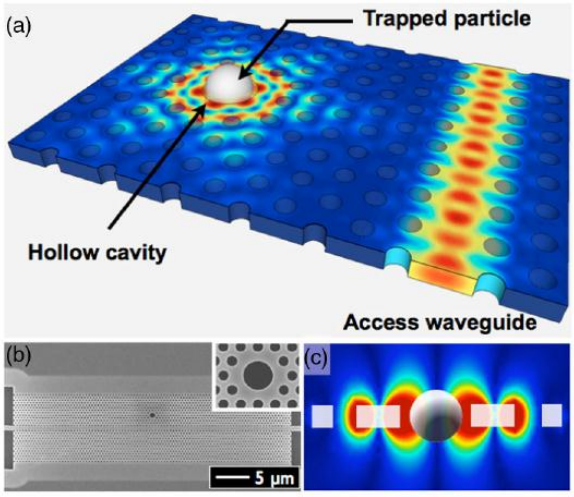

Fig. 4.9 Hollow photonic crystal cavity. (a) Computed electric field distribution in a hollow circular cavity in the presence of a 500 nm dielectric particle. (b) Scanning electron micrograph of the PhC device showing both the circular cavity and the coupling waveguide. Inset: 10 × magnification of the circular defect (700 nm in diameter). (c) Distribution of the electric field in a vertical cross section of the photonic crystal, centered on the particle, as computed with 3D finite elements (COMSOL) [9].

4.3.2.3 Simple manipulation

Apart from just propelling or accelerating the objects, or just fixing them at specific locations, the following configurations allow with simple manipulations to move the micro particles in the medium for some limited movements and/or rotate them. Here we present the optical fiber form of the Counter-propagating dual-beam traps and a multi patterns system created by a Multimode-interference (MMI) structure:

Fiber dual-beam traps:

As was previously mentioned, the counter-propagating dual-beam traps can be miniaturized and formed by two single-mode optical fibers. They have the advantage of confining the objects placed between the two opposite waves coming from the two fibers without the need of focusing components, because the generated opposed optical forces trap the particles as the result of the two scattering forces acting from both sides. According to the resulting mechanical stress produced by these two opposed forces, this could be advantageous to optically deform the cell without damaging it permanently but to do so, it is required to use relatively high powers (in order of a watt). This can be used to measure the deformability of a cell, which has been shown to be a promising indicator of whether cells are cancerous or not [36]; since the deformability is necessary for cancerous cells to invade healthy tissue (not

simply because it is less rigid as a side effect). Cell deformability is, therefore, a potential way to determine how likely cancer is to spread [26, 36]. Fig. 4.10 shows a schematic illustration for cell trapping and optically driven motion of single micro-object by using optical fiber dual-beam configuration. A cell can be trapped stably by the two beams emitted from the optical fibers when they are well aligned. When the optical fibers are slightly misaligned intentionally, a cell can be moved either counterclockwise or clockwise. It is also possible to trap more than one object along the optical axis [11]. To drive the particle along the axis, it can be achieved by disturbing the intensity balance between the two beams, but this needs separate control of the two beams, using two sources for example; but this may not work with the systems usually implemented in the counter-propagating setups, which are realized by splitting the source power by a 50/50 coupler to reduce the cost. Furthermore, if the splitted counter-propagating waves are coherent, a standing wave can be formed due to interference between these two waves traveling in opposite directions [12], but in some cases – if needed – this stationary wave can be avoided by slightly misaligning the fibers to simplify the system analysis [13].

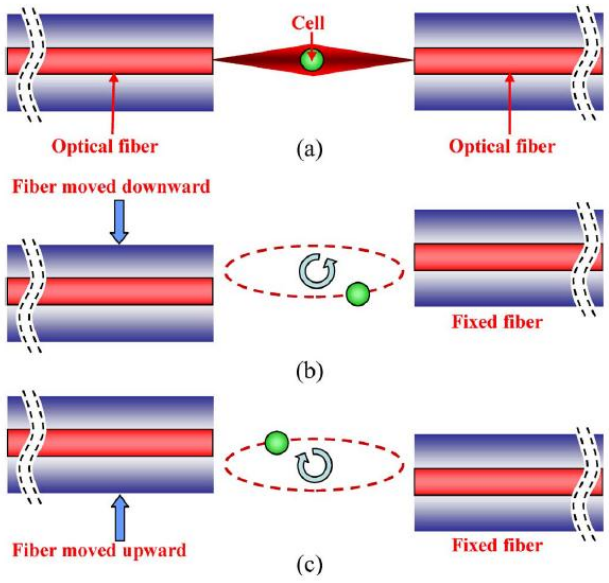

Fig. 4.10 Schematics illustrate: (a) an object stable trapping by the laser beams emitted from optical fibers, (b) an object moving counterclockwise along an elliptic trajectory, and (c) an object moving clockwise by slight misalignment of the two fibers [11].

Although the dual-beam trap is simple, it requires splitting the light path to provide double injection and it also strongly depends on the relative alignment of the opposite fibers and on the required power balance of light injected from both sides.

Multimode-interference structures:

This structure offers a two-dimensional optical trapping and manipulation capability of micro particles within a fluidic cell using an infrared beam. The key component is a 100 µm square-core silicon waveguide of millimeter length working as a Multimode-interference modulator that produces various patterns of optical spots arrays, by tuning the fiber coupling position (used for light injection) at the MMI waveguide input facet as described in Fig. 4.11.

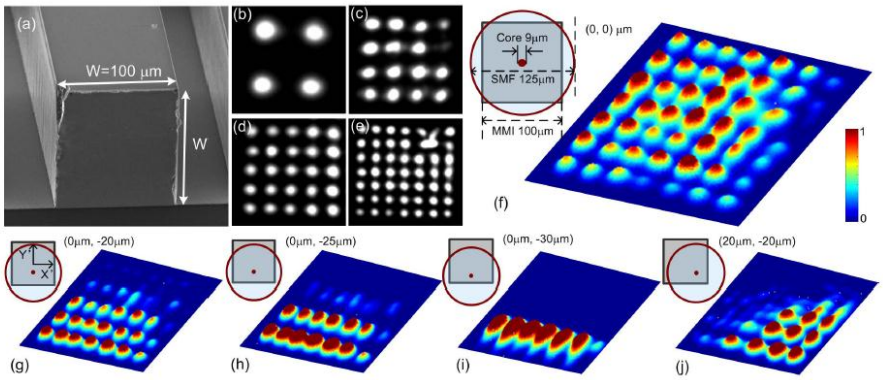

Fig. 4.11 Imaged light beam array patterns of the MMI waveguides. (a) SEM of the fabricated MMI waveguide presenting the square end-facet of 100 µm in side length. (b)-(e) NIR images (in gray scale) of the array patterns from the MMI waveguides of various lengths: (b) 11 mm, (c) 5.5 mm, (d) 4.5 mm and (e) 3 mm. (f) Imaged 7 × 7 array light intensity profile (in gray scale shown in false colors) of the MMI waveguide with 3mm length. Inset of (f): schematic of the relative position between the butt-coupled single mode fiber (SMF) and the MMI waveguide facet. (g)-(j) Imaged light intensity profiles (in gray scale shown in false colors) with the corresponding SMF core positions [8]

This scheme may demonstrate a holographic trapping on a small scale, but the spots are not focused enough in a proper position to facilitate the trapping along the beam, the particles can be only levitated, and their gravity is used to balance the scattering force and other forces in the upward direction. Also it can't be considered fully integrated since it still needs some bulky components: microscope objective is used to collect and collimate the light output from the MMI, and another one to focus the pattern array at the trapping plan inside the trapping cell, as illustrated in Fig. 4.12. The used power level is quite high for on-chip configurations: the source laser power is ~500 mW and estimated to be slightly less than 100 mW inside the fluidic cell. This high loss of power is expected due to the huge coupling loss between the different components; besides, enough power budget is necessary to account for the power division of the multi trapping spots.

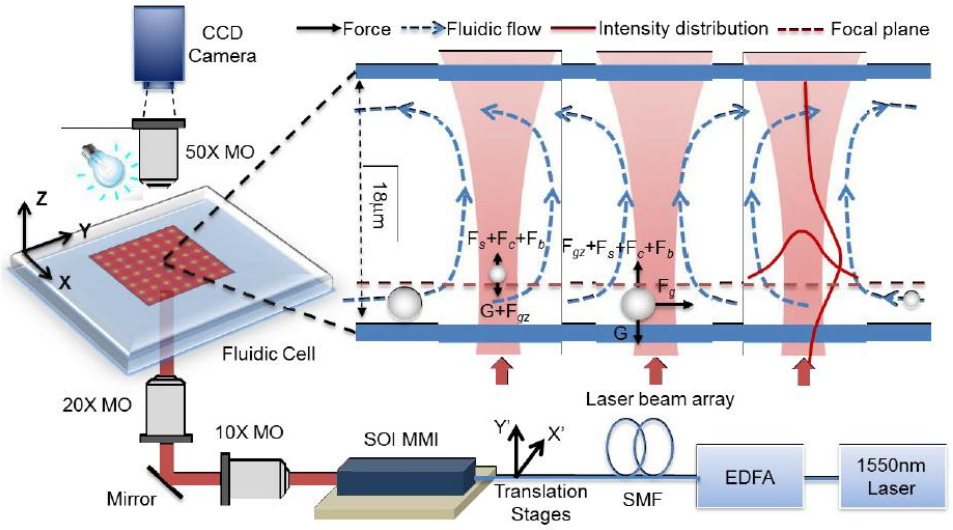

Fig. 4.12 Schematic of the experimental setup for optical trapping using MMI. Inset: Schematic of the optical trapping of the particles inside the fluidic cell. F_g: the optical gradient force exerted on the particle in the horizontal directions, F_{gz}: the optical gradient force exerted on the particle in the upward direction, F_s: the optical scattering force exerted on the particle in the upward direction, G: the gravitational force exerted on the particle, F_b: the buoyant force in water, F_c: the convection flow fluidic drag force exerted on the particle in the upward direction. Black solid arrows: the force exerted on the particle. Blue dashed arrows: the absorption-induced fluidic flow of water. Red solid curves: the light beam intensity distributions in the horizontal and longitudinal directions. Red dashed arrows: beam focal plane [8].

4.3.3 Our Configuration

Our optofluidic structure consists of a FP resonator formed by two cylindrical Silicon/air Bragg mirrors with cylindrical lens in-between. As described in previous chapters, the latter is actually formed by a capillary microtube holding a fluid with suspended particles. A schematic view of the device is illustrated in Fig. 4.13; the cylindrical mirrors achieve lateral confinement of the light field, while the tube with the liquid inside –acting as a cylindrical lens– achieves a vertical confinement, leading to field focusing and strong optical gradient, essential for efficient optical trapping. The second fiber is occasionally used to record the spectrum only, and has no function for trapping itself.

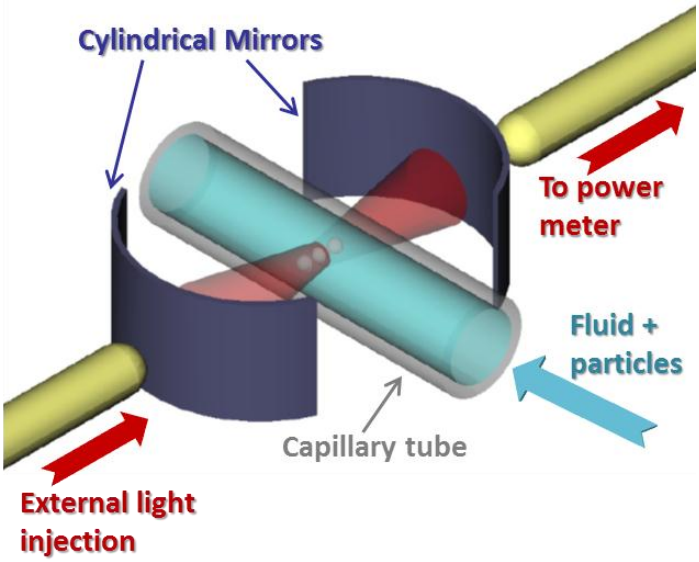

Fig. 4.13 Schematic diagram of the cylindrical Fabry–Pérot cavity with the capillary micro tube inside, also acting as a cylindrical lens, and the injecting/collecting lensed fiber pair.

This setup can be viewed in the sense of a counter propagating dual beam trap with coherent waves that form a standing wave, as the injected wave interferes with the coming and going multi-reflected ones by the mirrors. This is done here by single injection only, avoiding the need to provide two waves (either by splitting or by using two sources). Also one avoids the issues of the mutual fiber alignment, which may be tough and experience-demanding. But on the other hand, though this setup also enables experiments of cell deformation, it is less dynamic than the dual beam trap, as it lacks the ability to rotate the trapped particles or moving them for small distances as can be done by moving the fibers in the conventional counter propagating trap.

Our configuration employs a resonating cavity, and hence it also combines the advantages of the field building up, confined and enhanced inside the resonator, allowing the work at low input powers, especially with a low insertion loss cavity. And it simultaneously provides (optical) sensing/analysis device for the trapped particles. Table 4.4 summarizes the advantages and drawbacks of the different optical trapping configurations and compares them to our device, showing that it combines most of the advantages. The existing non-optical trapping techniques are not considered here. Indeed, we concentrate on optical trapping techniques only because they provide, together with the original trapping functionality, the additional potential for further implementation of optical sensing/detection techniques (including fluorescence and volume-sensitive refractometry) as well as spectroscopic analysis (such as Cavity-Enhanced Optical Spectroscopy - CEAS).

Table 4.4. Comparison of the advantages of different optical trapping configurations.

	System simplicity	Trapping & manip.	Low power	On chip	Single beam	Potential for Surface Sensing	Potential for Volume Sensing	Potential for *in-situ* Spectro. Analysis
Simple tweezer	×	✓	×	×	✓	×	✓	×
HOTs	×	✓	×	×	×	×	✓	×
Time-division tweezers	×	✓	×	×	✓	×	✓	×
Photonic crystals	✓	×	✓	✓	✓	✓	×	×
Optical patterns by MMI	×	**limited**	**medium**	✓	×	×	✓	×
Dual-beams traps by fibers	✓	**limited**	✓	✓	×	×	✓	×
Evanescent **field**s from WGM	✓	×	✓	✓	✓	✓	×	×
Fabry Pérot cavity	✓	***limited***	✓	✓	✓	×	✓	✓

4.4 Optical Binding

When a group of microparticles are trapped or enclosed within a monochromatic laser beam, the organization of the microparticles within the optical trap or the vicinity of the light field depends on the redistribution of the re-scattered rays that creates mutual optical forces amongst them. This redistribution of extra scattering forces between the microparticles

provides new force equilibrium in the particles distribution. It is worth mentioning that this effect is much pronounced in the counter propagating optical traps, since the trapping area is typically much longer than the size of the particles they hold, which leads to the possibility of multiple particles trapping inside the same trap. This effect was first observed with two beads in a long free-space trap created using cylindrical lenses and is referred to as "optical binding" [16], but similar dynamics have been observed in counter propagating traps in the longitudinal direction [13, 37]. The trapped particles along the axis of the trap show certain preference for equilibrium positions with specific inter-distance between them. Optical binding in the longitudinal direction has been observed whether Gaussian beams are used, or even Bessel beams although their cross sectional intensity profile doesn't change over significant propagation distances; in other words, the latter exhibit little or no divergence or spreading out along the propagation direction. Experiments have predominantly been performed in water using solid dielectric beads. Optically bound particles may conduct their own complex dynamics. For example, in extended optical traps with low stiffness, chains of particles can be formed, with certain inter-particles spacing between them, and the particles are held in positions relative to each other with *a stiffness that far exceeds that of the optical trap* for a single particle. This separation is a function of the number of particles in the group; and in certain conditions, these groups become unstable and may split into smaller groups. Fig. 4.14 shows an experimental example of such behavior.

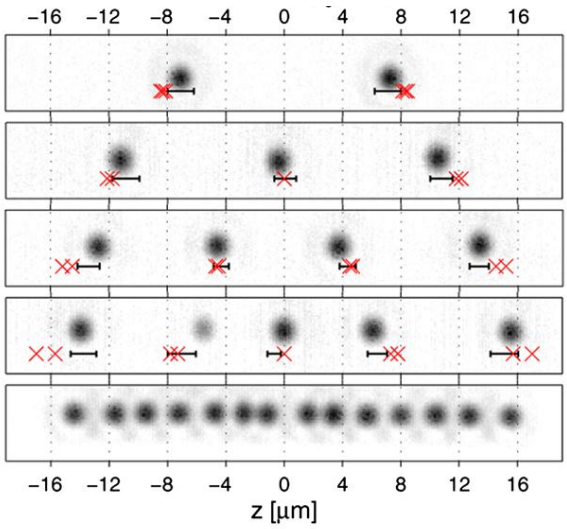

Fig. 4.14 Short-range self-arrangement of multiple identical 802 nm polystyrene particles in a single chain. The black spots represent the snapshots of a single particle (mean background intensity subtracted for each image). The horizontal black bar shows the standard deviation of particle positions. The red × denote the calculated position of the particle centre, clusters of × indicate the short-range multistability events for the cases we could theoretically model [37].

Also the observation of a breathing mode of the trapped particles array has been reported. If one of the trapping beams is moved axially to vary the position of the beam waist, the reduced light pressure force on the one side results in increasing the inter-particles spacing. As the focal point returns to its original position, the chain self-restores. In Fig. 4.15 we see the corresponding breathing behavior of a long particle chain (of 2.3 μm particles) [38].

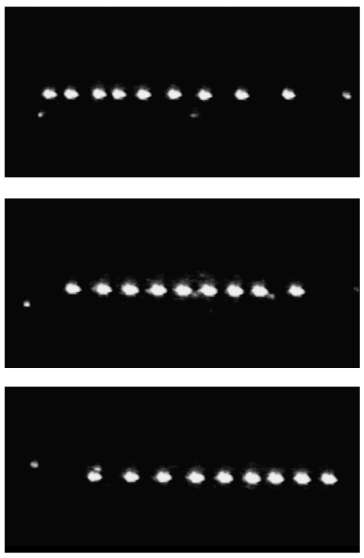

Fig. 4.15 Observation of a breathing mode: the displacement of the chain as a whole from the center with the inter-particles spacing increasing as one goes farther from the center of the array [38].

While counter propagating traps provide the simplest way to observe these effects due to the extended trapping range, it is also present in conventional single-beam tweezers. Particles can often be observed stacking up behind the bead which is held in the focus. One trap might hold four or more micrometer-sized beads. Also, due to the relatively high stiffness of the trap holding the first bead in place, the group of beads is not free to move along its axis [26].

In our experiments, we observe the two behaviors: on the one hand, the longitudinal binding in the form of a 1D array and on the other hand, the effect of beads stacking; the observed type of behavior depends on the particles size and/or concentration and the field distribution inside the cavity, as will be detailed in what follows.

4.5 Experimental

4.5.1 Setup and methodology

As previously indicated, we adopt a silicon FP cavity with cylindrical mirrors and a capillary tube in between holding the liquid and the suspended particles to be trapped. Fig. 4.16 photos the setup of the silicon chip with the capillary tube, connected to external larger tubing. The chip is placed on a positioner with 2 degrees of freedom (DOF) between the Input/Output fibers, which are manipulated using 5-DOF positioners. The inset shows a cavity with the cylindrical Bragg mirrors, the microtube in-between, and the placement of the injecting/collecting lensed fibers. The chip contains many FP cavities with different design dimensions to offer different quality factor/free spectral range tradeoffs. For our experiments, we selected a FP cavity having a physical length of 280 μm formed by cylindrical silicon-air Bragg mirrors, each consists of 3 curved silicon layers with radius of curvature of 140 μm and thickness of 3.67 μm for the silicon wall and 3.48 μm for the air gap (the equivalence of an odd multiple of quarter wavelength in each medium). A fused silica microtube with outer diameter of 128.1±1.2 μm and inner diameter of 75.3±1.2 μm (Polymicro Technologies TSP075150) is placed between the mirrors and is connected with an external larger diameter tube to allow injecting the fluid. The experiments are done by inserting the liquid with a suspension of spherical polystyrene beads (Polysciences) inside the tube using a syringe, then stopping the flow to provide static conditions for the experiments. Variable sizes of beads were used, ranging between 0.5 μm and 6 μm diameter. The liquid surrounding the particles was either DI water or acetone. Water may cause some losses due to its absorption at this wavelength range, but it was found to be affordable due to the short optical path across the microtube diameter. On the other hand, when using acetone, the polystyrene beads shouldn't be stored in it for long periods to avoid their dissolution. Un-polarized light in the near infrared region was injected into the cavity from a laser source tunable within the C and L bands, with power range from 4 mW to 30 mW, using single mode lensed fiber with a beam waist diameter of 18 μm.

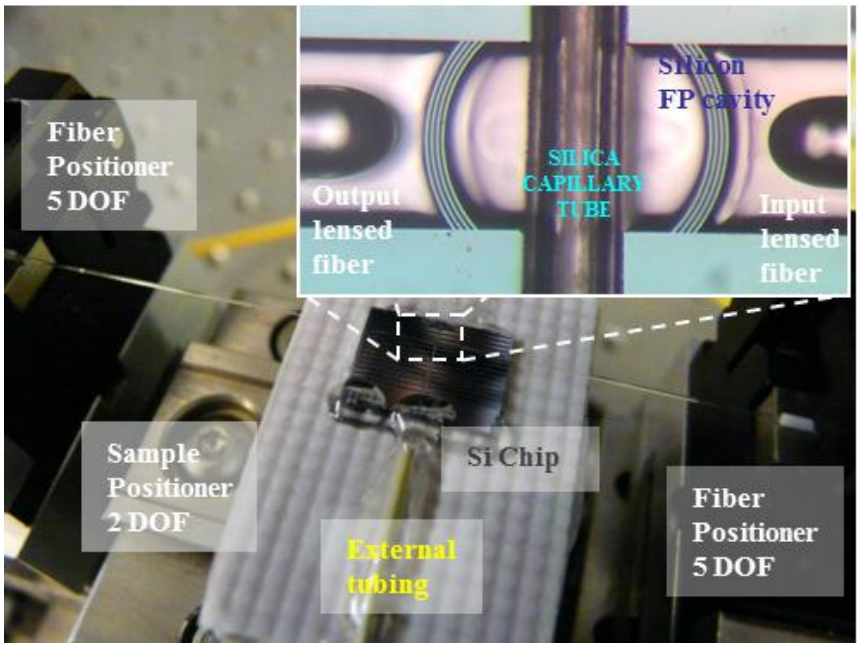

Fig. 4.16 Photo of the setup of the silicon chip with the capillary tube connected to the injection tubing, and the I/O fibers on their positioners. The inset is a zoom of the cavity indicating the placement of the lensed fiber pair, one being used for light injection and the other used only when needed for recording the spectral transmission response.

To determine the correct resonance wavelength that should be used for trapping, the spectral response was recorded first -as shown in Fig. 4.17- by performing a wavelength scan and recording the transmission by a second lensed fiber connected to a power meter. After this initial step, the input light for the trapping experiments was fixed at the selected resonance wavelength chosen with a reasonably high quality factor (in the order of 1000) and high transmitted power level. Note in Fig. 4.17 that beside the fundamental resonance peaks, there are other side peaks corresponding to other modes supported by these types of resonators [39]. The system is observed by a stereo microscope and the results are recorded by a C-Mount CMOS camera attached to the microscope.

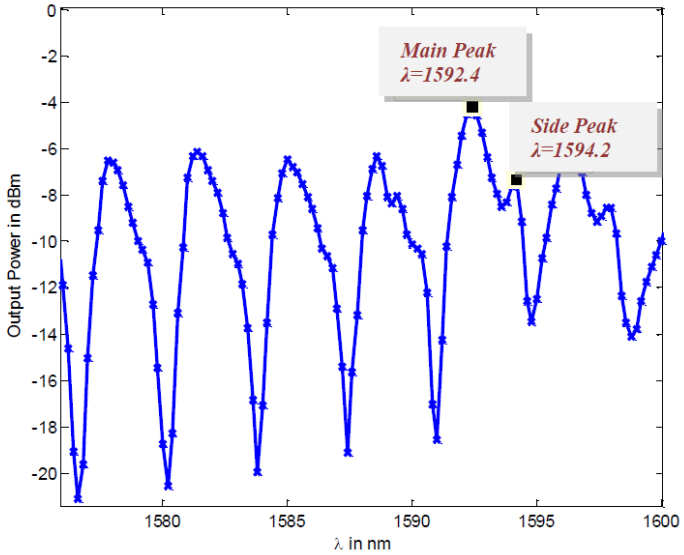

Fig. 4.17 The spectral response of the cavity with the microtube filled with deionized water and suspension of 1 µm diameter polystyrene beads with low concentration of about 6.68×10^7 particles/cm^3.

4.5.2 Results for small beads with low concentration

A few seconds after injecting the laser light set at 30 mW into the above-described optofluidic cavity, the microspheres get arranged in certain configuration depending on the particles size and concentration. Fig. 4.18 shows 1 µm diameter polystyrene beads in DI-water (concentration is about 6.68×10^7 particles/cm^3) aligned along the cavity axis when a 1592.4 nm wavelength beam –corresponding to cavity resonance – is injected. The quality factor at this peak is about 1090, and the finesse is about 7. The time taken by the beads to be completely arranged is about 1 min, and they get dismissed diffusing in random directions once switching the laser off.

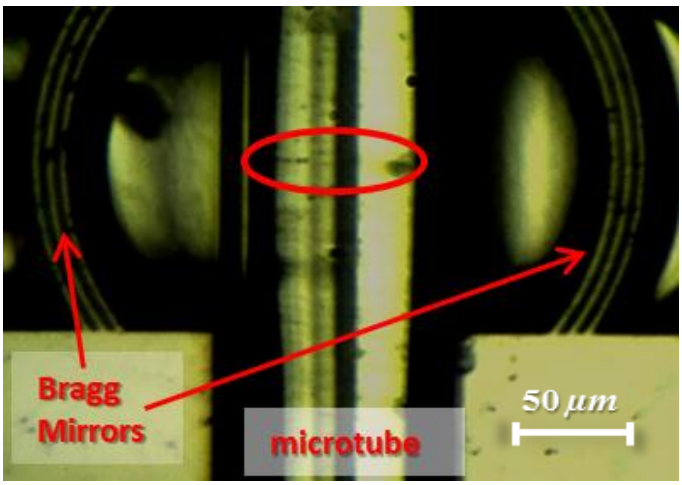

Fig. 4.18 A 1D array of 1 µm diameter polystyrene beads formed along the cavity axis at the fundamental resonance wavelength of 1592.4 nm.

As shown in Fig. 4.19, this one-dimensional line arrangement could also be obtained by injecting light at a wavelength of 1594.2 nm (corresponding to the side peak indicated in Fig. 4.17). The spacing between the particles is not uniform as indicated by the arrows in the zoomed area inside the inset, similar to that observed in Fig. 4.15 due to the breathing effect. This behavior will be explained in details in the Phenomenological Analysis section of this chapter.

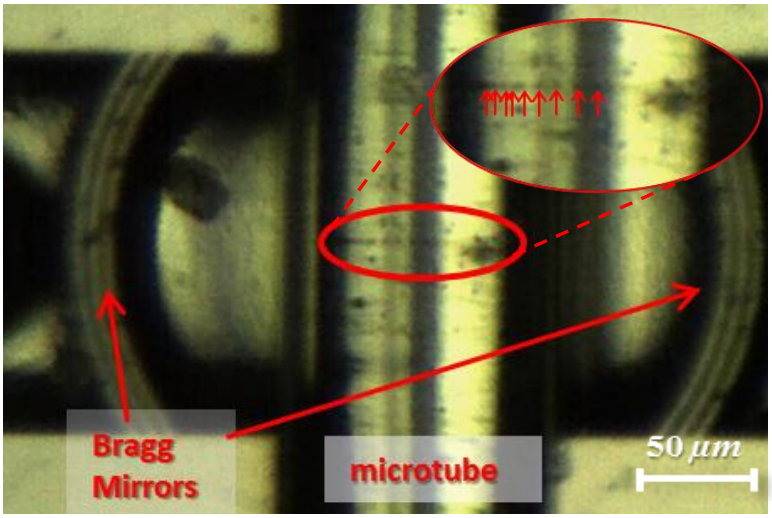

Fig. 4.19 One dimensional array of 1 μm diameter polystyrene beads formed along the cavity axis at the side peak wavelength of a side peak at 1594.2 nm. The inset is a zoom of the particles' array with their apparent positions indicated by arrows.

4.5.3 Results of small beads with high concentration

On the other hand, if the particles concentration is high, the observed behavior is different: the particles accumulate in the axial region but not necessarily forming an array as in the former situation. This behavior is shown in Fig. 4.20; the 1 μm diameter polystyrene beads in acetone solution have higher concentration within the region illuminated by the light inside the cavity as compared with the other regions. An important note is that this behavior happens even if the wavelength injected to the cavity is off-resonance, while the previously described alignment necessarily requires operation at resonance.

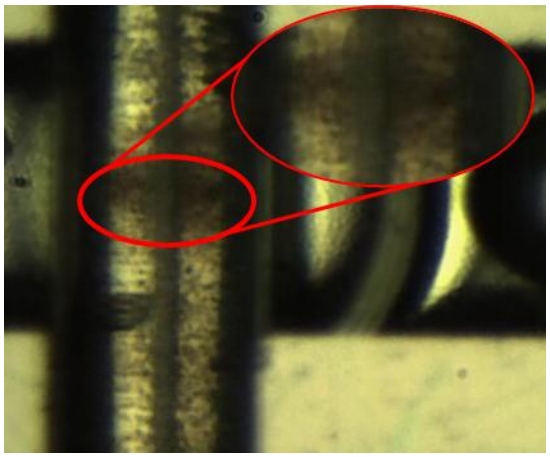

Fig. 4.20 Concentrated 1 µm diameter polystyrene beads in acetone solution in the vicinity of the cavity axial region. The inset represents a zoom of the selected area.

The same behavior was obtained also with 0.5 µm diameter polystyrene beads in DI-water. As shown in Fig. 4.21, the particles with initial concentration of about 6.27×10^{10} particles/cm^3 reach higher concentration after they accumulate within the region illuminated by the light. This accumulation takes nearly 20 min after switching the light source on. The amount of this accumulation strongly depends on the optical source power levels.

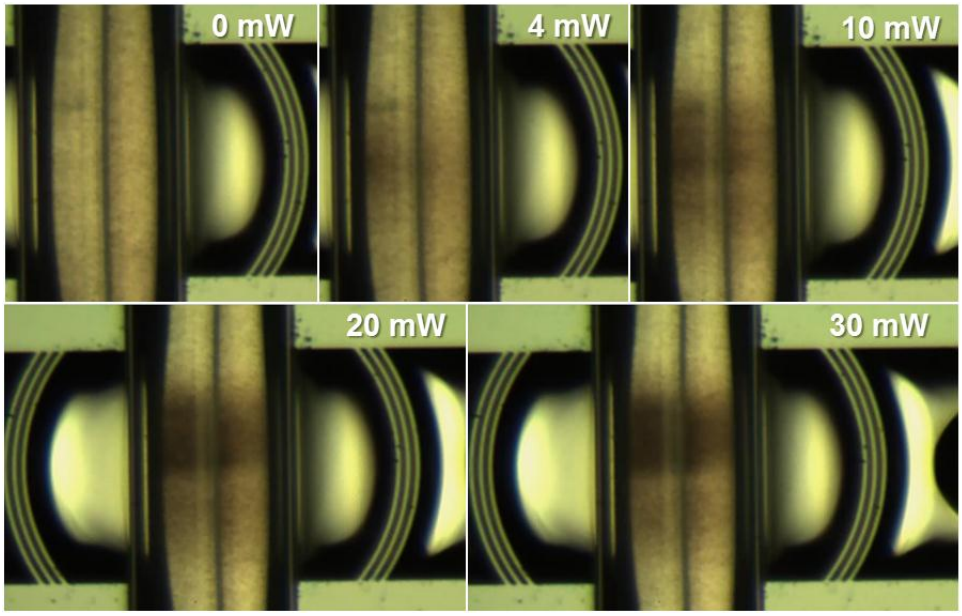

Fig. 4.21 The accumulation of 0.5um microspheres (initial concentration = 6.27×10^{10} particles/ml) after 20 min at different source powers tuned at any arbitrary wavelength even at off-resonance conditions.

As inherited from the snap shots at different power levels, this aggregation increases with the optical power. To characterize the trend of that accumulation building-up, simple image processing analysis has been done: a certain area at each shot was selected near the optical axis and its average intensity was calculated, then the increase was calculated with

respect to the initial average intensity before the accumulation. We will define a quantity ΔC to express this increase in the 2D images' average intensity. This probably can't give exact numerical values for the particles' new concentration, or even its surface concentration, especially because it is not uniform on the entire area due to the non-uniformly illuminating optical field, and also because the setup may suffer from some fluid currents that sweep the particles away along the micro tube, especially for long experiment times. That is why the particles cloud sometimes doesn't face the input fiber axis. But despite all of that, this may give an idea about the effect of the power on the aggregation process, as shown in Fig. 4.22.

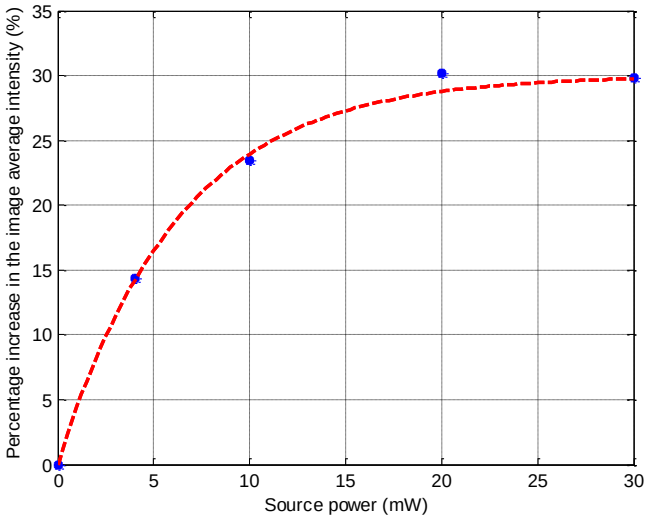

Fig. 4.22 The exponential trend of the accumulation process with the source power.

While normalizing the values to the maximal increment in the images' average intensity ΔC_{max} that is 30%, the fitting equation has been found to be:

$$\Delta C / \Delta C_{max} = 1 - exp^{-P/6.25} \qquad (4.13)$$

where ΔC is a quantity related to the increase in particles' aggregation, P is the optical source power.

This exponential behavior is usual in transient systems, including the aggregation of the colloids [40].

4.5.4 Results for large beads

The behavior of larger size beads is apparently similar to the latter phenomenon. As seen in Fig. 4.23, the 3 µm diameter microspheres (concentration of about 8.36×10^7 particles/cm^3) tend to gather slowly into a cluster, and it requires a longer time than the small

beads. Indeed, the initially randomly dispersed beads inside the cavity, shown in the section of Fig. 4.23 at time 0, needed more than 10 min to accumulate together and reach a bound assembly. This clustering behavior has been observed for beads with diameters of 2, 3, 4.5 and 6 μm in DI water or in acetone. Generally, larger beads require longer times to accumulate. The recovery time after cutting the light off in this case is also high, in the order of minutes depending on the particles' size and the degree of their clustering; while it was in the order of seconds, in the case of the accumulation of the smaller beads of 0.5 and 1 μm diameter. The process duration also increases if their initial concentration is higher. This is predictable as this behavior is related to the natural diffusion process of the particles. For the trapped pattern, the 1D array of the separated 1μm diameter beads almost instantaneous diffused after switching the laser off and it can be claimed to be in the order of fractions of a second.

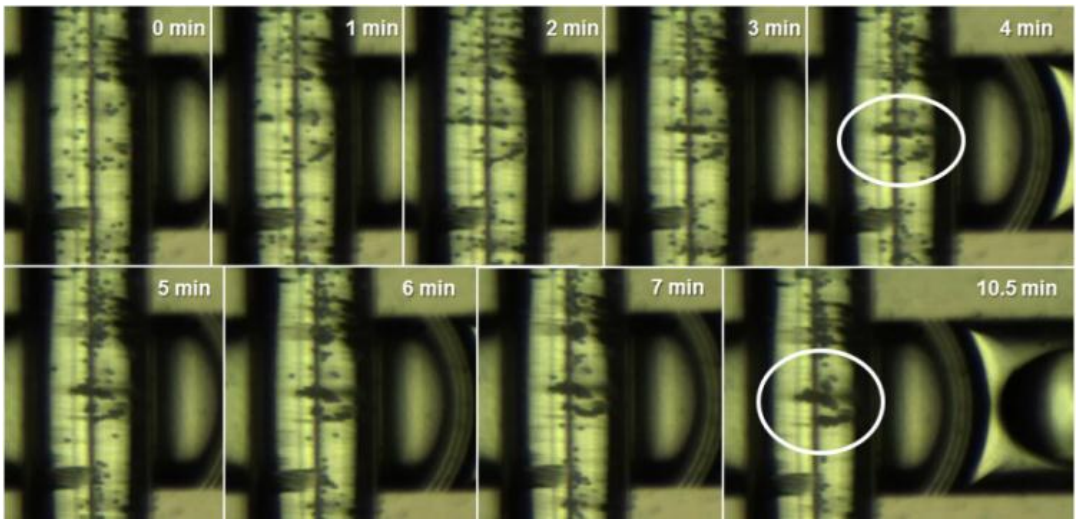

Fig. 4.23 The accumulation of 3 μm diameter polystyrene beads inside the cavity over time duration of about 10 min.

It is worth-noting that the low optical power levels involved in these experiments are not sufficient to trap particles moving in a flowing stream. In order to not increase difficulties, the beads are moving in a static liquid, naturally moving only due to the temperature-related Brownian motion that is counteracted by the applied optical forces within the resonant cavity.

4.6 Numerical Analysis

Since the diameter of our microspheres (d) is comparable to the wavelength (λ), it doesn't fall into any of the regions in which the calculations could be simplified, which are Ray Optics Regime ($d >> \lambda$) and Rayleigh Regime ($d << \lambda$). On the other hand, the Lorentz-Mie theory, which applies in principle in this dimension range, would be very difficult to implement in the case of multiple particles inside a resonant cavity as ours. Then, rigorous numerical finite element method (FEM) simulations need to be performed. We used the ANSOFT High Frequency Structural Simulator (HFSS) software, to get an idea about the field distribution inside the cavity. Since the behavior of beads suspension depends on the relative wavelength/particles relation, actual sizes of microspheres should be simulated; the cavity and the capillary dimensions as well as the beam waist size should be also at least in the same order of magnitude as the actual ones. To accomplish the simulation task with the limited computational resources, we adopted what may be called 2D simulations. A cavity with a small height (a slice) is modeled, and symmetry conditions are imposed as boundary conditions on the parallel planes delimiting the cavity height to mirror the structure. The height of the slice is taken as 0.1 μm. The planar dimensions are taken as the cavity actual size presented in section 4.5.1; but to limit the number of unknowns and thus the memory requirement, the cylindrical mirrors are modeled as one single layer having the smallest possible thickness that is one quarter of wavelength in silicon. The light source was chosen as a TE-polarized Gaussian beam (E-vector polarized along the vertical axis at the beam waist) located at a distance from the input side equivalent to the working distance of the lensed fiber used in the experiments.

Despite the few differences between the model and the actual physical case, this simulation may give an idea about the lateral field distribution at different resonance conditions, but first the spectral responses should be calculated to determine the frequencies correspond to (on-) or (off-) resonance. They have been obtained by performing a frequency sweep and plotting the transmitted power through a sheet at the output area versus the frequency (which can be scaled into wavelength in post processing). This output power is then normalized to the input power to obtain the spectral transmission for the cases where the capillary tube is filled with DI-water without any particles, with a single polystyrene bead of 1μm diameter, and with a single polystyrene bead of 3 μm diameter, leading to the resonance wavelength in each case, as indicated in Fig. 4.24.

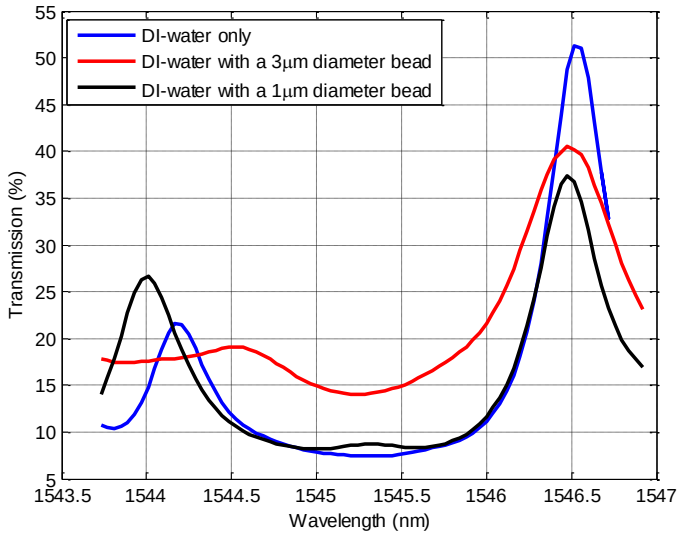

Fig. 4.24 The transmission responses when the microtube is filled with water only, with a polystyrene microsphere of 1 μm diameter, and with a polystyrene microsphere of 3 μm diameter.

From the transmission spectra shown in Fig. 4.24, one can notice that the main resonance peaks in case of the presence of a bead (either 1 μm or 3 μm diameter) experience a small shift to shorter wavelengths than the case of DI-water only due to the longer optical path along the cavity since the polystyrene particle has higher refractive index of 1.6 than water whose refractive index is 1.32. This shift is seen also with the side peak in the presence of the small bead (of 1 μm diameter). The transmission levels also get affected with the presence of the beads. Generally they are lower at resonance due to the perturbation imposed by the bead by scattering the light, and sometimes these perturbations modify the spectrum unexpectedly like the tiny peak in the black curve near the wavelength of 1545.3 nm, and that in the red curve near the wavelength 1544.5nm. Note also that the red curve show exhibits larger broadening in the main peak's width than the black curve, which implies that the perturbation due to the 3 μm diameter bead is larger and the field inside the cavity is less confined than the case of the 1 μm diameter bead (despite the higher transmission level at the resonance wavelength of both λ = 1546.48 nm), as will be emphasised by the field distribution plots in Fig. 4.25 and Fig. 4.26. Fig. 4.25 represents the field inside the cavity filled with water only. We observe spots of electric field along the cavity axis at the resonance wavelength of λ = 1546.52 nm (Fig. 4.25 (a)). Away from the resonance -at λ = 1545.48 nm as shown in Fig. 4.25 (b)- the electric field amplitudes are much less and hence no trapping is expected in this case, since the spots providing the strong intensity gradient are not available here. But still, the electric field is non-zero inside the cavity; it may lead to the scattering forces responsible for the optical binding.

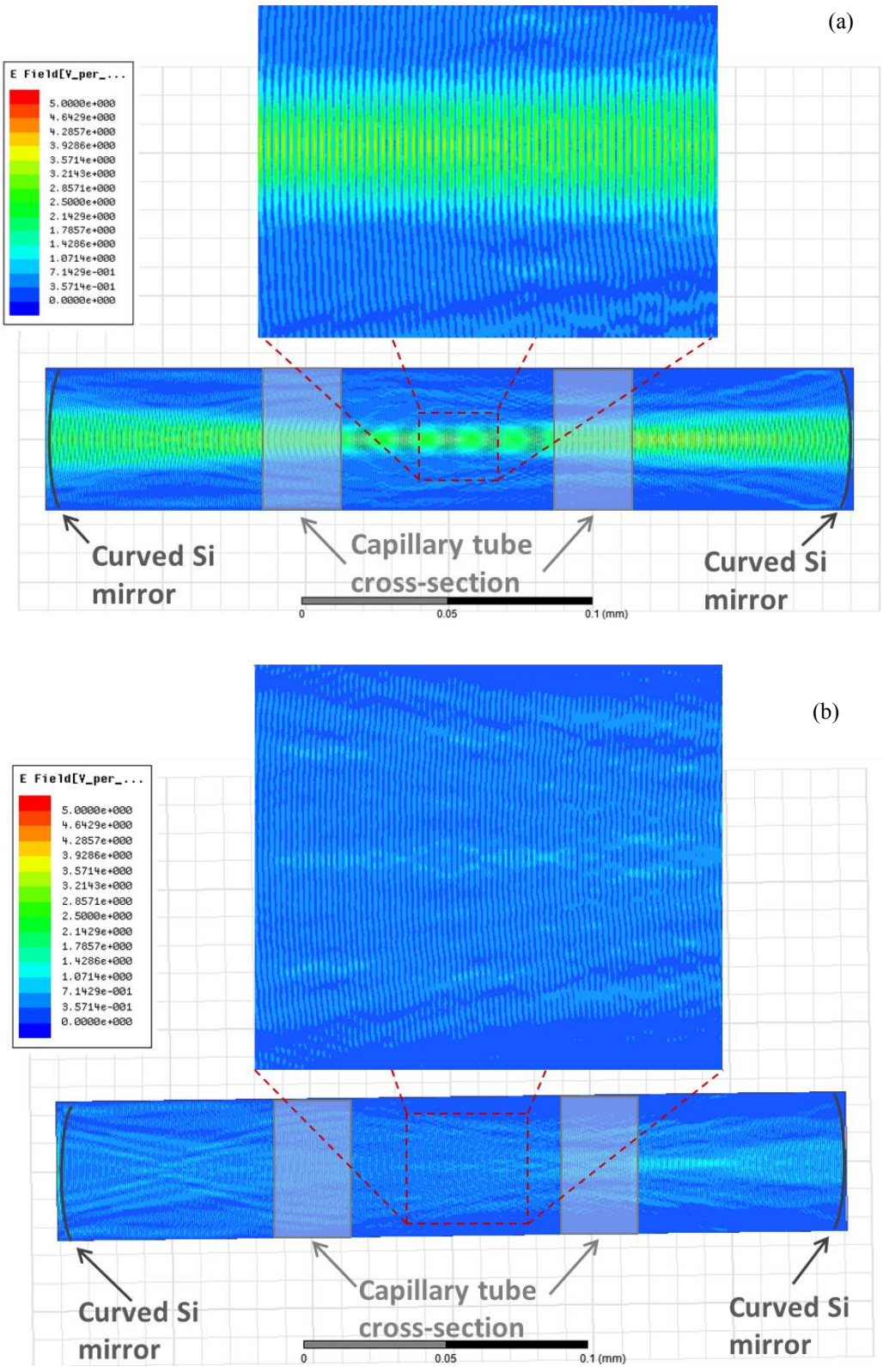

Fig. 4.25 Numerical simulations of the electric field within the microtube region inside the cylindrical FP cavity with the tube filled with water (a) at resonance: λ = 1546.52 nm. (b) Off-resonance, λ = 1545.48 nm. The insets are a zoom for the area inside the microtube region.

Now when the microspheres are presented in the DI-water, the field distribution is altered from the previous plots. If a polystyrene bead of 3 µm diameter is introduced near the axial line, the field distribution at the resonance wavelength of λ = 1546.48 nm experience severe disturbance that we have no more trapping spots as shown in Fig. 4.26 (a), which plots the field distribution at the new resonance wavelength. On the contrary, if a bead with 1 µm diameter is introduced at the same location, the field spots still exist despite the scattering due to the particle and hence the bead can in this case, continue traveling to its minimum energy position corresponding to the field intensity maxima, as shown in Fig. 4.26 (b) that plots the field distribution at the resonance wavelength corresponds to this case that is λ = 1546.48 nm. This may explain why only the small beads with 1 µm diameter could be trapped and arranged along the axial line (Fig. 4.18 and Fig. 4.19) while the larger beads could not (Fig. 4.23).

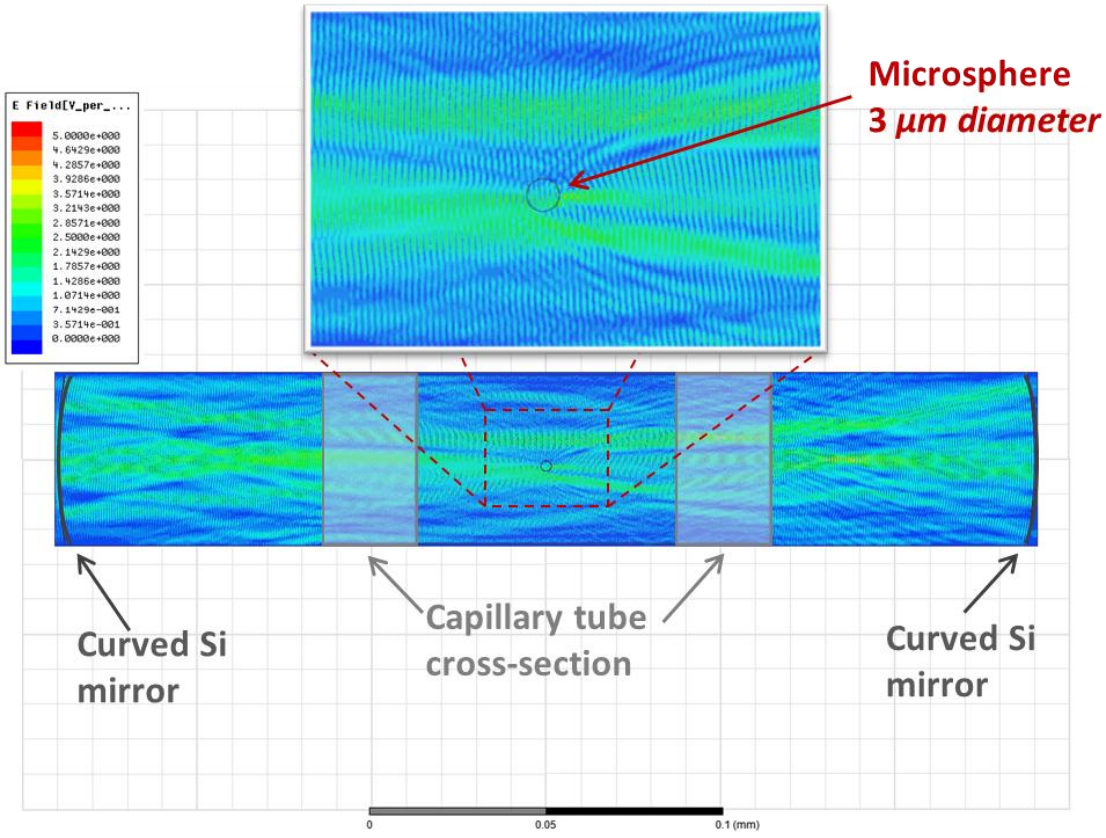

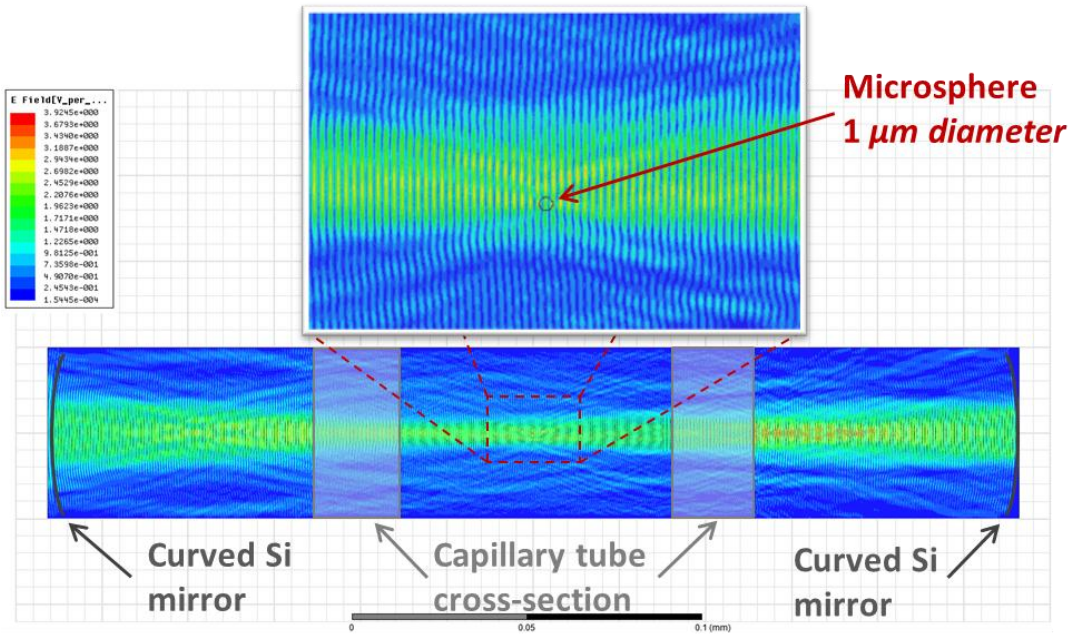

Fig. 4.26 Numerical simulations of the electric field within the cylindrical FP cavity enclosing the tube filled with water and a polystyrene microsphere (a) with 3 μm diameter at the resonance wavelength of λ = 1546.48 nm. (b) with 1 μm diameter at the resonance wavelength of λ = 1546.48 nm. The insets are a zoom for the area inside the microtube region.

4.7 Phenomenological Analysis

As we have seen, both experimental and simulated behaviors depend on particles size as they affect the field distribution in different manners. Generally, besides the Brownian motion of the particles, one may consider two components of the optical force governing the particles arrangement:

(i) The optical trapping gradient force resulting from the non-perturbed cavity field.

(ii) The additional perturbation force due to light re-scattered by the particles.

The particles final configuration depends whether stable states can be achieved or not and is probably based on the relative weight between the above-mentioned two components of the optical force, resulting in different equilibrium positions [12].

In our case, we observe different patterns depending on which force is the dominant one in each case. Let's start with the pattern of the one dimensional array of the 1 μm diameter microspheres along the axial line: as observed in the HFSS simulations in the case of one particle (Fig. 4.26 (b)) the high intensity spots of the standing wave antinodes are preserved despite the presence of the bead that forms intensity gradient. But the size of these spots is too small in the longitudinal direction (along the cavity axis) but wide enough in the

horizontal one (perpendicular to the cavity axis) as compared to the particle size. The size of the microsphere is too large to be confined in a single spot, so it covers more than one spot along the axis, but its width is sufficient to be trapped horizontally by the lateral intensity gradient. This part gets along with the term 'optical trapping' (which is a light-induced force that traps dielectric particles at the maximum of the light intensity with enough stiffness along the horizontal direction) although it is a partial effect. But for the longitudinal trapping the position is questionable. Now if we take several particles, the spot maxima can be preserved in the presence of low particles concentrations up to certain level. These particles may line up inside the tunnel formed by the horizontal intensity gradient of the multi spots along the axis. But the interspacing between them depends on a bit more complex behavior: the particles locations result from the balancing of two mechanisms:

- The first is the axial optical gradient force.

- The second mechanism is the interaction optical force due to multiple scattering of the light from the microspheres along the axis, which is known as the longitudinal binding [41].

It is well established that this multiple scattering mechanism can bind dielectric microspheres into an ordered 1D array even in a counter propagating wave system where their mutual interference is avoided, and hence with neither standing wave maxima nor axial intensity gradient [13]. The effect of this mechanism is pronounced in the experimental results shown in Fig. 4.19, where the distance between the beads is not uniform along the chain; the interspacing is large in the middle of the tube and is smaller at the left side (away from the light input side). This is somehow similar to that observed in the first image of Fig. 4.15 due to the breathing effect, that happens due to unbalance of the light pressure force coming from both sides and results in modifying the inter-particle spacing. This is analogous to our case since the ongoing and returning waves are not exactly balanced; the backward propagating wave suffers from extra reflection on the farthest mirror. Hence, this side may host the seed of the chain; and by the analogy with the observations in other cases of balanced counter-propagating waves (either Gaussian or Bessel beams) reported in literature, the inter-particle separating distance is smaller as the particles are placed closer to the chain center compared to its edges [37, 42, 43]. But in our case the chain is not symmetric and is incomplete at the right side due to its asymmetry with respect to the microtube center; hence we observe small distances between the particles at the left side and increases at the middle of the tube. Another expected reason behind this unequal spacing is the lensing effect of the cylindrical capillary

tube, the image of the particle array is deformed horizontally. Therefore, the spacing between the particles looks non uniform as indicated by the arrows in the zoomed area inside the inset of Fig. 4.19. But this effect is not considered the dominant one since the beads width should have been modified by the same amount; but roughly from the images, the distance between adjacent particles (light color) in the middle is wider by 2 to 3 times than near the edge, while the microspheres (dark color) almost have the same size in all locations. Still, the exact analysis of these effects requires proper definition of the particles positions and interspacing in the chain; but this couldn't be achieved due to the poor quality of the available images. Finally, it would have been interesting to investigate if the high intensity spots are alone sufficient to trap particles with diameters less than the axial distance between the standing wave maxima (< 0.5 μm), without the assisting effect of the longitudinal binding. But this requires a better imaging system since ours is insufficient to resolve such small dimensions bellow 1 μm.

Now concerning the second phenomenon of particles clustering or accumulation, it happens thanks to the optical binding or the multi-rescattering between the larger beads and even with the 1 μm and 0.5 μm diameter beads at high concentrations, where the presence of the particles disturbs the field trapping configuration significantly. Such clusters are not necessarily initiated by optical traps dictated by externally imposed field gradient. The mere presence of the objects in the area illuminated by the optical field exhibits its own field tapestry and even any new particle added in its vicinity, leads to a new spatial distribution. That is why the binding could happen even if we work off-resonance.

4.8 Conclusion

In this chapter, we demonstrated the theoretical background for optical trapping and binding and their different configurations and evaluate and compare them to our proposed new method for on-chip study of microparticles suspended in a liquid medium. This novel method is for low power particle localization inside an optofluidic FP using single side injection of light and taking advantage of both field confinement and field enhancement inside the optical cavity.

We also studied the phenomena of microspheres optical trapping and binding inside such resonator. Small beads of 1 μm diameter and low concentration get arranged in a 1D array along the cavity axis due to hybrid effect of optical trapping of the standing wave maxima and longitudinal binding induced by multi-particle scattering. Under certain conditions, the optical binding alone leads either to forming certain patterns of particles or to their accumulation. This phenomenon happens even if no optical traps exist in advance, or when this initial optical pattern gets disturbed by the existence of the micro beads. Numerical simulations have been demonstrated to aid the understanding of the field distributions and hence the optical behavior in each reported case.

The trapping of particles may be useful for further particles optical spectroscopy, which can be implemented, in principle, within the resonant FP cavity in the form of CEAS. This is particularly interesting for biological cells since this configuration doesn't require high power which may preserve their tissues, especially if a proper trapping wavelength in that near infrared range is selected to reduce the water absorption, and simultaneously to let silicon to be transparent like the O-band (wavelength from 1260 to 1360 nm) or U-band (wavelength from 1625 to 1675 nm). The aggregation behavior may be useful in speeding up the colloid gelling or coagulation process in some industries. This is particularly interesting especially as this effect may happen even by simple illumination without the need for meeting resonance conditions.

4.9 References for chapter 4

[1] A. Ashkin, "Acceleration and Trapping of Particles by Radiation Pressure," Phys. Rev. Lett., vol. 24, p. 156-159, 1970.

[2] A. Ashkin, J. M. Dziedzic, J. E. Bjorkholm, and Steven Chu, "Observation of a single-beam gradient force optical trap for dielectric particles," Opt. Lett., vol. 11, pp. 288-290, 1986.

[3] C. Sun, Y. Huang, P. C. Cheng, H. Liu, and B. Lin, "Cell manipulation by use of diamond microparticles as handles of optical tweezers," J. Opt. Soc. Am. B, vol. 18, pp. 1483-1489, 2001.

[4] P. Jákl, T. Čižmár, M. Šerý, and P. Zemánek, "Static optical sorting in a laser interference field," Appl. Phys. Lett., vol. 92, pp. 161110-1-161110-3, 2008.

[5] S. Lin, E. Schonbrun, and K. Crozier, "Optical Manipulation with Planar Silicon Microring Resonators," Nano Lett., vol. 10, pp. 2408-2411, 2010.

[6] M. Rosenblit, Y. Japha, P. Horak, and R. Folman, "Simultaneous optical trapping and detection of atoms by microdisk resonators," Phys. Rev. A, vol. 73, pp. 063805-1-063805-12, 2006.

[7] S. Arnold, D. Keng, S. I. Shopova, S. Holler, W. Zurawsky, and F. Vollmer, "Whispering gallery mode carousel – a photonic mechanism for enhanced nanoparticle detection in biosensing," Opt. Express, vol. 17, pp. 6230-6238, 2009.

[8] T. Lei, and A. W. Poon, "Silicon-on-insulator multimode-interference waveguide-based arrayed optical tweezers (SMART) for two-dimensional microparticle trapping and manipulation," Opt. Express, vol. 21, pp. 1520-1530, 2013.

[9] N. Descharmes, U. P. Dharanipathy, Z. Diao, M. Tonin, and R. Houdre, "Observation of Backaction and Self-Induced Trapping in a Planar Hollow Photonic Crystal Cavity," Phys. Rev. Lett., vol. 110, pp. 123601-1-123601-4, 2013.

[10] A. Constable, J. Kim, J. Mervis, F. Zarinetchi, and M. Prentiss, "Demonstration of a fiber-optical light-force trap," Opt. Lett., vol. 18, pp. 1867-1869, 1993.

[11] C. Lai, S. Hsiung, Y. Chen, A. Chiou, and G. Lee, "An Integrated 2-D Active Optical Fiber Manipulator with Microfluidic Channel for Optical Trapping and Manipulation," JMEMS, vol. 17, pp. 548-557, 2008.

[12] O. Brzobohatý, V. Karásek, M. Šiler, J. Trojek, and P. Zemánek, "Static and dynamic behavior of two optically bound microparticles in a standing wave," Opt. Express, vol. 19, pp. 19613-19626, 2011.

[13] W. Singer, M. Frick, S. Bernet, and M. Ritsch-Marte, "Self-organized array of regularly spaced microbeads in a fiber-optical trap," J. Opt. Soc. Am. B, vol. 20, pp. 1568-1574, 2003.

[14] O. Brzobohatý, M. Šiler, J. Ježek, P. Jákl, and P. Zemanek, "Optical manipulation of aerosol droplets using a holographic dual and single beam trap," Opt. Lett., vol. 38, pp. 4601-4604, 2003.

[15] M. M. Burns, J. Fournier, J. A. Golovchenko, "Optical Matter: Crystallization and Binding in Intense Optical Fields," Science, vol. 249, pp. 749-754, 1990.

[16] M. M. Burns, J. Fournier, and J. A. Golovchenko, "Optical binding," Phys. Rev. Lett., vol. 63, pp. 1233-1236, 1989.

[17] M. Malak, N. Pavy, F. Marty, Y. -A. Peter, A. Q. Liu, and T. Bourouina, "Micromachined Fabry–Perot resonator combining submillimeter cavity length and high quality factor," Appl. Phys. Lett., vol. 98, pp. 211113-1-211113-3, 2011.

[18] L. K. Chin, A. Q. Liu, C. S. Lim, X. M. Zhang, J. H. Ng, J. Z. Hao, and S. Takahashi, "Differential single living cell refractometry using grating resonant cavity with optical trap," Appl. Phys. Lett., vol. 91, pp. 243901-1- 243901-3, 2007.

[19] T. Ray, A. Sharma, S. Jyothi, and S. A. Rangwala, "Temperature measurement of laser-cooled atoms using vacuum Rabi splitting," Phys. Rev. A, vol. 87, pp. 033832-1-033832-6, 2013.

[20] H. J. Kimble, "Strong interactions of single atoms and photons in cavity QED," Physica Scripta., vol. T76, 127-137, 1998.

[21] J. Larson, and J. Martikainen, "Ultracold atoms in a cavity-mediated double-well system," Phys. Rev. A, vol. 82, pp. 033606-1-033606-10, 2010.

[22] Y. YU, "Theoretical Analys is, Design and Fabrication of Nano-Opto-Mechanical System (NOMS)," PhD thesis, Université Paris-Est, 2011.

[23] Q. Zhang, J. J. Xiao , X. M. Zhang, and Y. Yao, "Optical binding force of gold nanorod dimers coupled to a metallic slab" Opt. Commun., vol. 301-302, pp. 121–126, 2013.

[24] T. Li, "Fundamental Tests of Physics with Optically Trapped Microspheres," PhD thesis, the university of Texas at Austin, 2013.

[25] Y. Harada, and T. Asakura, “Radiation Forces on a dielectric sphere in the Rayleigh Scattering Regime,” Opt. Commun., vol. 124, pp. 529-541, 1996.

[26] R. W. Bowman, and M. J. Padgett, “Optical trapping and binding,” Rep. Prog. Phys., vol. 76, pp. 026401-1-026401-28, 2013.

[27] J. W. Shaevitz, "A Practical Guide to Optical Trapping," 22 August 2006, Online: http://genomics.princeton.edu/shaevitzlab/OT_Practicle_Guide.pdf.

[28] K. C. Neuman, E. H. Chadd, G. F. Liou, K. Bergman, and S. M. Block, “Characterization of Photodamage to Escherichia coli in Optical Traps,” Biophys. J., vol. 77, pp. 2856-2863, 1999.

[29] A. T. Ohta, P. Chiou, H. L. Phan, S. W. Sherwood, J. M. Yang, A. N. K. Lau, H. Hsu, A. Jamshidi, and M. C. Wu, “Optically Controlled Cell Discrimination and Trapping Using Optoelectronic Tweezers,” IEEE J. Sel. Top. Quant. Electron., vol. 13, pp. 235-243, 2007.

[30] D. G. Grier, “A revolution in optical manipulation,” Nature, vol. 424, pp. 810-816, 2003.

[31] K. C. Neuman, and S. M. Block, “Optical trapping: review article,” Rev. Sci. Instrum., vol. 75, pp. 2787- 2809, 2004.

[32] J. Yamamoto, and T. Iwai, “Stability Analysis of Particle Trapping in Time-Division Optical Tweezers by the Generalized Lorentz–Mie Theory,” Jpn. J. Appl. Phys., vol. 49, pp. 092701-1-092701-6, 2010.

[33] P. Zemanek, A. Jonas, L. Sramek, and M. Liska, “Optical trapping of Rayleigh particles using a Gaussian standing wave,” Opt. Commun., vol. 151, pp. 273-285, 1998.

[34] A. H. J. Yang and D. Erickson, “Stability analysis of optofluidic transport on solid-core waveguiding structures,” Nanotechnology, vol. 19, pp. 045704-1-045704-10, 2008.

[35] k. Grujic, O. G. Hellesø, J. P. Hole, and J. S. Wilkinson, “Sorting of polystyrene microspheres using a Y-branched optical waveguide,” Opt. Express, vol. 13, pp. 1-7, 2005.

[36] Y. Fu, L. K. Chin, T. Bourouina, A. Q. Liu, and A. M. J. Van Dongen, “Nuclear deformation during breast cancer cell transmigration,” Lab Chip, vol. 12, pp. 3774-3778, 2012.

[37] V. Karasek, T. Cizmar, O. Brzobohaty, and P. Zemanek, V. Garcés-Chàvez, and K. Dholakia, “Long-Range One-Dimensional Longitudinal Optical Binding,” Phys. Rev. Lett., vol. 101, pp. 143601-1-143601-4, 2008.

[38] S. A. Tatarkova, A. E. Carruthers, and K. Dholakia, “One-Dimensional Optically Bound Arrays of Microscopic Particles,” Phys. Rev. Lett., vol. 89, pp. 283901-1-283901-4, 2002.

[39] M. Malak, N. Gaber, F. Marty, N. Pavy, E. Richalot, and T. Bourouina, "Analysis of Fabry-Pérot Optical Micro-cavities Based on Coating-free All-Silicon Cylindrical Bragg Reflectors," Opt. Express, vol. 21, pp. 2378-2392, 2013.

[40] M. Elimelech, J. Gregory, X. Jia, R.A. Williams, *Particle Deposition & Aggregation: Measurement, Modelling and Simulation*, Butterworth-Heinemann, 1998, chapter 6, pp. 167.

[41] Z. H. Hang, J. Ng, and C. T. Chan, "Stability of extended structures stabilized by light as governed by the competition of two length scales," Phys. Rev. A, vol. 77, pp. 063838-1-063838-5, 2008.

[42] M. Kawano, J. T. Blakely, R. Gordon, and D. Sinton, "Theory of dielectric micro-sphere dynamics in a dual-beam optical trap," Opt. Express, vol. 16, pp. 9306- 9317, 2008.

[43] J. M. Taylor, and G. D. Love, "Optical binding mechanisms: a conceptual model for Gaussian beam traps," Opt. Express, vol. 17, pp. 15381-15389, 2009.

CHAPTER (5)

SPHERICAL RESONATORS

5.1 Introduction

As demonstrated earlier, Fabry–Pérot cavity using curved surfaces could exhibit high Q factors. But for much more superior Q factors, a totally different family of modes - also supported by resonators with curved surfaces - could be employed. This family of modes is called Whispering Gallery modes (WGMs), which can be supported by ring resonators [1], disks [2], micro-toroids [3], tubular resonators [3], and spherical resonators [4] which include droplets [5]. The WGMs supported by different resonators differ in performance, as will be shortly discussed, but typically almost all of them enable very high (or ultra-high) Q-factors and finesses at very low mode volumes, and these resonators can be much more easier in realizing, compared to "usual" (for example Fabry-Pérot) resonators, since they require no external mirrors to confine light.

Whispering gallery modes or waves are specific resonances or (eigen-) modes of a wave field (e.g. sound waves, electromagnetic waves …) inside a given resonator or a cavity with curved smooth edges and with a closed propagation path. They correspond to waves circling around the cavity. In ray optics representation of light, WGMs can also be seen as associated to rays travelling at the inner cavity periphery around the equatorial region and undergoing internal reflection on the cavity surface. The optical rays must meet the resonance condition: after one round trip light returns to the same point with the same phase and hence interfere constructively with the previous paths. These resonances depend greatly on the geometry of the resonator cavity [6], as well as on material properties and on surface quality.

In the WGMs supported by tubular resonators, light rays require reflection from the curved outer surface only [7]. Hence, these microcavities provide high Q values due to the superior two-dimensional optical confinement, although their performance is not up to the microspheres as those provide three-dimensionally (3D) confinement due to their additional boundaries, which introduce extra guiding effects and modify the cavity modes significantly. But still, the high Q of tubular resonators enables realizing low threshold lasers like for example, a fused-silica capillary tube filled with a dye-doped liquid having a high refractive

index; and this type of microcavity laser is called core-resonance capillary-fiber WGMs laser. Also they can provide micro-devices or microsystems with good optical performance and promising applications in bio/chem-sensing, gas detection; such as the capillary-based optical ring resonators (CBORRs) that can be used for chromatography [8].

Dielectric cylinders and disks (cylinders with small height) also support whispering gallery modes. Cylinders are in many ways similar to spheres in terms of the whispering gallery modes that they support (light circulates around the cylinder in an analogous way to light circling around the equator of the sphere), but there is one fundamental difference: while in a sphere the modes are stable under perturbations away from equatorial propagation, the same is not true for dielectric cylinders. Also in a sphere, the polar curvature of the sphere surface confines and focuses light in the polar direction, but in a dielectric cylinder a light beam, which is sufficiently perturbed from propagating around the equator, can escape through the top or bottom of the cylinder and thus leave the resonator. Because of this added mode instability due to the lack of focusing in the polar direction, and the fact that it is harder to manufacture disks with comparably low surface roughness as that of a spherical resonator, the Q-factors of cylinder and disk resonators are usually much lower than those of spheres (typically for disks) unless the cylinder diameter is locally increased so that to reach better confinement along the cylinder axis [9]. Because of their planar geometry, the fabrication of ring and disk resonators is easier, faster and more controllable, and they are much more easily integrated in an integrated optical network or on a chip, while at the same time taking up much less space than microspheres of comparable radii and having smaller mode volumes. This makes them very useful for practical applications [10].

Variants of disk resonators are ring resonators (basically disk resonators with a circular hole in the middle, although a more interesting shape consists of using a “donut” shape). Since WGMs are already highly localized at cavity-air interface, ring resonators have almost the same whispering gallery modal structure as disk resonators, while higher order radial modes are much better suppressed. An additional advantage of ring resonators is that they allow for many times smaller mode volumes (compared to microspheres or disk resonators), involving only a fraction of the volume of the dielectric material. Different types of resonators that support WGMs are shown in Fig. 5.1.

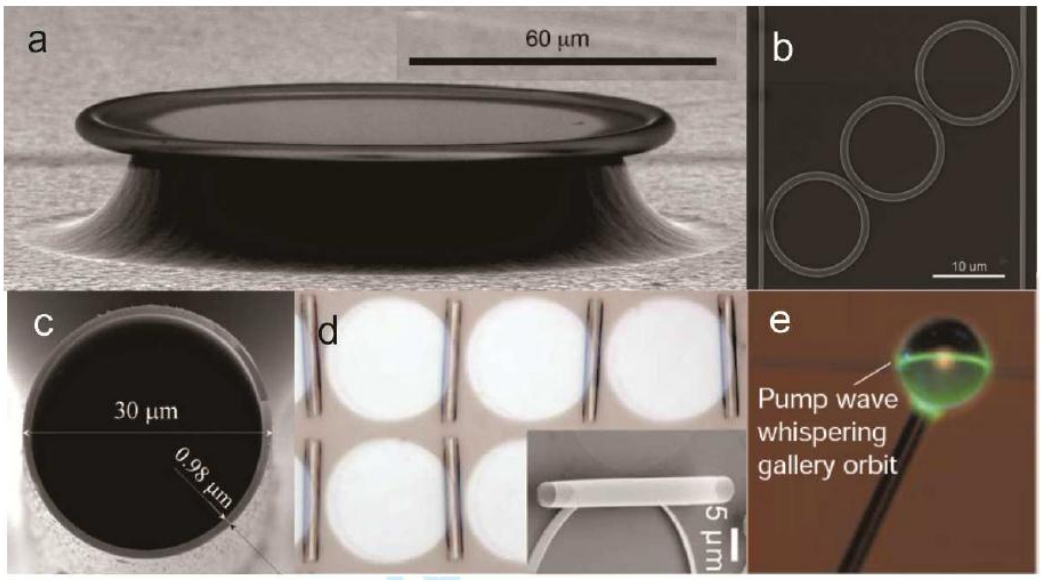

Fig. 5.1 Various WGMs resonator configurations: (a) Micro-toroid, (b) Slot waveguide ring resonator (c) Capillary-based micro-tubular resonator fabricated by the drawing method, (d) Micro-tubular resonator fabricated by self-rolled up processes, and (e) Microsphere [3]

From the previous discussion, the best performance is achieved through the sphere optical resonators, thereby they attracted huge interest -either solid or liquid that can be easy and fast to realize- due to their symmetrical shape and their potential to sustain very high-Q resonant WGMs up to $Q > 10^{10}$ [11]. Therefore they are able to provide excellent optical resonators for many photonics applications such as lasing [12], stimulated Raman scattering [13-15], and others [16]. Also the optical field has an evanescent part, that enables it to interact and sense changes in the environment [17]. Thus microspheres are suitable for chemical and biological sensing; in addition, they are label-free, affordable, and fast, with high throughput [18]. Good accuracy in detecting a single virus [19], DNA [17], or a single molecule [16], has been reported.

The high quality factor is bended to several mechanisms. One is the dielectric materials of microspheres, it is important to have ultra-low optical loss due to the material absorption at the frequencies of the supported whispering gallery modes. Another is the surface of the sphere; it should have low roughness and low inhomogeneities; since these can scatter photons out of the guided mode and decrease the quality factor [20]. If liquids with low loss are used to form the droplets to avoid the absorption problem, surface imperfections are also evaded due to their smooth surface (but of course the surface cleanness and low vibration environment still should be guaranteed).

All these factors govern the intrinsic (or internal) quality factor Q_{in} of the resonator itself. But unfortunately this is not enough to get an overall high Q; since it may be aggravated if the coupling (or external) quality factor Q_c is low. And hence low-loss coupling techniques are essential. Different coupling methods have been reported [15, 21-25]. Each has its merits as will be discussed. The coupling method should also be robust, flexible (coupling can be tuned over an acceptable range), and non-risky, beside its acceptable coupling quality factor; which is not the case for many of the conventional coupling methods reported, especially when considering on-chip coupling of light into spheres in the (sub-) millimeter diameter range. Thus, in our present work, we propose a novel coupling technique using a free-space propagating Gaussian Beam (GB) so as to harness the full benefit of using high-Q spherical resonators in the form of liquid droplets. It is worth mentioning that in previous literature reports, this technique of free-space coupling was thought initially to be inefficient for exciting the high-Q WGMs, which are supported by spheres that have large radii compared to the exciting wavelength, the invoked reason being that the evanescent field tail of such modes is extremely small [11]. The technique was therefore limited to the scope of studying Mie resonances in aerosol micro-droplets (whose size is comparable to wavelength), and their elastic and inelastic scattering [26], with very few practical applications. Almost all those resonators considered in the literature were in the range of micrometers [13-15, 27-29]. Free-space coupling into millimeter spheres by means of GB was insufficiently investigated [30], and to the best of our knowledge, this study is the first report of its implementation in a lab-on-chip environment, where its significant potential for analytical applications requires careful consideration.

In this work, we explore the potential of direct coupling of a droplet optical resonator using a free-space Gaussian beam produced by a lensed optical fiber, and compare it with the traditional coupling techniques. This method has the advantages of avoiding the physical contact between the droplet and all micro-optical parts, thus preserving the integrity of the droplet: its contents and its (nearly) spherical shape. The spherical shape is further preserved by using a super-hydrophobic surface, called “black-silicon”, a micro-structured silicon surface obtained by plasma processing at cryogenic temperatures [31, 32]. Our demonstration is also supported by simulations, and mathematical analysis of the quality factors related to this novel technique.

5.2 Different Coupling Methods of Light into WGM resonators

In the area of spherical resonators, there is a quite rich literature and different methods for coupling light into the resonators were reported; amongst the most spread ones: Prism couplers [23, 33, 34], and tapered fibers [15, 21, 25, 35]. Prism couplers and tapered fiber couplers are both based on evanescent field coupling. The prism couples light directly into the spherical cavity through the evanescent field of total internal reflection on the prism surface. In the case of the tapered fiber couplers there is an overlap between the above-mentioned evanescent field of the resonant mode and the evanescent field of the thin fiber, eventually leading to light coupling. Both methods have their advantages and drawbacks.

When considering droplets, the prism method is very risky and needs precise control to avoid physical contact between the prism and the droplet, or to reduce the effects of such contact. Indeed, light can be in principle coupled into the cavity by using a coupling prism placed at a small distance 0.1 – 1 λ away from the resonator surface. The beam is focused on the "touching point" with an angle providing total internal reflection, and the light tunnels through the small gap between the prism and the microsphere [33]. If we introduced the term of coupling ‘‘ideality’’ defined as the ratio of power coupled to a desired mode divided by power coupled or lost to all modes (including the desired mode) [35]; then the prism coupler method has the least coupling ideality because of the large number of its possible output modes (as evidenced by the observed spatial ‘‘fan’’ of output power), although only one is needed to be coupled into the resonator, hence a large amount of power is lost; besides its main drawback of lower coupling efficiency due to optical misalignment [23]. But it also has its advantages as it allows the control of the phase synchronism and the mode overlap between the coupler and the microsphere mode. This is achieved by the adjustment of the input beam parameters; which makes the prism coupler efficient and versatile for various applications of high-Q microsphere resonators [34].

For the tapered fiber technique, the setup for light coupling is less complicated; the tapered fiber can be placed alongside a resonator allowing simple focusing and alignment of the input beam, as well as collection of the output beam. But still the distance between them needs to be accurately adjusted within tens of nanometers (less than the evanescent tails) in order to obtain a significant coupling. This also introduces the risk of irreversible physical contact between the fiber and the droplet induced by the capillary forces. Regarding the coupling ideality, the small number of modes supported by the taped-fiber waveguide coupler

suggests that the situation could be improved over the prism coupling method. Tapered fibers have been shown to provide high coupling efficiency to microresonators, which can exceed 99.97% under appropriate conditions [35]. Fig. 5.2 shows a schematic of the different coupling methods; (a) and (b) are the prism and tapered fiber methods respectively.

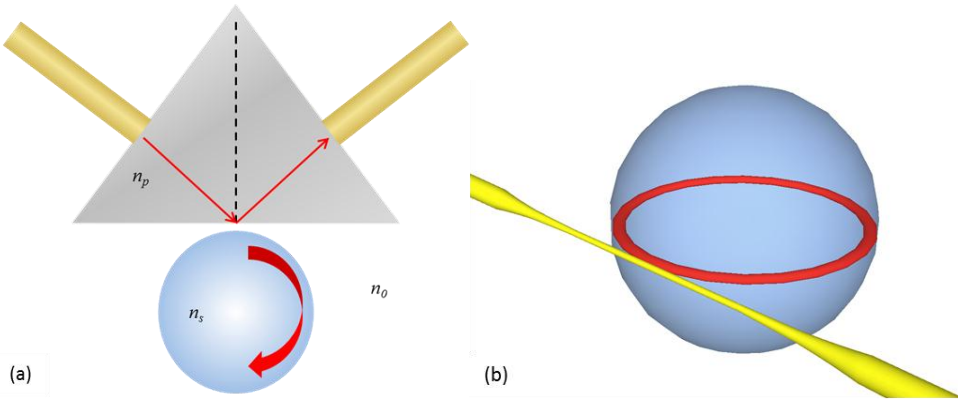

Fig. 5.2 Different coupling methods: (a) using a prism coupler [adapted from 23]. (b) Using a tapered fiber.

None of the above-mentioned methods can easily preserve the integrity of the droplet shape and in the same time produce significant coupling of light. Hence we investigate a new coupling method of direct coupling using a free-space Gaussian beam produced by an optical fiber with a lensed tip (Fig. 5.3). The free space approach avoids the collision between the resonator and optical injecting and collecting tools, thus it preserves the integrity of the tools as well as the integrity of the resonator. Also our method showed higher coupling quality factor than those of the tapered fiber or half block method [21]. And of course we don't have to worry about the coupling ideality in our case since there is no multimode supported by the coupler, as only a free space Gaussian beam is used for coupling. This method also has larger flexibility, as the range of the gap alignment between the droplet and the beam is in the order of micrometers (if GBs with sufficient beam waists are used) as will be demonstrated, while such gap needs to be in the order of hundreds of nanometers and even nanometers in the case of the above-mentioned conventional coupling techniques.

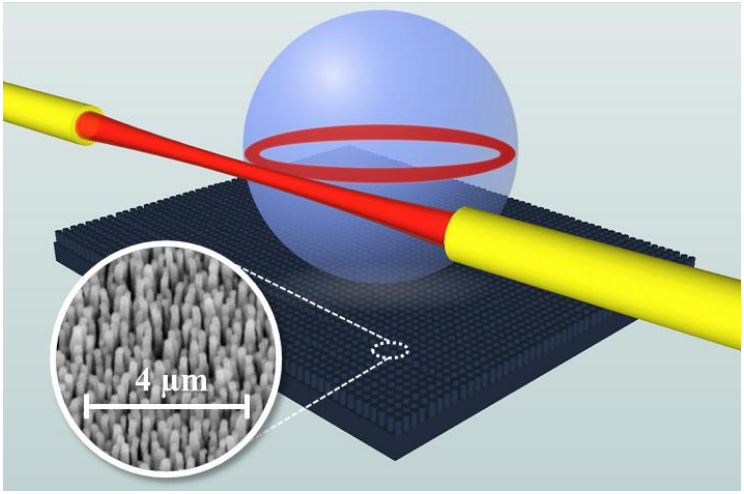

Fig. 5.3 Coupling using a free space Gaussian beam, the droplet is supported on a black silicon substrate, coated with Teflon, leading to a superhydrophobic surface. The inset is a Scanning Electron Microscope image of the substrate.

5.3 Micro-droplets versus millimeter droplets

In our work we adopt rather large, millimeter-size spheres (droplets), which differ from the micrometer-sized ones through several characteristics. The primary aspect is that, as the sphere size increases, the density of modes increases as well, and with it the principal number of the useful target resonance mode increases also according to Mie theory [36]. A consequence is that the mode intrinsic quality factor or the radiative quality factors Q_{rad} also increases. Therefore, increasing the diameter offers clear benefits in addition to easier production and handling. But on the other hand, the free space coupling was expected to become more difficult, and was even considered sometimes inefficient for exciting WGMs, as the radiative exchange of these modes with the external space is not sufficient when the radius exceeds several wavelengths [11]. More precisely, the highly confined WGMs, with radiative quality factors $Q_{rad} > 10^{20}$, possess negligible radiative losses, and hence are expected to be not accessible by free-space coupling including coupling using GB; therefore millimeter-sized droplets and even those with diameters in the hundreds of micrometers range were initially considered to require evanescent field coupling techniques [34]. In what follows, we will show that this *a priori* statement is not completely true since we succeeded demonstrating such coupling of WGMs using free-space propagating GB.

Another important difference between small and large sized droplet resonators is the validity of the Van de Hulst's localization principle [37] that relates the principal mode

number of the WGM to the external Gaussian beam position in order to obtain a maximized energy coupling to the spherical cavity mode. It states that a tightly focused Gaussian light beam passing outside but near a spherical microcavity will preferentially excite specific cavity modes, depending on its distance from the cavity center. But experimentally, it has been shown that this principle apparently fails because of surface perturbations in the low order modes, especially the first order, where most of the mode field is located near the surface; in such cases the optimal excitation position shifts to within the droplet, in disagreement with the Van de Hulst's principle. Hence, in droplets with radii larger than 20 μm, where there is a dramatic increase in the number of surface-limited modes, the Van de Hulst localization principle is not expected to play an important role [37].

5.4 Resonance Whispering Gallery Modes and Fields in a Sphere

In a dielectric sphere, the bound portion of the near field, which contributes to the coupling with the external excitations, can be written as [21]:

$$\Psi_{\ell,m,n}(r,\theta,\phi) = N_s \psi_r(r)\psi_\theta(\theta)\psi_\phi(\phi) \tag{5.1}$$

where, the components' contributions take the form:

$$\begin{aligned}
&\psi_r(r) = \begin{cases} j_\ell(kn_s r), & r \le R_0 \\ j_\ell(kn_s R_0)e^{-\alpha_s(r-R_0)}, & r > R_0 \end{cases} \\
&\psi_\theta(\theta) = e^{-\frac{m}{2}\theta^2} H_N\left(\sqrt{m}\theta\right), \qquad m \gg 1 \gg \theta \\
&\psi_\phi(\phi) = e^{\pm im\phi}
\end{aligned} \tag{5.2}$$

and the coefficients are

$$\beta_\ell = \frac{\sqrt{\ell(\ell+1)}}{R_0}, \qquad N = \ell - m$$

$$N_s = \left\{ \frac{\pi}{m} 2^{N-1} N! R_0^2 \left[\left(1 + \frac{1}{\alpha_s R_0}\right) j_\ell^2(kn_s R_0) - j_{\ell-1}(kn_s R_0)\, j_{\ell+1}(kn_s R_0) \right] \right\}^{-1/2}$$

$$\alpha_s = \sqrt{\beta_\ell^2 - k^2 n_0^2}, \qquad k = 2\pi/\lambda$$

where $k = 2\pi/\lambda$ is the wave vector and $\Psi_{\ell,m,n}$ the field distributions the WGM resonating modes of orders ℓ, m, n. The three terms of equation (5.2) consist of the following components in the spherical coordinates:

1- The radial contribution $\psi_r(r)$ is comprised in the exact Spherical Bessel functions form inside the sphere; while exterior to the sphere -but very close to the surface- the fields decay exponentially away from the sphere in the radial direction with a decay constant α_s, while β_ℓ is the propagation constant parallel to the surface of the sphere. The propagation constant parallel the surface of the sphere, but along the equator, is the projection of β_ℓ onto the equator. This propagation constant has the value $\beta_m = m/R_0$. Fig. 5.4 indicates these propagation constants on a schematic of the spherical resonator.

2- The polar contribution $\psi_\theta(\theta)$ which is often expressed in terms of the Associated Legendre Polynomials $P_m^\ell(\cos\theta)$ as the exact solutions. But since we are mainly interested in large m and ℓ values and small polar angles with the approximation of $\theta \approx 0$, in this case the polynomials are well represented by the Hermite–Gaussian functions, with Hermite polynomials H_N of order $N = \ell - m$. This form of the polar dependency facilitates the closed-form evaluation of overlap integrals that will be presented in section 5.8.

3 - The azimuthal contribution $\psi_\phi(\phi)$ with integer mode number m, which is defined over a positive range only and $m \le \ell$.

N_s is the normalization constant associated with the intensity flow through a plane transverse to the effective direction of propagation that is along the equatorial plane. It is evaluated from the volume integral of $\Psi^2_{\ell,m,n}$ over all the space, divided by the equatorial path length $2\pi R_0$.

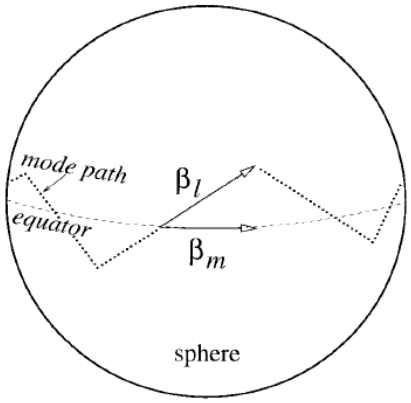

Fig. 5.4 Schematic of the mode propagation constants along the surface of the sphere [21].

The characteristic equation which describes the relationship between the wave vector k and the eigenvalues n and ℓ is determined by matching tangential electric and magnetic fields across the surface $r = R_0$. This gives the following simple characteristic equation [21]:

$$\left(\eta_s \alpha_s + \frac{\ell}{R_0}\right) j_\ell \left(k n_s R_0\right) = k n_s j_{\ell+1}\left(k n_s R_0\right) \tag{5.3}$$

where

$$\eta_s = \begin{cases} 1, & \text{TE modes} \\ \dfrac{n_s^{\,2}}{n_0^{\,2}}, & \text{TM modes} \end{cases}$$

Fig. 5.5 shows the radial and polar dependence of field intensity for different m, n and ℓ eigen values of spherical modes, supported by photographs of actually excited whispering gallery modes.

(a)

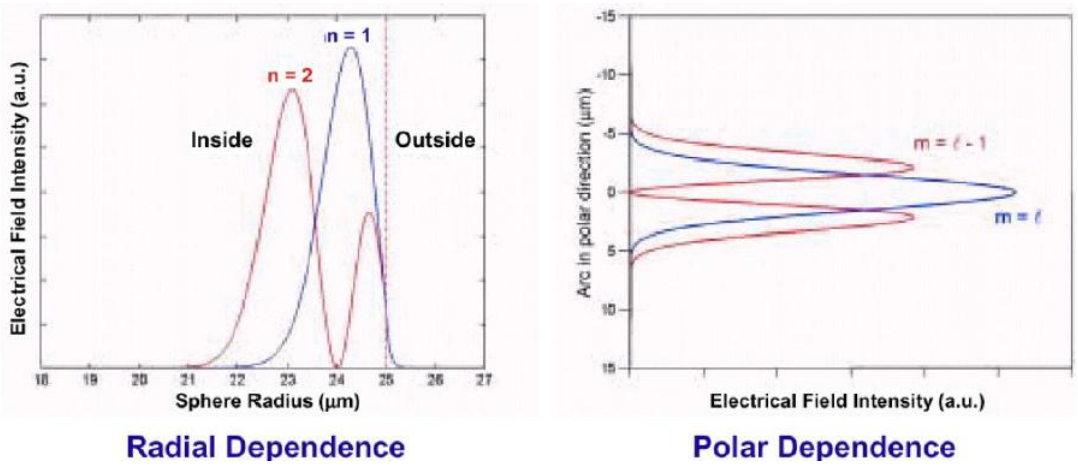

(b)

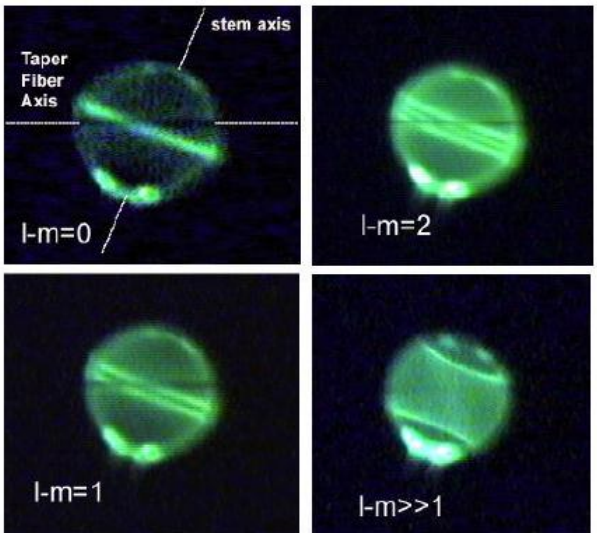

Fig. 5.5 (a) The radial and polar dependence of field intensity for eigen-modes of a spherical resonator, demonstrating the meaning of mode numbers. (b) A photograph of individual excited whispering gallery modes [38].

5.5 Numerical Simulations

To get a better figure about what may happen if a droplet is excited by a GB, simulations have been performed with the High Frequency Structural Simulator (HFSS) software from ANSOFT, based on the Finite Element Method (FEM). Though the simulations are performed on small-scale spheres, due to size limitations of the calculation domain, these simulation results provide a schematic representation of the field distribution involving coupling between a Gaussian Beam and a WGM of a sphere resonator as well as the resulting spectral response. Fig. 5.6 shows a sphere of radius 1.5 μm and refractive index (n) of 1.47, excited by a GB, at wavelength λ = 1385 nm (at one of the resonances seen in the spectral response shown in Fig. 5.7).

(a)

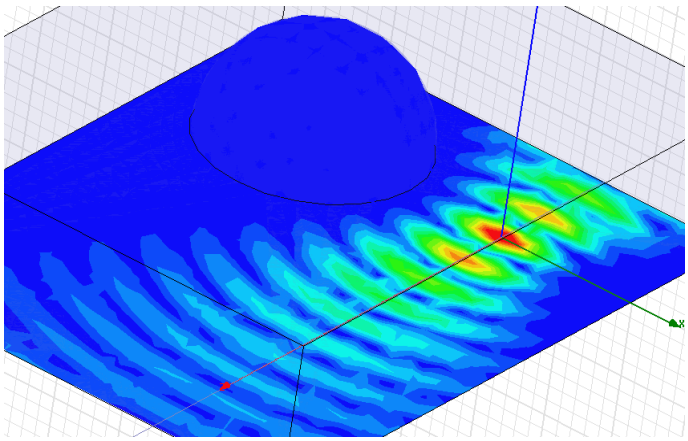

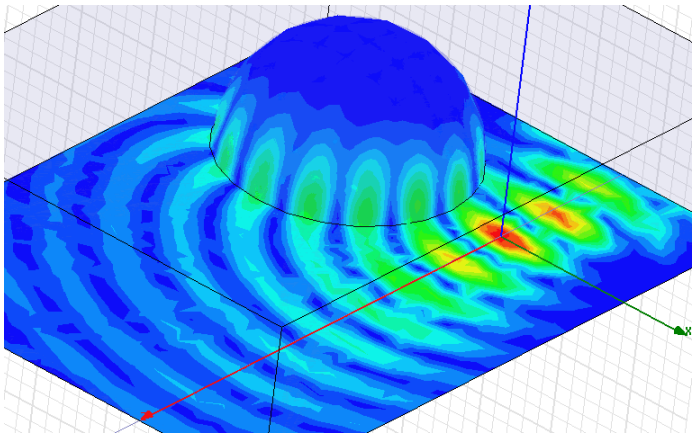

(b)

Fig. 5.6 Amplitude of the simulated electromagnetic field at the vicinity of a 1.5 μm droplet, n=1.47 excited by a Gaussian beam as the optical axis is located at different distances S_0 from the dielectric sphere expressed in units of the beam waist W_0: (a) $S_0 = 4W_0$; (b) $S_0 = 2W_0$, at resonant wavelength λ = 1385 *nm* of a Whispering Gallery Mode. At the beam waist, the tangential component of the incident electric field is chosen normal to the incident plane.

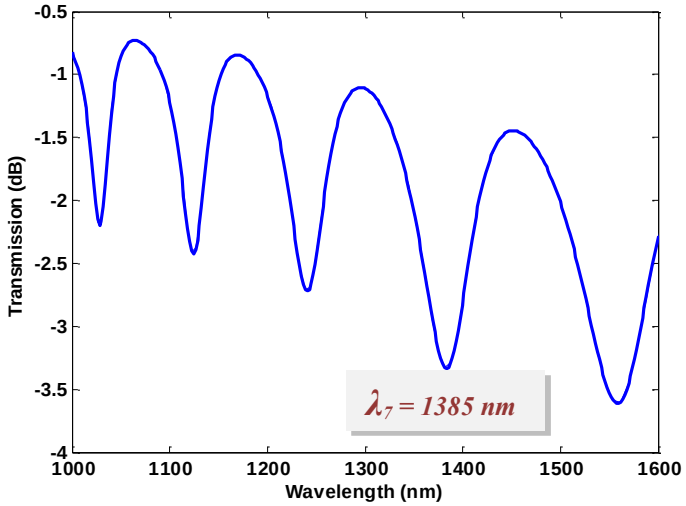

Fig. 5.7 Simulated spectral transmission response of a 1.5 μm radius droplet, n = 1.47 excited by a Gaussian beam whose axis is located at a distance $S_0 = 2W_0$ from the dielectric sphere. The 7th order resonance drop peak at λ = 1385 nm relates to the mode shape shown in Fig.1.3.

Due to the mirror symmetry of the structure, the simulation domain can be reduced to a hemisphere, improving the computation time. Several positions for the GB optical axis placed at a distance S_0 from the sphere edge have been investigated. The field distributions show that when the GB axis is too far from the resonator (at a distance $S_0 = 4W_0$, where W_0 is the beam waist), no significant coupling could be seen, as show in Fig. 5.6 (a). However, significant coupling can be observed at $S_0 = 2W_0$ as indicated in Fig. 5.6 (b), where the WGM excited inside the droplet can be recognized. Indeed, from this field distribution, the number of field maxima along the half circumference is 7, with single maxima in the polar direction; hence it is identified as a fundamental mode with angular mode order ℓ=7. Almost the same

value of the mode order is also evaluated for similar radius-to-wavelength ratio using the characteristic equation of the WGM (equation 5.3) by solving it numerically.

The spectral transmission response for this droplet over a wavelength range from 1000 nm to 1600 nm has been obtained from numerical simulations as indicated in Fig. 5.7, where the different resonances can be noticed including the resonance at λ = 1385 nm, whose mode shape was shown in Fig. 5.6 (b).

5.6 Experimental Results

5.6.1 Shape of Glycerol droplets on a Black Silicon surface

To realize the spherical resonators, glycerol droplets with different diameters were mounted on the Teflon-coated black silicon substrates to achieve high contact angles. Glycerol is chosen for this kind of experiments due to its high viscosity (limiting droplet shape deformations due to thermal fluctuations and air currents), and to its low vapor pressure (less than 0.1 Pa at 20°C), thus avoiding droplet size variation through evaporation over the duration of the experiment. The generated droplets radii were in the range of hundreds of micrometers; created by flowing Glycerol through small syringe needles. Droplets of this size may be subjected to residual torques and undergo rotation, if they were levitated, for instance by means of an acoustic levitator [30]. This was avoided by choosing the technique of supporting them on hydrophobic surfaces. All the experiments have been done in normal room conditions as far as temperature and humidity are concerned.

For the sake of high quality factors, the sphericity of the droplet resonator is an important issue, especially in the equatorial region, in which the coupled wave is confined. Two effects are important to assure nearly-perfect sphericity in the equatorial plane: the Bond number, and the contact angle of the droplet on the surface.

The Bond number $B_o = \rho g R_0^2 / \sigma$ defines whether gravity forces affect the droplet spherical shape (ρ being the density of the fluid, g the gravitational acceleration, R_0 the droplet radius, and σ its surface tension). In our case, $B_o < 0.4$ in all experiments, implying little, but not completely negligible, deformation of the droplet due to its own weight, as will be confirmed later. The contact angle Θ on the substrate is a very important indicator of the equatorial sphericity as well: low contact angles lead to a highly deformed shape (possibly even without an equatorial plane if $\Theta < 90°$), thus preventing the wave from resonating inside

the cavity and leading to a very small quality factor Q. Ideally, a nearly-perfect spherical shape is desired, which is obtained for contact angles approaching 180°. In our experiments we used a Teflon-coated black silicon nanostructured surface to obtain high droplet contact angles, following prior reports that micro- and nano-structured silicon can exhibit hydrophobic surface characteristics [39]. Black silicon, consisting of needle-like structures spaced 200 to 400 nm apart (SEM image in Fig. 5.8), is a material that is formed spontaneously during certain cryogenic plasma etching processes, and represents a cost-effective way of obtaining large-area nanostructured surfaces. Due to its light trapping capability and the resulting low reflectivity, such surfaces look black to the human eyes, hence their name of Black Silicon [31, 32].

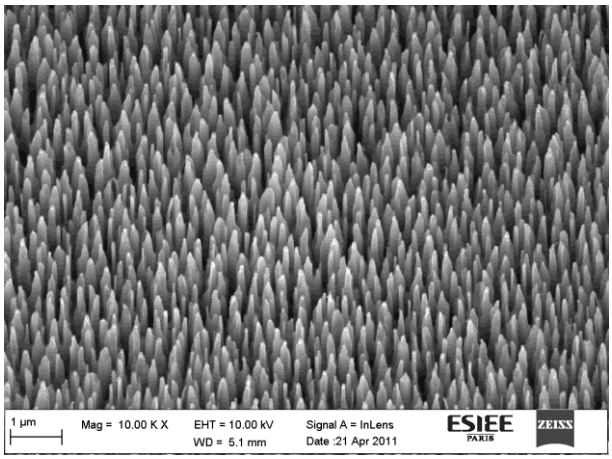

Fig. 5.8 SEM image of black Si obtained by a cryogenic DRIE process.

Black silicon samples were obtained from p-type B-doped, (100) oriented, polished silicon wafers (resistivity 1-20 Ω.cm). The wafers were subjected to SF_6/O_2 plasma etching with cryogenic process at -120 °C; such wafers were exposed to the plasma for about 10 minutes to obtain the required texture. SF_6 gas generates F* radicals for chemical etching of silicon leading to volatile SiF_4 whereas O_2 produces O* radicals leading to sidewall passivation with $Si_xO_yF_z$. Typical conditions of the inductively-coupled plasma were a power of 1000 W, a bias source of 30 V, and a chamber pressure of 1.5 Pa using an ALCATEL 601 system; the gases employed for the process were SF_6/O_2 (flow ratio of 20/1). After the black silicon formation step, the samples were exposed to a C_4F_8 plasma passivation step, which resulted in a 100 nm-thick Teflon-like layer deposited on the nanostructured black silicon substrate.

The liquid used to form the droplets was anhydrous Glycerol (purity > 99%, purchased from Merck Chemicals). The contact angles and the vertical and horizontal axes lengths were

recorded from side-view images. Fig. 5.9 represents the contact angle versus the droplet diameter. It slightly increases with the droplet size, but maintains values larger than 130° throughout the experiments, within a suitable range to support WGM resonances in the equatorial plan. The error bars are taken by ± 3°, as the typical value of error in measuring the contact angles.

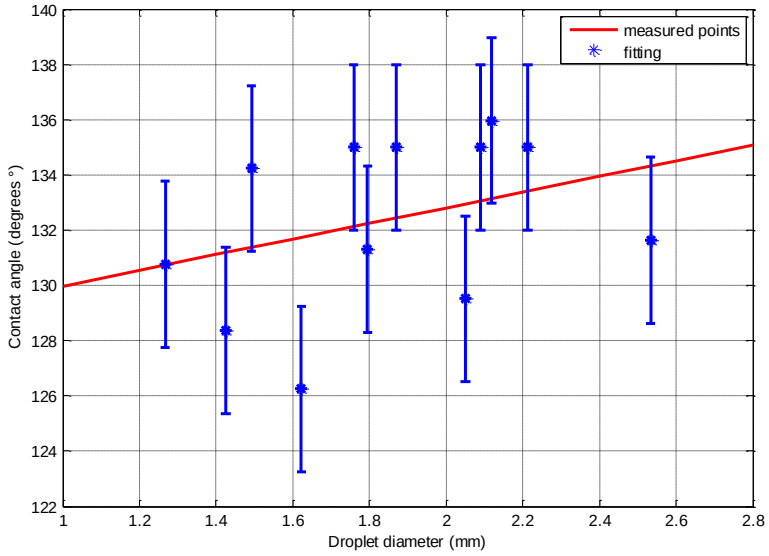

Fig. 5.9 Contact angle for different Glycerol droplet sizes mounted on the black silicon substrate.

Fig. 5.10 (a) captures the effect of increasing droplet size on its sphericity, represented as the ratio between the double upper half lengths of the vertical axis (2H) over the droplet diameter (D). The error bars are taken by 2×0.031/2.5335 as the value 0.031 mm is the error in determining the exact altitude of the equator to which the upper half vertical distance is determined (starting from the droplets upper pole) to get the value of H in the case of the largest droplet of diameter 2.5335 mm. As the ratio 2H/D is less than 100%, the droplets have a slight pancake-like deformation, which increases with the droplet size as expected from the orders of magnitude of the Bond number. Nevertheless, the horizontal equatorial plan can still provide a nearly perfect circle as can be seen in Fig. 5.10 (b), which shows top view images for the Glycerol droplets in the two extreme cases considered in the experimental study of droplet sphericity: the 1.27 mm and the 2.53 mm diameters. The diameter is visibly the same for both the vertical and the horizontal axes of the photo, which indicates a circular path capable of attaining high quality factors for a wave successfully confined within the equatorial plan, or within its neighborhood.

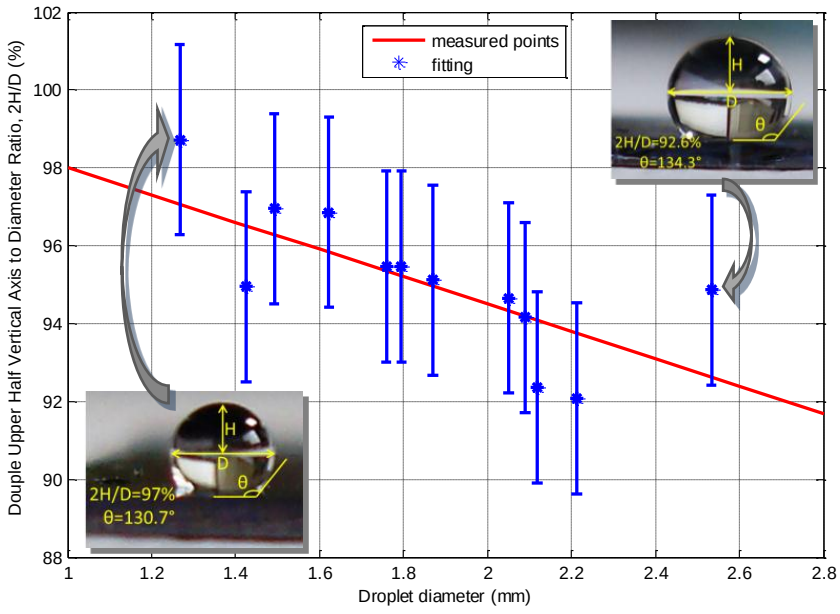

(a)

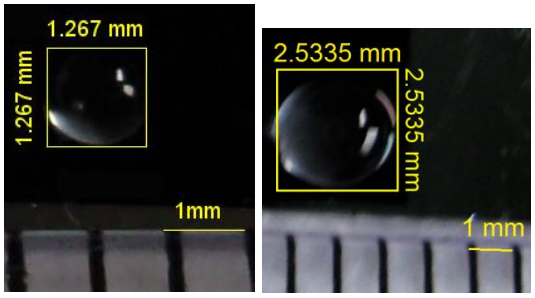

(b)

Fig. 5.10 (a) Shape Ratio 2H/D for different Glycerol droplet sizes mounted on the black silicon substrate. The two insets are images of the droplet in the two extreme cases, indicating the axes ratio and the contact angle geometry. (b) Top view for the Glycerol droplets in the smallest and the largest size, which indicates in both cases a circular path in the equatorial plan.

5.6.2 Experimental Validation of WGM excitation

An optical setup for injecting the Gaussian beam into a glycerol droplet and measuring the spectral response has been prepared for testing the proposed coupling method. The input light is produced by a source covering the near infrared (NIR) wavelength range around λ = 1550 nm, injected and collected through single mode lensed fibers with beam waist radii of 9 or 25 μm. Fig. 5.11 shows a photograph for the real droplet resonator on its supporting hydrophobic substrate and the injecting and collecting fibers. The red gluing light is the visible light coupled with the NIR input, used for the alignment purposes only.

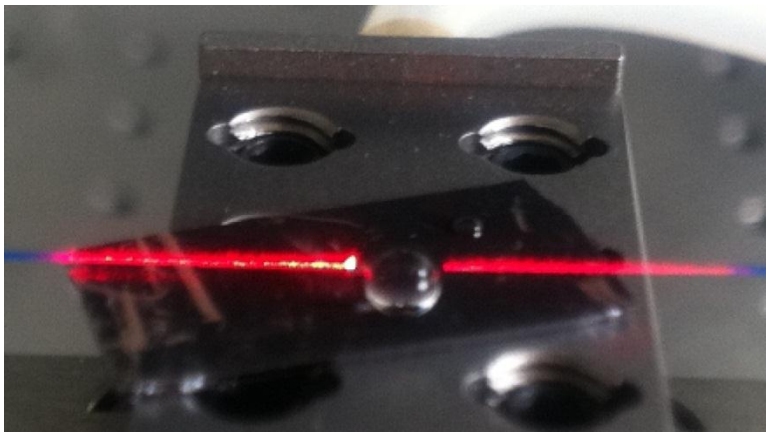

Fig. 5.11 A photograph for the droplet resonator on its substrate and the lensed fiber pair used to inject and collect the light.

The NIR is our spectral range of interest, but the visible red light can also be coupled into the resonator as shown in Fig. 5.12, which allows visualization of the WGM circulating near the perimeter edge of the sphere as a red ring.

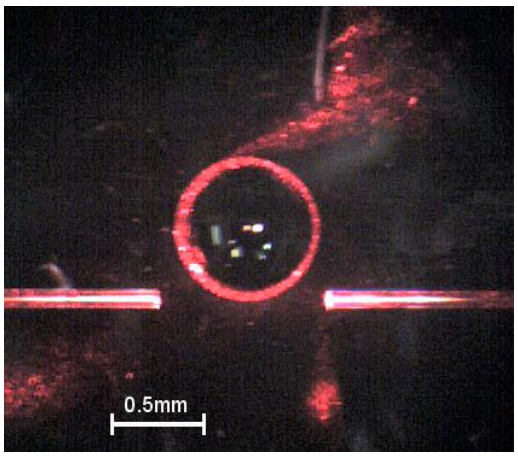

Fig. 5.12 Experimental demonstration of Whispering Gallery Mode excited by a Gaussian beam using a set of lensed fibers having a beam waist radius of 25 µm, within a Glycerol droplet that has a diameter of about 0.86 mm. Though measurements were performed using infrared light; visible in the figure is light from a secondary red laser used for alignment.

The transmitted light intensity is recorded either using an optical spectrum analyzer while illuminating the sample with SLED, or an optical power meter while using a tunable laser as a source. In some experiments, the spectrum shows high noise as can be noticed from Fig. 5.13. The source of this noise can be attributed to several factors:

1- The radiation pressures exerted by the resonating optical power inside the cavity that may cause mechanical changes in the cavity dimensions [40, 41].
2- Thermally induced noise due to light dissipation caused by the liquid absorption losses.

3- Instrumental and environmental noise which is highly pronounced in such low power levels.

Fast Fourier Transform (FFT) is done to the data recorded from the measured spectrum to verify the observations of the optical modes despite the high noise. But to be able to measure the quality factor from the spectral peaks, signal processing has to be done previously on the recorded raw data to filter the noise.

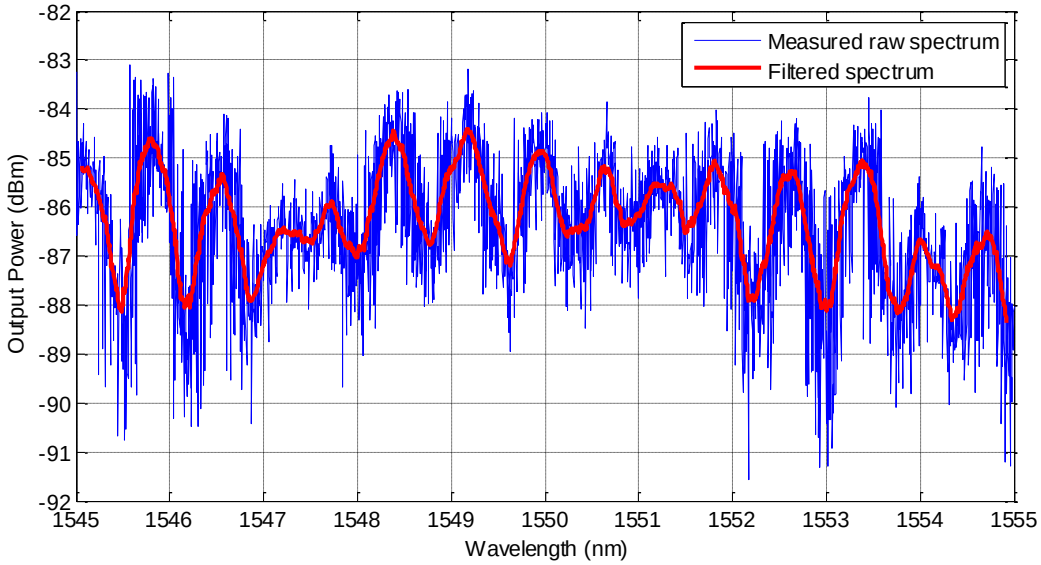

Fig. 5.13 The transmission spectrum recorded from a droplet resonator which shows high power fluctuations.

The spectral response corresponding to the input light wavelength range is recorded for droplets with diameters of about 0.78 and 1.16 mm. Due to the selective coupling of the resonant modes into the resonator, the response exhibit drop peaks at certain wavelengths, as shown in Fig. 5.14. The quality factor depends on the droplet size, and it increases as expected with its diameter, as can be noted from comparing the values in Fig. 5.14(a), and Fig. 5.14 (b). In the range of the sizes studied, quality factors from 3.9×10^3 (for the 0.78 mm droplet) to 6.7×10^3 (for the 1.16 mm one) could be reached.

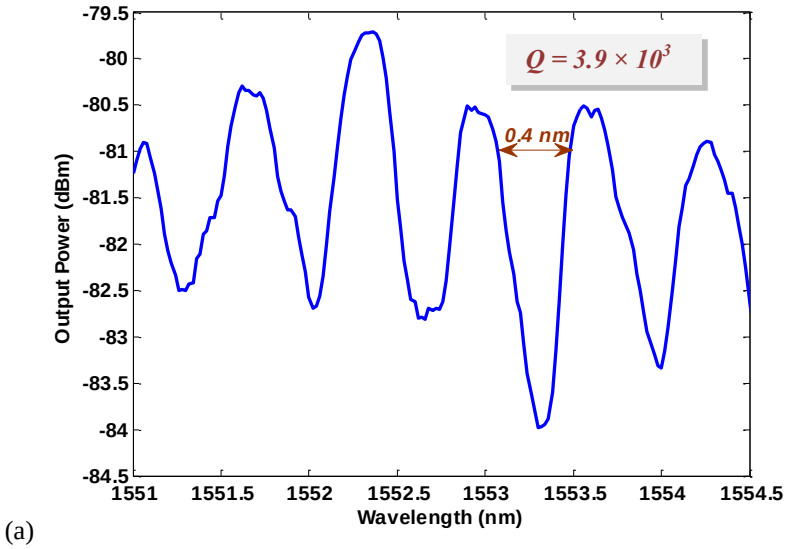

(a)

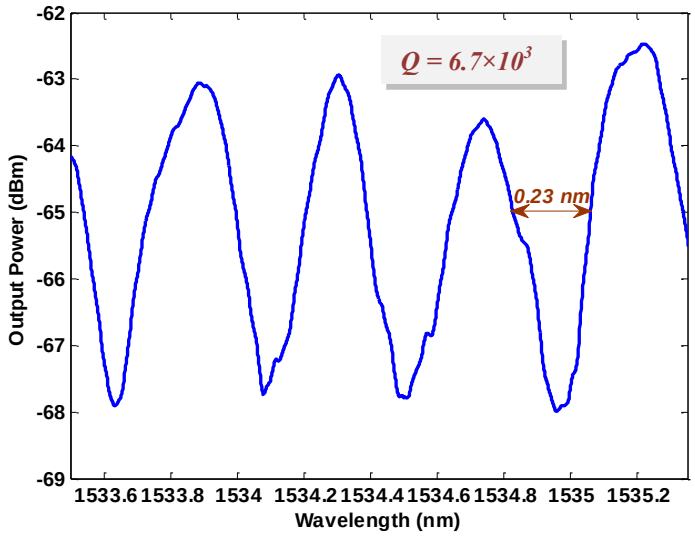

(b)

Fig. 5.14 Output power spectrum for: (a) The 0.78 mm diameter droplet. (b) The 1.16 mm diameter droplet; excited by a Gaussian beam with a beam waist radius of 9 µm. The 3 dB bandwidths are 0.4 nm and 0.23 nm, achieving total quality factors of 3.9×10^3 and 6.7×10^3, respectively.

As can be noticed from Fig. 5.15, which shows the FFT for the spectrum in Fig. 5.14(b), the optical path length is 5.36 mm that gives a droplet diameter of 1.16 mm assuming a circular path within the equatorial plane and noting that the used substance for the resonator -which is Glycerol in this case- has a refractive index (n_s) of 1.46. This is almost the same diameter value measured from magnified images of the droplet, which is evaluated to be around 1.143 mm. The higher value found optically suggests that the optical path might deviate a little bit from a the perfect circle, as expected from the ray optics representation of total internal reflection within a droplet supporting WGMs

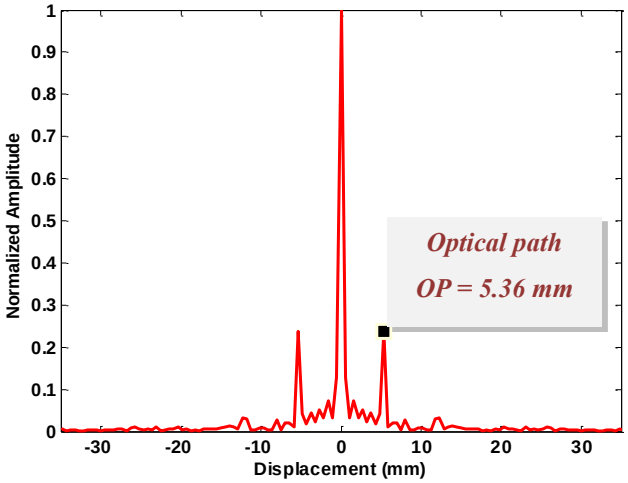

Fig. 5.15 FFT of the spectral response for the 1.16 mm diameter droplet.

5.7 Quality Factor Considerations

The quality factor is affected by losses in the system, some of which being from the resonator itself. Those internal losses set a certain internal quality factor Q_{in} for that resonator: $Q_{\text{in}}^{-1} = Q_{rad}^{-1} + Q_{ss}^{-1} + Q_{cont}^{-1} + Q_{mat}^{-1}$, where Q_{rad}^{-1} denotes radiative losses of the WGMs due to the curvature of the spherical guiding boundaries in the direction of propagation; Q_{ss}^{-1}, the scattering losses on the surface inhomogeneity; Q_{cont}^{-1}, losses introduced by surface contaminants; and Q_{mat}^{-1}, the material losses [42]. On the other hand, the loss due to coupling the light into the resonator sets a certain external or coupling quality factor Q_c. The total quality factor Q_{total} depends on both the intrinsic and coupling quality factors [23, 34, 43]: $Q_{total}^{-1} = Q_c^{-1} + Q_{\text{in}}^{-1}$ and is smaller than either one. Hence, we have different coupling regimes depending on the dominating loss processes. The coupling regime can be identified as under-coupled ($Q_{in} < Q_c$), critically coupled ($Q_c = Q_{in} = 2\,Q_{total}$) or over-coupled ($Q_{in} > Q_c$). At small radii microspheres, Q_{rad} is small and hence it is the dominant, as the WGM radiation loss is high due to the large curvature in the resonator. But it increases very fast as the sphere size increases until it becomes ineffective at radii in the range of few tens of micrometers and more [21, 42]. So, for millimeter diameter spheres, the overall quality factor is limited by either the coupling loss or the material and/or scattering losses.

In our case, we believe that the limit arises from the material loss as the light absorption of Glycerol is non-negligible. The coupling quality factor estimation gives extremely high-Q values ($Q_c > 10^{17}$) as will be demonstrated in the following section. While

glycerol is a very suitable candidate for our experiment since its viscosity is high, its evaporation rate is low, and its contact angle to the substrate is relatively large, but it possesses non-negligible absorption in the NIR range, with an absorption coefficient α of about 1.1 to 1.36 mm^{-1} at the wavelength from 1530 to 1570 nm [44]; which limits the material quality factor Q_{mat} to about 5.5 × 10^3 if estimated by the bulk losses as $Q_{mat} = 2\pi n_s / \alpha\lambda$. This value is for bulk losses, but in a microsphere, it may actually be slightly higher due to the bulk scattering losses suppression that takes place inside microspheres. This lower loss is estimated when we take into consideration the modifications in deriving the attenuation for closed resonant circulating waves such as WGMs, from that of plane waves in the bulk medium [45].

5.8 Analytical Expression for Gaussian Beam Coupling into a Sphere Resonator

As we have seen, the total quality factor Q_{total} in governed by the intrinsic and coupling quality factors. Precise analysis of the contribution of each Q component is important. While it is essential to have a sufficient coupling inside the droplet to excite the modes, the trapped photons tend to leave the resonator sooner as the coupling is increased, thus increasing the losses and decreasing Q_c [43]. Hence, we set a model for calculating Q_c in the case of coupling light into a sphere with radius R_0 by means of a GB of half beam waist radius W_0. Fig. 5.16 (a) shows a schematic for the cross-sectional view of our system geometry when the Gaussian beam waist is located at the droplet edge.

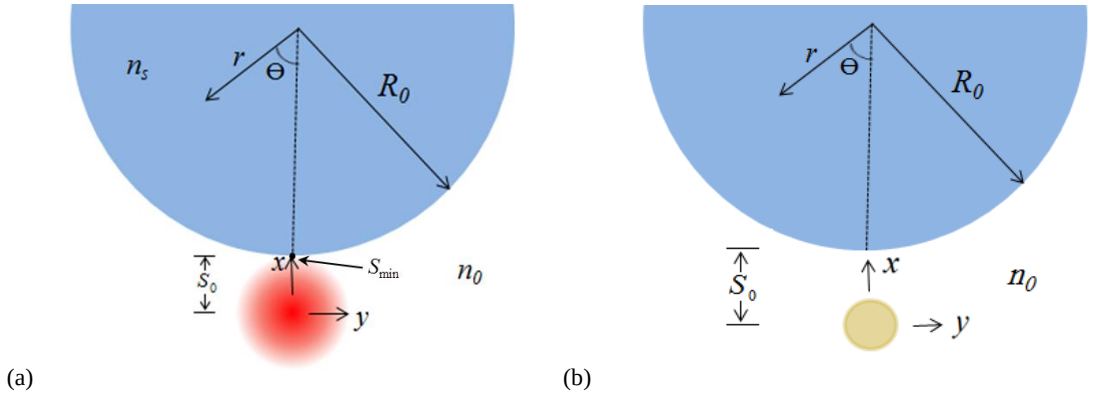

Fig. 5.16 (a) Cross-sectional view of the geometry of the excitation Gaussian beam coupled to the sphere. (b) Cross-sectional view of the geometry of a tapered fiber coupled to a sphere [Adapted from 21].

Different parameters that may affect the coupling are illustrated, like the separation distance S_0 between the resonator and the beam, the sphere radius R_0, the refractive index of the resonator's material n_s. Calculation of the coupling quality factor Q_c is derived here following the same steps as in reference 21 (whose case is illustrated in Fig. 5.16 (a) Cross-sectional view of the geometry of the excitation Gaussian beam coupled to the sphere. (b) Cross-sectional view of the geometry of a tapered fiber coupled to a sphere [Adapted from 21].), but replacing the tapered fiber evanescent mode by a Gaussian beam of the following form:

$$E(x,y,z) = E_0 \frac{W_0}{W(z)} e^{-\frac{x^2+y^2}{W^2(z)}} e^{-ikz-ik\frac{x^2+y^2}{2R(z)}+i\eta(z)} \tag{5.4}$$

Note that, the Gaussian beam form is a special case from the Hermite-Gaussian beams family that was introduced earlier in chapter 2, where both lateral mode orders m, $n = 0$. The parameter definitions are the same as given by equations (2.22) to (2.25). But here they represent the parameters of the input beam from the lensed fiber used to excite the droplet resonator, not the resonance modes like the earlier case. Here, the resonance modes inside the droplet spherical resonator are given by the equations (5.1) to (5.3).

The calculation steps are as following: First we get the interaction strength $\kappa(S_{\min})$ at the point of minimum separation S_0 between the sphere and the beam. It is given by the overlap integral:

$$\kappa(S_{\min}) = \frac{k}{2}\int_x\int_y \left(n_s^{\,2} - n_0^{\,2}\right) E\ \Psi_{\ell,m,n}\ dxdy \tag{5.5}$$

Then, we integrate over the propagation coordinate z, taking into consideration that the separation S_0 now becomes variable along z with the function $S(z)$. After a rigorous mathematical treatment, detailed in the Appendix, one finally obtains the coupling κ between the WGM in the region near the equatorial plan (small θ angle) with a GB, in the following form:

$$\kappa = \frac{k}{2}\left(n_s^{\,2} - n_0^{\,2}\right) N_s W_0 \frac{R_0}{\sqrt{m}} H_N(0) \int_z \frac{E_0(z)}{W(z)} \sqrt{\frac{2\pi}{q(z)+1}} \cdot \left|\frac{q(z)-1}{q(z)+1}\right|^{\frac{N}{2}}$$
$$\cdot \left[B\sqrt{\frac{\pi R_0^{\,2}}{2mq(z)}} \left(1 - erf\left(\sqrt{\frac{mq(z)}{2R_0^{\,2}}} S(z)\right)\right) - \frac{R_0^{\,2}}{mq(z)} \cdot De^{-\frac{m}{2R_0^{\,2}} q(z).S^2(z)} \right] \cdot e^{-i(\Delta\beta z - \xi(z))} dz \tag{5.6}$$

where

$$B = (1+\ell)\, j_\ell(kn_s R_0) - R_0 kn_s\, j_{\ell+1}(kn_s R_0)$$
$$D = \frac{\ell}{R_0}\, j_\ell(kn_s R_0) - kn_s\, j_{\ell+1}(kn_s R_0)$$
$$\Delta\beta = k - \frac{m}{R_0}$$

This integral is solved numerically in a region near the sphere edge. Once the coupling κ is obtained, one can accordingly calculate the coupling quality factor Q_c from

$$Q_c = m\pi/\kappa^2 \tag{5.7}$$

The previous derived formula for Q_c is used to examine the effect of the different coupling parameters, like separation distance S_0 between the resonator and the beam, the sphere radius R_0, the refractive index of the resonator material n_s. Among the coupling conditions, the most effective parameter is the separation distance S_0. If it is too large, there might be no coupling at all as demonstrated in Fig. 5.6 Amplitude of the simulated electromagnetic field at the vicinity of a 1.5 μm droplet, n=1.47 excited by a Gaussian beam as the optical axis is located at different distances *S0* from the dielectric sphere expressed in units of the beam waist *W0*: (a) *S0* = 4W0; (b) *S0* = 2W0, at resonant wavelength λ = 1385 *nm* of a Whispering Gallery Mode.; if it is too close (less than about 1.5**W0*), the GB may get deformed. In Fig. 5.17, the behavior of the coupling quality factor Q_c is calculated for a GB whose beam waist radius W_0 is 9 μm in (a) and 25 μm in (b), exciting droplets of radii 390 μm and 580 μm (corresponding to the radii diameters of the actual droplets used in the experimental measurements introduced in section 5.6.2) as they are moved away from the beam axis, starting from 1.5**W0* to 2.5**W0*. In all cases, the nearest resonances to an exciting input wavelength of 1550 *nm* are the ones involved in calculating the Q_c values. The

integration on z for equation (5.6) is limited to ±0.14 R_0; which corresponds to a small angle of ±8°.

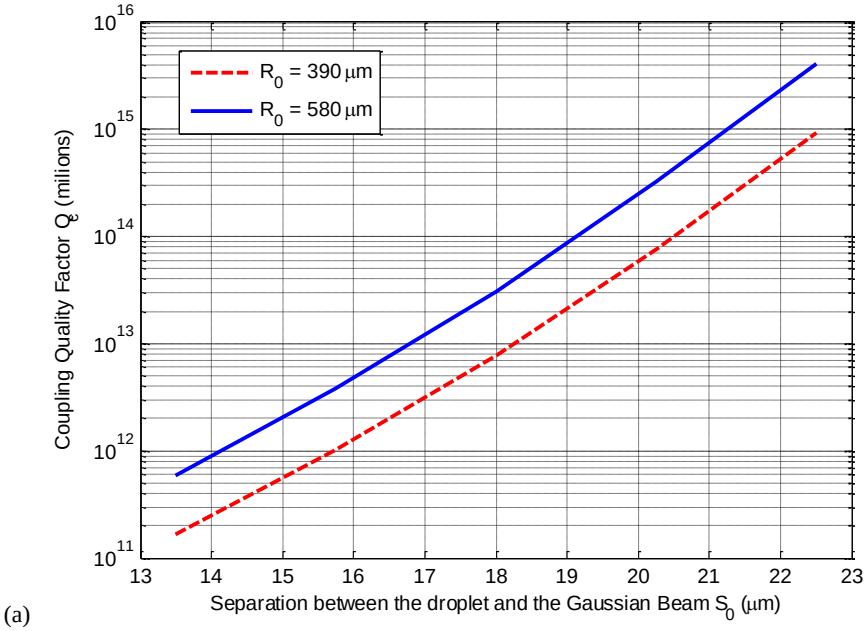

(a)

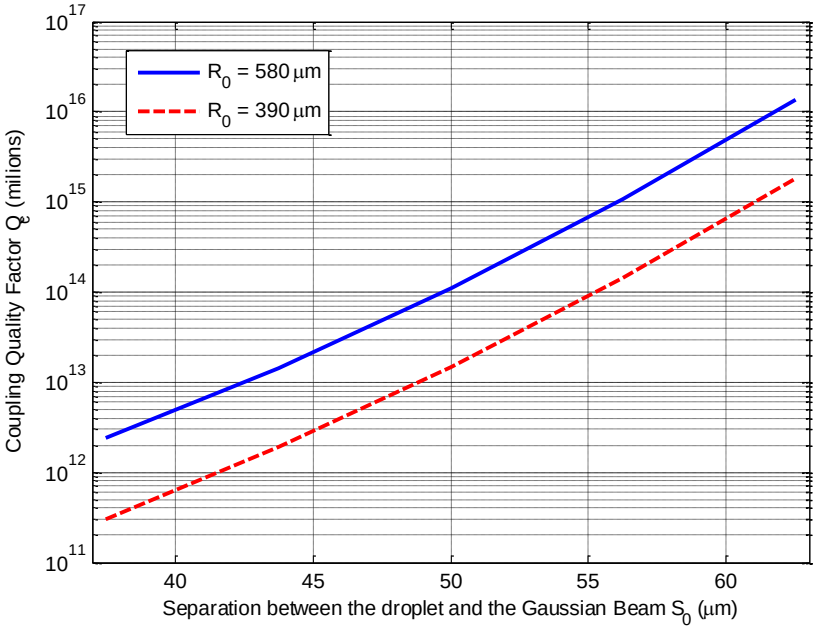

(b)

Fig. 5.17 Coupling Quality Factor Q_c at different separation distance S_0 for Glycerol droplets with radii 580 µm and 390 µm; using beam waist radii: (a) W_0 =9 µm, (b) W_0 = 25 µm.

One can first notice that Q_c increases due to the decreasing of the coupling strength as the resonator is moved away from the beam. Also it is apparent that larger droplet radii may lead to larger quality factors. Note that changing the material refractive index has the same effect as changing the radius because the optical path length is the multiplication of both the physical length and the refractive index. One can also notice from Fig. 5.17 the extremely

high values of Q_c , in excess of 10^{16}, which suggests that the coupling conditions will not be the limiting factor, as long as the intrinsic quality factor does not reach such levels. This is actually the case for the resonators dimensions under consideration in this study. Indeed, for a 1.5 μm radius droplet, Q_c is typically about 10^{23}, but for no use since the total quality factor is limited by Q_{in} of only 10, calculated from the following whispering gallery intrinsic loss expression [21], dominated in this case by radiation losses, assuming negligible other kinds of losses.

$$Q_{rad} = \frac{\ell^2 n_s}{k^3 c\varepsilon_0 N_s{}^2 n_0{}^2 R_0{}^5 Z_0}.\left[n_0 \left(\frac{\pi}{\gamma_1}\right)^{1/4} j_\ell(kn_s R_0)\, j_{\ell+1}(kn_0 R_0) - n_s \left(\frac{\pi}{\gamma_2}\right)^{1/4} j_{\ell-1}(kn_s R_0)\, j_\ell(kn_0 R_0) \right]^{-2} \tag{5.8}$$

where

$$\gamma_1 = \ell - \frac{1}{2} - kn_0 R_0 \frac{j_\ell(kn_0 R_0)}{j_{\ell-1}(kn_0 R_0)} + \frac{(kn_0 R_0)^2}{\ell}$$

$$\gamma_2 = \ell + \frac{1}{2} - kn_0 R_0 \frac{j_{\ell+1}(kn_0 R_0)}{j_\ell(kn_0 R_0)} + \frac{(kn_0 R_0)^2}{\ell} ,$$

and c is the vacuum speed of light, ε_0 is the permittivity of free space, $Z_0 \approx 377\ \Omega$ is the impedance of free space.

For a droplet with radius in the millimeter range, Q_{rad} is above 10^{11} [21, 42], still leaving enough margin for exciting resonant modes of very high quality factors. It is worth mentioning that the extremely high values of Q_c found through this study also suggests that in principle, the coupling method through Gaussian beams might be suitable for reaching very high quality factors, at least up to 10^{17}, as wide degrees-of-freedom are available in terms of coupling conditions and sphere dimensions.

5.9 Conclusion

The method for direct on-chip light coupling into millimeter-size and sub-millimiter size droplet optical resonators using a free-space Gaussian beam has been validated and discussed. This method has many advantages over the conventional coupling methods like simplicity, easier coupling, low risk of collapsing the droplet resonator, and coupling distance adjustment in the range of microns.

Quality factors up to 6.7×10^3 were experimentally observed in the near infrared range, the main limitation being internal material absorption of glycerol. An analytical model for calculating the coupling quality factor in this method has been derived for the purpose of evaluating the ultimate limits of the proposed coupling method. The effects of the different types of losses on the total quality factor at the different coupling regimes and for different droplet sizes have been discussed. The effects of geometrical parameters on the coupling quality factor have also been analytically investigated. The proposed free-space coupling method has high potential to be reused on non-absorbing liquid droplet resonators (in which case significantly higher quality factors can be expected due to the diminished absorption) as well as on solid-state spherical and disk resonators that exhibit much higher intrinsic quality factors.

As finding a suitable liquid regarding the optical and physical properties may be hard to find and limits the practical applications; a hollow glass sphere with thin wall could be used to contain the liquid to be tested or even the active material in the case of a liquid core laser, as an extinction of the current work done on ring and tubular resonators [46-48].

5.10 References for chapter 5

[1] S. Lin, E. Schonbrun, and K. Crozier, "Optical Manipulation with Planar Silicon Microring Resonators," Nano Lett., vol. 10, pp. 2408-2411, 2010.

[2] M. Rosenblit, Y. Japha, P. Horak, and R. Folman, "Simultaneous optical trapping and detection of atoms by microdisk resonators," Phys. Rev. A, vol. 73, pp. 063805-12, 2006.

[3] J. Wang, T. Zhan, G. Huang, P. K. Chu, and Y. Mei, "Optical microcavities with tubular geometry: properties and applications," Laser Photon. Rev., published online: 26 Jun. 2013, DOI: 10.1002/lpor.201300040.

[4] S. Arnold, D. Keng, S. I. Shopova, S. Holler, W. Zurawsky, and F. Vollmer, "Whispering gallery mode carousel – a photonic mechanism for enhanced nanoparticle detection in biosensing," Opt. Express, vol. 17, pp. 6230-6238, 2009.

[5] N. Gaber, M. Malak, X. Yuan, K. N. Nguyen, P. Basset, E. Richalot, D. Angelescua, and T. Bourouina, "On the free-space Gaussian beam coupling to droplet optical resonators," Lab Chip, vol. 13, pp. 826-833, 2013.

[6] P. Féron, "Whispering Gallery Mode Lasers in Erbium doped fluoride glasses," Ann. Fond. Louis de Broglie, vol. 29, pp. 317-329, 2004.

[7] V. A. B. Quiñones, G. Huang, J. D. Plumhof, S. Kiravittaya, A. Rastelli, Y. Mei, and O. G. Schmidt "Optical resonance tuning and polarization of thin-walled tubular microcavities," Opt. Lett., vol. 34, pp. 2345-2347, 2009.

[8] S. I. Shopova, I. M. White, Y. Sun, H. Zhu, X. Fan, G. Frye-Mason, A. Thompson, and S. Ja, "On-column micro gas chromatography detection with capillary-based optical ring resonators," Anal. Chem., vol. 80, pp. 2232-2238, 2008.

[9] K. H. Kim, G. Bahl, W. Lee, J. Liu, M. Tomes, X. Fan, and T. Carmon, "Cavity optomechanics on a microfluidic resonator with water and viscous liquids," Light: Science & Applications, vol. 2, pp. e110, 2013.

[10] L. Y. M. Tobing, and P. Dumon, *Fundamental Principles of Operation and Notes on Fabrication of Photonic Microresonators*, Photonic Microresonator Research and Applications, Springer Series in Optical Sciences, vol. 156, 2010, chapter 1.

[11] A. B. Matsko and V. S. Ilchenko, "Optical Resonators With Whispering-Gallery Modes—Part I: Basics," J. Sel. Top. Quantum Electron., vol. 12, pp. 3-14, 2006.

[12] M. Himmelhaus, "Whispering gallery mode-microlasers embedded into a dense medium," Opt. Commun., vol. 284, pp. 4843-4846, 2011.

[13] H. Taniguchi, H. Tomisawa and R. Nagashima, “Morphology-Dependent Multiorder Raman Spectra from a Liquid Glycerol Droplet by Low-Power He-Ne Laser Pumping,” Jpn. J. Appl. Phys., 1993, 32, L1621.

[14] A. Biswas, H. Latifi, R. L. Armstrong and R. G. Pinnick, “Double-resonance stimulated Raman scattering from optically levitated glycerol droplets,” Phys. Rev. A, 1989, 40, 7413.

[15] S. M. Spillane, T. J. Kippenberg, and K. J. Vahala, “Ultralow-threshold Raman laser using a spherical dielectric microcavity,” Nature, vol. 415, pp. 621-623, 2002.

[16] V. S. Ilchenko and A. B. Matsko, “Optical Resonators With Whispering-Gallery Modes—Part II: Applications,” J. Sel. Top. Quantum Electron., vol. 12, pp. 15-32, 2006.

[17] H. K. Hunta, and A. M. Armani, “Label-free biological and chemical sensors,” Nanoscale, vol. 2, pp. 1544-1559, 2010.

[18] S. Selimovic and A. Khademhosseini, “Research highlights,” Lab Chip, vol. 12, pp. 503-505, 2012.

[19] F. Vollmer, S. Arnold, and D. Keng, “Single virus detection from the reactive shift of a whispering-gallery mode,” Proc. Natl. Acad. Sci. U.S.A., vol. 105, pp. 20701- 20704, 2008.

[20] J. P. Barton, “Effects of surface perturbations on the quality and the focused-beam excitation of microsphere resonance,” J. Opt. Soc. Am. A, vol. 16, pp. 1974-1980, 1999.

[21] B. E. Little, J. P. Laine, and H. A. Haus, “Analytic Theory of Coupling from Tapered Fibers and Half-Blocks into Microsphere Resonators,” J. Lightwave Technol., vol. 17, pp. 704-715, 1999.

[22] Y. F. Yu, T. Bourouina, C. S. Lim, M. K. Chin, A. Q. Liu, “High Sensitivity Sessile Droplet Resonator for Low Concentration Protein. Detection,” μTAS2008, San Diego, USA, pp. 302-304, 2008.

[23] Y. F. Yu, V. Kanna, T. Bourouina, S. H. Ng, P. H. Yap, and A. Q. Liu, "An on-chip glass sphere resonator for label free detection", Proc. 23rd IEEE Int. Conf. Micro Electro Mech. Syst., pp. 831, 2010.

[24] Y. F. Yu, T. Bourouina, S. H. Ng, P. H. Yap, A. Q. Liu, “A Single Droplet Carrier with Optical Detector”, μTAS2009, Jeju, Korea, pp. 979-981, 2009.

[25] A. Chiba, H. Fujiwara, J. Hotta, S. Takeuchi, and K. Sasaki, “Fano resonance in a multimode tapered fiber coupled with a microspherical Cavity” Appl. Phys. Lett., vol. 86, 261106 1-3, 2005.

[26] R. K. Chang and Y-L Pan, "Linear and non-linear spectroscopy of microparticles: Basic principles, new techniques and promising applications," Faraday Discuss., vol. 137, pp. 9, 2008.

[27] E. E. M. Khaled, S. C. Hill, P. W. Barber and D. Q. Chowdhury, "Near-resonance excitation of dielectric spheres with plane waves and off-axis Gaussian beams," Appl. Opt., vol. 31, pp. 1166-1169, 1992.

[28] R. Sharma, J. P. Mondia, J. Schäfer, Z. H. Lu and L. J. Wang, "Effect of evaporation on blinking properties of the glycerol microdrop Raman laser," J. Appl. Phys., 2009, 105, 113104-1-113104-4.

[29] R. M. Sayer, R. D. B. Gatherer, R. J. J. Gilham, and J. P. Reid, "Cavity enhanced droplet spectroscopy: Principles, perspectives and prospects," Phys. Chem. Chem. Phys., vol. 6, pp. 474-487, 2004.

[30] A. Biswas, R. G. Pinnick, J.-G. Xie, T. E. Ruekgauer, and R. L. Armstrong "Observations of stimulated Raman scattering and laser-induced breakdown in millimeter-sized droplets," Opt. Lett., vol. 17, pp. 1569-1571, 1992.

[31] K. N. Nguyen, D. Abi-Saab, P. Basset, E. Richalot, F. Marty, D. Angelescu, Y. Leprince-Wang, and T. Bourouina, "Black silicon with sub-percent reflectivity: Influence of the 3D texturization geometry," Proc. 16th Int. Conf. Solid-State Sens.,Actuators Microsyst., Transducers, Beijing, China, pp. 354-357, 2011.

[32] K. N. Nguyen, D. Abi-Saab, P. Basset, E. Richalot, M. Malak, N. Pavy, F. Flourens, F. Marty, D. Angelescu, Y. Leprince-Wang, and T. Bourouina, "Study of black silicon obtained by cryogenic plasma etching: approach to achieve the hot spot of a thermoelectric energy harvester," Microsyst. Technol., vol. 18, pp. 1807-1814, 2012.

[33] M. L. Gorodetsky, V. S. Ilchenko, "High-Q optical whispering-gallery microresonators: precession approach for spherical mode analysis and emission patterns with prism couplers," Opt. Commun., vol. 113, pp. 133-143, 1994.

[34] M. L. Gorodetsky, and V. S. Ilchenko, "Optical microsphere resonators: optimal coupling to high-Q whispering-gallery modes," J. Opt. Soc. Am. B., vol. 16, pp. 147-154, 1999.

[35] S. M. Spillane, T. J. Kippenberg, O. J. Painter, and K. J. Vahala, "Ideality in a Fiber-Taper-Coupled Microresonator System for Application to Cavity Quantum Electrodynamics," Phys. Rev. Lett., vol. 91, pp. 043902-1-043902-4, 2003.

[36] H. C. van de Hulst, *Light Scattering by Small Particles*, Dover Publications, New York, 1981.

[37] H. B. Lin, J. D. Eversole and A. J. Campillo, and J. P. Barton "Excitation localization principle for spherical microcavities," Opt. Lett., vol. 23, pp. 1921-1923, 1998.

[38] M. Gomilšek, *Whispering gallery modes*, Seminar, university of Ljubljana, 2011.

[39] T. Baldacchini, J. E. Carey, M. Zhou, and E. Mazur, "Superhydrophobic surfaces prepared by microstructuring of silicon using a femtosecond laser," Langmuir, vol. 22, pp. 4917-4919, 2006.

[40] Young-Shin Parkv and Hailin Wangv "Radiation pressure driven mechanical oscillation in deformed silica microspheres via free-space evanescent excitationv" Opt. Express, vol. 15, pp. 16471-16477, 2007.

[41] T. J. Kippenberg, and K.J. Vahalav "cavity optomechanics," Opt. Express, vol. 15, pp. 17172-17205, 2007.

[42] M. L. Gorodetsky, A. A. Savchenkov, and V. S. Ilchenko, "Ultimate Q of optical microsphere resonators," Opt. Lett., vol. 21, pp. 453, 1996.

[43] F. Vanier, C. La Mela, A. Hayat, and Y-A. Peter, "Intrinsic quality factor determination in whispering gallery mode microcavities using a single Stokes parameters measurement," Opt. Express, vol. 19, pp. 23544-23553, 2011.

[44] K. Izutsu, Y. Hiyama, C. Yomota and T. Kawanishi, "Near-Infrared Analysis of Hydrogen-Bonding in Glass- and Rubber-State Amorphous Saccharide Solids," AAPS PharmSciTech., vol.10, pp. 524-529, 2009.

[45] M. L. Gorodetsky, A. D. Pryamikov, and V. S. Ilchenko, "Rayleigh scattering in high-Q microspheres," J. Opt. Soc. Am. B, vol. 17, pp. 1051-1057, 2000.

[46] G. Bahl, K. H Kim, W. Lee, J. Liu, X. Fan, and T. Carmon, "Brillouin cavity optomechanics with microfluidic devices," Nat. Commun., published online: 7 Jun. 2013, DOI: 10.1038/ncomms2994.

[47] S. I. Shopova, H. Zhou, X. Fan, and P. Zhang, "Optofluidic ring resonator based dye laser," Appl. Phys. Lett., vol. 90, pp. 221101-1-221101-3, 2007.

[48] H.Zhu, I. M. White, J. D. Suter, M. Zourob, and X. Fan, "Integrated Refractive Index Optical Ring Resonator Detector for Capillary Electrophoresis," Anal. Chem., vol. 79, pp. 930-937, 2007.

CHAPTER (6)

CONCLUSION AND PERSPECTIVES

6.1 Thesis Conclusion

In this PhD dissertation, different types of optical resonators have been studied with the ultimate goal of realizing optofluidic lab-on-a-chip resonant devices, with applications for sensing and trapping at rather reduced costs. Thereby, we presented the design, analytical and numerical modelling, and experimental measurements for different architectures of optical micro-cavities; and used one of them for refractometry and optical trapping applications.

First, we focused on the study of a new generation of FP cavities based on curved Bragg mirrors and a capillary tube in between to allow inserting the test sample –that can be homogeneous liquid or containing particles – to be optically characterized. Experimental results demonstrated the ability of this device to be used as a refractometer with a detection limit as low as 1.9×10^{-4} RIU in case of measuring nonlinear homogeneous liquids. Moreover, for liquid containing solid particles the ability of this device to trap micro particles with the effect of optical trapping and/or binding has been successfully demonstrated.

Second, another type of resonators that may support higher quality factor modes, which are the Whispering Gallery modes (WGMs) inside spherical resonators, is investigated. It has been demonstrated that the free space coupling technique is still able to access such modes with very low interacting evanescent tail supported by large droplets, in contradiction to what was believed previously in the literature. A quality factor as high as 6.7×10^{3} has been achieved, using a 1.16 mm diameter glycerol droplet supported by a hydrophobic surface made of Black Silicon coated with Teflon. This value is believed to be only limited by the absorption loss of glycerol in this wavelength range.

6.2 Recommendations

After doing the experimental work, one gains some experience and has the comprehension of some small -however important- details in the process. Here we present some hints that may be helpful during conducting future work.

For the refractometry experiments by the silicon FP cavities, in order to eliminate the effect of the environmental disturbance due to vibrational noise and/or thermal noise, the fibers should be glued to the silicon chip with a proper kind of glues. Precious lensed fibers should be avoided because they will be damaged in the process. Then, the cavity design should be tailored on the Gaussian beam distribution of a cleaved single mode fiber. Also the device should be packaged to protect it from dust and reduce the thermal variations.

For the optical trapping experiments, better trapping may be achieved if higher intensities of light are reached inside the cavity. This may be done by increasing the cavity finesse and reducing its insertion losses; which may be achieved by having better design and fabrication quality for the mirror, and coat the capillary tube by an antireflection coating to reduce the losses from reflections at the silica-air interfaces. A major improvement in the power levels can be done by using higher source powers. Using an Erbium Doped Fiber Amplifier (EDFA) can be more economical solution for wavelengths in the C and L bands instead of affording expensive high power laser sources.

6.3 Future prospects

The work that has been done in this thesis provides many axes for future investigation with very promising prospects. Indeed, this is an important field of research that has many hygienic, biomedical, environmental and industrial applications. Amongst these axes:

6.3.1 Perspectives for the curved Fabry-Perot cavity

For the first device of FP cavity with a micro-tube, it can be improved on the technological level, design level and application level. The technology aspect may include adopting totally different technological direction to improve the quality of the curved mirrors. Focused Ion Beam (FIB) might be used to etch the Bragg mirrors, which allows for dimensions with minimum feature sizes in the sub-micron range [3]. This reflects on the design aspect, as pushing the limits further gives more freedom in design. Also to get rid of the parasitic reflections at the silica-air interfaces of the capillary tube, it can be coated with an antireflection coating using (Atomic Layer Deposition) ALD; which may lead to reduce the parasitic reflection losses from the tube interface and improving the quality factor. But the possibility of causing internal parasitic Fabry Pérot cavities by this way has to be investigated.

For the application aspects, the possibility of achieving simultaneous trapping and spectral analysing of particles and cells seems very promising. It can be experimentally investigated by coupling a laser source at resonance along with a wide spectrum light from a broadband source, and record the spectrum on a spectrum analyser. This way, the particles can be optically trapped in order to immobilize them inside the area that has best light illumination in order to increase the efficiency of their sensing. Another promising field of applications is the liquid chromatography (LC). Our refractometer can be connected to the output tubing of a separation column to serve as a refractive index detector for the different separated analytes to obtain the chromatogram. Furthermore, it can be integrated with capillary columns [4] to have an on-column, non-destructive detector in a more compact LC system. Fig. 6.1 shows an example for the capillary columns available in the market with its dimensions. The diameter is in the range of hundreds of micrometers, which is rather compatible with our cavity lengths. But for a micro-tube with a width different from the optical fibers, this may cause the light to pass away from the axis of the column. If that can't be afforded, the possibility to have a two levels silicon chip may be investigated, but this comes on the expenses of needing additional mask.

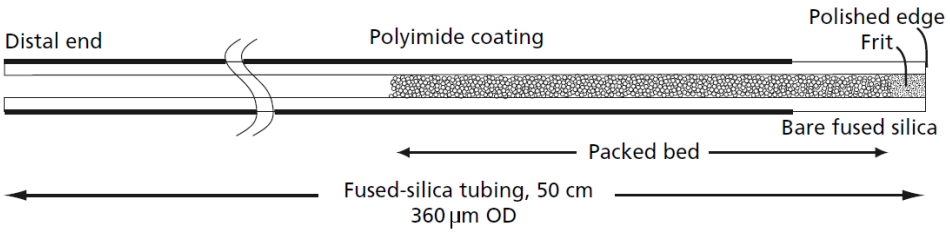

Fig. 6.1 IntegraFrit™ Column [5].

6.3.2 Perspectives for the resonators supporting WGM

For the second resonator of the liquid droplet supported by the hydrophobic surface, better quality factors might be obtained if other more suitable liquids are used. Essential properties of these liquids are to have: (1) Low vapor pressure in normal temperature-pressure conditions to have a slow evaporation rate. (2) Low optical absorption in the used wavelength range. (3) High contact angle to the used substrate. Another solution of this challenge may include adopting a hollow glass sphere to contain the liquid to be tested or the active material

for liquid core laser. But then the thickness of this hollow sphere should be thin enough to have part of the resonating wave passes inside the internal liquid.

As for the application aspects, small particles may be introduced inside the droplet to investigate the ability to trap them along the resonating wave at the equatorial region, which will introduce resonance shift, allowing sensing application.

6.4 References for chapter 6

[1] S. I. Shopova, I. M. White, Y. Sun, H. Zhu, X. Fan, G. Frye-Mason, A. Thompson, and S. Ja, "On-column micro gas chromatography detection with capillary-based optical ring resonators," Anal. Chem., vol. 80, pp. 2232 -2238, 2008.

[2] I. M. White, H. Oveys, and X. Fan, "Liquid-core optical ring-resonator sensors," Opt. Lett., vol. 31, pp. 1319, 2006.

[3] M. Malak, "A Contribution to Photonic MEMS: Study of Optical Resonators and Interferometers Based on All-Silicon Bragg Reflectors", PhD thesis, Université Paris-Est, 2011.

[4] T. Takeuchi, "Capillary columns in liquid chromatography," Anal Bioanal Chem, vol. 375, pp. 26-27, 2003.

[5] "Handling IntegraFrit™ Columns," Technical Note IF-1, new objective Inc., 2006.

APPENDIX

The calculation of the coupling quality factor Q_c is derived here in the case of coupling light into a sphere resonator with radius R_0 by means of a Gaussian Beam. We follow the same steps as in reference 1, but replacing the tapered fibre by a Gaussian beam propagating in the direction as illustrated in Fig. 5.16. The calculation steps described in chapter 5 will be detailed here with the genuine mathematical equations.

First the interaction strength $\kappa(S_{\min})$ at the point S_{min} of minimum separation between the sphere resonant field $\Psi_{\ell,m,n}$ and the input Gaussian beam $E(x,y,z)$, is given by the following overlap integral (similar to equation 5.5):

$$\kappa(S_{\min}) = \frac{k}{2}\int_x\int_y \left(n_s^{\,2} - n_0^{\,2}\right) E\ \Psi_{\ell,m,n}\ dxdy \tag{A.1}$$

where the field distribution of the input Gaussian beam is as follows [2],

$$E(x,y,z) = E_0 \frac{W_0}{W(z)} e^{-\frac{x^2+y^2}{W^2(z)}} e^{-ikz - ik\frac{x^2+y^2}{2R(z)} + i\eta(z)} \tag{A.2}$$

where

$$\begin{aligned} W^2(z) &= W_0^{\,2}\left[1+\left(\frac{z}{z_0}\right)^2\right] \\ R(z) &= z\left[1+\left(\frac{z_0}{z}\right)^2\right] \\ \eta(z) &= \tan^{-1}\left(\frac{z}{z_0}\right) \\ z_0 &= \frac{\pi W_0^{\,2} n_0 n_r}{\lambda} \end{aligned} \tag{A.3}$$

z_0 is the Rayleigh range, W_0 is the beam waist radius.

and the excited WGM has the field distribution

$$\Psi_{\ell,m,n}(r,\theta,\phi) = N_s \psi_r(r)\psi_\theta(\theta)\psi_\phi(\phi) \tag{A.4}$$

where the components for different coordinated are

$$\begin{aligned}
&\psi_r(r) = \begin{cases} j_\ell(kn_s r), & \mathrm{r} \le R_0 \\ j_\ell(kn_s R_0)e^{-\alpha_s(r-R_0)}, & \mathrm{r} > R_0 \end{cases} \\
&\psi_\theta(\theta) = e^{-\frac{m}{2}\theta^2} H_N\left(\sqrt{m}\,\theta\right), \qquad \mathrm{m} \gg 1 \gg \theta \\
&\psi_\phi(\phi) = e^{\pm im\phi}
\end{aligned} \tag{A.5}$$

and the coefficients are

$$\begin{aligned}
&\beta_\ell = \frac{\sqrt{\ell(\ell+1)}}{R_0} \\
&N = \ell - m \\
&N_s = \left\{ \frac{\pi}{m} 2^{N-1} N! R_0^{\,2} \left[\left(1 + \frac{1}{\alpha_s R_0}\right) j_\ell^{\,2}(kn_s R_0) - j_{\ell-1}(kn_s R_0)\, j_{\ell+1}(kn_s R_0) \right] \right\}^{-1/2} \\
&\alpha_s = \sqrt{\beta_\ell^{\,2} - k^2 n_0^{\,2}} \\
&k = 2\pi/\lambda
\end{aligned} \tag{A.6}$$

The integration in equation (A.1) has to be carried out over the extent of the sphere only, in a plane perpendicular to the Gaussian beam propagation direction (z axis) at the point S_{min}. The common phase is omitted for now:

$$\begin{aligned}
\kappa(S_{\min}) = \frac{k^2}{2\beta_0}\left(n_s^{\,2} - n_0^{\,2}\right) N_s E_0 \frac{W_0}{W(z)}. \\
\int_x \int_y j_\ell(kn_s r) e^{-\frac{x^2}{W(z)^2} - ik\frac{x^2}{2R(z)}} . H_N\left(\sqrt{m}\theta\right) e^{-\frac{m\theta^2}{2}} e^{-\frac{y^2}{W(z)^2} - ik\frac{y^2}{2R(z)}} dxdy
\end{aligned} \tag{A.7}$$

Rather than integrating along the y-axis in the overlap integral of the equation (A.7), we integrate along an axis coincident with the sphere perimeter. The sphere perimeter approximately follows the path $x = S_0 + y^2/2R_0$ in the vicinity of S_{min}. The y dependence of the field is projected onto the perimeter.

Although this perimeter axis and the x-axis are not orthogonal, they are nearly so over the region of interest, which is a tight extension around the point S_{min}, i.e. small y values (corresponding also to small θ angles). Calling the distance along the perimeter p as measured from the x-axis. Now using the expressions for the Gaussian field and the WGM

field with the exact substitution $p = R_0\theta$ in the integral, the separable part in y of the coupling integral I_y or more precisely I_p, becomes:

$$I_y \simeq I_p = \int_{-\infty}^{\infty} H_N\left(\frac{\sqrt{m}p}{R_0}\right) e^{-\frac{mp^2}{2R_0{}^2}} . e^{-\left(\frac{1}{W(z)^2}+i\frac{k}{2R(z)}\right)p^2} dp \qquad \text{(A.8)}$$

A useful formula for calculating the convolution of the Hermite–Gaussian $H_N(t)e^{\frac{-1}{2}t^2}$, with the Gaussian $e^{\frac{-q}{2}(u-t)^2}$ where q and u are arbitrary parameters is:

$$\int_{-\infty}^{\infty} H_N(t) e^{\frac{-1}{2}t^2} e^{\frac{-q}{2}(u-t)^2} dt$$
$$= \sqrt{\frac{2\pi}{q+1}}\left|\frac{q-1}{q+1}\right|^{N/2} H_N\left(\frac{qu}{\sqrt{|q^2-1|}}\right) . e^{\frac{-qu^2}{2(q+1)}} \qquad \text{(A.9)}$$

In our case we have:

$$t = \frac{\sqrt{m}p}{R_0}, \qquad u = 0, \qquad q = \frac{2R_0{}^2}{m}\left(\frac{1}{W(z)^2} + i\frac{k}{2R(z)}\right), \qquad dt = \frac{\sqrt{m}}{R_0}dp$$

And hence the separable part in p of the coupling integral renders to:

$$I_p = \frac{R_0}{\sqrt{m}}\sqrt{\frac{2\pi}{q+1}}\left|\frac{q-1}{q+1}\right|^{\frac{N}{2}} H_N(0) \qquad \text{(A.10)}$$

Now for the rest of the integral, it can be simplified by expanding the spherical Bessel function $j_\ell(kn_s r)$ in a Taylor series about the position $r = R_0$, since it is the only portion of the sphere mode closest to the sphere surface which contributes significantly to the coupling. Only the first two terms from the Taylor expansion are considered for easiness:

$$j_\ell(kn_s r) \simeq j_\ell(kn_s R_0) - (x - R_0) kn_s j'_\ell(kn_s R_0)$$
$$= j_\ell(kn_s R_0) - (x - R_0).\left[\frac{\ell}{R_0} j_\ell(kn_s R_0) - kn_s j_{\ell+1}(kn_s R_0)\right] \qquad \text{(A.11)}$$

The separable part in x of the coupling integral I_x inside the sphere then becomes

$$
\begin{aligned}
I_x &= \int_{S_0}^{\infty} \left(j_\ell\left(kn_s R_0\right) - \left(x - R_0\right)\left[\frac{\ell}{R_0} j_\ell\left(kn_s R_0\right) - kn_s j_{\ell+1}\left(kn_s R_0\right)\right]\right). e^{-\frac{x^2}{W(z)^2} - ik\frac{x^2}{2R(z)}} dx \\
&= \left[\left(1+\ell\right) j_\ell\left(kn_s R_0\right) - R_0 kn_s j_{\ell+1}\left(kn_s R_0\right)\right] \int_{S_0}^{\infty} e^{-\left(\frac{1}{W(z)^2} + i\frac{k}{2R(z)}\right)x^2} dx \\
&\qquad - \left[\frac{\ell}{R_0} j_\ell\left(kn_s R_0\right) - kn_s j_{\ell+1}\left(kn_s R_0\right)\right] \int_{S_0}^{\infty} x \,.\, e^{-\left(\frac{1}{W(z)^2} + i\frac{k}{2R(z)}\right)x^2} dx \\
&= B \int_{S_0}^{\infty} e^{-\left(\frac{1}{W(z)^2} + i\frac{k}{2R(z)}\right)x^2} dx - D \int_{S_0}^{\infty} x \,.\, e^{-\left(\frac{1}{W(z)^2} + i\frac{k}{2R(z)}\right)x^2} dx
\end{aligned}
\tag{A.12}
$$

where

$$
\begin{aligned}
B &= \left(1+\ell\right) j_\ell\left(kn_s R_0\right) - R_0 kn_s j_{\ell+1}\left(kn_s R_0\right) \\
D &= \frac{\ell}{R_0} j_\ell\left(kn_s R_0\right) - kn_s j_{\ell+1}\left(kn_s R_0\right)
\end{aligned}
\tag{A.13}
$$

Using the known formula for the Gaussian function integration [3]:

$$
\int e^{-cx^2} dx = \sqrt{\frac{\pi}{4c}} erf\left(\sqrt{c}x\right) \tag{A.14}
$$

where we have in our case:

$$
c = \frac{1}{W(z)^2} + i\,\frac{k}{2R(z)} = \frac{m}{2{R_0}^2} q
$$

and the integral in x then becomes:

$$
\begin{aligned}
I_x &= B \int_{S_0}^{\infty} e^{-cx^2} dx - D \int_{S_0}^{\infty} x \,.\, e^{-cx^2} dx \\
&= B \,.\, \sqrt{\frac{\pi}{4c}} erf\left(\sqrt{c}x\right)\Big|_{S_0}^{\infty} - D\left(\frac{-1}{2c}\, e^{-cx^2}\right)\Big|_{S_0}^{\infty} \\
&= B \,.\, \sqrt{\frac{\pi}{4c}} \left(1 - erf\left(\sqrt{c}S_0\right)\right) - D \,.\, \frac{-1}{2c}\left(0 - e^{-cS_0{}^2}\right) \\
&= B \,.\, \sqrt{\frac{\pi {R_0}^2}{2mq}} \left(1 - erf\left(\sqrt{\frac{mq}{2{R_0}^2}} S_0\right)\right) - D \,.\, \frac{{R_0}^2}{mq}\left(e^{-\frac{m}{2{R_0}^2} q S_0{}^2}\right)
\end{aligned}
\tag{A.15}
$$

noting that $erf\left(\infty\right) = 1$ and $e^{-\infty} = 0$.

Then the overall integral in the perpendicular plane becomes:

$$\kappa(S_{\min}) = \frac{k^2}{2\beta_0}\left(n_s{}^2 - n_0{}^2\right) N_s E_0 \frac{W_0}{W(z)} \cdot \frac{R_0}{\sqrt{m}} \sqrt{\frac{2\pi}{q+1}} \left|\frac{q-1}{q+1}\right|^{\frac{N}{2}} H_N(0) \cdot \left[B\sqrt{\frac{\pi R_0{}^2}{2mq}} \left(1 - erf\left(\sqrt{\frac{mq}{2R_0{}^2}} S_0\right)\right) - \frac{R_0{}^2}{mq} . De^{-\frac{m}{2R_0{}^2} q S_0{}^2} \right] \tag{A.16}$$

Now the net interaction strength is gotten by integrating $\kappa[S(z)]$ over the whole interaction region along *z*-axis (not in the perpendicular plane only), weighted by the phase mismatch between the propagation constants of the input beam and the WGM in the direction of propagation, which is the *z*-axis in this case [4]:

$$\kappa = \int_{-\infty}^{\infty} \kappa[S(z)] e^{-i\Delta\beta z} \tag{A.17}$$

where $\Delta\beta = k - \frac{m}{R_0}$

We consider the separation *S* varying in *z* by the approximate surface equation

$$S(z) = S_0 + \frac{1}{2R_0}(z - z_{0\_sph})^2 \tag{A.18}$$

where z_{0_sph} is the shift between the beam waist and the sphere center or the point S_{min}.

Using equation (A.16) to get the whole interaction strength in equation (A.17), we get:

$$\kappa = \frac{k^2}{2\beta_0}\left(n_s{}^2 - n_0{}^2\right) N_s W_0 \frac{R_0}{\sqrt{m}} H_N(0) \int_z \frac{E_0(z)}{W(z)} \sqrt{\frac{2\pi}{q(z)+1}} \left|\frac{q(z)-1}{q(z)+1}\right|^{\frac{N}{2}} \cdot \left[B\sqrt{\frac{\pi R_0{}^2}{2mq(z)}} \left(1 - erf\left(\sqrt{\frac{mq(z)}{2R_0{}^2}} S(z)\right)\right) - \frac{R_0{}^2}{mq(z)} . De^{-\frac{m}{2R_0{}^2} q(z).S^2(z)} \right] . e^{-i(\Delta\beta z - \xi(z))} dz \tag{A.19}$$

After solving the integral, possibly numerically by Matlab, the coupling quality factor can be calculated from [1]:

$$Q_c = \frac{m\pi}{\kappa^2} \tag{A.20}$$

Note that this derivation implicitly assumes that the presence of the sphere doesn't disturb the GB as we use the field equations for both the GB and the WGM without any perturbation. This assumption has been proven to be valid for separation between the GB and the resonator more than $1.5*W_0$ through observation of the field distributions obtained by the numerical simulations using HFSS.

References for the appendix

[1] B. E. Little, J. P. Laine, and H. A. Haus, "Analytic Theory of Coupling from Tapered Fibers and Half-Blocks into Microsphere Resonators," J. Lightwave Technol., vol. 17, pp. 704-715, 1999.

[2] B. E. A. Saleh, M. C. Teich, *Fundamentals of Photonics*, John Wiley & Sons, 1991, chapter 3.

[3] K. Gieck, and R. Gieck, *Engineering Formulas*, 7th edition, McGraw-Hill, 1997.

[4] B. E. Little, S. T. Chu, H. A. Haus, J. Foresi, and J.-P. Laine, "Microring resonator channel dropping filters," J. Lightwave Technol., vol. 15, pp. 998-1005, 1997.

PUBLICATIONS LIST

Journal papers

1. **Noha Gaber**, Maurine Malak, Frédéric Marty, Dan E. Angelescu, Elodie Richalot and Tarik Bourouina, "Particles Optical Trapping and Binding in Optofluidic Stable Fabry–Pérot Resonator with Single-Sided Injection," Lab Chip, Royal Society of Chemistry (RSC) vol. 14, pp. 2259-2265, 2014.
2. **Noha Gaber**, Maurine Malak, Xichen Yuan, Kim Ngoc Nguyen, Philippe Basset, Elodie Richalot, Dan Angelescu and Tarik Bourouina, "On the free-space Gaussian beam coupling to droplet optical resonators," Lab Chip, Royal Society of Chemistry (RSC) vol. 13, pp. 826-833, 2013.
3. Maurine Malak, **Noha Gaber**, Frédéric Marty, Nicolas Pavy, Elodie Richalot, and Tarik Bourouina, "Analysis of Fabry-Pérot Optical Micro-cavities Based on Coating-free All-Silicon Cylindrical Bragg Reflectors," Optics Express, Optical Society of America (OSA) vol. 21, pp. 2378-2392, 2013.
4. **Noha Gaber**, Yasser Sabry, Frédéric Marty, Dan E. Angelescu, Elodie Richalot and Tarik Bourouina, "On the volume refractive index measurement of liquids and complex fluids in a stable optofluidic micro-cavity", Light: Science and Applications, Nature Publishing Group (NPG), 2014, Under preparation.

International conference

1. **Noha Gaber**, Ajith Sivadasan, Maurine Malak, Antoine Leblanc, Yves-Alain Peter, Dan E. Angelescu, Elodie Richalot, Tarik Bourouina, "Localized Particles Trapping in Optofluidic Stable Fabry-Pérot Resonator with Single Sided Injection", 3rd international conference on Optofluidics, OPTOFLUIDICS 2013, Hong-Kong, 17 August 2013. *

***Winner of the best paper award in the conference.*

Resumé : Ce travail porte sur l'étude de propriétés optiques des fluides à échelle micrométrique. A cet effet, nous avons conçu, réalisé et étudié différents types de micro-résonateurs optofluidiques, sous forme de laboratoires sur puce. Notre analyse est fondée sur la modélisation analytique et numérique, ainsi que sur des mesures expérimentales menées sur des micro-cavités optiques; nous utilisons l'une d'entre elles pour des applications de réfractométrie de fluides homogènes et de fluides complexes ainsi que pour la localisation par piégeage optique de microparticules solides. Nous nous sommes d'abord concentrés sur l'étude d'une nouvelle forme de micro-cavité Fabry-Pérot basée sur des miroirs courbes entre lesquels est inséré un tube capillaire permettant la circulation d'une solution liquide. Les résultats expérimentaux ont démontré la capacité de ce dispositif à être utilisé comme réfractomètre avec un seuil de détection de $1{,}9 \times 10^{-4}$ RIU pour des liquides homogènes. De plus, pour un liquide contenant des particules solides, la capacité de contrôler la position des microparticules, par des effets de piégeage optique ou de liaison optique, a été démontrée avec succès. Dans un second temps, un résonateur optique est formé simplement à partir d'une goutte de liquide disposée sur une surface super-hydrophobe. La forme quasi-sphérique résultante est propice à des modes de galerie. Il est démontré que, jusqu'à des tailles de gouttelettes millimétriques, la technique de couplage en espace libre est toujours en mesure d'accéder à ces modes à très faible queue évanescente d'interaction, contrairement à ce qu'indiquait jusqu'ici la littérature. De tels résonateurs optofluidiques à gouttelette devraient trouver leur application notamment comme capteur d'environnement de l'air ambiant ou encore comme incubateur de micro-organismes vivants pouvant être suivis par voie optique.

Mots-clés : optofluidique, micro-résonateur optique, laboratoire sur puce, analyse des liquides, résonateur Fabry-Pérot, surfaces incurvées, résonateur à gouttelette.

Abstract: This work focuses on the study of optical properties of fluids at the micrometer scale. To this end, we designed, implemented and studied different types of *optofluidic* micro-resonators in the *Lab-on-Chip* format. Our analysis is based on analytical and numerical modeling, as well as experimental measurements conducted on optical microcavities; we use one of them for refractometry applications on homogeneous fluids and on complex fluids, as well as for the localization of solid microparticles by optical trapping. We first focused on the study of a new form of Fabry-Perot micro-cavity based on curved mirrors between which a capillary tube is inserted for injecting a fluidic solution. Experimental results demonstrated the ability of this device to be used as a refractometer with a detection limit of 1.9×10^{-4} RIU for homogeneous liquids. Furthermore, for liquid containing solid particles, the ability to control the microparticles position either by optical trapping or optical binding effects has been successfully demonstrated. In a second step, an optical resonator is simply formed from a liquid droplet placed on top of a superhydrophobe surface. The resulting quasi-spherical shape supports resonant whispering gallery modes. It is shown that, up to millimeter size droplets, the proposed technique of free-space coupling of light is still able to access these modes with very low evanescent tail interaction, contrary to what was indicated in the literature so far. Such optofluidic droplet resonators are expected to find their applications for environmental air quality monitoring, as well as for incubator of living micro-organisms that can be monitored optically.

Keywords: optofluidics, optical micro-resonators, lab on a chip, liquid analysis, Fabry-Pérot cavity, curved surfaces, droplet resonator.